THE IMPACT OF EXTREME STORM WAVES AT THE COAST; THE ROLE OF INFRAGRAVITY WAVES

by

OLIVER BILLSON

A thesis submitted to The University of Liverpool in partial fulfilment of the requirements for the degree of

DOCTOR OF PHILOSOPHY

March 2021

Authors Declaration

I declare that this thesis entitled 'The impact of extreme storm waves at the coast; the role of infragravity waves' and the work presented in it are my own work. The material contained in the thesis has not been presented, nor is currently being presented, either wholly or in part, for any other degree or qualification. The word count does not exceed 100,000 words.

This copy of the thesis has been supplied on condition that anyone who consults it is understood to recognise that its copyright rests with its author and that no quotation from the thesis and no information derived from it may be published without the author's prior consent.

Abstract

Infragravity (IG) waves are long period waves with frequencies lower than wind-waves and swell, usually in the frequency band 0.003 to 0.05 Hz. IG waves are known to dominate hydrodynamic and sediment transport processes close to the shoreline on low sloping sandy beaches, especially when the incoming swell and wind-driven waves (incident waves) are large. However, in extreme wave conditions, how their importance varies on coarser grain sized and steeper beaches, and with different mixes of incoming swell and wind-waves, is largely unknown.

Here, a new dataset comprising in-situ and remote observations from five contrasting sites (one low-sloping sandy beach, two steep gravel beaches and two compound/mixed sand and gravel beaches), under extreme wave conditions is used to assess infragravity response across a wider range of wave heights & periods, beach slopes and grain sizes than has been previously explored. The beaches studied ranged in slope from $\tan\beta = 0.02 - 0.35$ with median grain sizes (D_{50}) of between $0.25 - 60$ mm. During the experiments significant wave heights (H_s) of up to 7 m and peak periods (T_p) up to 20 s were observed. During the five storms recorded, waves in excess of the 95th percentile of the long-term record of H_s were observed at all sites, with waves representative of a 1-in-1, 1-in-5, 1-in-10, 1-in-20 and 1-in-40 year event at the five sites respectively.

Video observations of a 1-in-40 year storm, '*Emma*', impacting a steep gravel beach revealed that significant infragravity swash height (S_{ig}) dominated over significant gravity swash height (S_g) at the shoreline when offshore wave height (H_0) exceeded 1.5 m, where 'dominance' was defined by the ratio of S_{ig}/S_g exceeding 1. S_{ig} increased linearly with offshore wave height (H_0), as has been reported in previously published field work on sandy beaches. However, for a given wave height, S_{ig} was between one third and three times larger on the steep gravel beach than values quoted in the literature for sandy beaches.

Observations collected on the steep gravel beach during storm '*Emma*' were compared to data collected at an additional four sites (a low-sloping sandy beach, a second steeper gravel beach and two compound/mixed sand and gravel beaches). S_{ig} at the shoreline in excess of 0.5 m was consistently observed at all five contrasting beaches. The largest infragravity swash heights were observed at the steeper gravel beach (S_{ig} up to 11.4 m), followed by the low-sloping sandy beach (S_{ig} up to 3.2 m), and the less steep gravel beach (S_{ig} up to 2.6 m) and were lowest at the compound/mixed sites. Due to contrasting incident wave breaking and dissipation processes, infragravity frequencies were observed to be most dominant over gravity frequencies on the low-sloping sandy beach (S_{ig}/S_g up to 4.4), occasionally dominant on the gravel beaches (S_{ig}/S_g up to 2.5), and rarely dominant on the compound/mixed beaches (S_{ig}/S_g up to 1.1).

An existing equation commonly used to parameterize S_{ig} on sandy beaches was tested on the new dataset, performing well on data from the sandy beach but less well on data from the gravel beach. An existing equation commonly used to parametrize runup on gravel beaches was modified to produce a new gravel specific parametrization of S_{ig}, which performed well on the gravel sites and less well on the sandy site. Both equations performed poorly when applied to the dataset combining sand and gravel beaches. H_0^2T, proportional to deep water wave power, was found to accurately predict S_{ig} on both the sand and gravel beaches, demonstrating that, under extreme storm wave conditions, combined wave height and period are the main drivers of infragravity oscillations at the shoreline, with the beach morphology playing a secondary role.

In-situ observations were collected seaward of the incident wave breakpoint by bed-mounted acoustic Doppler current profilers and through the surf zone by intertidal arrays of pressure transducers at two of the five sites (the low-sloping sandy beach and the less steep of the two gravel beaches). Analysis revealed that energy transferred to the IG band seaward of the surf zone at the sandy beach and landward of breakpoint

at the gravel beach. The surf beat similarity parameter ($\xi_{Surfbeat}$) indicated that bound long wave release was the dominant IG wave generating mechanism on the low sloping sandy beach ($\xi_{Surfbeat} < 0.05$) whilst breakpoint forcing was the dominant mechanism on the steep gravel beach ($\xi_{Surfbeat} > 0.1$).

The findings presented in this thesis highlight the importance of collecting field data over a wide range of conditions. When deep water significant wave height (H_0) exceeds 2 m, IG energy dominates the inner surf zone and swash on both sand and gravel beaches. Therefore, in addition to their well-known importance on sandy sites, infragravity waves are also implicated in the inundation and erosion of gravel beaches during storms.

<u>**Contents**</u>

PhD Outputs

First author papers

Billson, O., Russell, P., Davidson, M., Poate, T., Amoudry, L. O., and Williams, M. E., 2020. In-situ observations of infragravity response during extreme storms on sand and gravel beaches. Journal of Coastal Research 95(sp1), 382-386. DOI: https://doi.org/10.2112/SI95-074.1

Billson, O., Russell, P., Davidson, M., Wiggins, M., McCarroll, R. J., Poate, T., Leonardi, N., 2019b. Observations of infragravity dominance in the swash zone of a steep gravel beach. Coastal Sediments 2019, Proceedings of the 9th International Conference, St Petersburg, Florida, U.S.A, 1866-1878. DOI: https://doi.org/10.1142/9789811204487_0161

Billson, O., Russell, P., & Davidson, M., 2019a. Storm waves at the shoreline: When and where are infragravity waves important? Journal of Marine Science and Engineering, 7(5), 139. DOI: https://doi.org/10.3390/jmse7050139

Co-authored papers

Brewin, R. J. W., Cyronak, T., Bresnahan, P. J., Andersson, A. J., Richard, J., Hammond, K., **Billson, O.**, Mora, L. D., Jackson, T., Smale, D., Dall'Olmo, G.,

2020. Comparison of Two Methods for Measuring Sea Surface Temperature

When Surfing. Oceans, 1, 6-26. DOI: https://doi.org/10.3390/oceans1010002

McCarroll, R. J., Masselink, G., Wiggins, M., Scott, T., **Billson, O.**, Conley, D. C.,

Valiente, N. G., 2019. High-efficiency gravel longshore sediment transport and

headland bypassing over an extreme wave event. Earth Surface Processes and

Landforms, 44, 13, 2720-2727. DOI: https://doi.org/10.1002/esp.4692

Brewin, R. J. W., Hyder, K., Andersson, A.J., **Billson, O.**, Bresnahan, P. J., Brewin,

T. G., Cyronak, T., Dall'Olmo, G., Mora, L., Graham, G., 2017. Expanding

aquatic observations through recreation. Frontiers in Marine Science, 4, 351.

DOI: https://doi.org/10.3389/fmars.2017.00351

Brewin, R. J. W., de Mora, L., **Billson, O.**, Jackson, T., Russell, P., Brewin, T. G.,

Shutler, J. D., Miller, P. I., Taylor, B. H., Smyth, T. J., 2017. Evaluating

operational AVHRR sea surface temperature data at the coastline using surfers.

Estuarine, Coastal and Shelf Science, 196, 276-289. DOI:

https://doi.org/10.1016/j.ecss.2017.07.011

McCarroll, R. J., Masselink, G., Wiggins, M., Scott, T., **Billson, O.**, Conley, D. C.,

2019. Gravel beach cross- and alongshore response to an extreme event: beach

length and headland proximity controls. Coastal Sediments 2019, Proceedings of

the 9th International Conference, St Petersburg, Florida, U.S.A, 2735–2745.

DOI: https://doi.org/10.1142/9789811204487_0234

Conference Presentations

Billson, O., Russell, P., Davidson, M, Poate, T., 2019c. Storm waves at the coast: A new dataset with a wide variety of swell-dominated vs wind-wave dominated conditions. 2nd International Workshop on Waves, Storm Surges, and Coastal Hazards, 16th International Workshop on Wave Hindcasting and Forecasting, Melbourne, Australia, November 2019.

Billson, O., Russell, P., Davidson, M, Poate, T., 2019b. Observation of coastal storms, over an unprecedented range of wave and beach conditions. 13th Graduate Climate Conference, Woods Hole, Massachusetts, U.S.A, November 2019.

Billson, O., Russell, P., Davidson, M. A., Wiggins, M., McCarroll, R. J., Poate, T., Leonardi, N., 2019a. Observations of infragravity dominance in the swash zone of a steep gravel beach. 9th International Conference on Coastal Sediments, St Petersburg, Florida, U.S.A, May 2019.

Billson, O., Russell, P., Davidson, M. A., Masselink, G., Inch., K., 2017. Coastal response to extreme storms: the role of infragravity waves. 13th UK Young Coastal Scientists and Engineers Conference (YCSEC), Bath, UK, March 2017.

McCarroll, R. J., Masselink, G., Wiggins, M., Scott, T., **Billson, O.**, Conley, D. C., 2019. Gravel beach cross- and alongshore response to an extreme event: beach

length and headland proximity controls. 9th International Conference on Coastal

Sediments, St Petersburg, Florida, U.S.A, May 2019.

Published Datasets

McCarroll R. J., Masselink, G., Wiggins, M., Scott, T., **Billson, O.**, Conley, D. C.,

Valiente, N. G., Storm Emma, Start Bay, 2018 (U.K. Natural Environment

Research Council, Grant Number NE/M004996/1; BLUE-coast project). DOI:

https://doi.org/10.24382/c3ee-6p96

Unpublished Datasets

Poate, T. (2008 – 2011), Prodger, S. (2012 – 2016), **Billson, O. (2017 – 2020)**,

Collection and analysis of monthly sediment record, Perranporth (2008 –

Present).

Meetings and Seminars

BLUEcoast Annual meeting 2019 (Presentation) – Storm Waves at the Shoreline:

When and Where are Infragravity Waves Important? Plymouth University,

Devon, U.K. July 2019.

University of Liverpool Postgraduate Research Conference (Presentation): Storm
Waves at the Shoreline: When and Where are Infragravity Waves Important?
Liverpool, U.K. May 2019.

BLUEcoast Work Package 1 meeting 2018 (Presentation) - Observations of
variability in infragravity run-up under extreme forcing. Plymouth University,
Devon, U.K. November 2018.

University of Liverpool Postgraduate Research Conference (Presentation): Coastal
response to extreme storms: The role of infragravity waves. Liverpool, U.K.
May 2018.

Stokenham Parish Council/South Devon and Channel Shellfisherman (Combined
meeting), (Presentation): The Impact of a 100-year storm on Start Bay.
Stokenham, Devon, U.K. April 2018.

BLUEcoast Annual meeting 2017 (Presentation): Monitoring high energy conditions
and impacts at Perranporth during January and February 2017. Slapton Field
Centre, Devon, U.K. October 2017.

Penhale Special Area of Conservation (SAC) Management Group, Perranporth,
Cornwall, U.K. (Presentation): Monitoring typical winter conditions and
resultant impacts to the beach and dune faces at Penhale during January and
February 2017. Perranporth, Cornwall, U.K. July 2017.

University of Liverpool Postgraduate Research Conference (Presentation): Coastal

response to extreme storms: The role of infragravity waves. Liverpool, U.K.

May 2017.

Grants Awarded

Journal of Marine Science and Engineering Travel Awards for Postdoctoral

Researchers and Ph.D. Students, 2020, one of two CHf. 800 travel grants

awarded to attend The International Coastal Symposium, Seville, Spain, May

2021.

13th Graduate Climate Conference (GCC), 2019, $325 travel grant awarded to attend

GCC, Graduate Climate Conference, Woods Hole Oceanographic Institute,

Massachusetts, U.S.A. November 2019.

Plymouth Marine Science and Education Foundation (PlyMSEF), Grant-in-aid

2018/19, £400 awarded to attend the Coastal Sediments 2019 conference in

Florida, USA. January 2019.

Prizes Won

Plymouth Marine Science and Education Foundation 'Making Waves' Conference

'Best Presentation', runner up. Plymouth Marine Laboratory, Devon, U.K.

February 2020.

Plymouth University 'Images of Research Competition 2019', one of twelve entries

   selected for the 2019/2020 Diversity and Wellbeing Calendar. January 2019.

University of Liverpool Postgraduate Research Conference, 'Best Presentation' (£50

   prize), Liverpool, U.K. May 2018.

Training Courses Attended

1st and 2nd Annual Low Carbon Eco-Inventory Workshop, Brathay, Cumbria, U.K.

   June 2018/19.

Xbeach Basic Course: Morphodynamic modelling during storms, Deltares, Delft,

   Netherlands, October 2017.

LANTRA All-Terrain Vehicle – Sit – Astride Award. Looe, Cornwall, U.K. March

   2017.

SALT: Supporting Assessment, Learning and Teaching, Plymouth University,

   Devon, U.K., January 2017.

Demonstrating

Managing Human Impacts in the Marine Environment. Supervision of 2nd year

   undergraduate field trip to Seaton Beach, Cornwall, U.K. March 2018/19/20.

Research Skills and Methods. Assisted in master's computing workshops (MATLAB and Arc GIS), University of Plymouth, Devon, U.K. October 2019.

Waves, tides and coastal dynamics. Assisted with 2nd year undergraduate dry-sieving practical assessment, University of Plymouth, Devon, April 2018.

Consultancy

Assisted Coastal Marine Applied Research (CMAR), drifter experiment. Ventnor Harbour, Isle of Wight, U.K. November 2017.

Assisted Coastal Marine Applied Research (CMAR), North Devon Biosphere Tidal Survey. Barnstaple, U.K. December 2018.

Field Work

90 days field experience - See Appendix A for detailed breakdown

- 5 Storm surveys (2016 – 2019)
- Monthly topographic/ sediment sample collection
- Single Beam Bathymetric (land crew)
- UAV surveys (ground crew)
- Depth to bedrock (Trimino) – BLUEcoast

Media

Interviewed by BBC Radio Devon during storm '*Emma*', March 2018.

List of Tables

List of Figures

List of Abbreviations and Symbols

BEE   Beesands

CAM   Camber

CSL   Chesil

D   Storm Duration

DGPS   Differential global positional system

I   Meteorological independence criterion

MHWS   Mean high water springs

MLWS   Mean low water springs

MMR   Minsmere

ODN   Ordnance Datum Newlyn

PPT   Perranporth

POT   Peaks over threshold

PSD   Power Spectral Density

PT   Pressure sensor

PUV   Co-located pressure and velocity instrument rig

P2016   Poate predictor of run-up (Poate et al., 2016)

RCRU   Rapid Coastal Response Unit

RMSE   Root-mean-squared error

SWL   Still Water Level

S2006   Stockdon predictor of run-up (Stockdon et al., 2006)

X-beach-G   Gravel specific module of X-beach

C   Constant

D_{50} Median sediment grain size

H_0 Deep water (offshore) significant wave height

$H_{0\_95\%}$ 95th percentile wave height

$H_{(Thresh)}$ Storm threshold

IG   Infragravity

L_0 Deep water (offshore) wavelength

N   Number of Observations

p Statistical significance

P   Wave Power

R^2 Goodness of fit/ correlation squared

R2%	2% exceedance level of run-up
S	Significant swash height
S_g	Significant swash height (gravity band)
S_{ig}	Significant swash height (infragravity band)
T	Wave Period
$\tan \beta$	Beach Gradient
T_p	Peak Wave Period
$T_{p\_95\%}$	95th percentile wave period
α	Proportional to
Δf	bandwidth
ξ	Iribarren number
σ^2	Vertical runup variance

Acknowledgements

The author wishes to thank The University of Liverpool's School of Environmental Sciences, Department for Geography and Planning. In addition, all members of Plymouth Universities' Coastal Processes research group (CPRG) as well as the Plymouth Coastal Observatory and Channel Coast Observatory. The author also gratefully acknowledges the input of Professor Janet Hooke and Professor Nadia Sénéchal whilst examining the thesis and thanks them for an insightful and stimulating discussion during The Viva.

First and foremost, I must thank my supervisory team of Paul Russell, Mark Davidson Nicoletta Leonardi and Andy Plater. Paul has been everything one could wish for in a supervisor and more! Being ever available and getting back to my emails almost before I've sent them. After supervising my Master's project, it was Paul who suggested I apply for this PhD back in 2016, recognising ability in me that I didn't know I had. Thank you for getting me over the line and doing it all with a smile! I thank Mark for patiently working through the more technical aspects of my PhD and making complex maths digestible. It was always great talking triathlon too! Thanks also to Gerd Masselink for offering his expert opinion and supporting my attendance of international conferences.

My Liverpool supervisors have always made me feel hugely welcome at Uo. Thanks to Nicoletta for keeping me on track with the Liverpool PGR system and her support with the publications associated with this PhD. Andy has been a fabulous supervisor, always knowing the right thing to say, even in times of minor crisis. He has always made time for me on my visits to Liverpool and worked hard to make me feel like one of '*the gang*'. He provided me with the opportunity to attend conferences in Florida, Boston and Melbourne for which I am eternally grateful. It has been a pleasure working with you Andy and look forward to catching up more in the future. Thanks too, to my colleagues at Liverpool, Jenny Brown, Ben Phillips, Charlotte Lydon and Doug McInnes.

Thanks go to all members of CPRG past and present but in particular, Kris Inch, Olivier Burvingt, Ben Hall and Sam Prodger for their assistance with storm surveys and help me get started with the PhD. Also, to Raph Krier for checking in on me from the other side of the world! Thank you to the Plymouth Coastal Observatory crew for letting me gate crash your office when I needed a change of scenery, a trip downstairs always put a smile on my face.

The post-doctoral team at Plymouth have been particularly supportive of my studies. I offer thanks to Tim Poate for teaching me everything I know about how to collect and process data

1 <u>Introduction</u>

1.1 <u>Context and motivation</u>

Globally, the coastal zone is characterised by high population density, significant socio-economic activity and a focusing of critical infrastructure (Vousdoukas et al., 2018) as well as some of the most dynamic weather on the planet. Increasing human demand on the world's oceans, termed the *Blue Acceleration* by Jouffray et al. (2020), has rendered coastal environments among the most imminently threatened by global climate change. In the U.K. expected annual damages resulting from coastal flooding are estimated to more than double from £540 million at present to £1.2−1.7 billion by the 2080s (Haigh et al., 2020). In particular, extreme waves associated with storms can lead to the destruction of coastal environments. Projected sea-level rise of up to 1.1 m by 2100 (IPCC, 2019) will result in more wave energy reaching further inland, exacerbating existing inundation and erosion. Over recent decades increases have been reported in the significant deep water wave height (H_0) (e.g. Dodet et al., 2010; Young et al., 2011; Bertin et al., 2013) and storminess (e.g. Donat et al., 2011; Mölter et al., 2016; Martinez-Alvarado et al., 2018; Ruosteenoja et al., 2019) impacting northern Europe. In particular extreme waves (defined as the 90th percentile) in parts of the North Atlantic Ocean increased by up to 0.8 cm/year between 1985 – 2018 (Young and Ribal, 2019) and are forecast to increase by up to 10% by 2100 (Meucci et al., 2020; Wolf et al., 2020). In addition to height, wave climate is comprised of wave period (T) and direction, meaning that climatic trends

are more holistically represented by combinations of these terms. For example, deep

water wave power (which, in linear wave theory is proportional to the square of deep

water wave height multiplied by the period, $H_0^2 T$) was identified as a 'potentially

valuable climate change indicator' by Reguero et al. (2019). They reported a 0.26 %

increase in the deep water wave power of the Atlantic Ocean and an increase of 0.47

% globally between 1948 – 2008 (Figure 1-1).
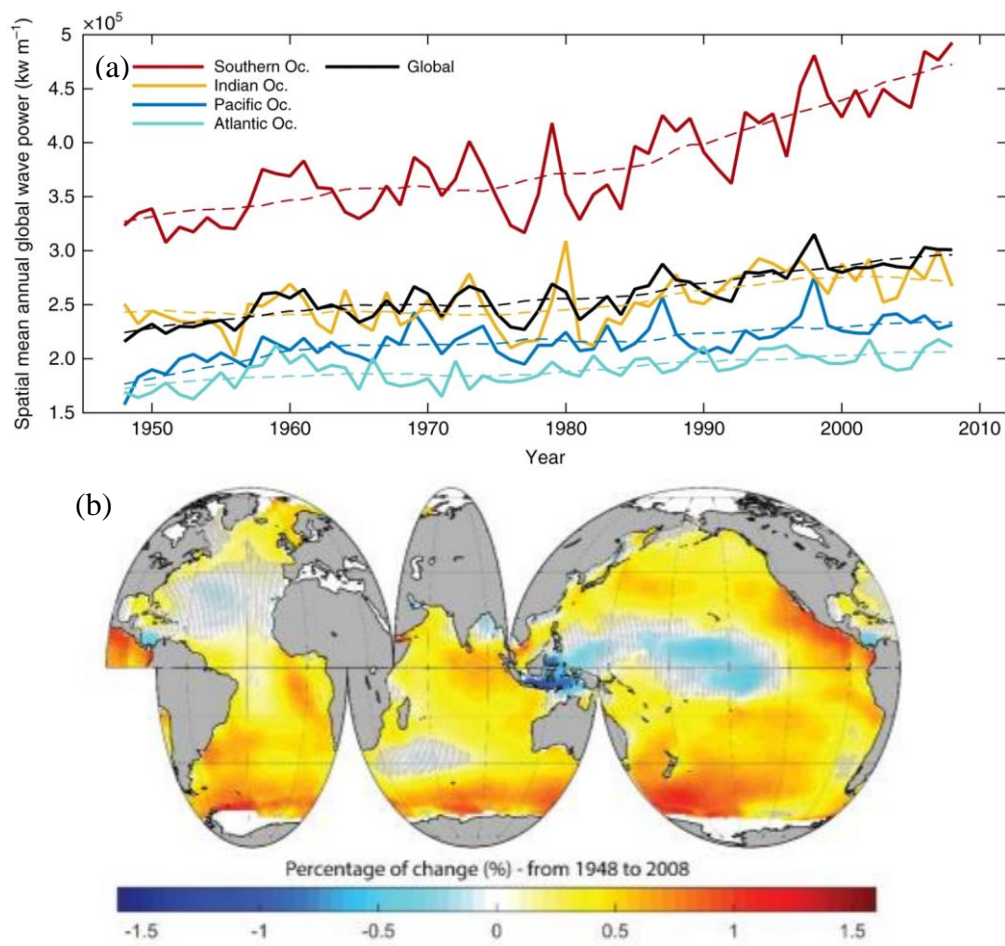
Figure 1-1 Trends in deep water wave power presented by Reguero et al. (2019): (a) Spatial mean annual wave power calculated globally and by ocean basin. Dashed lines represent 10-year moving averages. Mean regional wave power is calculated as the spatial average of each historical wave power time series. Their Figure 1. (b) Spatial trend (percent change per year) in mean wave power from 1948 to 2008. Hatched areas represent points that are not statistically significant at the 95% confidence level. Their Supplementary Figure 5.

Of particular importance during storms, infragravity (IG) waves, which occur at frequencies of between 0.003 – 0.05 Hz, are known to dominate the inner surf zone of sandy dissipative beaches under high energy wave conditions (e.g. Guza and Thornton, 1982; Russell, 1993; Ruessink et al., 1998b; Fiedler et al., 2015; Inch et al., 2017; Bertin et al., 2020). IG waves communicate storm information from the deep ocean to the shoreline, playing a crucial role in the hydrodynamics (e.g., Elgar et al., 1992; Reniers et al., 2002; Guedes et al., 2013), inundation (e.g., Roelvink et al., 2009) and beach/dune erosion (e.g., Russell, 1993; de Bakker et al., 2016) of sandy beaches (Figure 1-2).

Figure 1-2 Upper Left Panel: Author surveying severely eroding sand dunes, Crantock, Cornwall U.K. October 2019. (Photograph, Simon Hird); Upper Right Panel: Coastal defenses overtopping, Teignmouth Devon, U.K. February 2019. (Photograph, Author); Lower Panel: Storm erosion inflicted over a single high tide, Beesands, Devon, U.K. February 2018. (Photograph, Author).

Gaining an understanding of the influence of IG waves on hydrodynamics and sediment transport is crucial in the prediction of shoreline change and resultant coastal management decisions (Bertin et al., 2018). However, understanding of how IG waves vary on different beach types with variable swell and wind-wave dominance is restricted by a lack of observational datasets. The timing of many previous field campaigns has been governed by funding, staffing and resource constraints and carried out in the hope of, rather than targeted at, a specific storm event. As a result, only a few studies have successfully captured an extreme storm wave event (e.g., Senechal et al., 2011a; Fiedler et al., 2015; Bertin et al., 2020). de Bakker (2016) suggested that a more successful approach for obtaining such measurements would be a 'quick-response unit', whereby instruments are installed when a storm is approaching. As such, the research presented here targeted data collection around specific storm wave conditions. By developing an instrument array and deployment technique capable of mobilisation with just a few days' notice, The University of Plymouth's Rapid Coastal Response Unit (RCRU) was able to capture infragravity wave processes during exceptional wave events at a range of contrasting beaches.

This research aims to understand how the role of infragravity waves varies across contrasting beaches, encompassing sand and gravel morphologies, under the full range of wave conditions from small, short period wind waves to extreme, energetic swells. A new dataset is presented comprising observations collected during storms

at five U.K. beaches. The sites ranged in slope from $\tan\beta = 0.02 - 0.35$ with median grain sizes (D_{50}) of between $0.25 - 60$ mm. During the experiments significant wave heights (H_s) of up to 7 m and peak periods (T_p) up to 20 s were recorded. These data are used to examine how the role of infragravity waves in nearshore processes varies on a range of beaches and in a range of wave conditions outside of those reported in most field studies to date.

At present, short-term forecasts and early warning systems used to reduce storm impact rely on numerical models originally developed for open-coast sandy shorelines, such as X-beach and Delft 3D, limiting their applicability to other coastal environments. The improved understanding of the role of infragravity waves in coastal storm impacts across the range of environments studied here can benefit coastal communities by enhancing predictions of, and protection against, extreme wave events and their impacts.

1.2   <u>**Thesis aims and objectives**</u>

The overarching aim of this thesis is to understand how the prevalence and significance of infragravity waves varies, on beaches with a range of grain sizes and slopes, and with different mixes of incoming swell and wind-waves, in particular focusing on extreme storms. To achieve this, the following five objectives were defined:

1.   Develop and refine a technique for in-situ and remote observation of infragravity waves, suitable for rapid deployment, during extreme storms, across a range of beach morphologies and sediment grain sizes.

2.   Compile a new dataset of infragravity wave observations, encompassing combinations of unprecedentedly large wave heights and periods, impacting beaches ranging from steep sloping gravel to shallow sloping sand.

3.   Analyse the extent to which infragravity waves are present at the shoreline on steep gravel beaches during high energy wave conditions.

4.   Contextualise results pertaining to objective 3 by assessing when and where infragravity waves become important at the shoreline of a further four beaches of contrasting morphology and grain size.

5.   Examine whether infragravity generation and dissipation mechanisms vary between sites with contrasting morphology during storms using

observations collected seaward of the short-wave breakpoint, through the

surf zone, to the shoreline.

1.3   Key concepts

In Chapter 1.3 relevant concepts pertaining to the thesis are presented. Research

contributions are critically reviewed to outline the current state of the art in the

following topics: coastal storms (Chapter 1.3.1), infragravity waves in shallow water

(Chapter 1.3.2) and infragravity swash (Chapter 1.3.3).

1.3.1 Coastal storms

Coastal systems, such as reefs, rock platforms, beaches and dunes act as natural

buffers between the ocean and hinterland, dissipating wave energy and forming

barriers between the marine and terrestrial environment (Stive et al., 2002). They act

as the first line of defence to storms which propagate shoreward across oceans.

However, extreme hydrodynamic forcing exerted by coastal storms result in the most

significant and sometimes irreversible changes to coastal environments (Burvingt et

al., 2018). It is therefore of utmost importance that those charged with managing

coastal areas understand how storms shape the nearshore. Such insight is gained by

analysis of data collected during storms which can also be used to inform numerical

modelling and prediction of future events. The following Chapter defines coastal

storms (Chapter 1.3.1.1), summarises their impacts on a range of environments

(Chapter 1.3.1.2), and describes how they can be monitored (Chapter 1.3.1.3).

1.3.1.1 <u>Defining a coastal storm</u>

Qualitatively, Harley (2017) defines a coastal storm as a "meteorologically-induced disturbance to the local maritime conditions (i.e. waves and/or water levels) that has the potential to significantly alter the underlying morphology and expose the backshore to waves, currents and/or inundation". Increases in total water levels during storms comprise both atmospheric (storm surge) and wave (setup and run-up) induced forcing. According to Harley, for an event to be defined as a storm, significant alteration to the underlying morphology must occur, followed by a period of recovery. During recovery, the system moves back toward its modal form, often on time scales much longer than the storm itself. The extreme wave forcing exerted by storms is the focus of this research.

Quantitative methods of storm identification typically apply a statistical rule to a suitable proxy, such as time series of significant wave height (H_s) to isolate storms in the record. The 'peaks over threshold' (POT) method defines a storm by the following three parameters (Harley, 2017) (Figure 1-3):

- Storm threshold (H_{thresh}): The minimum significant wave height separating storm and non-storm waves.

- Duration (D): The period between exceedance and relaxation through the storm threshold (H_{thresh}).

- Meteorological independence criterion (I): Minimum separation between successive storms to ensure they have resulted from independent forcing.
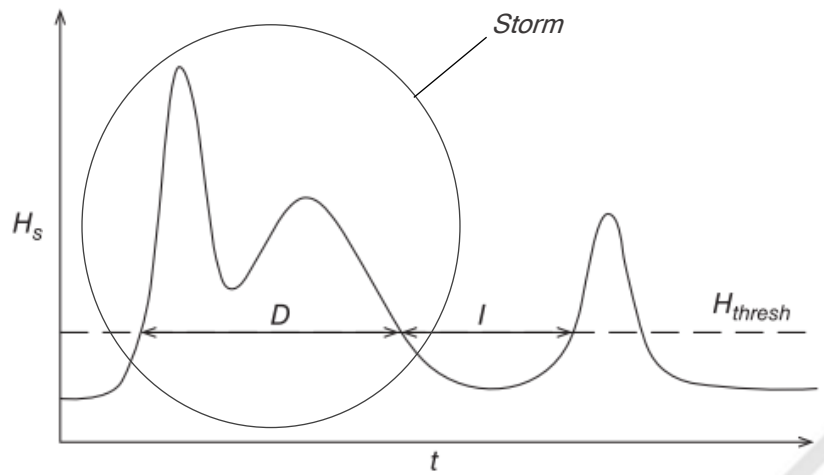
Figure 1-3 POT method for defining individual storm events from a significant wave height time series. Adapted from Harley (2017).

In reality, the storm threshold (H_{Thresh}) is governed by the modal wave conditions of the study site. Frequently in coastal research the 95th percentile of a long-term record of H_s is taken as H_{Thresh}, meaning the value varies significantly between locations with differing wave climates.

Defining a minimum duration (D) also depends on the site in question. The length of time storm waves persist above H_{thresh}, is of comparable importance to their size. For example, whether storm waves coincide with high tide can influence the level of impact (e.g. Macclenahan and Mckenna, 2001; Dhoop and Mason, 2018). Therefore, the most damaging storms would have to persist over at least half a tidal cycle (~6 hours for most UK coastlines). Further, storm waves persisting over multiple high

tides exert a larger cumulative force than the comparable sized waves over a single tide. The impact of individual versus cumulative event forcing is discussed further in Chapter 1.3.1.2.

The meteoritical independence criterion (I) is governed by the type of weather system driving the storm. Over north west Europe relatively slow-moving extratropical cyclones are responsible for the majority of coastal storms (Harley, 2017) and therefore 24-72 hours is a typical value of I (e.g. Masselink et al., 2014).

1.3.1.2 How do storms impact coastal environments?

During the most extreme storms, hydrodynamic forcing can exceed the equilibrium conditions responsible for the formation of the morphological system on which it is acting. Under these conditions, the landward extent of wave influence increases as a result of a larger infragravity contribution to wave runup (e.g. Poate et al., 2016). Such regions are inherently less resilient to wave dissipation and currents, resulting in rapid, sizeable (and sometimes irreversible) changes to the landscape such as beach and dune erosion (e.g. Coco et al., 2014; Castelle et al., 2015; Senechal et al., 2017) and cliff collapse (e.g. Earlie et al., 2015) and barrier over wash (e.g. Almeida et al., 2017) (Figure 1-4). Therefore, waves which differ from the long-term antecedent wave climate, referred to as disequilibrium waves, are more critical in coastal change than instantaneous hydrodynamic conditions (e.g. Davidson et al., 2013; Splinter et al., 2014)
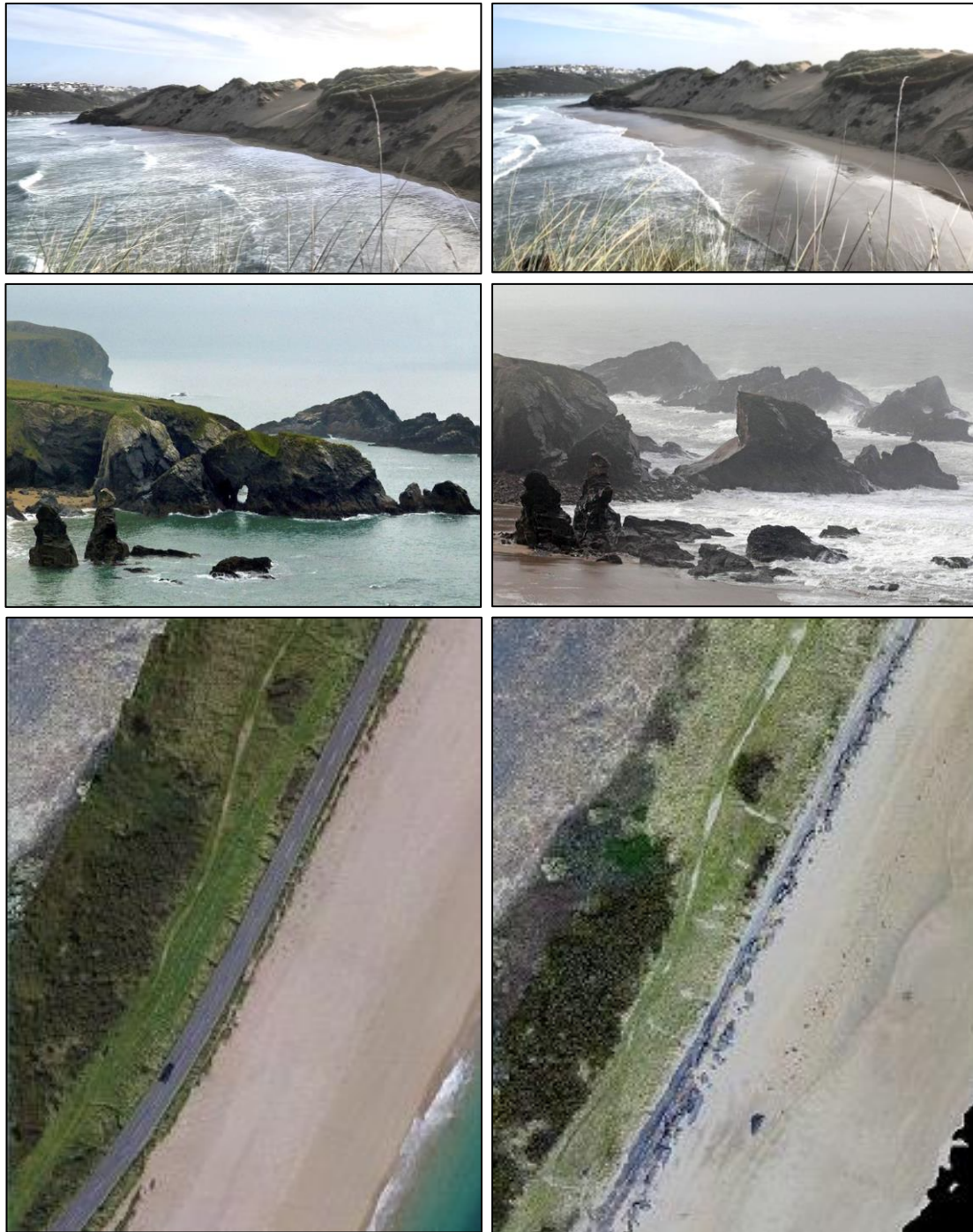
Figure 1-4 Extreme storm impacts: Top: Infragravity swash impacting dune foot, causing slumping during Storm Lorenzo, Crantock, Cornwal, U.K., October 2019. (Photographs, Oliver Billson); Middle: Rock arch destroyed at Porthcothan, Cornwall, U.K., following a storm on 6th January 2014 (Before (left) and after (right) © SWNS); Bottom: A379 'Slapton Line' road destroyed by storm '*Emma*', Slapton Sands, Devon, March 2018. (Before (left) and after (right) photographs, Peter Ganderton).

Temporal proximity to other high energy events also influences storm impact. A succession of high energy wave events (storm cluster), has a greater impact than the sum of their individual affects (e.g. Pinto et al., 2014; Castelle et al., 2015; Masselink et al., 2016; Garrote et al., 2018). This can result in disproportionate damage from seemingly innocuous conditions. However, taking into account the aforementioned disequilibrium theory, if storm sequences persist long enough a coastal system will reach a new equilibrium with the high energy conditions, resulting in reduction in impact of events toward the end of the sequence (Coco et al., 2014). In general terms, a storm of equal intensity occurring at the start of an active storm season will result in greater impacts than one occurring at the end. As such, storm clustering hampers predictions of coastal impact (Senechal et al., 2017).

The character and behaviour of storm waves as they reach the coast depends both on (1) their generating mechanism and the (2) environment on which they are acting. Firstly, waves are generated by the wind blowing on the sea surface, causing the periodic rise and fall of the sea surface. Wave height (H_0) and period (T) depend not only on the intensity of the wind but also the duration and fetch (the distance over which the wind can act unimpeded). Once generated, waves can travel many thousands of kilometres across open oceans. Therefore, the overall sea state can be made up of locally generated wind waves and swell waves of longer periods, far displaced from where they were generated.

A key characteristic in determining the impact of waves at the coast is their

steepness. In other words, how their height (H_0) compares to their wavelength (L_0)

(Eq. 1-1):

$$\text{Wave steepness} = H_0/L_0 \qquad\qquad \text{Eq. (1-1)}$$

where: $L_0 \, \alpha \, T^2$.

According to linear wave theory, as waves move shoreward, water depth (h) reduces.

Given that wave energy flux must be conserved as h reduces, wave height (H) must

increase, and length (L) decrease to compensate, known as shoaling. As shoaling

persists wave steepening will eventually mean that the horizontal velocities of the

water particles in the wave crest exceed that of the wave form and the wave breaks.

During wave breaking, energy is dissipated and transferred to higher frequencies in

the form of turbulence and lower frequencies in the form of infragravity waves and

nearshore currents. During storms, large high steepness waves break further offshore

and do not impact the coast directly instead transferring a large proportion of their

energy to infragravity frequencies which translate the storm impact to the coastline.

Secondly, the environment in which these waves are acting governs how they are

transformed between deep water and land. Bed roughness, slope and shoreline

orientation relative to the angle of wave approach all affect where energy is

dissipated, and where currents responsible for sediment transport are generated. Both

wave and beach characteristics are taken into account by the Iribarren or surf
similarity parameter (Iribarren and Nogales, 1949) (see Chapter 1.3.3).

Furthermore, local water level at the peak of a storm can dictate the severity of
impacts. Tidal stage and residual as well as wave setup and runup (particularly
during extreme events) modulate local water levels during storms (Lyddon et al.,
2019).

1.3.1.3 <u>Observing coastal storms</u>

Uncertainty remains over how coastal storms are changing in frequency and
intensity, however, it is likely that the return period between extreme events is
reducing (Wang et al., 2012). Understanding the physical processes and how they
combine is crucial to reducing the impact of coastal storms. Thus far this has been
limited by the quality and appropriateness of the datasets available (Coco et al.,
2014) owing to the dynamic and high energy conditions associated with storms being
inherently difficult, expensive, and dangerous to capture. One of the few field
campaigns to successfully capture in-situ nearshore data during extreme conditions
was Truc Vert 08 (TV08), an internationally collaborative experiment aiming to
capture coastal process at a range of temporal and spatial scales (Senechal et al.,
2011a). During TV08, significant wave height (H_s) in excess of 8 m was recorded by
a local wave buoy 1.5 km offshore of the study site, in approximately 20 m water
depth.

One of the few examples of a study examining infragravity waves targeted at a specific storm event was that of Bertin et al. (2020). They explored the generation and transformation of infragravity waves on the dissipative sandy Saint-Trojan beach on Oléron Island, France, during very energetic wave conditions associated with Storm Kurt (February 2017). In-situ data collection coincided with deep water wave heights of 10 m, observed by the Biscay Wave buoy, located approximately 300 km offshore in a water depth of at least 1000 m. On first reading, these waves appear significantly larger than other examples, however measurements here were collected in deeper water than other examples. In fact, H_s of 10 m at the Biscay Buoy corresponded to a return period on the order of 1 year (Nicolae Lerma et al., 2015). Significant wave height (H_s) of 6 m was recorded by an acoustic Doppler current profiler (ADCP) approximately 3 km offshore of the experiment in 11 m water depth. However, during the most energetic conditions wave breaking occurred at the ADCP, potentially limiting the recorded wave heights. Therefore, untransformed waves may have been larger than 6 m.

To overcome issues associated with in-situ storm data collection a range of remote techniques have been employed to monitor coastal storms and their impacts. These include: video observation of runup (e.g. Poate et al., 2016); airborne LiDAR (e.g. Burvingt et al., 2017) and aerial photography (e.g. Garrote et al., 2018) of beach topography; and satellite imagery of shoreline migration (e.g. Vos et al., 2019). Additionally, pre- and post-storm monitoring of beach volumes have been used to

quantify storm response (e.g. Ruiz De Alegria-Arzaburu and Masselink, 2010; McCarroll et al., 2019). While such techniques have informed accepted theory around wave-driven storm response of nearshore systems, they fail to provide insight into processes occurring during the storm; information arguably more critical for coastal communities (Brodie and McNinch, 2009).

Brodie and colleagues presented the first spatially extensive and temporally high-resolution data set of intra-storm beach volume and nearshore bathymetry evolution. In the decade since, a small number of studies have employed comparable 'rapid response' techniques to record a range of storm processes and impacts on a specific substrate. These include: sand (e.g. Senechal et al., 2011a; Coco et al., 2014; Fiedler et al., 2015) and gravel (e.g. Almeida et al., 2015) beaches, shore platforms (e.g. Poate et al., 2020), coral reefs (e.g. Péquignet et al., 2009) and cliffs (e.g. Earlie et al., 2015). Across the diverse range of environments, all of the research listed refers to the importance of wave-driven processes at infragravity (IG) frequencies. While infragravity wave dynamics have been examined on some of these substrates individually, until now, how their role varies between contrasting environments has yet to be thoroughly investigated. Chapters 1.3.2 and 1.3.3 will further outline and discuss infragravity wave theory and research contributions relevant to this thesis.

1.3.2 <u>Infragravity waves in shallow water</u>

Infragravity waves are known to increase in importance during storms and have been implicated in the erosion and inundation of a range of coastal systems. While their role in nearshore hydrodynamics and sediment transport is fairly well understood on sandy beaches, how their importance varies between different types of beach is as yet unknown. In the following Chapter, current understanding of infragravity waves and their importance on beaches, in particular during storms, is summarised.

1.3.2.1 <u>Discovery and background</u>

Infragravity motions were first recorded during field deployments carried out by both Munk (1949) and Tucker (1950). Examination of wave records collected seaward of the surf zone at La Jolla, California, U.S.A. and Perranporth, U.K., respectively, revealed low-frequency motions (christened 'surf beat' by Munk), with periods on the order of 30 – 300 s and amplitudes around one-tenth of incoming short waves. Through cross-correlation, Tucker identified a linear relationship between the short wave energy envelope and long wave amplitude, apparently independent of short-wave period, seaward of the surf zone. Tucker suggested that variations in the mass transport of water between groups of large and small incident waves may be responsible for the observed long wave. This theory was demonstrated mathematically by Biésel (1952) and developed by Longuet-Higgins and Stewart (1962) (referred to hereafter as LHS62) who referred to the force exerted by the

variation in mass transport described by Tucker as '*radiation stress*'. LHS62 showed that in a 1-D bichromatic wave field, radiation stress exerted by the grouped structure of short waves depressed and enhanced the water level below and between groups respectively, producing a second-order long wave, 180° out of phase with the short-wave group. This long wave travelled phase-locked to the wave groups becoming known as a bound longwave (BLW).

1.3.2.2 Sources of infragravity energy

The mathematical description of radiation stress offered by LHS62 is only valid for a non-sloping laboratory bed. In reality, the range of beach slopes and wave conditions observed on natural beaches affect how IG waves develop, highlighting the importance of studying them across a range of field sites. As depth decreases shoreward, long waves lag behind the short wave group and the phase difference with the short wave envelope shifts away from 180° (e.g. Masselink, 1995; Inch et al., 2017). This results in the transfer of energy from the short-wave energy envelope to the IG wave, which shoals, increasing in height. IG shoaling has been shown to occur at a rate between $h^{-1/4}$ and $h^{-5/2}$, by a range of numerical, lab and field experiments. Phase shifts have been shown to depend on bed slope (e.g. Battjes, 2004) and IG frequency, with the most substantial lags and subsequent growth in IG height being observed at the lowest (e.g. de Bakker et al., 2013) or highest IG frequencies (e.g. Battjes, 2004), a phenomena which is yet to be explained (Bertin et

al., 2018). Further investigation of phase lag between the bound long wave and short wave group by Guérin et al. (2019) found that as well as bed slope, phase lags also depended on water depth, short wave period and short wave group period. They showed that IG growth (due to phase lags) increase with long period incident waves in shallow water. Further, steeper beach slopes produce smaller lags in shallow water but higher ones in deep water, while higher group periods result in greater lags on gentle slopes than steep slopes.

The majority of free infragravity energy in nearshore waters originates from incident wave shoaling or breaking. This occurs either through the release of the BLW or the generation of further IG waves by oscillation of the short wave break point (Symonds et al., 1982), both of which are explained in more detail next.

Field observations suggest that as short waves break, the grouped structure to which the long wave was previously 'bound' breaks down, releasing a freely propagating long wave (e.g. Masselink, 1995). Using a range of laboratory datasets, Baldock (2012) argued that the long wave is released when the shallow water dispersion relationship is satisfied (when $kh < 0.3$, where k is the wavenumber and h is water depth), which does not necessarily coincide with the short wave breakpoint. Therefore, during storms when incident waves are particularly steep, short wave breaking can occur in intermediate water depths, before the shallow water dispersion relationship is satisfied, meaning that the long wave's energy begins to dissipate

before it's released. The contrasting nature of these results further emphasises the importance of studying IG waves, in the field, during storms.

The second source of free IG energy relating to short wave breaking is the time-varying breakpoint mechanism (TVBP) proposed by Symonds et al. (1982). Dynamic set-up/down oscillations resulting from the spatially fluctuating breakpoint of different sized wave groups generate both shoreward and landward freely propagating infragravity waves of equal frequency to the group. TVBP generated IG waves have been observed both in the laboratory (e.g. Baldock and Huntley, 2002; Masselink et al., 2019) and the field. (e.g. Pomeroy et al., 2012; Contardo and Symonds, 2013).

To identify conditions favourable to either mechanism, Baldock (2012) proposed the surf beat similarity parameter:

$$\xi_{\text{surfbeat}} = \beta_{\text{norm}}\sqrt{\frac{H_0}{L_0}} \qquad \text{Eq. (1-2)}$$

where L_0 is the incident wave deep water wavelength, H_0 is the incident wave height at the breakpoint, and β_{norm} is the normalized bed slope as proposed by Battjes (2004):

$$\beta_{norm} = \frac{h_x}{\omega_{low}}\sqrt{\frac{g}{h_b}} \qquad \text{Eq. (1-3)}$$

where h_x and h_b are the beach slope and the depth at breakpoint, respectively, ω_{low} is the long wave frequency, and g is acceleration due to gravity. Masselink

et al. (2019) suggested that values of $\xi_{surfbeat} < 0.05$ were conducive with infragravity waves generated via bound long wave release, while $\xi_{surfbeat} > 0.1$ implied the break point forcing mechanism.

Like IG shoaling, Eq. 1-2 and 1-3 show that the dominant IG generating mechanism depends on wave height, period and beach slope, implying that the characteristics of IG waves are likely to vary with beach type and hydrodynamic conditions.

1.3.2.3 <u>Infragravity waves and sediment transport</u>

Interest in the behaviour of free IG waves and their potential role in shaping nearshore morphology stimulated an upsurge in IG wave research at the end of the 20th century which was reviewed by Bertin et al. (2018). Gallagher (1971) demonstrated how reflected IG waves can progress offshore as leaky waves or when wave approach angle is sufficiently high, become refractivity 'trapped' resulting in the development of quasi-periodic longshore patterns known as edge waves (e.g. Huntley and Bowen, 1975). This led to the proposal of 'pattern theory' linking edge waves to the development of periodic 3-D features on sandy beaches (e.g. BAVEN and INMAN, 1971; Bowen, 1980; Holman and Bowen, 1982). However, this has since been largely superseded by self-organisation theory (e.g. Werner and Fink, 1993; Falqués et al., 2000; Caballeria et al., 2002; Coco and Murray, 2007).

Several authors have examined the role of infragravity waves in sediment transport, reporting a range of rates and directions of IG transport and sand suspension

mechanisms (e.g. Beach and Sternberg, 1988; Shibayama et al., 1992; Osborne and Greenwood, 1992; Russell, 1993; Aagaard and Greenwood, 1994; Ruessink et al., 1999; Conley and Beach, 2003; Aagaard and Greenwood, 2008; Baldock et al., 2010; Alsina and Caceres, 2011; Kularatne and Pattiaratchi, 2014; de Bakker et al., 2016). This lack of coherence is likely due to the range of boundary conditions present during the above experiments. Depending on the cross-shore position and water depth at which measurements were collected and/or the beach slope and wave conditions, velocities controlling sediment transport vary, as is explained next.

Wave orbital motion dictates that sediment transport is onshore directed under a peak and offshore directed under a trough. Therefore the direction of sediment transport at IG frequencies has been shown to depend on whether maximum sand suspension occurs at an infragravity peak where velocities are positive (onshore-directed) or a trough where velocities are negative (offshore-directed) (Roelvink and Stive, 1989). This can be represented by the correlation, r_o, between the short-wave envelope and infragravity velocity.

Seaward of the surf zone, the largest short waves coincide with an IG trough and r_o is negative, resulting in offshore directed sediment transport.

de Bakker et al. (2016) hypothesised that the ratio of IG wave height to incident (or as they term it 'sea-swell') height (H_{IG}/H_{SW}), combined with the correlation r_o determines the direction of IG sediment transport in the inner surf zone. Under low energy conditions the largest sea-swell coincide with IG peaks, r_o is positive and

sediment transport is directed onshore. Conversely, as conditions become more

energetic and infragravity waves become dominant over short waves, the IG waves

suspend sediment under IG troughs. Now, the combined velocity of undertow and

infragravity wave induced cross-shore currents result in net offshore directed

sediment transport.

Using data collected at a moderately sloping ($\tan\beta \approx 0.029$) and a gently sloping

beach ($\tan\beta \approx 0.013$), during reasonably high energy conditions ($H_0 < 4.4$ m, $T_0 < 7.0$

s and $H_0 < 4.3$ m, $T_0 < 7.1$ s respectively) de Bakker et al. (2016) developed a

conceptual model incorporating the effect of beach slope on IG sediment transport

(Figure 1-5).
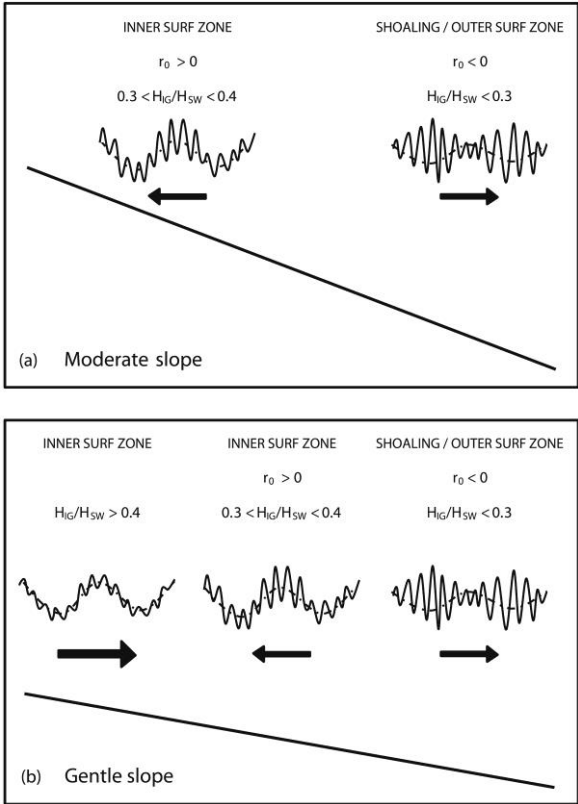
Figure 1-5 Conceptual figure for sand suspension mechanisms and resulting infragravity-wave flux directions for (a) a moderately sloping beach and (b) a gently sloping beach. Note that the size of the smallest waves for negative r_0 is similar to the largest waves for positive r_0. The magnitude of the arrows might change with height above the bed, but the direction is not expected to change (de Bakker et al., 2016).

On the gently sloping beach (Figure 1-5b), H_{IG}/H_{SW} exceeds 0.4 during high energy

conditions in the inner surf zone. Under such conditions, IG waves are capable of

suspending sediment. Acting in combination with significant undertow, net sediment

transport at IG frequencies is now directed offshore, thus providing a mechanism for

erosion of the beach face, as observed by Russell (1993).

On the moderately sloping beach (Figure 1-5a), a lack of short-wave dissipation,

even close to shore and under high energy conditions, results in relatively low values

of H_{IG}/H_{SW} (<0.4). This limits suspension by the IG waves and, as such, the direction

of sediment transport at IG frequencies depends entirely on r_o (negative, onshore

transport in the inner surf zone; positive, offshore transport in the outer surf zone).

de Bakker et al. (2016) hypothesised that on the moderate slope H_{IG}/H_{SW} would

never become large enough to result in offshore transport, even at the shoreline.

Given that measurements were not collected up to the shoreline, it is possible that

offshore directed sediment transport at IG frequencies was occurring shoreward of

the shallowest sensor.

Whether the conceptual model can be applied to environments other than fetch

limited sandy beaches could be examined by collecting data on a range of slopes and

sediment grain sizes (including gravel barriers) in both high energy swell and wind

wave conditions. The model could be validated using data collected at more depth

increments, in particular the shallowest region of the surf zone extending into the

swash zone. Validation of existing IG theory over unprecedented boundary conditions shaped the data collected effort used for this thesis.

As has been shown, the relative importance of IG frequencies compared with short wave frequencies increases shoreward, as short waves dissipate their energy and long waves shoal. As such, many IG studies have focused on the shallowest region of coastal waters: the swash zone.

1.3.3 <u>Infragravity Swash</u>

The importance of IG waves in runup (the maximum vertical extent of wave uprush on the beach) has been established on low sloping sandy beaches (e.g. Butt and Russell, 2000). Defined as the elevation of the shoreline above still water level, runup comprises a mean (set-up) and oscillatory component (swash) (Stockdon et al., 2006). The swash transfers energy from the waves to the shore, playing a pivotal role in sediment transport, and can drive significant erosion during storms (Masselink and Puleo, 2006). Swash is often separated into infragravity and gravity ($f = 0.05$–1 Hz) frequency bands and quantified as significant swash height, S, equal to 4σ, where σ^2 is vertical runup variance in each band. While infragravity swash has previously been studied on a range of sandy beaches, how its importance varies on different beach types, and with different mixes of swell and wind-waves, is currently unknown.

To summarise the parameter space covered by field work carried out to date, environmental conditions and significant infragravity swash height (S_{ig}), observed during 13 prominent experiments which underpin much of the understanding of infragravity swash processes on sandy beaches, were compiled and are presented in Table 1-1. The locations and relative exposure of the 10 sites are shown in Figure 1-6. Mean values were obtained from Passarella et al. (2018) and ranges from Gomes da Silva et al. (2018). Further information and reference to published works relating to the data in Table 1-1can also be found in Stockdon et al. (2006).

Table 1-1 Summary (range and mean) of environmental parameters and significant infragravity swash height (S_{ig}) sampled during previous research.[1]. Subscript 0 indicates parameters calculated using deep water values, linearly deshoaled to 80 m water depth. N = number of observations.

Map No.	Site/Experiment	Date	H_0 (m)	T_p (s)	Tan β	D_{50} (mm)	ξ_0	N	S_{ig} (m)
1	Duck, NC (USA) Duck82	5–25 Oct 1982	0.7–4.1 1.71	6.3–16.5 11.9	0.09–0.16 0.12	0.75	0.68–2.38 1.44	36	0.4–2.4 1.2
2	Scripps, CA (USA)	26–29 Jun 1989	0.5–0.8 0.69	10–10 10	0.03–0.06 0.04	0.20	0.4–0.92 0.6	41	0.3–0.7 0.33
1	Duck, NC (USA) Duck90–Delilah	6–19 Oct 1990	0.5–2.5 1.40	4.7–14.8 9.3	0.03–0.14 0.09	0.36	0.44–1.70 0.90	138	0.4–1.7 0.91
4	San Onofre, CA (USA)	16–20 Oct 1993	0.5–1.1 0.8	13–17 14.9	0.07–0.13 0.1	-	1.6–2.62 2.2	59	0.5–1.8 0.96
3	Gleneden, OR (USA)	26–28 Feb 1994	1.8–2.2 2.1	10.5–16 12.4	0.03–0.11 0.08	-	0.26–1.2 0.9	42	0.9–1.9 1.4
5	Terschelling (Netherlands)	2–22 Apr 1994 1–21 Oct 1994	0.5–3.9 1.9	4.8–10.6 8.3	0.01–0.03 0.02	0.22	0.07–0.22 0.1	14	0.2–0.9 0.54
1	Duck, NC (USA) Duck94	3–21 Oct 1994	0.7–4.1 1.5	3.8–14.8 10.5	0.06–0.1 0.08	0.20–2.5	0.33–1.43 0.81	52	0.5–2.2 0.81
6	Agate, OR (USA)	11–17 Feb 1996	1.8–3.1 2.5	7.1–14.3 11.9	0.01–0.02 0.02	0.20	0.1–0.19 0.15	14	0.7–1.5 1.1
1	Duck, NC (USA) Duck97–SandyDuck	3–30 Oct 1997	0.4–3.6 1.3	3.7–15.4 9.5	0.05–0.14 0.09	0.90–1.66	0.34–3.22 1.1	95	0.3–1.8 0.88
7	Truc Vert (France)	3 Mar– 13 Apr 2008	1.1–6.4 2.4	11.2–16.4 13.7	0.05–0.08 0.06	0.35	0.49–0.9 0.68	88	0.63–2.37 1.3
8	Tairua (New Zeland)	15–17 Jul 2008	0.7–1.0 -	9.9–12.5 11.0	0.09–0.13 -	0.4	1.4–2.25 -	25	0.6–0.95 0.75
9	Ngarunui (New Zeland)	8–9 Nov 2010	0.6–1.3 -	8.1–12.4 9.0	0.01–0.03 -	0.29	0.13–0.42 -	32	0.24–0.90 0.60
10	Somo (Spain)	4 May 2016	0.3–0.7 0.31	11.0–13.0 12.0	0.04–0.1 0.06	0.28–0.35	0.9–2.5 1.5	12	0.28–0.90 0.57

Further information and datasets are available for sites 1–6: https://pubs.usgs.gov/ds/602/#intro; site 7: (Senechal et al., 2011b); site 8 (Guedes et al., 2011); site 9 (Guedes et al., 2013) and site 10: https://data.mendeley.com/datasets/6yh2b327gd/4.
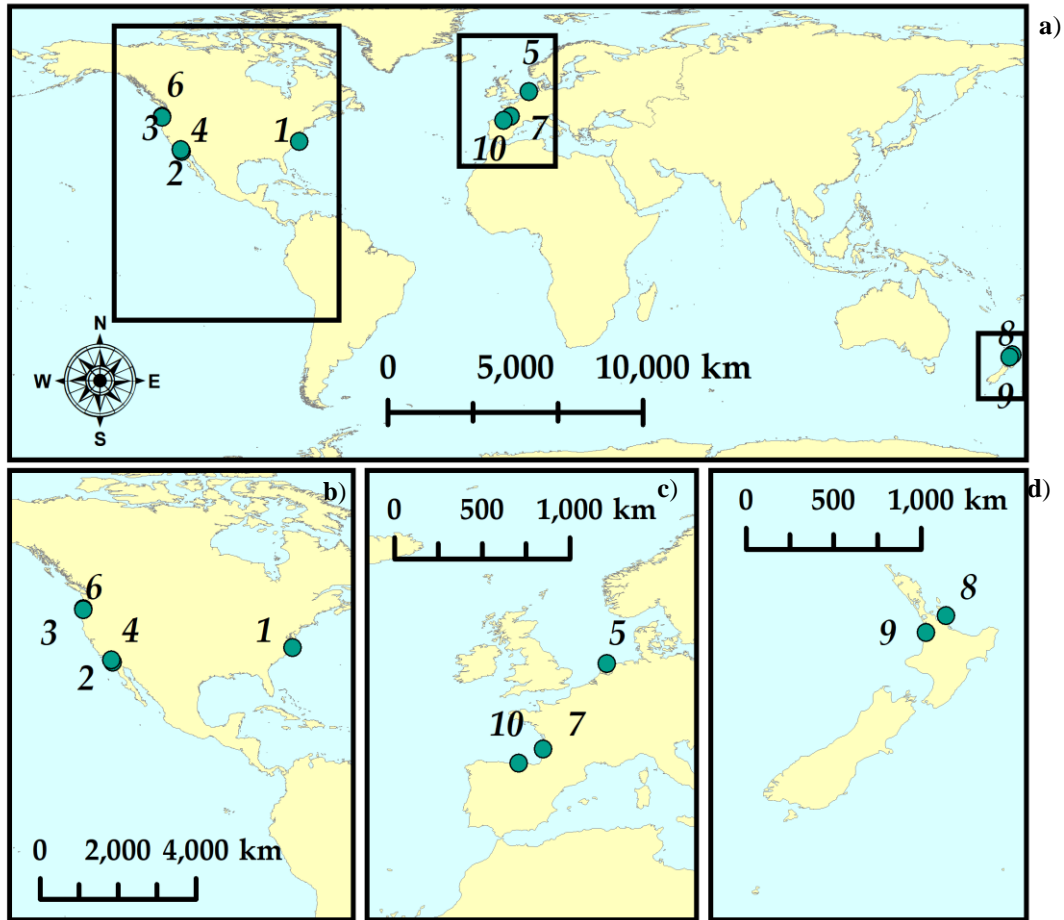
Figure 1-6 Location of sites previously studied, listed in Table 1-1, showing variation between ocean-facing and fetch-limited sites: (a): World map; (b): USA; (c): Western Europe; (d): New Zealand.

Table 1-1 highlights the combined importance of incident wave height and period to infragravity response at the shoreline. The four experiments where mean values of S_{ig} exceeded 1 m were exposed, open ocean sites, where both wave height and period were large (Duck82, Gleneden, Agate and Truc Vert (Figure 1-6b)). In contrast, despite large wave heights (H_0 up to 3.9 m), short wave periods (mean T_p 8.3 s) typical of the fetch limited Tersheling (Figure 1-6c), resulted in a low mean S_{ig} of 0.54 m. In an attempt to understand the conditions which result in infragravity frequencies becoming important in the swash, much of the sandy beach data

presented in Table 1-1 has previously been used to try and establish empirical

relationships between S_{ig}, wave statistics and beach gradient. Prior to the field

experiments listed in Table 1-1, Hunt (1959) demonstrated in the laboratory that

monochromatic wave runup scaled well with the Iribarren number:

$$\xi = \frac{\tan \beta}{\sqrt{H_0/L_0}}$$
Eq. (1-4)

where $\tan \beta$ is the beach gradient, and H_0 and L_0 are the deep water (offshore)

significant wave height and wavelength, respectively. The Iribarren number

represents a dynamic beach steepness comparing beach slope to wave steepness, with

the application of Eq. (1-4) to natural data sets facilitating the examination of runup

in a morphodynamic parameter space (Poate et al., 2016). As such, the terms in Eq.

(1-4) form the basis of many runup (and more specifically) swash predictors.

The pioneering work of Guza and Thornton (1982) demonstrated a contrasting

relationship between H_0 and horizontal swash in the gravity and infragravity band,

whereby swash was seen to be saturated in the gravity band but increased linearly

with H_0 in the infragravity band. Other researchers have since reported a similar

linear relationship between vertical significant infragravity swash height (S_{ig}) and H_0,

with a range of constants of proportionality (Ruessink et al., 1998b; Ruggiero et al.,

2004; Senechal et al., 2011b).

Attempting to find a universal parametrisation of S_{ig}, applicable to a range of sandy

beaches, Stockdon et al. (2006) found that including a wavelength term, $(H_0L_0)^{1/2}$,

improved predictions of S_{ig}, a result corroborated under high energy conditions observed at a single site by Senechal et al. (2011b). Although, not an example of a swash parameterisation, Inch et al. (2017) found that at an exposed sandy site, a stronger correlation existed between infragravity wave height in the surf zone and H_0^2T, than with Stockdon's equation, citing it's proportionality to deep water wave power as more physically correct than Stockdon's $(H_0L_0)^{1/2}$.

While observations focusing specifically on infragravity swash are almost entirely limited to sandy environments, an example of similar research on gravel beaches is that of Poate et al. (2016) who, without focusing specifically on infragravity frequencies, assessed runup elevation under extreme conditions on a range of gravel beaches. They found that existing runup predictors developed on sandy beaches, including that of Stockdon, under-predicted runup elevation on gravel beaches, instead finding that $(\tan \beta^{1/2}H_0T_p)$ provided a more accurate estimate.

Prior to this research, observations of infragravity swash under storm wave conditions were limited to a small number of experiments carried out on sandy beaches, as presented in Table 1-1. The comparisons of infragravity swash behaviour on sand, gravel and mixed sediment beaches presented here are, at the time of writing, the first of their kind.

1.4   <u>Thesis structure</u>

In Chapter1.1, a changing ocean climate and increased reliance on coastal regions was used to justify the presented research into the role of infragravity waves in nearshore processes under high energy wave conditions. The aims and objectives of the thesis were outlined in Chapter 1.2. Key concepts pertaining to coastal storms were discussed with a particular focus on the role of infragravity waves and low frequency swash hydrodynamics Chapter 1.3.

Chapter 2 describes the methodology used by Plymouth University's Rapid Coastal Response Unit (RCRU) to measure infragravity response during storms at five contrasting sites in the south of England, which are described in Chapter 2.1. Chapter 2.2 begins by outlining the development of the RCRU (2.2.1) which laid the foundations for development of the infragravity specific technique deployed in this thesis (2.2.2).

The dataset comprising storm survey data from the five sites is presented in Chapter 3. This dataset is analysed further in Chapters 4, 5 and 6.

First the role of infragravity waves at the shoreline of a gravel beach is examined in Chapter 4. Results from the gravel beach are compared to four other contrasting sites in Chapter 5. These findings are quantitatively compared to existing empirical relationships linking beach and wave conditions to infragravity motions. In Chapter 6 the behaviour of infragravity waves between the breakpoint and the inner surf zone

are compared on a sand and gravel beach. Chapter 7 synthesises the conclusions

drawn in Chapters 3-6 linking back to the thesis aims introduced in Chapter 1.2.

Chapter 8 states the major conclusions drawn from the thesis.

2   <u>Methodology</u>

In Chapter 2, the five beaches selected for storm surveys are described in detail,
outlining their typical morphology and wave climate (Chapter 2.1). Chapter 2.2 is
divided into two halves. First, field campaigns contributing to the development of
rapid coastal response units are discussed (2.2.1) before the infragravity specific
rapid coastal response unit developed in this thesis is presented (2.2.2).

2.1   <u>Description of five contrasting study sites</u>

Five beaches in the south of England, UK, were specifically selected as study sites
owing to their contrasting wave climates, and morphology (Figure 2-1 a-e). From
west to east: one low-sloping sandy beach - Perranporth (PPT), two steep gravel
beaches - Beesands (BEE) and Chesil (CSL), and two compound/mixed sand and
gravel sites - Camber (CAM) and Minsmere (MMR) (Figure 2-1). These two sites
can be divided, according to the classification of Jennings and Shulmeister (2002),
into a composite beach (CAM), and a mixed sand and gravel beach (MMR). Storm
surveys designed specifically to answer the objectives set out in Chapter 1.2 were
carried out between 2016 and 2018 at four of the five sites. These data were
complemented by reanalysis of a previously published dataset from a fifth site,
Chesil Beach (Poate et al., 2016) (Figure 2-1 c).

Figure 2-1 : Location (Top left corner), photographs (left) and representative profiles (right) of: a): Perranporth (PPT); b): Beesands (BEE); c): Chesil (CSL); d): Camber (CAM); e): Minsmere (MMR). Dashed black lines on profiles represent mean high and low water spring tidal elevation. Chesil photograph (c) is licensed under the Creative Commons Attribution-Share Alike 3.0 Unported license (https://creativecommons.org/licenses/by-sa/3.0/deed.en).

At each site, a nearby wave buoy was selected to characterise the local wave climate and monitor incoming wave conditions. Table 2-1 summarises key information about each of the five buoys and Figure 2-2 shows their approximate location. All buoys were Datawell Directional WaveRider Mk IIIs. The maintenance and data dissemination for all buoys except Minsmere (Southwold Approach WaveNet Site) was managed by the Channel Coast Observatory; Minsmere was managed by the Centre for Environment, Fisheries and Aquaculture Science (CEFAS).

Table 2-1 Information relating to the wave buoys (and their data record) used in further analysis. Regional setting and approximate location of wave buoys are shown in Figure 2-2.

Site	Wave buoy name	Location	Depth relative to chart datum (m)	Approximate distance to instrument array (km)	Record used for analysis
Perranporth	Perranporth	50° 21.19' N 005° 10.48' W	14	2.0	01/2007 – 12/2020
Chesil	Chesil	50° 36.13' N 002° 31.37' W	12	6.5	06/2007 – 12/2020
Beesands	Start Bay	50° 17.53' N 003° 36.99' W	10	4.5	06/2007 – 12/2020
Camber	Pevensey	50° 46.91' N 000° 25.10' E	9.8	30	01/2007 – 12/2020
Minsmere	Southwold Approach WaveNet Site	52° 18.75' N 001° 47.03' E	23	12.5	01/2010 – 12/2020

While exact values vary with prevailing wave conditions, typical values of beach face slope ($\tan\beta$) and median sediment grain size (D_{50}) for each of the five sites are presented in Figure 2-3.
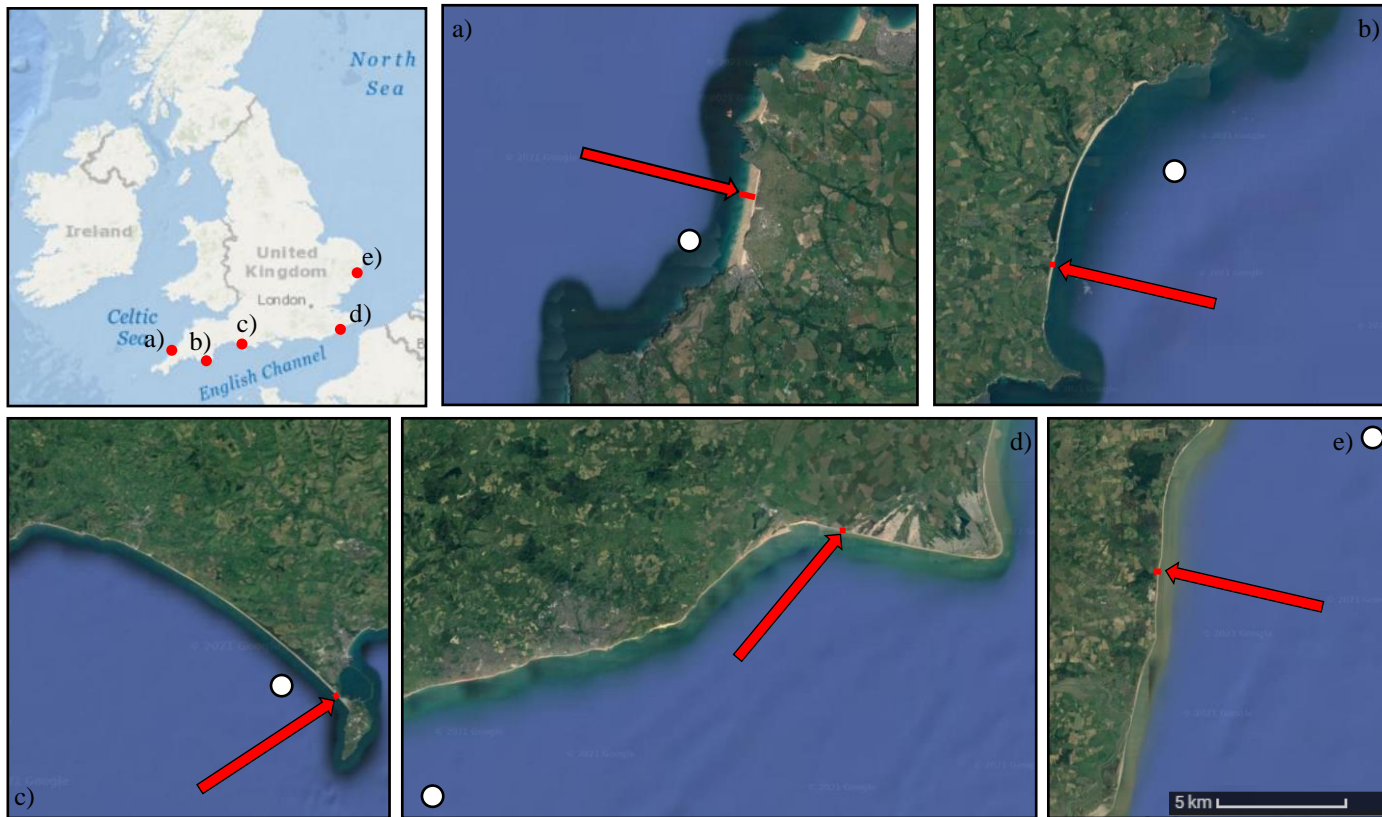
Figure 2-2 Regional setting of study sites and approximate location of local wave buoys described in Table 2-1 (white circles) and survey equipment (red arrows and lines). a): Perranporth (PPT); b): Beesands (BEE); c): Chesil (CSL); d): Camber (CAM); e): Minsmere (MMR). Satellite images obtained from Google Earth ©.

Perranporth (Figure 2-1a + 2-2a) is a high energy, dissipative sandy beach on the north coast of Cornwall. Orientated approximately west north west, the 3.5 km beach is exposed to both energetic North Atlantic swells from the south west to west north west and locally generated wind waves from the south south west to the north west. Mean annual H_s and T_p at the nearby 'Perranporth' directional wave rider buoy are 1.9 m and 12 s, respectively, with monthly mean wave height and period varying seasonally between 1.2 m and 8.7 s in the summer (June, July, August) to 2.1 m and 12.8 s during winter (December, January, February) respectively (Figure 2-4). The region is subject to a semidiurnal tidal regime with a mean spring range of 6.1 m. In contrast to many previous studies which focused on the southern section of Perranporth beach (e.g., Masselink et al., 2014; Puleo et al., 2014; Stokes et al., 2015; Inch et al., 2017), the north end of beach, Perran Sands, was selected here to minimize the impact of (by maximizing distance to) headlands on hydrodynamics Figure 2-2. During the deployment, Perran Sands was characterized by a relatively featureless and longshore homogenous intertidal zone of approximately 400 m in width, with low tide bar rip morphology apparent during spring low tides. The concave profile, comprised of medium sand (D_{50} = 0.25 mm) (Figure 2-3), ranged in slope from $\tan\beta$ = 0.1 at the foot of the dune to 0.015 through the intertidal zone. As such the 'active slope' bound by the maximum runup elevation and short-wave break point ranged from 0.04 during higher tides to 0.02 during lower tides with a mean of 0.034 (Figure 2-1a).

Facing east south east up the English Channel, Beesands (Figure 2-1 + 2-2b) is sheltered from large south westerly swell waves by Start Point and is instead dominated by oblique wind waves approaching between the north east and south east, with occasional southerly swell able to refract into the beach. Studies of the long-term wave climate have highlighted the bi-modality between short periods waves from the east and longer period from the south west (e.g. Mason et al., 2009; Wiggins et al., 2019). Mean annual H_s and T_p at the nearby 'Start Bay' directional wave rider buoy are 0.7 m and 8.2 s, respectively, with monthly mean wave height and period varying seasonally between 0.46 m and 7.1 s in the summer to 0.95 m and 9.4 s during winter, respectively (Figure 2-4). Whilst partially sheltered from the region's prevailing storm conditions (from the south west), Beesands is fully exposed to episodic easterly gales, which have been seen to cause significant erosion and inundation during previous events, e.g. 1979 and 2001 (Denbigh, 2017). The area has a meso- to macrotidal regime with mean spring range of 4.3 m. The cross-shore profile at Beesands is fairly longshore uniform and is characterized by typical tidally modulated gravel barrier morphology (Figure 2-1b). The profile comprises fine gravel ($D_{50} = 5$ mm) with a mean foreshore slope of 0.1 from an elevation of 3 to -6 m (relative to Ordnance Datum Newlyn) (Figure 2-3).

Chesil Beach (Figure 2-1 + 2-2c) is an 18 km-long, steep gravel barrier facing south west down the English Channel, exposed to both Atlantic swell and locally generated wind sea. Mean annual H_s and T_p at the nearby 'Chesil' directional wave rider buoy

are 0.96 m and 8.1 s, respectively, with monthly mean wave height and period

varying seasonally between 0.75 m and 7.0 s in the summer to 1.3 m and 9.4 s during

winter, respectively Figure 2-4. Chesil has a mesotidal regime with a spring tidal

range of 3.1 m. The south eastern extreme of the barrier is backed by a 1.5 km stretch

of hard defence. In order to limit the impact of anthropogenic structures on the runup

statistics, a profile north west of the hard defences was used for further analysis

Figure 2-2. Chesil was the largest grain size of the sites (D_{50} = 65 mm) and the

steepest (tanβ = 0.32) (Figure 2-3). Similarly to Beesands, Chesil is a pure gravel

beach maintaining a relatively constant slope between 8 m and -6 m ODN.

Camber Sands (Figure 2-1 + 2-2d) is a 15 km beach facing south south west up the

English Chanel. Backed by sand dunes in the west north westernmost 2 km and a

combination of seawall and rock armour for 2.5 km southward of this, the profile is

characterized by a steep gravel upper beach (tanβ = 0.1, D_{50} = 10 mm) discreetly

separated from a lower slope intertidal sandy bar system where tanβ = 0.02, D_{50} =

0.33 mm (Figure 2-3). Mean annual H_s and T_p at the nearby 'Pevensey' directional

wave rider buoy are 0.76 m and 5.7 s, respectively, with monthly mean wave height

and period varying seasonally between 0.58 m and 5.0 s in the summer to 1.0 m and

6.4 s during winter, respectively (Figure 2-4).

Minsmere (Figure 2-1 + 2-2e) is 3 km stretch of straight coastline, situation in the

south east of the UK, facing due east in the North Sea. The site is fetch limited and

typically low energy. Minsmere possesses a mixed sand and gravel morphology with

a reasonable steep upper profile (0.1) of predominantly gravel grains (D_{50} = 20 mm), reducing to (0.03) comprising a majority mediums sand (D_{50} = 0.33 mm) around low water (Figure 2-3) and an offshore bar ~200 m offshore of low water and submerged 1-3 m which dissipates incoming waves. Mean annual H_s and T_p at the nearby 'Southwold Approaches' directional wave rider buoy in 23 m water depth are 0.83 m and 5.5 s, respectively, with monthly mean wave height and period varying seasonally between 0.66 m and 5.1 s in the summer to 1.0 m and 5.1 s during winter, respectively (Figure 2-4).
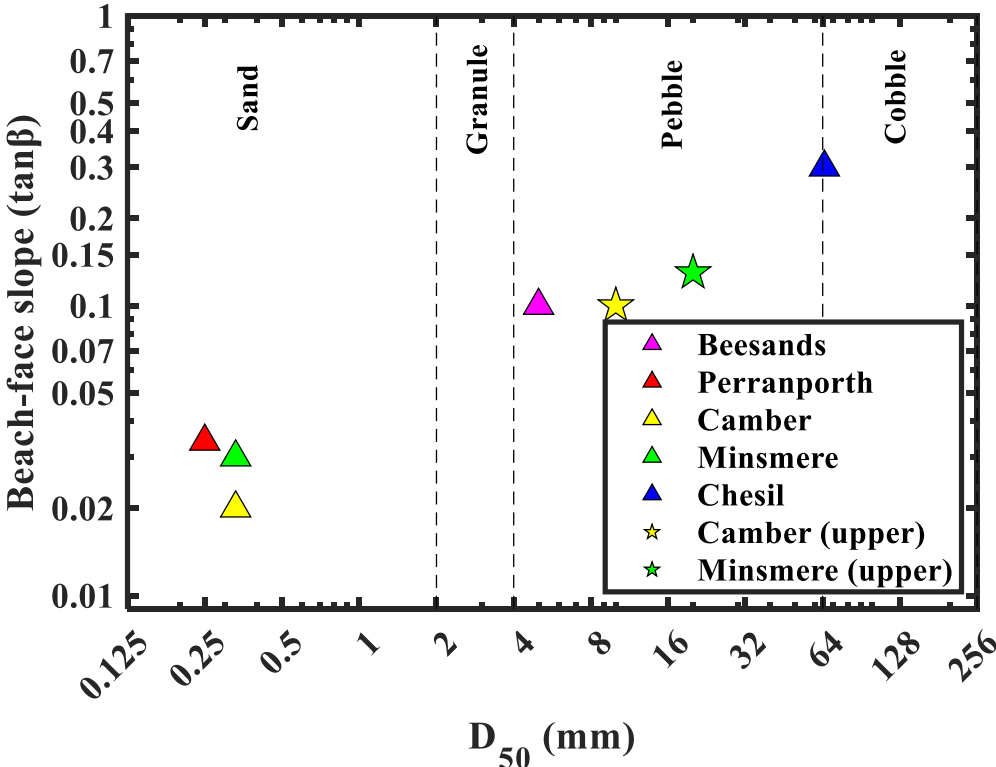
Figure 2-3 Typical values of beach face slope (tanβ) and median sediment grainsize (D_{50}) of the five study sites.
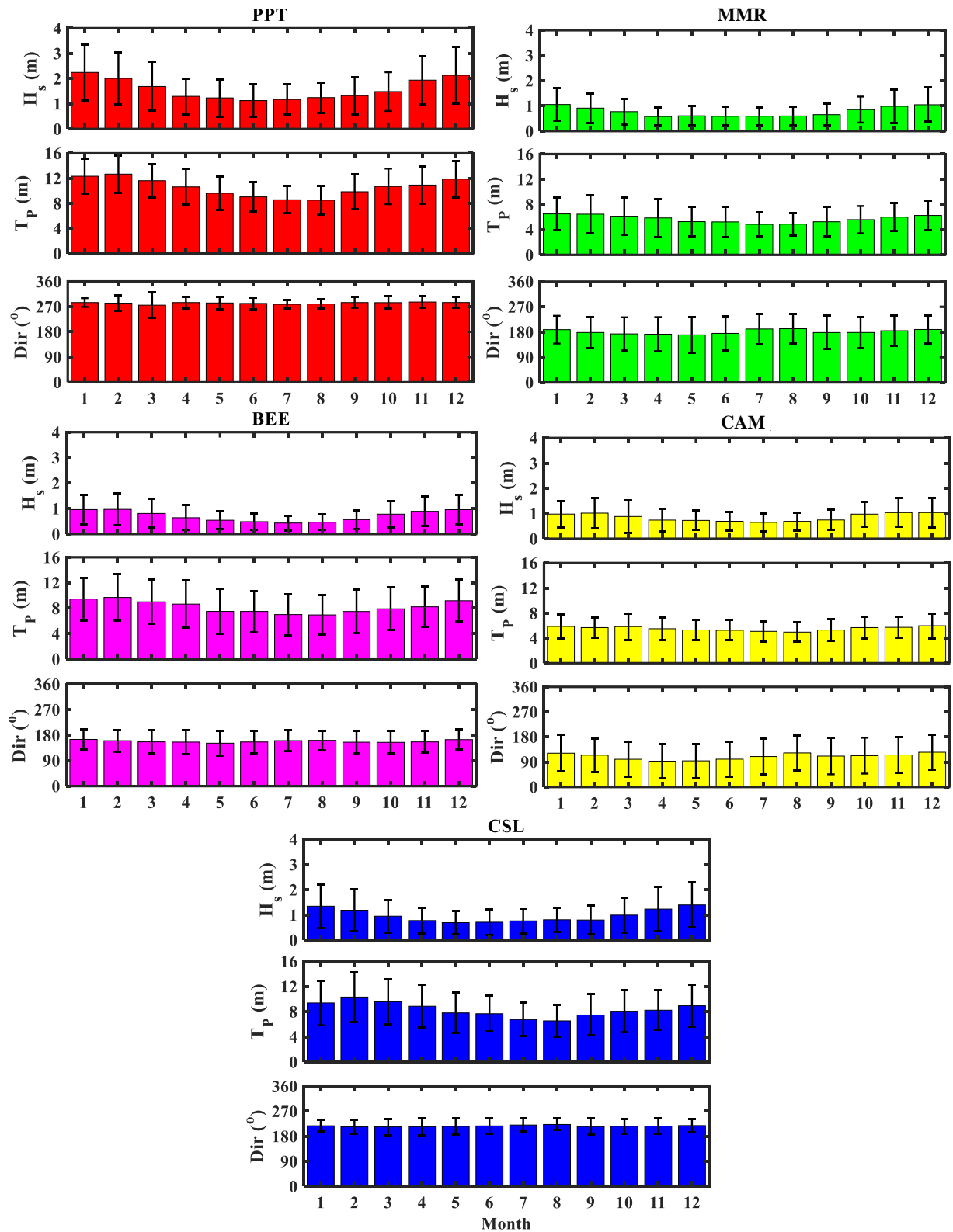
Figure 2-4 Monthly average wave height (H$_s$), peak period (T$_P$) and direction (Dir) at nearest wave buoy for the five study sites (detailed in Table 2-1); Perranporth (PPT), Beesands (BEE), Minsmere (MMR), Camber (CAM), and Chesil (CSL). Filled bars represent average for all years on record and error bars, the minimum and maximum recorded monthly value.

The five sites cover a wide range of beach slopes, sediment grain sizes and wave climates. Figure 2-5 facilitates comparison of the range of significant wave heights (H_s) and peak periods (T_p) typical of each site. The upper right axis is T_p scattered against H_s for each half hourly data point in the records defined in Table 2-1. Below the x-axis and to the left of the y-axis are percentage occurrence plots of peak T_p and H_s respectively. In order to generate the percentage occurrence plots, each data point was discretised by being placed into a bin. The number of times data fell into each bin was then compared to the total number of data points to calculate percentage occurrence. For H_s bins were evenly spaced, 0.1 m wide and ranged from 0 – 8 m. For T_p, data binning had already been applied when generating the frequency spectra used to calculate T_p. As such, values of T_p were already discretised in the downloaded data record.

Beginning with the two highest energy sites, the scatter of T_p against H_s at PPT and CSL were broadly similar. These two sites were the only two where H_s exceeds 6 m. The coincidence of the largest height and longest period waves in the CSL and PPT record indicates that they were susceptible to large swell waves during storms. While periods in excess of 14 s were observed at all the sites, these weren't typically associated with the largest wave heights in the record at MMR and CAM, where H_s was always less than 2 m when T_p exceed 14 s. The largest waves at these sites (H_s <4.75 m) occurred when T_p was 12 s or less. This shows that storms waves

impacting MMR and CAM were typically locally generated wind sea rather than swell as observed at PPT and CSL.

The bi-modal wave climate of BEE referred to earlier in this Chapter was clearly visible in both the scatter plot and the T_p percentage occurrence plot. Similarly to MMR and CAM, the largest waves (H_s < 5.8 m) at BEE, did not coincide with the longest periods. In contrast, when T_p was between 14-18 s at BEE, waves of up to 5 m in height were observed. Similarly to CSL and in contrast to PPT, as T_p increased above 18 s at BEE, associated maximum H_s fell rarely exceeding 2 m. This highlights that Beesands was susceptible to both wind and swell waves during storms, albeit swell of limited T_p.

The percentage occurrence plots highlight the swell dominated nature of PPT with T_p of 10 – 14 s the most common. Longer period swell waves of 14-19 s occur more commonly at PPT than any of the other four sites. This compared to CSL where T_p in the range of 7-10.5 s is most typical. While longer period swell waves are present in the record, occurrence falls with increasing wave periods from 11-18 s. While rare (occurring less than 1% of the time) waves in the range 19-25 s have been observed at PPT, CSL and BEE, to an even lesser extent at CAM and almost never at MMR. The tendency toward far shorter values of T_p at CAM and MMR is demonstrated in the shape of the occurrence curve. The flatter peak occurrence of between 4 – 8 s at Camber and lower gradient drop in occurrence of periods between 8 – 14 s shows subtle differences to the wave climate of MMR, where a narrow peak occurrence

centred around 6 s. Occurrence of waves of shorter and long period than this fell rapidly. It can be seen that waves in excess of 14 s in period are highly unusual at MMR. The distribution of wave periods at BEE shared characteristics each of the other 4 sites, with a wind wave peak of around 6 s and a swell peak of around 12 s, again highlighting the bimodality of the wave climate.

In terms of wave height, the percentage occurrence plot showed that H_s of between 0.75 – 1.5 m were the most commonly observed at PPT. H_s exceed 1 m more frequently at PPT than any of the other four sites. A gradual decrease in percentage occurrence with increasing H_s (up to a maximum of 7.8 m) clearly set PPT apart, experiencing larger waves, more frequently than the remaining sites. The joint second largest peak H_s occurrence was observed in the MMR and CSL records ($H_s =$ 0.6 m). However, while CSL had the second largest H_s maximum of any of the five beaches (<7.8 m), MMR had the lowest ($H_s < 4.5$ m). This highlights the similarity of the modal wave climate at the two sites and highlights the contrast in storm wave characteristics. The most commonly observed H_s at both CAM and BEE was $H_{s =} 0.4$ m, the joint lowest of the five sites, however, the maximum H_s in the record for BEE ($H_s < 5.6$ m) was larger than CAM ($H_s < 4.8$ m), highlighting that BEE is more exposed to larger storm waves than CAM.

Overall, the sandy site (PPT), had the highest energy wave record both in terms of wave height and period, followed by the two pure gravel sites where CSL experienced both larger modal and extreme wave heights than BEE. The two mixed

sediment sites (MMR and CAM) were least susceptible to extremes in both wave

height and period.
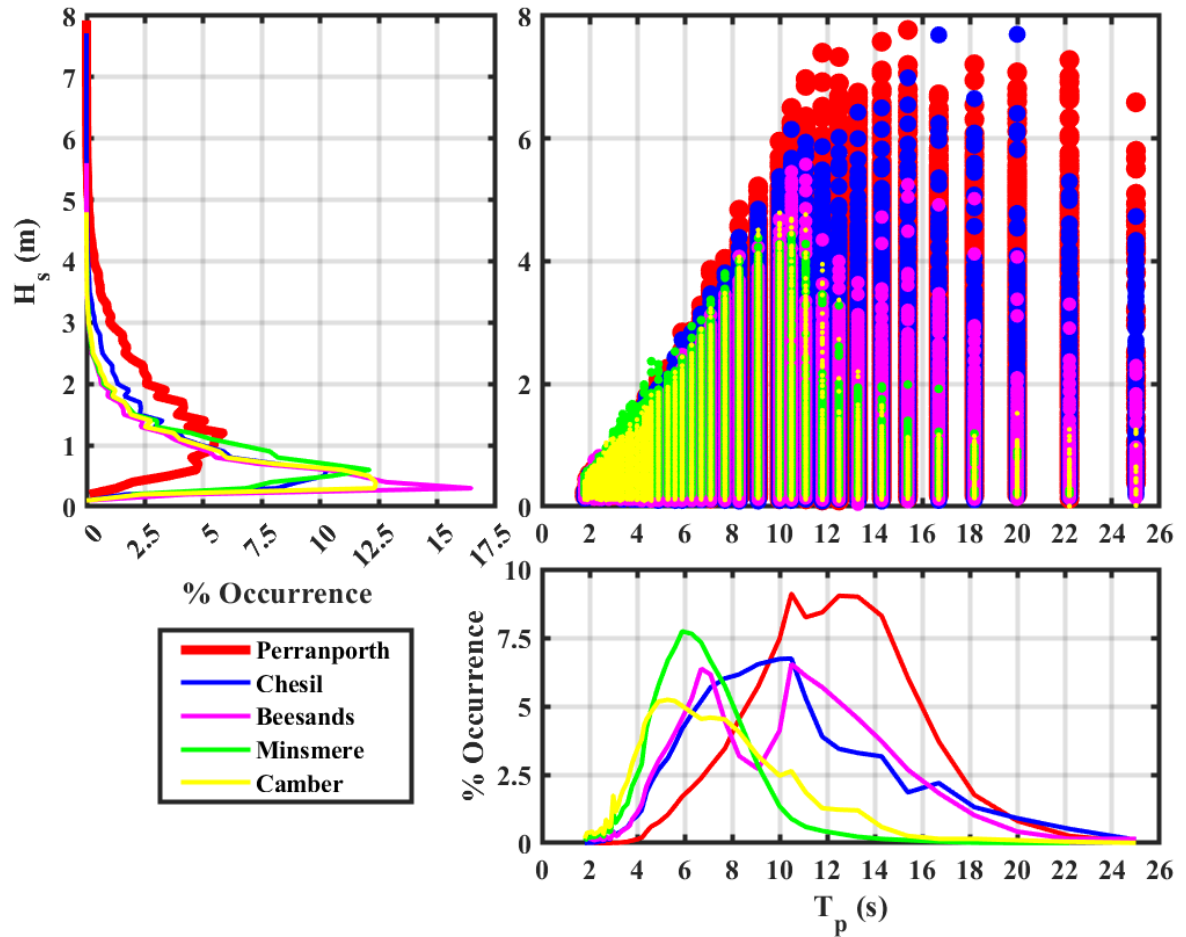
Figure 2-5 Scatter plot of peak period (T_p) against significant wave height (H_s) measured at local wave buoys to each of the five study sites. Adjacent to the relevant axis is a plot percentage occurrence of T_p and H_s respectively.

2.2 <u>Rapid coastal response unit (RCRU)</u>

To collect intra-storm data at the sites described in Chapter 2.1, a bespoke technique resilient to storm impacts on a range of beaches was required. The University of Plymouth's Coastal Processes Research Group (UoP - CPRG) has over 30 years of experience collecting data during storms, refining their approach after each deployment. Chapter 2.2.1 summarizes how previous work led to advances in storm forecasting, instrument technology and deployment. The experiments discussed aimed to assess a range of research questions. While none were designed specifically to measure infragravity waves, elements of each deployment were combined to produce the technique employed in this thesis.

2.2.1 <u>Development of techniques to observe extreme storms</u>

Substantial experience deploying in-situ sensors on sandy beaches was gained during The ECORS – Truc Vert 08' (TV08) experiment. TV08 was one of the largest multi-institutional international nearshore field experiments ever carried out, taking place on a sandy, open stretch of coastline in western France from 3rd of March to 6th of April 2008. A detailed account of the experiment was produced by (Senechal et al., 2011a). The aim of the TV08 was to investigate processes at different spatial and temporal scales during a range of hydrodynamic conditions. This included a major storm event where $H_s < 8$ m. Peak wave conditions during data collection are still some of the highest energy presented in the literature.

While monitoring infragravity waves was not a central aim of TV08, many of the instruments deployed could have been used for this purpose. Therefore, the survivability of in-situ intertidal instrument rigs, in particular pressure transducers, was of particular interest when planning the data collection described in this thesis. At TV08, cross-shore arrays of sensors were fixed to scaffold frames, hard wired to data loggers and networked to ensure synchronised data recording. Limited by the technology available at the time, deployment of such arrays was time consuming and therefore not well suited to rapid deployment. Pressure transducers (such as the RBR solo used in this thesis) now exist with sufficient internal battery, memory and processing power that they can be programmed, synchronised and deployed for several weeks at a time. The size of these sensors means they can be fixed to smaller 'sand anchors', which are faster and less labour intensive to install than scaffold. However, these are only suitable for sites where limited topographic change is expected, such as sandy beaches. On gravel sites a different approach is required. Changes to the profile on the order of meters can occur over a single tide, and suspended grains of 2 – 60 mm can exert huge forces on sensors.

Between 2012 – 2014, CPRG collected data on 10 occasions at six gravel beaches in the U.K. under high energy conditions. This effort formed part of the 'new understanding and prediction of storm impacts on gravel beaches' (NUPSIG) project, which explored the morphodynamics of gravel barriers during overtopping events. Details of the deployments can be found in Poate et al. (2016).

Similarly with TV08, NUPSIG did not investigate infragravity waves. However, the instrumentation deployed would be capable of doing so with some minor modification. For the first experiment, an extensive intertidal array of sensors was installed at Loe Bar, Cornwall during March 2012. As with TV08, the intertidal array at Loe Bar was hard wired and labour intensive to install. The following nine deployments were targeted around storm events, including five during the infamous winter of 2013/14. As such these deployments were designed to be installed at short notice, becoming CPRG's first Rapid Coastal Response Unit (RCRU). Predominantly, data collection was remote, via video camera (e.g. McCall et al., 2015; Poate et al., 2016) or scanning LiDAR (e.g. Almeida et al., 2013, 2015, 2017). Experience gained during these deployments aided the RCRU design implemented in this thesis, which is described in full in Chapter 2.2.2. Selecting appropriate camera lenses, knowing how to maintain a clear field of view, and how best to orient the video cameras with respect to the sun were all skills acquired during the NUPSIG deployments. In addition to remote sensing, a single pressure transducer was deployed at four of the six sites. Owing to the difficulties of deploying in-situ instruments on gravel beaches highlighted above, bespoke housings were developed to protect the PTs from impacts with gravel particles whilst not impeding performance of the sensor. Metal tubes were cut to just larger in length and diameter than the PTs, with a grate at one end and bolt through the other so that the sensor (wrapped in foam cladding) could be fixed in place. Individual vertical scaffold

poles, roughly 3 m in length, were driven into the beach face leaving only a few centre meters exposed which were used to fix the housed PT at bed level.

The housings developed during NUPSIG were adapted to be made suitable for fixing to rock platforms during CPRG's Waves Across-shore Platform (WASP) project which investigated wave transformation on a range of reefs in the U.K. and New Zealand between 2014 – 2016 (Poate et al., 2020). Following the success of NUPSIG, additional PTs were purchased to facilitate the deployment of extensive, intertidal arrays of sensors. Arrays were installed on six intertidal rock platforms using bolts and quick drying epoxy to secure PT housings. These deployments were also focused on storm events, extending CPRG's rapid response portfolio to another environment. The ability to prepare and install arrays of up to 15 PTs in a single tide was vital for the deployment technique required for this contribution.

2.2.2 <u>Infragravity wave specific RCRU</u>

Using knowledge gained during the deployments described in Chapter 2.2.1 as a foundation, a new rapid response methodology was devised which aimed to deploy consistent arrays of instrument across four of the sites described in Chapter 2.1. The various phases of RCRU deployment (survey planning, forecasting, mobilisation and deployment) along with associated time frames are summarised in Figure 2-6 and detailed in Chapters 2.2.2.1-4.

Figure 2-6 Implementing an infragravity wave specific rapid coastal response storm survey flow diagram

2.2.2.1 <u>Survey Planning (Months prior)</u>

To maximise the chance of capturing a storm at each of the four sites within the time constraints of the PhD, two surveys per winter season were planned, as summarised in Table 2-2.

Table 2-2 Time period over which each storm survey could be carried out (waiting period).

Site	Waiting period
Camber Sands	October 2016 – March 2017
Perranporth	October 2016 – March 2017
Minsmere	October 2017 – March 2018
Beesands	October 2017 – March 2018

For each of the four deployments a planning document was prepared (Appendix D-G). The success of rapid deployments hinged almost entirely on adequate planning, ensuring that data was collected as safely and efficiently as possible. Before any field work could take place, risk assessments were carried out to assess the likelihood and severity of an accident occurring and any relevant mitigation put in place. Planning documents began by detailing the broad context and motivation for the research and listing the relevant permissions and contact detail of local stakeholders. Next survey logistics were outlined. This detailed the type and positions of instrumentation to be

deployed, a timeline for the deployment, personnel requirements and availability and forecast hydrodynamic and weather conditions. These documents were circulated to all personnel involved prior to the experiment.

A kit list detailing all equipment needed, including where items were stored, the required quantity and any other comments was also circulated to ensure survey mobilisation was as efficient as possible. An example is presented in Appendix B.

2.2.2.2 Forecasting (weeks and days in advance)

Accurately predicting the magnitude of upcoming storms, as well as where and when they were most likely to arrive, was crucial to a successful survey. Before a decision to deploy instruments could be taken, what constituted a storm had to be decided. At each site, time and budget constraints meant that only one attempt could be made to complete a survey and therefore identifying the best time to deploy was key. If the threshold to deploy was set too low, the data collected would fail to extend the boundary conditions as intended in thesis aim 2; set the threshold too high and data may never have been collected. Therefore, the method used to define a storm needed to be based on statistics in the first instance and potentially revised if data collection was becoming threatened by time constraints. In the presented research, a POT method comparable to that introduced in Chapter 1.3.1.1 was implemented. 95th and 99th % threshold values of offshore wave height ($H_{0\_95/99}$) were calculated using data collected at each local wave buoy (details of which are provided in Table 2-1).

Figure 2-7 shows time series of H_s with the waiting period for each survey (green box), H_{s_95} (orange dashed line) and H_{s_99} red dashed line for each site. Forecast wave conditions were monitored using a range of online resources: Magicseaweed.com, Windguru.com, Winndytv.com and Surfforecast.com. Time periods where H_s was predicted to exceed H_{s_99} for at least two full tidal cycles (24 hours) were defined as storms and an opportunity to deploy equipment. While long range forecasts were used as early warning, full scale mobilisation was only triggered when a storm was forecast to arrive within the next five days and tides were suitable for deploying inter tidal instruments. To ensure deployment was triggered at all sites, the initial threshold of 99th percentile (H_{s_99}) was later revised to the 95th (H_{s_95}) if the higher threshold had not been exceeded by halfway through the waiting periods in Table 2-2. Waves in excess of the 99th percentile H_s were observed at all 5 sites (Figure 2-7), with particularly extreme named storm events being observed at Beesands (*'Emma'*), Camber (*'Angus'*) and Chesil (*'Petra'*) where mean H_s for the entirety of the experiment exceeded the 95th percentile. A full description of the meteorological forcing and resultant hydrodynamic conditions associated with each storm survey are provided in Chapter 3.
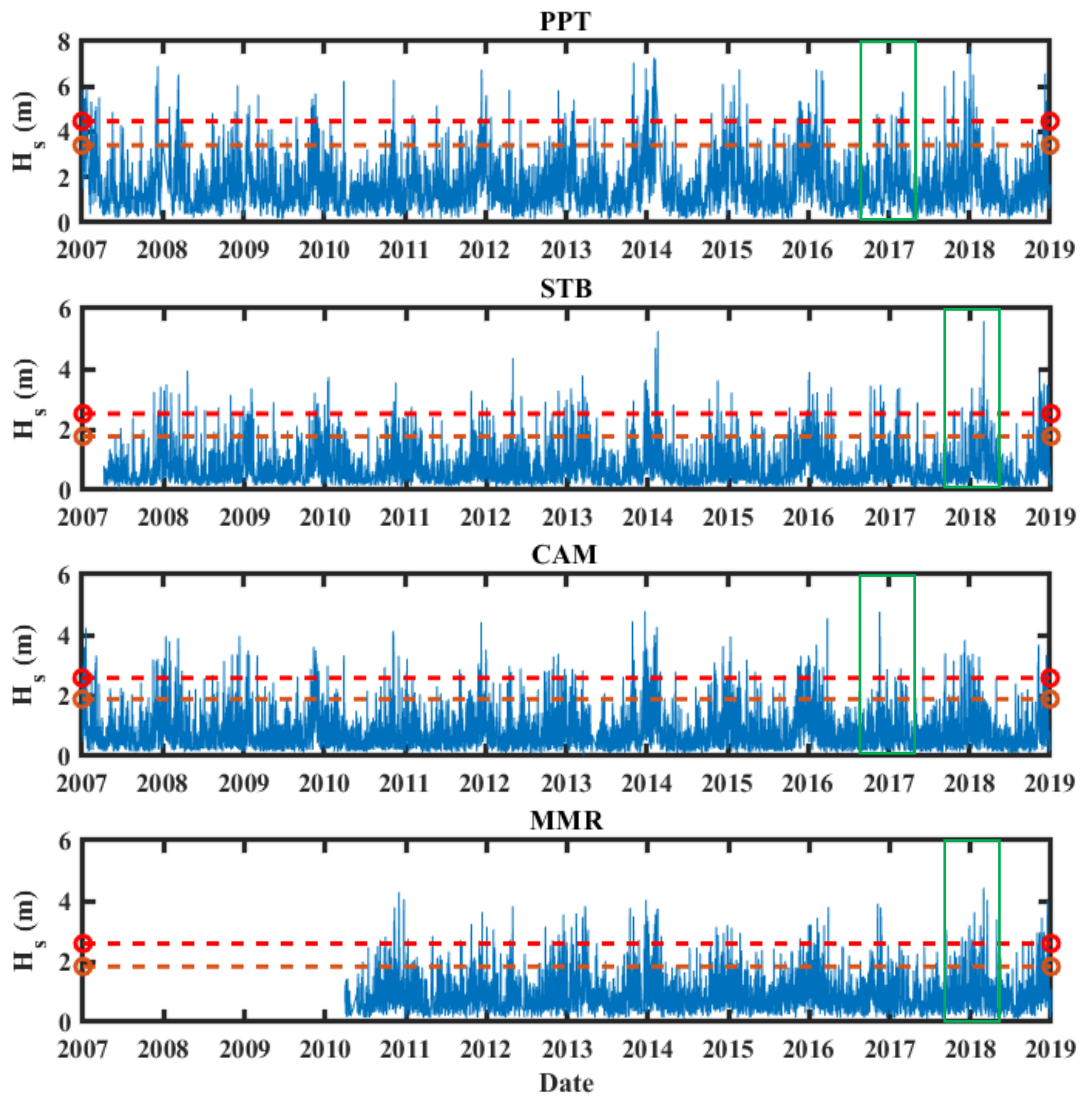
Figure 2-7 Time series of H_s measured at nearest wave buoy. Orange and red dashed lines indicate the 95th and 99th percentile wave heights respectively, specific to each site. Green boxs indicate the waiting period for each storm survey (Table 2-2). Wave buoy data courtesty of Channel Coast Observatory (CCO).

2.2.2.3 Mobilisation (> 2 days in advance)

Using a kit list (Appendix B), equipment could be quickly gathered together, be

checked and prepared for deployment. This included replacing batteries and

programming sensors to log at the correct rate and length of time Figure 2-8.

Figure 2-8 Preparing pressure transducers during storm survey mobilization

Specific instructions for preparing and programming the RBR solo pressure

transducers used in this thesis can be found in Appendix C.

All equipment was securely boxed up ready for transport to the site in a van and covered trailer, capable to being towed into position adjacent to each study site.

2.2.2.4 Deployment (> 6 hours in advance)

Data collection aimed to capture the approach as well as the peak and decay of a storm, therefore, deployment was ideally carried out at least the day before the target storm was due to arrive.

Due to the macrotidal nature of the study sites, instrument deployment was focused around low tide. Ideally spring tides were targeted to maximise cross-shore coverage. Key tidal and daylight information were summarised in planning tables, like the example for Perranporth shown in Table 2-3. Colour coding was used to highlight good deployment opportunities offered by larger tidal ranges in green and vice versa in red. Other relevant information was included in the comments box, such as other demands on equipment, staff and the deployment of other institution's instruments.

Table 2-3 Deployment planning table for Perranporth storm survey, January 2017

	Day	Date	Low Water				First light (GMT)	Last Light (GMT)	Comments
			AM		PM				
			Time (GMT)	Height above Chart Datum (m)	Time (GMT)	Height above Chart Datum (m)			
January	S	1	00:50	1.3	13:13	1.3	07:48	17:07	
	M	2	01:27	1.4	13:51	1.4	07:47	17:08	
	T	3	02:05	1.5	14:31	1.5	07:46	17:09	
	W	4	02:47	1.7	15:17	1.7	07:45	17:10	
	T	5	03:35	1.9	16:10	1.9	07:44	17:11	
	F	6	04:34	2.1	17:16	2	07:43	17:12	
	S	7	05:47	2.2	18:31	2	07:42	17:14	
	S	8	07:08	2	19:47	1.8	07:41	17:16	
	M	9	08:22	1.7	20:54	1.5	07:40	17:17	ADCP Deployed at Perranporth
	T	10	09:26	1.4	21:52	1.2	07:39	17:18	
	W	11	10:22	1	21:44	0.9	07:38	17:20	Monthly survey planned for Perranporth
	T	12	11:13	0.7	23:32	0.7	07:37	17:21	Monthly survey planned for Start Bay
	F	13	11:58	0.6			07:36	17:22	
	S	14	00:18	0.7	12:46	0.6	07:35	17:24	
	S	15	01:01	0.7	13:28	0.7	07:34	17:25	
	M	16	01:41	0.9	14:08	1	07:33	17:27	
	T	17	02:20	1.2	14:47	1.3	07:32	17:28	
	W	18	02:58	1.5	15:26	1.7	07:31	17:29	
	T	19	03:37	1.9	16:08	2.1	07:30	17:31	
	F	20	04:23	2.3	17:01	2.4	07:29	17:33	
	S	21	05:24	2.5	18:10	2.6	07:28	17:34	
	S	22	06:41	2.6	19:28	2.6	07:27	17:35	
	M	23	07:58	2.5	20:34	2.3	07:26	17:36	
	T	24	08:58	2.2	21:25	2.1	07:25	17:37	
	W	25	09:47	1.9	22:08	1.8	07:24	17:39	
	T	26	10:28	1.6	22:46	1.5	07:23	17:42	
	F	27	11:06	1.3	23:23	1.3	07:22	17:43	
	S	28	11:43	1.1			07:21	17:45	
	S	29	00:00	1.1	12:21	0.9	07:20	17:46	
	M	30	00:37	1	12:59	0.9	07:19	17:48	
	T	31	01:14	1	13:37	0.9	07:18	17:49	

Once on site, the RCRU trailer was used as an operational base Figure 2-9. This

could be used to shelter and brief personnel, make final instrument preparations and

store spare equipment. Information about the deployment was affixed to the trailer to

keep the general public informed of potential hazards.

Figure 2-9 Plymouth CPRG team alongside specialized trailer preparing to deploy instruments
at Perranporth, January 2017.

An all-terrain vehicle (ATV) was used to transport bulky items rapidly over large

distances. Once in position, rigs for mounting instrument arrays were constructed and

anchored into the profile. Further information on deploying instrument rigs is

provided in Chapter (6.2.2). Instrument rigs were covered in hi-visibility material to

minimise risk to beach users. Once in position, instruments were 'surveyed in',

recording their position and height using RTK DGPS as well as the beach profile.

This data was taken as a pre-experiment baseline against which subsequent

adjustments to instruments or the profile could be measured (Figure 2-10).
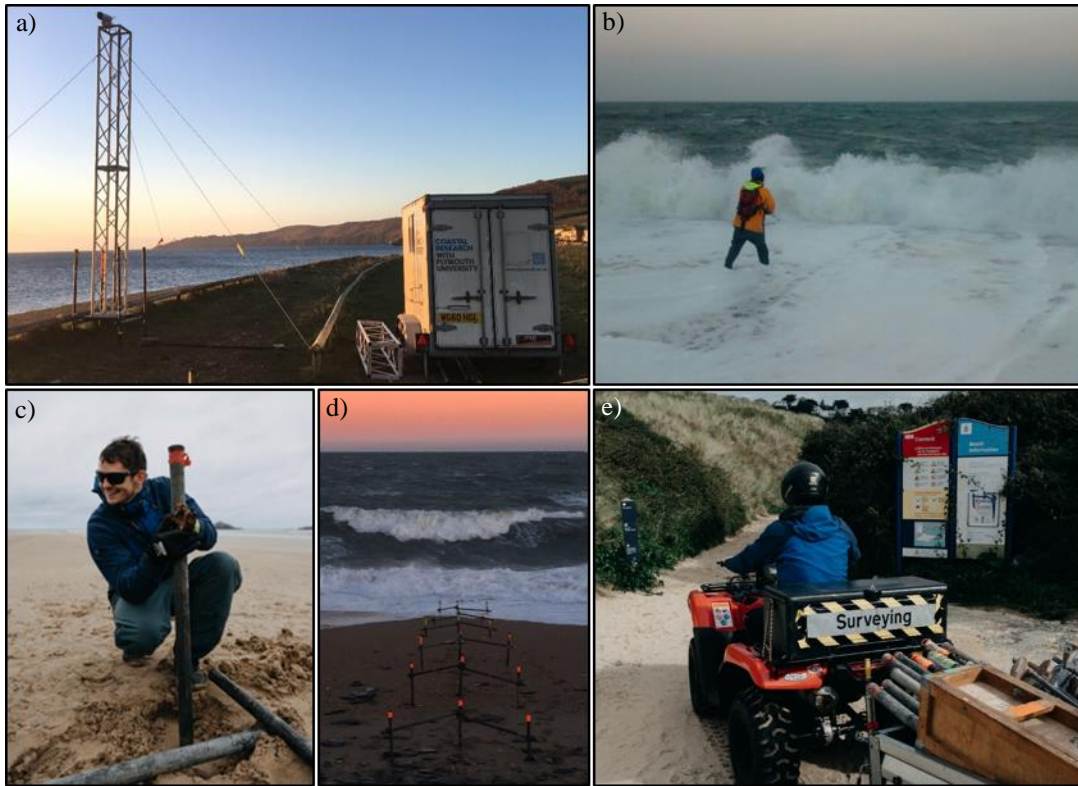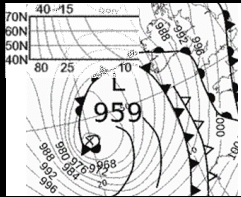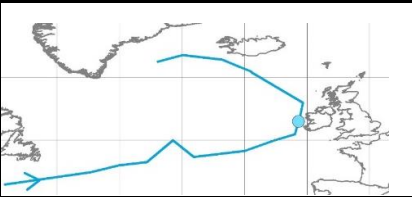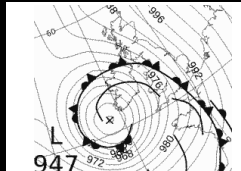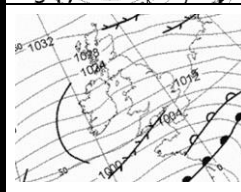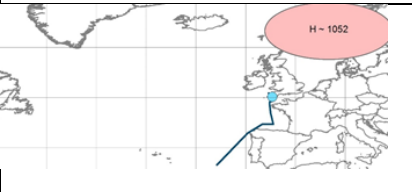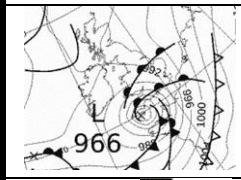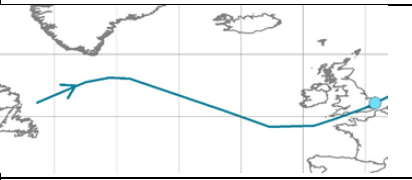
Figure 2-10 a): RCRU trailer and video tower used to measure swash; b): Author carrying out an intertidal topographic survey; c): Author installing scaffold frame to mount intertidal instruments, Storm Lorenzo, Crantock, October 2019; d): Intertidal array of pressure sensors, deployed during storm '*Emma*', Beesands, February 2018; e): All-terrain vehicle used to transport equipment and carry out topographic surveys. (c and e, photographs Simon Hird).

3   <u>Storm survey environmental conditions</u>

Between October 2016 and March 2018, the infragravity specific RCRU was

deployed to measure storms at four beaches in the south of the UK. For the purposes

of this thesis, these data were complemented by previously published storm survey

data from a fifth site, storm '*Petra*', at Chesil Beach in February 2014. Table 3-1

summarises key information about each storm including its name (where applicable)

and the dates over which it was active over the study site. The national

meteorological offices of most European countries name a storm if impacts are

forecast in region. The U.K. Met Office has partnered with Met Éireann since 2015

to name storms affecting either the UK and/or Ireland respectively. The description

column describes briefly the development of each system, if it had an alternative

name and most noteworthy impacts. Links to media coverage and further information

are also provided. Surface pressure charts show the position and scale of the

causative systems. Using daily U.K. Met Office charts of surface pressure, the

Channel Coast Observatory (CCO) produced maps of 'storm tracks' which are

included to show the path taken by each storm on its approach to the UK. Finally, a

photograph of each storm at, or close to, the study site is included for reference.

Photographs are captioned and credited within the table.

Table 3-1 Storms studied. Columns from left to right; site studied, storm name and dates active; description and links to media coverage; surface pressure charts [1]; storm tracks [2]; and photograph

Site/Experiment *Storm Name* *Date*	Description and impacts Media Coverage	Surface pressure chart	Storm Track	Photograph
Perranporth, U.K. *Unnamed storm* 22nd Jan – 8th Feb 2017	The first of three depressions to sweep north east over the UK during Feb 2017. Named 'Leiv' by Meteo-France, coastal regions in the south west of the country were placed on 'maximum alert level' experiencing wave heights in excess of 10 m and wind gusts of up to 148 km/h. 1. http://vigilance-public.meteo.fr/ 2. https://www.lemonde.fr/climat/article/2017/02/04/foyers-sans-electricite-et-rafales-de-vents-la-tempete-leiv-deferle-sur-le-sud-ouest_5074610_1652612.html			 *Storm waves arrive at Perranporth, 5th Feb 2017, Oliver Billson*
Chesil, U.K *'Petra'* 3 - 9th February 2014	One of four named low pressure systems to impact the UK between mid-December 2013 and February 2014, the most energetic 8-week period of waves to impact south-west England since 1950. Most damaging storm to affect Devon and Cornwall in 50 years, severing the main railway link between south west England and London. 1. https://www.bbc.co.uk/news/uk-26042990			 *Waves breaking at Chesil Beach during storm Petra, Richard Broome*
Beesands, U.K. *'Beast from the east/Emma'* 14th Feb – 5th March 2018	A deep depression named *'Emma'* in Portugal and '*Ulrike*' in Germany collided with an anticyclone dubbed the '*Beast from the East*', leading to snow falls of up to 60 cm and widespread temperatures as low as −11 ° Southwest England and Wales were worst affected with widespread easterly gales leading to exceptionally large waves from an unusual easterly angle of approach. The Slapton Line A379 road in Devon England was destroyed. 1. https://www.dailypost.co.uk/news/north-wales-news/we-stood-utter-disbelief-boat-18585545 2. https://www.bbc.co.uk/news/uk-43236763			 *Slapton line A379 destroyed, Gerald Taylor*
Camber Sands, U.K. *'Angus'* 18 – 23rd Nov 2016	The first storm named by the UK Met Office of the 2016/17 season. *'Angus'* travelled northeast affecting southern and southeastern England, especially along the Channel coast. A cargo ship collided with a barge and a passenger ferry was stranded in the Channel. The sea wall was damaged at Swanage, Dorset and the main south-west railway line was closed for the second time in two years due to wave driven flooding and damage. 1. https://www.bbc.co.uk/news/uk-38038992			 Waves lash Newhaven Harbour, Hannah McKay
Minsmere, U.K *Unnamed storm* 4-10th Jan 2018	An area of high pressure over Scotland combined with a shallow depression over Catalonia resulted in a shortlived period of strong north easterly wind along the south east coast of England. This generated two days of energetic wind driven waves at Minsemere, Sizewell and Southwold in Suffolk, England. No significant impacts were reported.		No defined storm track as development not associated with low pressure system Storm track derived from the Met Office's sea level pressure charts	 *Energetic storm waves breaking over an offshore bar, Minsmere, Oliver Billson*

1. metoffice.gov.uk   2. https://www.channelcoast.org/ccoresources/stormcatalogue

Table 3-2 summarises the hydrodynamic conditions associated with each of the storms studied. From left to right the table details the site, storm name and date the storm was active in the first column. Next, the range of significant wave height and peak period measured at the each of the local buoys is provided, with maximum observed H_s and T_p in bold. The mean wave height and peak period calculated for the entirety of each survey is given below. The 95th and 99th percentile of long-term wave record defined in Table 2-2 is reported in the adjacent column to the measured ranges and means to aid comparison. In the next column, the return period of the peak in H_s at each of the local buoys is listed. This data was extracted from the Channel Coast Observatory Storm Catalogue along with the plots of regional return period H_s in the adjacent column. These plots describe the spatial footprint of each storm, showing where experienced the largest waves and how localised or otherwise they were. Finally, in the furthest right hand column time series of H_s and T_p measured at the local wave buoys are presented. Dashed orange and red lines represent the 95th and 99th percentiles respectively of the long-term record of H_s and T_p. The largest Hs and T_p observed during each event are marked with circles and triangles respectively. Given that peak H_s and T_p did not necessarily coincide, the coincident T_p during the peak H_s and vice versa are marked with circles and triangles respectively. Below this time series of beach volume (Q) along the instrument profile expressed as meter cubed of beach volume per longshore meter of beach face (m^3/m) are presented. Crosses indicate times of topographic surveys.

Comparing the measured values with the long-term percentiles (Table 3-2), it can be seen that waves in excess of the 99th percentile H_s were captured at all sites as well as smaller waves associated with the approach and decay of the storm. T_{p_99} was exceeded at three of the five sites with Camber and Minsmere exceeding T_{p_95}.

The return period of observed H_s was on the order of multiple years for all sites except Perranporth (<1 in 1 year), with the largest seen at Beesands (>40 years) (Table 3-2). This demonstrates the extraordinary nature of each as a standalone event notwithstanding the exceptional range of conditions covered in the combined dataset.

The plots of regional return period H_s observed across the wave buoy network demonstrate the unique footprint of each storm (Table 3-2). The highly varied orientation of coastlines in southern England mean that wave heights measured across the wave buoy network depend on direction from which waves approach. All five storms appeared to generate the largest return period waves at buoys along the south facing channel coast. Clear contrast can be seen between the swell dominated events approaching from the west (PPT) and south west (CSL) and the wind driven events from the fetch limited east (BEE, MMR). Storm *'Angus'* (CAM) produced locally generated short period southerly waves, the effects of which were felt widely across the south coast. In contrast the easterly wave events were highly localised, with long return periods restricted to the east facing coasts of south Devon, Kent and Suffolk.

The time series plots in Table 3-2 show that the PPT event was dominated by long period waves with T_p in excess of 15 s, with a short-lived spell of small wind waves in the middle of the deployment. Wave heights began small ($H_s \sim 1$ m) during the largest peak period ($T_p < 20$ s), rising in the second week of the experiment to a H_s peak of 4.7 m and a T_p of 16.7 s.

Similarly, storm '*Petra*' at Chesil was swell dominated. The start of the deployment was characterised by moderate wind waves ($H_s \sim 2$ m, $T_p < 10$ s) before rapidly rising to a peak in both peak period ($T_p < 20$ s) and wave height ($H_s < 7$ m) on the third day.

In contrast, the storm at MMR and '*Angus*' at CAM were wind dominated throughout ($T_P < 11.8$). At CAM, peak H_s (4.8 m) and T_p (11.8 s) associated with '*Angus*' overnight on day 3 were short lived (< 12 hours). This was followed by a secondary peak on 5th day of the experiment ($H_s < 3.9$ m) and ($T_p < 11.1$ s). The MMR event was characterised by a more persistent event, with H_s exceeding the 95th percentile for the entirety of days 4 and 5.

At BEE, the experiment began with a 7-day period of exceptionally long period ($T_p < 20$ s) but small waves ($H_s < 1$ m). This was followed by a drop in T_p to less than 10 second accompanied by a steady rise in H_s to a peak of 5.6 m. Waves in excess of the 99th percentile H_s persisted for 3 days and the 95th percentile for the majority of the final two weeks of the experiment.

Time series of beach volume (Q) along the instrument profile (Table 3-2) were calculated by taking the area under the measured profile at each site. The area bounded by largest and smallest value of Q per site was taken to be the profile envelope. Profile envelopes as well as the temporal mean profile observed during each storm survey are displayed in Figure 3-1.

At all sites, perhaps unsurprisingly, the lowest Q followed the peak H_s. However, the extent to which the profile responded during the experiment varied dramatically between the five sites. The largest response was seen at the two gravel sites, Beesands (BEE) and Chesil (CSL), with reductions in Q of 65 and 15 m^3/m respectively (Table 3-2) and a cross shore recession in the upper profile of up to 10 m (Figure 3-1). The Chesil profile exhibited a partial 'cut and fill', with some of the material removed from the upper profile being deposited on the lower profile. At Beesands, sediment removed from the profile was transported both along and cross shore, contributing to the $2.3 \pm 0.8 \times 10^5$ m^3 of gravel transported from the sub-aerial to the sub-tidal across the wider Start Bay region as a whole during Storm Emma (McCarroll et al., 2019).

The third largest topographic response was observed at Perranporth. At the start of the experiment a period of steady accretion (Q increasing from 770 to 780 m^3/m over 4 days) associated with relatively small, long period waves was observed. Following H_s exceeding the 95th percentile threshold, up to 9 m^3/m was removed from the instrument profile. In particular, the upper beach (>2 m ODN) saw a horizontal

recession of up to 6 m (Figure 3-1). A slight gain in material below 0 m ODN implies that some of the material lost from the upper beach face may have been deposited lower on the profile. However, behaviour of the beach profile at Perranporth has been shown to be complex, with sediment transport occurring via longshore beach face rotation, exchange between the intertidal beach and subtidal bar and even material leaving and entering the system via headland bypassing during storms (Valiente et al., 2019).

The topographic response was slightly smaller at Camber, with a reduction in Q of 7 m^3/m observed following the peak in wave height and period. A cross shore recession of up to 5 m was observed on the steeper, coarser grained upper beach, above 2 m ODN. This material may have been deposited lower on the profile or transported long shore. The smallest topographic response was observed at Minsmere, whereby Q only fell by up to 2 m^3/m after the peak wave height was reached. This was reversed by a 3 m^3/m accretion over the following two tides. As a result, the profile was fairly stable and the envelope reasonably narrow, exhibiting a small amount of cut and fill between 2.5 and 1.5 m ODN (Figure 3-1).

Table 3-2 Hydrodynamic conditions associated with the storms studied in this thesis. Columns from left to right; site studied, storm name, dates each storm was active; range of Hs and Tp over these dates (maximum values quoted in bold), mean Hs and Tp; 95th and 99th percentile of long term wave record defined in Table 2-2; return period in years[1]; return period plot of Hs measured at CCO wave buoy network around southern England, where bubble size and shade represent increasing return period[2]; time series of Hs and Tp over dates each storm was active. Hs and Tp at peak wave height and period are represented circles and triangles respectively. 95th and 99th percentile of long term wave record are marked by orange and red dashed lines respectively. Time series of beach volume (Q) along the instrument profile expressed as meter cubed of beach volume per longshore meter of beach face (m^3/m). Crosses indicate times of topographic surveys.

Site/Experiment *Storm Name* Date	Range during storm Mean of storm		Long Term Threshold		Return period (years)	Regional wave buoy H$_s$ return period	Time series of H$_s$ and T$_p$
	H$_s$ (m)	T$_p$ (s)	H$_{0\_95}$ (m) T$_{p\_95}$ (s) H$_{0\_99}$ (m) T$_{p\_99}$ (s)				○ Peak H$_s$ △ Peak T$_p$ − ⊖ − 95% − ⊖ − 99% × Survey
Perranporth, U.K. *Unnamed storm* 22nd Jan – 8th Feb 2017	0.73–**4.7** 1.9	5–**20** 15.7	3.4 4.5	15.4 18.2	<1 in 1		
Chesil, U.K *'Petra'* 3 - 9th February 2014	1.33–**7.0** 3.1	5.6–**20** 10.5	2.4 3.4	15.4 18.2	1 in 10		
Beesands, U.K. *'Beast from the east/Emma'* 14th Feb – 5th March 2018	0.29–**5.6** 1.6	3.9–**20** 8.9	1.8 2.5	14.3 16.7	1 in 40		
Camber Sands, U.K. *'Angus'* 18 – 23rd *Nov 2016*	0.61–**4.8** 1.8	2.8–**11.8** 7.0	1.9 2.6	11.1 13.3	1 in 20		
Minsmere, U.K *Unnamed storm* 4-10th Jan 2018	0.44–**2.7** 1.4	2.6–**10.5** 6.3	1.8 2.6	8.3 11.1	1 in 5		

1. Source: https://www.channelcoast.org/ccoresources/stormcatalogue/CCO_ExtremeWaves_2017_2018.xlsx

2. https://www.channelcoast.org/ccoresources/stormcatalogue
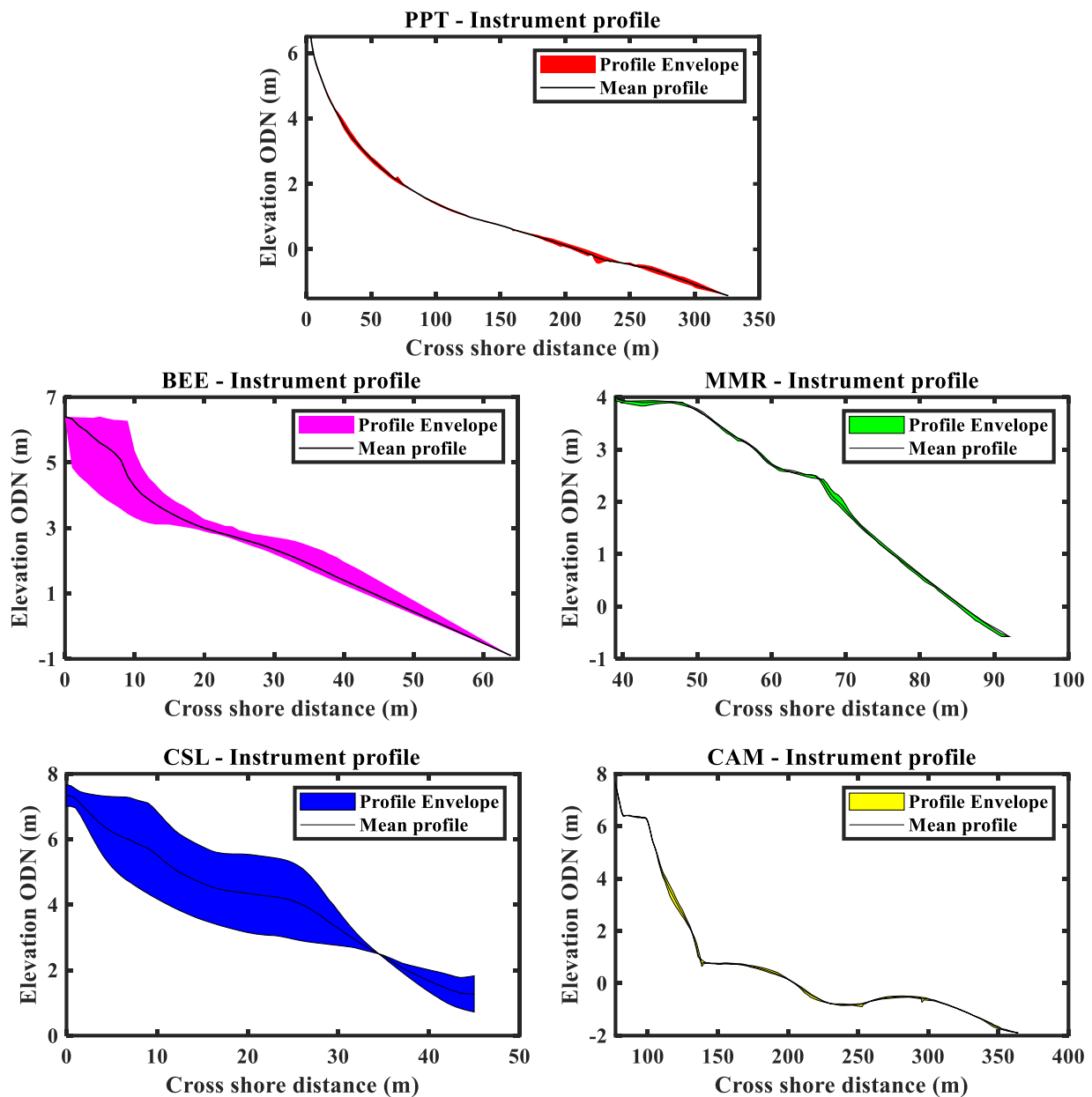
Figure 3-1 Topographic response observed along the instrument profile during storm surveys at Perranporth (PPT), Beesands (BEE), Chesil (CSL), Minsmere (MMR) and Camber (CAM). The profile envelope, taken as the region bounded by the largest and smallest beach profile volume (Q) is shown by the shaded area and the mean profile displayed as a black line.

In the Chapters that follow, subsets of the dataset presented in Chapter 3 are analysed

to address the thesis aims. First, video data is used to examine the role of infragravity

waves at the shoreline of a gravel beach, Beesands, in Chapter 4. Results from

Beesands are compared to the four remaining sites in Chapter 5. These findings are

quantitatively compared to existing empirical relationships linking beach and wave

conditions to infragravity motions. In Chapter 6 in-situ measurements collected by

intertidal arrays of pressure transducers are used to compare the behaviour of

infragravity waves between the breakpoint and the inner surf zone at the sandy

Perranporth and gravel Beesands.

4   <u>Observations of infragravity dominance in the swash zone of a steep gravel beach</u>

This Chapter contains work published in the following paper:

Billson, O., Russell, P., Davidson, M., Wiggins, M., McCarroll, J., Poate, T., & Leonardi, N. 2019b. Observations of infragravity dominance in the swash zone of a steep gravel beach. In: Coastal Sediments 2019 (pp. 1866–1878). World Scientific.

4.1   <u>Introduction</u>

Accurate prediction of wave runup is vital in coastal management and engineering as extreme water levels associated with storms can result in inundation and overtopping (Serafin et al., 2017). Runup, defined as the elevation of the shoreline above still water level, comprises a mean (set-up) and oscillatory component (swash) (Stockdon et al., 2006). The swash transfers energy from the waves to the shore, playing a key role in sediment transport, and can drive significant erosion during storms (e.g., Russell, 1993; Masselink and Puleo, 2006; de Bakker et al., 2016). Commonly, swash oscillations are considered by separating the gravity (frequency (f) = 0.05 – 0.3 Hz) and infragravity (IG) bands (f = 0.003 – 0.05 Hz) and quantified as significant swash height, S, equal to 4σ, where σ^2 is vertical runup variance in each band. After breaking, incident waves dissipate much of their energy, with heights tending toward saturation at the shoreline. In contrast, infragravity waves shoal

shoreward, increasing in height, resulting in their increasing dominance of the total

energy spectrum as depth decreases across the surf zone (e.g., Guza and Thornton,

1982; de Bakker et al., 2014). Gravel beaches, in contrast to sandy beaches, have an

absence of offshore bars, very narrow surf zones and a close proximity of wave

breaking to the shoreline (Masselink et al., 2010). It is therefore not surprising that

existing runup predictors, developed on sandy beaches, have been shown to under

predict runup when applied to gravel beaches (e.g., Poate et al., 2016).

Inherent difficulties associated with collecting measurements on gravel beaches

(Orford et al., 2003), such as instrument damage caused by the violent breaking

process, have limited most previous observations to lower energy conditions (e.g.,

Masselink et al., 2010). While observations of swash on gravel beaches remain

limited, numerous swash experiments have been conducted on sandy sites. Non-

linear processes occurring in the surf zone are hard to characterise, therefore a range

of simplified parameterizations of swash exist based on differing combinations of

incident wave statistics and beach slope.

The contrasting behaviour of the gravity and infragravity swash components with

offshore wave height was originally identified by Guza and Thornton (1982). They

observed that, on a low slope sandy beach, the swash height at gravity frequencies

(S_g) showed no relationship with offshore significant wave height (H_0), but the

infragravity swash height (S_{ig}) increased linearly with H_0. Other researchers have

since reported similar linear relationships between S_{ig} and H_0, with a range of

constants of proportionality(e.g. Ruessink et al., 1998b; Ruggiero et al., 2004; Senechal et al., 2011b). Stockdon et al. (2006) quantified infragravity swash dominance as the ratio between the two bands ($S_{ig}/S_g > 1$) and found this ratio increased as ξ_0 reduced, owing to increasing levels of short-wave dissipation on wide, low-sloping beaches and increasing S_{ig} associated with larger values of H_0.

In stark contrast to previous contributions to the topic, here, data were collected on a steep (0.14 slope), gravel (median grain size (D_{50}) = 5 mm) beach during high energy wave conditions. These waves were associated with the 'Beast from the East', a prolonged period of exceptional strong onshore (easterly) winds (Met Office, 2018) that hit the U.K. in February/March 2018. During this time, local wave heights exceeded the 95% storm threshold of 2.17 m (Wiggins et al., 2019) on five consecutive days. Spanning eight days during the 'Beast from the East', 40 hours of shoreline video data were collected and used to look for the presence and potential dominance of infragravity waves in the swash. The relationship between infragravity swash and offshore wave height was investigated to see if infragravity swash on gravel beaches also increased linearly with increases in offshore wave height. Finally, the presented results are discussed in the context of previous research in order to draw conclusions on the behaviour of infragravity swash on a gravel beach.

4.2   Method

For a detailed description of the field site (Beesands) and additional information on the environmental conditions surveyed during storm '*Emma*', the reader is referred back to Chapter 3.

4.2.1 Video data processing

At each of the sites, data collection was targeted around storm events using the infragravity specific RCRU, described in detail in Chapter 2.2.2. In the present example, a 10 m tower, equipped with high-resolution video cameras fed data to a computer inside the RCRU, storing over 70 h of video images across the 5 deployments.

At all sites a representative cross-shore profile ('analysed profile' Figure 4-1a) was carefully selected to monitor runup, minimising the impact of longshore sediment transport, headlands or sea defences on the beach profile. Daily monitoring of the profile was carried out using real-time kinematic (RTK) GPS, capturing changes every other low tide. A value of beach slope (tan β) was defined per 20-min data-run as the average gradient between the 2% exceedance level of runup (R2%) and still water level (SWL), minus twice the offshore significant wave height ($SWL–2H_0$), following (Poate et al., 2016).

In order to calculate swash statistics, images captured at a rate of 4 Hz by a Pointgrey Grasshopper camera fitted with a 25 mm lens were used to produce pixel stacks as follows. Ground control points, where both the real world and image positions were known, were used to generate a geometry solution, facilitating conversion of co-ordinates from a 2-D (U,V) image to a 3-D (X,Y,Z) real-world system and vice versa. The method used here for obtaining photogrammetric relationships was developed by Holland et al. (1997) and is widely used in comparable works (Stockdon et al., 2006; Senechal et al., 2011b; Poate et al., 2016). The line of pixels corresponding to the 'analysed profile' (Figure 4-1a) were extracted from each image and stacked horizontally against time. The blue-red ratio and intensity of each pixel was evaluated and threshold values defined which corresponded to the discrete transition from dry beach to swash, after Stockdon et al. (2006), yielding a digitized time series of swash. Finally, this was converted from UV to XY space to produce a time series of horizontal swash (Figure 4-1b) with the elevation (Z) associated with each cross-shore position used to quantify vertical swash height (Figure 4-1c). 8-point unweighted sliding-average frequency smoothed spectral estimates were computed for each 20-min time series of vertical swash (Figure 4-3), each with 16 degrees of freedom. The same frequency smoothing was applied to the offshore spectral estimates (Figure 4-3). These were calculated using 20-minute time series of raw surface elevation, collected at local wave buoys.

The horizontal resolution of the video method depends on the camera's focal length, field of view, separation between the camera and the shoreline and how high above still water level the camera is positioned (Holland et al., 1995). Across the five sites, horizontal resolution ranged between 0.2 – 0.7 m.

In this study, the vertical measurement of swash (Z) was extracted from a 'representative' beach profile, surveyed with RTK GPS at the start of the deployment. This method was felt to be more accurate than previous studies which have employed a constant beach slope, rather than survey information to obtain Z. In this case, vertical resolution of the video method depends on the accuracy of the RTK GPS (+-0.03 m), plus how much the profile in the swash zone adjusts compared to the 'representative' profile used to obtain Z. Across the five sites the vertical resolution ranged between 0.05 - 0.06 m at the sandy beach, Perranporth and between 0.1 - 0.2 m at the gravel beaches Chesil and Beesands. Vertical resolution at the mixed sediment Camber was 0.07 m and at Minsmere was 0.08 m. The rapid adjustment of the beach profile in the swash zone observed at the gravel sites limited the vertical resolution compared to that achievable at sandy sites. However, both the horizontal and vertical resolution achieved here were comparable to previously published experiments on both sand (0.43 - 0.63 m horizontal and 0.04 - 0.06 m vertical (Gomes da Silva et al., 2018)) and gravel (0.25 - 0.65 m horizontal and 0.1 - 0.2 m vertical (Poate et al., 2016)) beaches.

Spectral variance was used to calculate total significant swash height (S) and separate incident (S_g) ($f = 0.05$–0.3 Hz) and infragravity (S_{ig}) ($f = 0.003$–0.05 Hz) band heights according to Eq. (4-1):

$$S = 4\sqrt{\sum\nolimits_{f1}^{f2} PSD(f)\Delta f} \qquad\qquad \text{Eq. (4-1)}$$

where, $f1$ and $f2$ are the upper and lower frequency bounds of S, S_g or S_{ig} respectively, PSD is power spectral density, f is frequency, and Δf is bandwidth in (Hz).
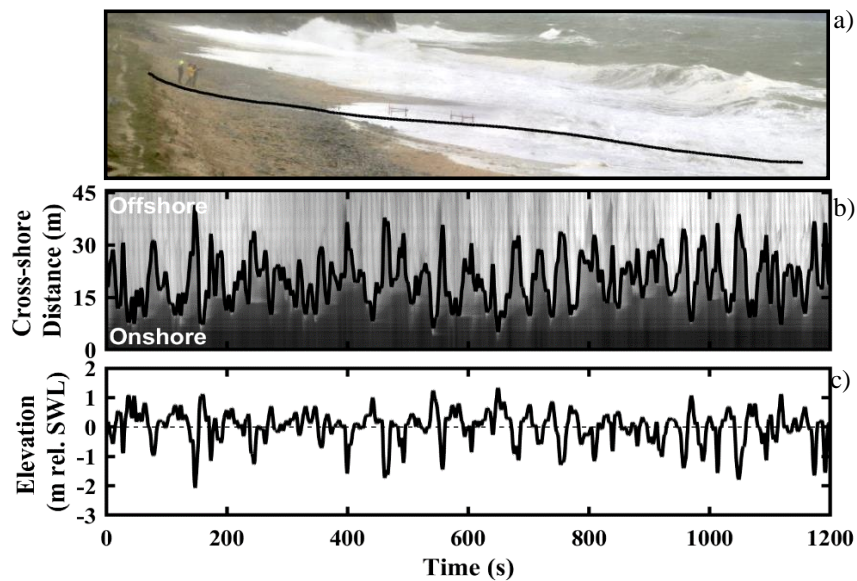
Figure 4-1 Video processing technique: Example from 26 February 2018 from 15:30–15:50 at Beesands: (a): Analysed profile to be extracted (black line); (b): Pixel stack with shoreline detected/ time series of horizontal swash (black line); (c): Vertical swash time series relative to still water level (SWL).

4.3   Results

4.3.1   Environmental conditions

Wave conditions were measured in 10 m mean water depth by the 'Start Bay'
directional wave rider buoy, approximately 5 km north west of Beesands. Tidal
heights were recorded at the nearest gauge (Devonport, 40 km west of the site, data
available at: bodc.ac.uk). An overview of the hydrodynamic conditions during the
field experiment is given in Figure 4-2. A short period (tides 1 – 3) of small (H_s = 0.5
m) southerly swell (T_p = 13 – 18 s) was followed by a prolonged spell (tides 4 – 15)
of larger (H_s = 1.0 – 3.1 m) shorter period (T_p = 4 – 9 s) easterly waves, culminating
in the 'Beast from the East', when, through tides 10 – 14, wave heights persistently
exceeded the 95% storm threshold of 2.17 m. Tides transitioned from springs (tides 1
– 4) to neaps (tides 9 -12). For the eight day field experiment, mean significant wave
height (H_s) was 1.6 m, ranging from 0.5 to 3.1 m. Mean peak period (T_p) was 8.2 s
and ranged from 4 to 18 s. Consistent with previous contributions, an offshore
significant wave height (H_0), approximated by linearly deshoaling values of H_s to 80
m depth (dashed line Figure 4-2a), was used in all further analysis. Over the eight-
day deployment, H_0 varied between 0.5 and 3.3 m and had a mean of 1.8 m.
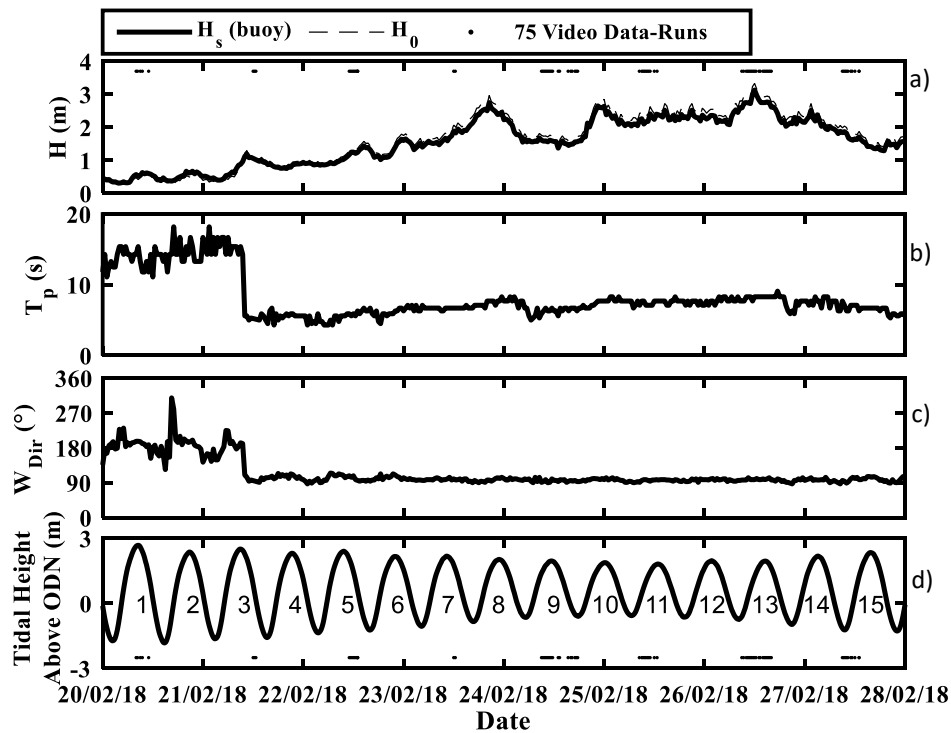
Figure 4-2 Hydrodynamic conditions and times of video data (black dots on a and d). (a,b,c) recorded at Start Bay Wave rider buoy in 10 m mean depth and (d), at Devonport Tide gauge: a): Significant wave height (H_s), solid line and offshore significant wave height (H_0), dashed line; b): Peak wave period (T_p); c): Wave direction (W_{Dir}); d): Tidal elevation relative to ODN with tides numbered.

The cross-shore profile selected to monitor runup ('analysed profile' Figure 4-1a) was carefully selected at the node of longshore rotation (Wiggins et al., 2019), to minimize the impact of longshore sediment transport on the beach profile. Daily monitoring of the profile was carried out using real time kinematic GPS, capturing changes every other low tide, except on February 24th and 25th, when both low tides were surveyed. A value of beach slope (tan β) was defined per 20-minute data-run as, the average gradient between the 2% exceedance level of runup (R_2) and still water level (SWL) minus twice the offshore significant wave height (SWL – 2H_0), following Poate et al. (2016).

4.3.2 <u>Infragravity swash on a gravel beach (Beesands)</u>

The wave energy spectrum measured at the buoy in 10 m mean water depth was

typically dominated by incoming wind-wave frequencies. Figure 4-3 (upper) shows

an example from tide 13 when $H_0 = 2.8$ m and $T_p = 8.3$ s with a corresponding

spectral peak frequency of 0.12 Hz (8.3 s). In contrast, the coincident spectra of

vertical swash at the shoreline (Figure 4-3 lower) showed that the wind-wave peak

peak had totally dissipated and was, instead, dominated by energy in the infragravity

band, with a signifiant peak at 0.026 Hz (39 s).
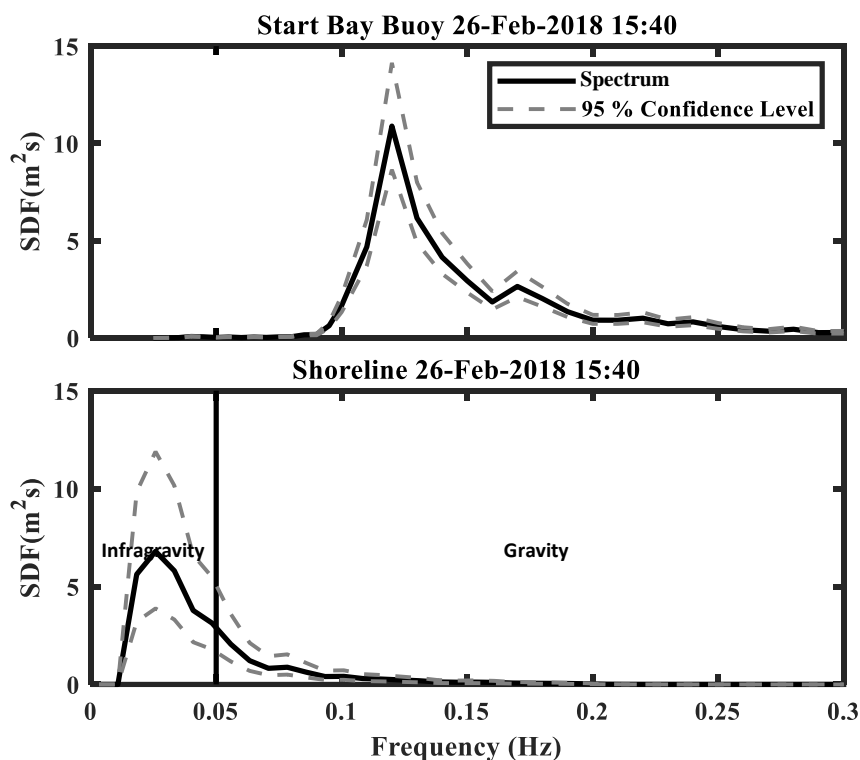
Figure 4-3 Spectral Density Functions (SDFs) showing simultaneous offshore and shoreline wave
spectra for 26-Feb-2018 from 15:40 – 16:00. Upper: Waves measured at Start Bay wave buoy in 10 m
mean water depth (solid black line). Lower: Vertical swash at the shoreline (solid black line). Both: 95 %
confidence interval (dashed grey line).

4.3.3 <u>Relationship between S_{ig} and H_0 on a gravel beach (Beesands)</u>

Linear regression was used to assess the relationship between swash and offshore wave height, where significance was given by (*p*), goodness of fit summarized by correlation squared (R^2) and root mean square error (RMSE) and the relationship quantified by regression slope (m) and y-axis intercept (c).

Partitioning vertical swash into the gravity (S_g) and infragravity (S_{ig}) bands highlighted their contrasting relationship with increasing offshore significant wave height (H_0) (Figure 4-4, left and right respectively).

S_g showed no relationship with H_0 ($R^2 = 0.01$, p = 0.43), implying saturation at short wave frequencies (Figure 4-4, left). Conversely, S_{ig} displayed a scattered (RMSE = 0.28 m) but significant linear relationship with H_0 ($R^2 = 0.65$, p = 0.00), (Figure 4.4, right). This implies that the observed increase in swash height with offshore wave height was mainly in the infragravity band, as observed by Guza and Thornton (1982). Linear regression (Figure 4-4, right, black line) revealed the relationship:

$$S_{ig} = 0.51H_0 + 0.3 \qquad \text{(Eq. 4-2)}$$

Following Senechal et al. (2011b), a regression was also forced through the origin so that when $H_0 = 0$ m, $S_{ig} = 0$ m, (Figure 4-4, right, red line) a more physically correct formulation. Doing so, Eq. 4-2 became:

$$S_{ig} = 0.65H_0 \qquad \text{(Eq. 4-3)}$$

This forced formulation maintained a significant relationship between S_{ig} and H_0 and

resulted in a slight reduction in R^2 and a small increase in RMSE (Figure 4-4, right,

red text.)
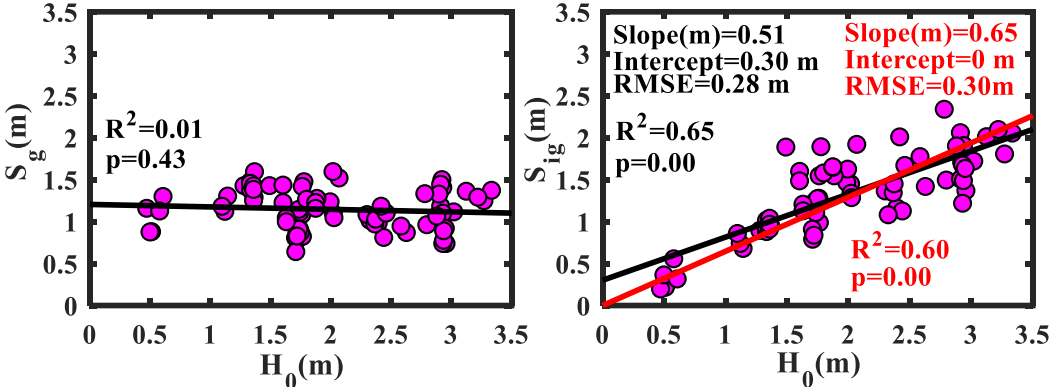
Figure 4-4 Significant swash height against offshore significant wave height (H_0). Left: Incident band (S_g). Right: infragravity band (S_{ig}). Black lines represent linear best fit. Red line (right only) represents linear best fit forced through the origin.

4.3.4 Infragravity dominance on a gravel beach (Beesands)

Taking the ratio $S_{ig}/S_g > 1$ as a measure of infragravity dominance, the relationship with H_0 was again tested using linear regression. The swash became infragravity (IG) dominated when H_0 exceeded approximately 1.5 m (Figure 4-5, upper). The data also suggested a linear trend in dominance with wave height, with S_{ig} values reaching up to twice the height of S_g in large wave conditions ($H_0 \sim 3$ m).

To examine which conditions were consistent with infragravity (IG) energy being observed, the ratio S_{ig}/S_g was plotted against ξ_0 for all 75 20-minute data-runs (Figure 4-5, lower). Short (1990) described morphodynamic conditions as reflective when $\xi_0 > 1$, intermediate when $0.23 < \xi_0 < 1$ and dissipative when $\xi_0 < 0.23$. Breaker types were defined by Battjes (1974) as surging ($\xi_0 > 3.3$), plunging $0.5 < \xi_0 < 3.3$ and spilling $\xi_0 < 0.5$ respectively. In Figure 4-5 (lower), colour refers to breaker type, with magenta points representing plunging breakers and green points representing surging breakers. Applying these definitions to our gravel beach results showed that the swash became infragravity dominated ($S_{ig}/S_g > 1$) when breakers were plunging in morphodynamically intermediate conditions, while under morphodynamically reflective conditions, plunging and surging breakers resulted in no IG dominance, ($S_{ig}/S_g < 1$). This suggests that incident wave dissipation, through breaking, is required to observe IG dominance on a steep gravel slope.
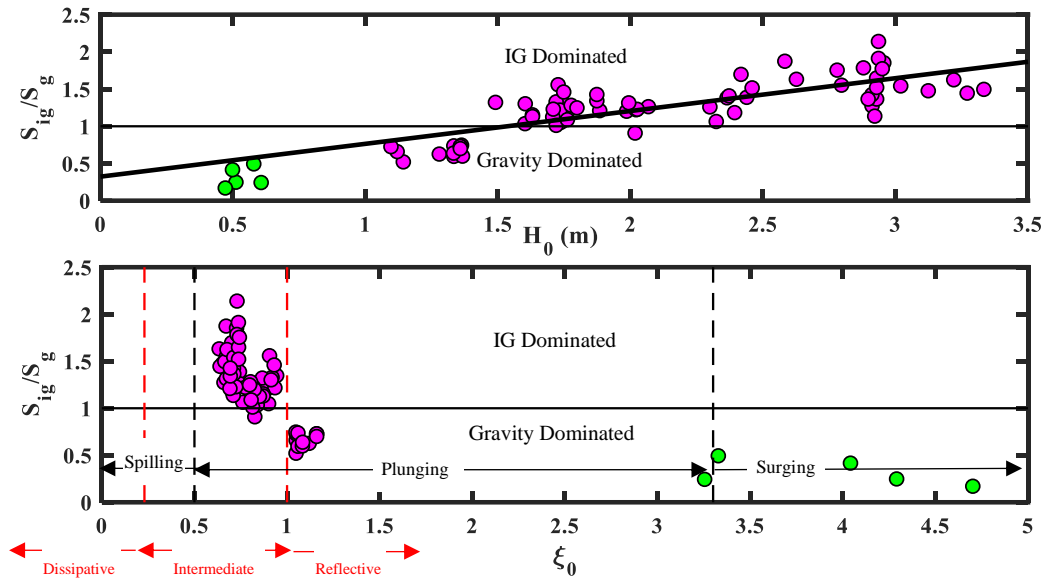
Figure 4-5 Upper: S_{ig}/S_g against H_0. Lower: S_{ig}/S_g against Iribarren number for 75 data-runs. Transition between breaker types (vertical dashed black lines), transition between morphodynamic conditions (vertical red dashed lines). Both: Plunging breakers (magenta), surging breakers (green). Transition from S_g (below) to S_{ig} dominated (above) (horizontal black line). Note different horizontal axis.

4.3.5 Comparing gravel beach results to sand

The new observations presented here of the relationship between offshore wave

conditions and infragravity swash on a gravel beach (Figure 4-4 and Figure 4-5) can

be compared with previous observations, collected under high energy conditions on

sandy sites. Table 4.1 summarises linear relationships between S_{ig} and H_0, obtained

during field experiments where video analysis of the shoreline was used to obtain S_{ig}

(as was the case at Beesands) and the maximum offshore significant wave height

(H_0) exceeded 2.5 m.

Table 4-1 Environmental Conditions* and Linear Relationships Between S_{ig} (Calculated Using Video Analysis), and H_0 Observed During High Energy Experiments**

Site (Citation)	Date	$S_{ig} = mH_0+c$ $(c = 0)^\Delta$	$H0_{(m)}$	$\overline{T_P}(s)$	$\overline{\tan\beta}$	$D50(mm)$
Agate, USA (Ruggiero et al., 2004)	02/1996	$0.33H_0 + 0.3$	2.5 ± 0.5	13.2 ± 2.5	0.02 ± 0.01	0.2
Truc Vert, France (Senechal et al., 2011b)	03/2008	$0.29H_0 + 0.6$ $(0.48H_0)$	2.4 ± 1.2	13.7 ± 1.6	0.06 ± 0.02	0.35
Terschelling, Netherlands (Ruessink et al., 1998b)	11/1994	$0.18H_0 + 0.2$	2.8 ± 0.9	8.7 ± 1.5	0.02 ± 0.01	0.2
Beesands, UK (Presented)	02/2018	$0.51H_0 + 0.3$ $(0.65H_0)$	1.8 ± 0.8	8.2 ± 3.0	0.14 ± 0.02	5.0

* Quoted mean values $\pm$ 1 standard deviation. ** Maximum H_0 for the experiment > 2.5 m.

Δ Where available, equations with an intercept forced through the origin, (c = 0) are included.

For formulations including an intercept (c), the gradient of the regression observed at

Beesands (Eq. 4-2) is nearly three times that observed by Ruessink et al. (1998b) and

significantly larger than reported by Ruggiero et al. (2004) and Senechal et al.

(2011b), suggesting a larger S_{ig} response to comparable values of H_0. Given the large

difference in intercept between the Senechal et al. (2011b) equation (c = 0.6) and the

Beesands equation (c = 0.3), equations forced through the origin (c = 0) provide a

more reasonable comparison. Here, the regression slope at Beesands was over a third

higher than that observed by Senechal et al. (2011b). The larger values at Beesands

suggest that values of S_{ig} for comparable wave heights are in the range of a third to

three times larger at Beesands than the sandy examples presented (Table 4.1).

The contrasting regression gradients observed at Beesands compared to the other

sites in Table 4.1 are potentially caused by morphological differences between gravel

and sandy beaches. The measurements of shoreline infragravity waves presented here are unique as they come from a steep gravel beach. Therefore, wave breaking is violent and plunging (surging in small wave conditions) close to shore. This is in contrast to all the other sites in Table 4.1, which are finer grained sandy beaches with lower sloping offshore profiles, promoting wider surf zones more traditionally associated with infragravity wave observations at the shoreline.

At our gravel beach, transition to S_{ig} dominance occurred as conditions crossed the threshold from morphodynamically reflective to intermediate ($\xi_0 = 1$) with Figure 4-5 (lower) strongly suggesting that an increase in short wave dissipation with decreasing ξ_0 is required for infragravity dominated conditions. The unusually large incident wave heights but comparatively short incident wave periods (and wavelengths) experienced for the majority of 'The Beast from the East' meant that, despite the typically steep beach slope (0.14) observed at Beesands, much of the time ξ_0 fell within the intermediate range, with values varying between 0.6 – 0.9. This is comparable with the range of ξ_0 observed by Senechal et al. (2011b) (0.5 – 0.9) on a lower slope (0.06), sandy beach. It is therefore intuitive that infragravity energy was detected and can dominate in the swash on the gravel beach, as was observed on the sandy beach by Senechal et al. (2011b).

While the presented data implies increased infragravity swash response on gravel beaches compared to sand, for a given wave height, observations from a wider range of gravel sites are required to corroborate and quantify these differences.

5 Storm Waves at the Shoreline: When and Where Are Infragravity Waves Important?

Revised version to complement thesis structure of: Billson, O., Russell, P., & Davidson, M. 2019a. Storm waves at the shoreline: When and where are infragravity waves important? Journal of Marine Science and Engineering, 7(5), 139.

5.1 Introduction

For a full discussion of key concepts relevant to Chapter 5, the reader is referred back to Chapter 1.3.2.2 – sources of infragravity energy and Chapter 1.3.3 - Infragravity swash.

5.1.1 Scope of research

In Chapter 5 findings reported in Chapter 4 using observations from the steep gravel beach (Beesands) during storm '*Emma*' are compared to data collected at an additional four sites (a low-sloping sandy beach (Perranporth), a second steeper gravel beach (Chesil) and two compound/mixed sand and gravel beaches (Camber and Minsmere respectively). Of the four additional sites, new data were collected as part of this thesis at all except Chesil, where the complementary dataset previously published by Poate et al. (2016) was re-analysed. Chapter 5 aims to assess: *how the*

importance and dominance of infragravity waves vary at the shoreline of five

contrasting beaches by:

- Assessing how swash height in the gravity (S_g) and infragravity bands (S_{ig})

  relates to offshore wave height (H_0).

- Examining how accurately previous parameterisations of S_{ig}, developed over a

  limited range of wave and morphological conditions, can be used to predict S_{ig}

  across the range of morphologies in the new dataset and whether an improved

  parameter can be obtained.

- Developing a conceptual model to illustrate the importance of infragravity

  swash at the shoreline on a wide variety of beach morphologies under a wide

  range of high energy swell and wind-wave combinations.

5.2   Method

The methodology used in this Chapter was described previously. As such the reader

is referred to the following Chapters for further details:

5.2.1 Description of field sites
See Chapter 2.1

5.2.2 Field data collection
See Chapter 2.2.2

5.2.3 Environmental conditions
See Chapter 3

5.2.4 Video data processing
See Chapter 4.2.1

5.3   Results

5.3.1   Environmental conditions

Data collection was targeted around extreme storm wave events at each of the five

sites, summarised in Table 5-1. At Chesil, both exceptionally long period waves

(<16.7 s) in excess of the 95th percentile and shorter period swell waves (>10 s)

yielded a mean period of 13.8 s. Perranporth was dominated by exceptionally long

period swell waves with mean T_p (15.7 s) in excess of the 95th percentile threshold.

At Beesands, two days of small swell waves extended the upper limit of observed T_p

to 15 s. However, the comparatively low mean T_p (7.4 s) demonstrates that the

deployment was dominated by locally generated wind waves. Deployments at

Minsmere and Camber were characterised by large wind waves, as reflected in the

mean period of 7.7 s and 6.4 s respectively.

Of the 5 sites, the largest significant infragravity swash height (S_{ig}) (11.4 m) and

largest mean S_{ig} (5.1 m) was observed at Chesil. The extreme heights can be

explained by the exceptionally high beach slope $\tan \beta < 0.38$ and wave heights $H_0 <$

6.6 m and are comparable to the exceptionally high runup values obtained by Poate

et al. (2016) during the same experiment (R2% up to 13 m). The second-largest S_{ig}

heights were observed at Perranporth, a site more typically associated with

infragravity dominance. While the mean (2.2 m) and largest (3.6 m) observed S_{ig}

were smaller than observed at Chesil, Perranporth was the only site where S_{ig} was

always above 1 m. Significant levels of infragravity energy were also present in the

swash at Beesands, where S_{ig} heights of up to 2.3 m and a mean height of 1.3 m were

observed. The lowest S_{ig} heights were observed at the compound/mixed sand and

gravel sites, Camber and Minsmere, where the maximum S_{ig} (0.81 and 0.68 m

respectively) was lower than mean S_{ig} observed at any other site.

Table 5-1 Summary (range and mean) of environmental parameters sampled during the presented research. Subscript 0 indicates parameters calculated using deep water values linearly deshoaled to 80 m depth. N = number of 20 min data runs.

Site/Experiment	Date	H_0 (m)	T_p (s)	Tan β	D_{50} (mm)	ξ_0	N	S_{ig} (m)
Beesands, U.K.	20–27 Feb 2018	0.4–3.3 2.0	5.1–15.0 7.4	0.09–0.11 0.10	- 5	0.53–2.84 0.71	75	0.20–2.3 1.3
Perranporth, U.K.	31 Jan–07 Feb 2017	1.6–3.2 2.4	11.1–18.2 15.7	0.02–0.08 0.034	- 0.25	0.19–0.96 0.44	31	1.1–3.6 2.2
Camber Sands, U.K.	19-22nd Nov 2016	0.9–3.8 2.2	5.5–10.0 7.7	0.02–0.10 * -	0.33–10 * -	0.059–1.1 1	16	0.30–0.81 0.53
Minsmere, U.K	6–9 Jan 2018	0.52–2.5 1.6	3.3–7.7 6.4	0.03–0.13 ** -	0.33–20 ** -	0.1–0.97 0.21	43	0.01–0.68 0.33
Chesil, U.K	5–6 Feb 2014	1.6–6.6 3.9	10.3–16.7 13.8	0.24–0.38 0.32	65 -	2.21–3.84 3.7	40	0.65–11.4 5.1

* Camber is a compound beach with a steeper gravel upper and low slope sandy lower; ** Minsmere is a mixed sand and gravel site (as reflected in the wide-ranging D50 with a steep gravel upper and lower sloped lower profile.

5.3.2 Comparison of incoming wave spectra with vertical swash spectra at the shoreline

Offshore spectra calculated at local wave buoys (Figure 5-1 a,c,e,g,i) were compared

to those calculated at the shoreline from time series of vertical swash (Figure 5-1

b,d,f,h,j). The examples presented were specifically selected as most clearly

representing extreme conditions at each site. Times where exceedance of H_{0_95}

coincided with high water (±1.5 h) were targeted in order to minimise contamination

of the spectra with tidal signal.

The buoy spectra can be divided into swell dominated (Perranporth and Chesil, Figure 5-1 a,c respectively) and wind-wave dominated (Beesands, Camber and Minsmere, Figure 5-1 e,g, and i respectively). At the shoreline, spectra can be divided into three groups: infragravity dominated due to dissipation of gravity energy and growth of IG energy (Perranporth and Beesands, Figure 5-1 b,f respectively); high energy gravity and infragravity due to minimal incident wave dissipation (Chesil, Figure 5-1 d); and low energy in both bands, due to maximum minimal incident wave dissipation (Camber and Minsmere, Figure 5-1 h and j respectively).

At Perranporth, a single, significant peak in the wave buoy spectrum (0.056 Hz, 17.9 s) (Figure 5-1 a) was replaced by a single significant peak in the infragravity band in the shoreline spectrum (0.011 Hz, 90 s) (Figure 5-1 b). As a result, significant gravity swash height (S_g = 0.57 m) remaining at the shoreline was less than 1/5 of the offshore wave height in the gravity band (H_{sg} = 3.1 m). At Chesil, a single incoming swell peak (0.063 Hz, 15.8 s) in the wave buoy spectrum (Figure 5-1 c) was maintained in the shoreline spectrum (Figure 5-1 d). In addition, an IG peak at 0.013 Hz (77 s) was also present in the shoreline spectrum (Figure 5-1 d). Significant wave and swash height were similar at the buoy and the shoreline (H_{sg} = 5.6 m, S_g = 5.2 m).

The contrast in the development of spectra between the buoy and the shoreline at Perranporth and Chesil resulted from differences in short wave breaking and dissipation. At Perranporth, incoming swell waves were efficiently dissipated across

a wide surf zone as spilling breakers. At Chesil, dissipation of swell waves appeared

to be minimal. The steep beach face and large, low-steepness incoming waves

resulted in high energy surging and plunging breakers breaking directly on the beach

face as a shore break, conserving the swell peak in the shoreline spectrum.

At the wind-wave dominated sites, a reduction in total energy from the buoy to the

shoreline indicated energy dissipation, where steep storm waves produced spilling

breakers on the shallow lower profile of the compound/mixed sites (Minsmere and

Camber) and plunging breakers on the gravel site (Beesands).

At Beesands the shoreline spectrum (Figure 5-1 f) shows energy at gravity band

frequencies (incident wave peak, 0.12 Hz, 8.3 s) was dissipated with the growth of a

broad low-frequency peak at 0.026 Hz (38 s). In the gravity band, swash height ($S_g =$

1.1 m) reduced to around half that of H_{sg} (2.7 m) and in the infragravity band

significant swash height (S_{ig}) = 1.9 m.

At Camber (Figure 5-1 g) and Minsmere (Figure 5-1 i), the majority of the incoming

short-wave energy (concentrated at wind-wave frequencies of around 0.11 Hz (9.1 s)

and 0.15 Hz (6.0 s) respectively) was dissipated by the shoreline. This resulted in an

absence of energy in the gravity band and a single low energy, low-frequency peak in

the shoreline spectra of both sites (Figure 5-1 h,j).
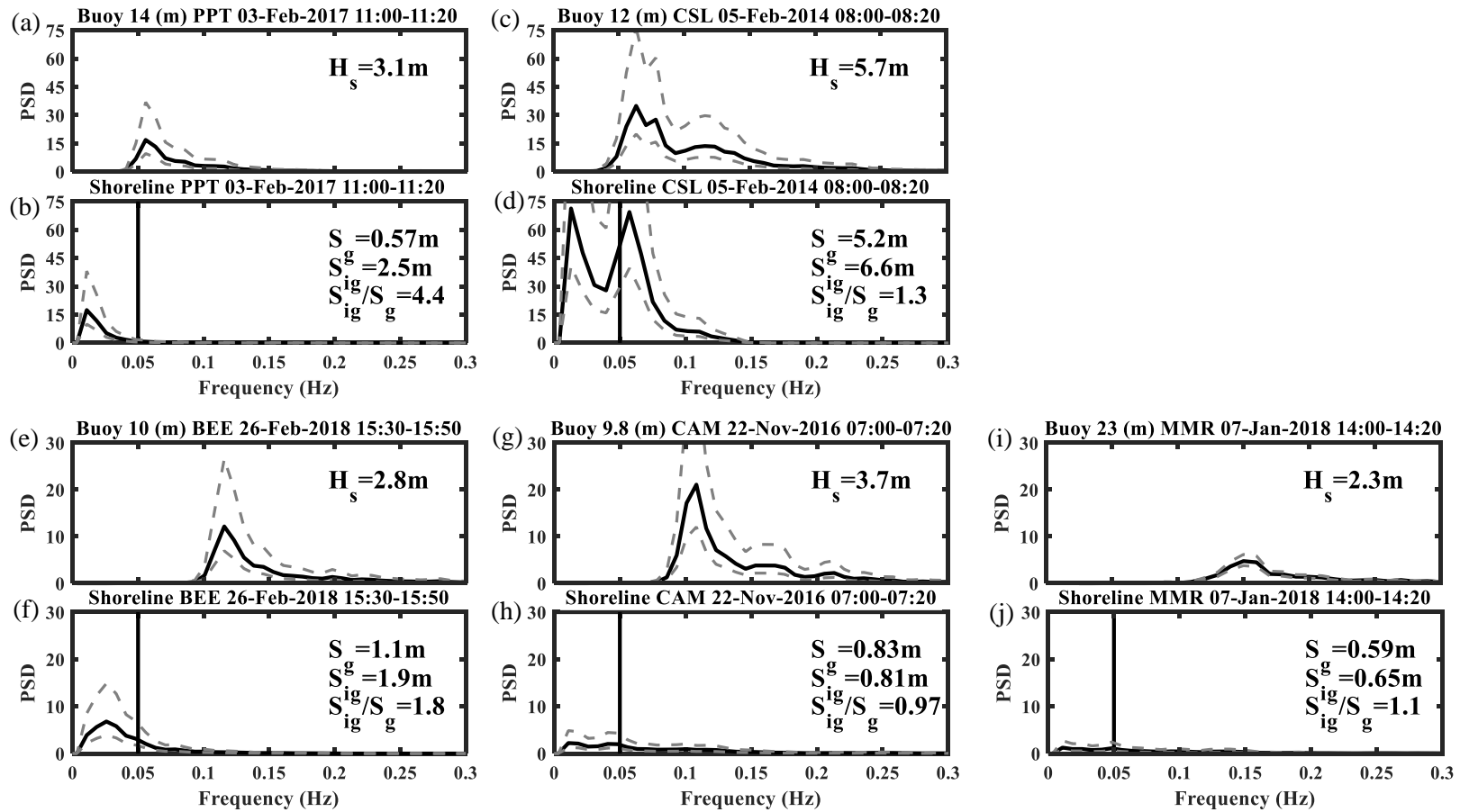
Figure 5-1 Frequency smoothed wave spectra showing examples of simultaneous power spectral densities (PSD) offshore and at the shoreline. a,c,e,g and i: Waves measured at local wave buoys (solid black line). b,d,f,h and j: Vertical swash at the shoreline (solid black line). Both: 95% confidence interval (dashed grey line). Infragravity and gravity bands are separated by a vertical black line at 0.05 Hz in the vertical swash spectra. a + b = Perranporth (PPT), c + d = Chesil (CSL), e + f Beesands = (BEE), g + h = Camber (CAM), i + j = Minsmere (MMR).

5.3.3 <u>Relationship between swash and offshore Wave Height (H_0)</u>

Linear regression was used to assess the relationship between swash and offshore wave height, where a significant relationship at the 99.5% confidence limit was given by ($p <$ 0.005). Goodness of fit was summarised by correlation squared (R^2), and root mean square error (RMSE) and the relationship quantified by regression slope (m) and y-axis intercept (c). Partitioning vertical significant swash height into the gravity (S_g) and infragravity (S_{ig}) bands highlighted their contrasting relationship with increasing offshore significant wave height (H_0) (Figure 5-2, left and right respectively). Regression statistics for the relationship between S_{ig} and H_0 at each of the sites individually and all sites combined are summarised in Table 5-2.

Significant swash height in the *gravity band* (S_g) showed no significant increase with H_0 ($p >$ 0.005) at all sites (except Chesil) implying saturation in the gravity band. As such, no line of best fit is shown in Figure 5-2 (left). At Chesil the increase of S_g with H_0 shows that the gravity band was not saturated, resulting in large amounts of energy in the gravity band reaching the shoreline during large offshore wave conditions.

In contrast, significant swash height in the *infragravity band* (S_{ig}) showed significant ($p <$ 0.005) and well-correlated relationships ($R^2 = 0.65$–0.86) with H_0 at all sites (except Camber where $p = 0.51$), showing that S_{ig} at the shoreline continued to increase with increasing H_0. The diversification in the behaviour of swash in the gravity and infragravity band at all sites except Chesil shows that an increase in offshore wave height (H_0) has no influence on gravity band swash heights but leads to a linear increase of infragravity band

124

swash heights. This implies that swash heights in the gravity band are saturated as a result of short wave dissipation.

Both the largest offshore wave ($H_0 < 6.7$ m) and shoreline infragravity swash heights ($S_{ig} < 11.4$ m) were observed at Chesil, resulting in the steepest regression slope ($m = 2.0$). The next largest S_{ig} heights were observed at Perranporth where S_{ig} ranged between 2.5–3.2 m for $H_0 = 2.5$–3.6 m, over twice the S_{ig} heights (1.4–2.6 m) observed over the same range of H_0 at Beesands. Despite their contrasting regression slopes, Chesil ($m = 2.02$), Beesands ($m = 0.51$) and Perranporth ($m = 1.1$), showed comparable S_{ig} heights (0.75–2 m) when H_0 ranged between 1.5–2.5 m.

The dataset as a whole showed a strong and significant linear correlation between S_{ig} and H_0, ($p < 0.005$, $R^2 = 0.78$) with a regression slope (m) of 1.7 and an intercept (c) of −2.0. The negative value of c caused the line of best fit to intercept the x-axis, facilitating the tentative definition of a threshold of H_0 of around 1.3 m, above which infragravity energy becomes apparent in the swash.

The spread of values of S_{ig} for a given value of H_0 at Chesil may be attributed to variability in the incoming wave conditions and/or the profile and beach slope over which waves were breaking and running up. It is feasible that values of H_0 varied within a given 20-min run, resulting in variability in S_{ig}, owing to the linear relationship described in Figure 5-2. Further, gravel morphology is known to respond rapidly to wave forcing (Austin and Masselink, 2006) and so the assumption of a constant slope throughout a tidal cycle may not be representative of reality.
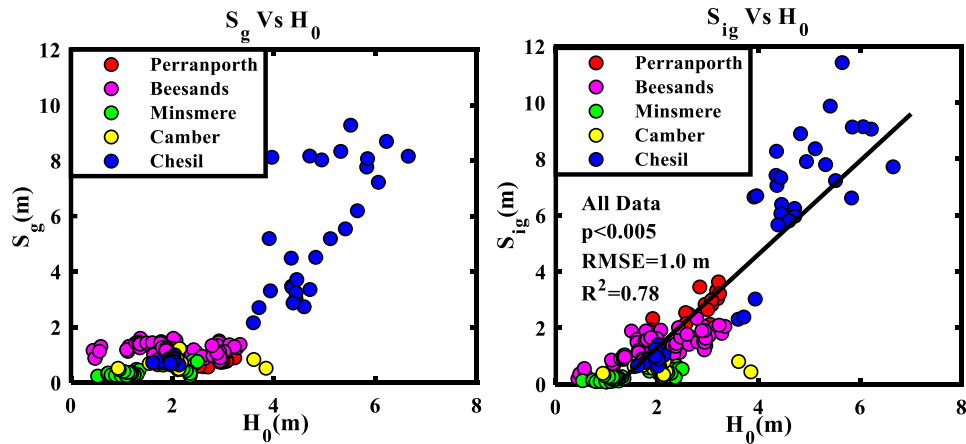
Figure 5-2 Significant swash height against offshore significant wave height (H_0). Left: Incident gravity band (S_g). Right: infragravity band (S_{ig}), where black line represents the linear best fit for all sites.

Table 5-2 Relationship between significant swash in the infragravity band (S_{ig}) and offshore wave height (H_0).

Site	Regression Slope (m)	Intercept ©	R^2	p	RMSE (m)
CSL	2.02	−2.82	0.86	<0.005	1.29
PPT	1.06	−0.40	0.67	<0.005	0.44
BEE	0.51	0.30	0.65	<0.005	0.28
MMR	0.25	−0.06	0.67	<0.005	0.11
CAM	0.04	0.44	0.03	0.51	0.16
Combined	1.66	−2.01	0.78	<0.005	1.00

The relative contributions of infragravity and gravity energy to the swash were assessed using the ratio S_{ig}/S_g, where values greater than (less than) one imply infragravity (gravity) dominance. Figure 5-3 shows the ratio of S_{ig}/S_g plotted against H_0.

Perranporth was most dominated by infragravity swash, with an S_{ig}/S_g ratio of up to 4.4 for the largest incident wave conditions, $H_0 = 3.2$ m (Figure 5-3). At Chesil, despite the absolute magnitude of S_{ig} being largest at this site (Figure 5-2, right), values of S_{ig}/S_g were smaller and varied between 0.7 and 2.5 across the entire observed range of wave heights ($H_0 = 1.6 – 6.8$ m). The difference in infragravity dominance at the two sites can in part be

126

explained by the contrasting short wave dissipation pattern shown in Figure 5-2 (left). Spilling breakers dissipated much of their energy across the wide surf zone resulting in saturated values of S_g at Perranporth. In contrast, high energy plunging and surging breakers produced a shore break on the steep beach face at Chesil, resulting in a lack of dissipation and S_g increasing linearly with H_0.

Infragravity dominance increased with offshore wave height (H_0) at Beesands. However, it can be seen from Figure 5-3 that S_{ig}/S_g at Beesands increased at a lower rate than Perranporth, implying that, for a given wave height, infragravity frequencies were less dominant. Unlike at Perranporth, short wave dominance ($S_{ig}/S_g < 1$) was observed at Beesands. At this site specifically, a transition from gravity dominated to infragravity dominated swash occurred at a threshold of H_0 1.5 m.

At Minsmere, the ratio of S_{ig}/S_g increased with low values H_0 (<1.3 m) but crucially, barely exceeded 1, signifying gravity dominance. At Camber, no relationship with H_0 was apparent, with the maximum observed ratio of $S_{ig}/S_g = 0.9$. This clearly demonstrated that, even during large waves ($H_0 > 1.3$ m), infragravity frequencies rarely became dominant over gravity frequencies in the swash on the compound/mixed beaches.
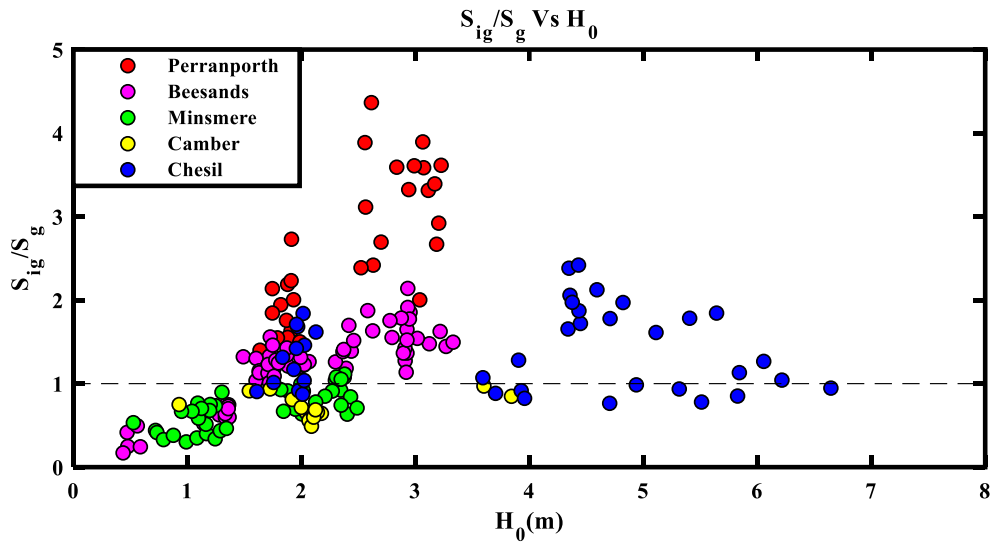
Figure 5-3 S_{ig}/S_g against H_0. Transition from S_g (below) to S_{ig} dominated (above) (horizontal dashed line).

5.3.4 The role of wave height, period and beach slope in the prediction of significant infragravity swash height (S_{ig})

In addition to wave height, previous research has highlighted the potential importance of wave period and beach slope in the prediction of significant infragravity swash height (S_{ig}). As such, in Chapters, 5.3.5, 5.3.6 and 5.3.7, three predictors of S_{ig} are applied to the presented new dataset, and the strength of relationship assessed using linear regression and bias as:

$$\text{Bias} = \sum(x_{predicted} - x_{observed})/n \qquad \text{Eq. (5-1)}$$

where n represents the number of observations in both $X_{predicted}$ and $X_{observed.}$

In addition to the combinations of wave and beach statistics presented in Chapters 5.3.5, 5.3.6 and 5.3.7 ($(H_0L_0)^{0.5}$, $(\tan \beta)^{0.5} H_0T_p$, (H_0^2T)), the following parameters were tested and

found to show weak or no significant relationship with S_{ig}: $\tan \beta (H_0L_0)^{0.5}$, $(\tan \beta H_0L_0)^{0.5}$, $(\tan \beta)^{0.5}$, $(\tan \beta)^{0.5}H^2T$, and as such are not presented.

5.3.5 <u>Stockdon Equation (S2006) – Predicting significant infragravity swash height (S_{ig}) on sandy beaches</u>

Eq. (5-2) (Stockdon et al., 2006) (Herein referred to as S2006) was developed empirically using a range of data from 10 sandy beaches:

$$S_{ig} = 0.06(H_0L_0)^{0.5} \ (4) \hspace{4cm} \text{Eq. (5-2)}$$

where H_0 is deep water wave height and L_0 deep water wavelength. Note that Stockdon forced the intercept (c) through the origin.

S_{ig} observed at our five sites was plotted against $(H_0L_0)^{0.5}$ to assess how the relationship compared with Stockdon's observations (Figure 5-4 a), yielding a significant correlation ($p < 0.005$) at all sites except Camber, with a variety of regression slopes.

S_{ig} at Perranporth (red points) plotted well with the S2006 equation (orange line) over a comparable range of $(H_0L_0)^{0.5}$ (20–35 m), an unsurprising result, given the similarity of Perranporth to the beaches in Stockdon's dataset. The majority of the Beesands data plotted above the S2006 line (Stockdon under-predicting), while the compound/mixed sites fell on or narrowly below it (Stockdon over-predicting). At Chesil, moderate values of $(H_0L_0)^{0.5}$ (19–24 m) matched closely to the S2006 line while large values were severely under-

predicted, implying that infragravity frequencies in the swash were enhanced under high energy conditions at this site.

The largest S_{ig} values observed at Perranporth (> 2.5 m) were slightly under-predicted by S2006, resulting in a negative bias of -0.33 m (Figure 5-4 c). Of the significantly correlated sites, the largest biases and lowest correlations were observed at the gravel sites (Beesands and Chesil) where S2006 under-estimated S_{ig} heights by 0.57 m and 3 m respectively (Figure 5-4 d,g respectively).

Overall, S_{ig} was well-predicted by S2006 at Perranporth and Minsmere, under-predicted at the gravel sites (Beesands and Chesil) and showed no significant relationship at Camber (Figure 5-4 f). This shows that S2006 can be applied over a similar range of conditions to that which it was developed, but cannot be extended to use on gravel beaches or beyond the range of conditions in the original dataset.

Poate et al. (2016) showed an underestimation of runup on gravel beaches, under high energy conditions when employing a runup predictor containing S2006. The findings here suggest that this is due to an underestimation of the IG component of swash.
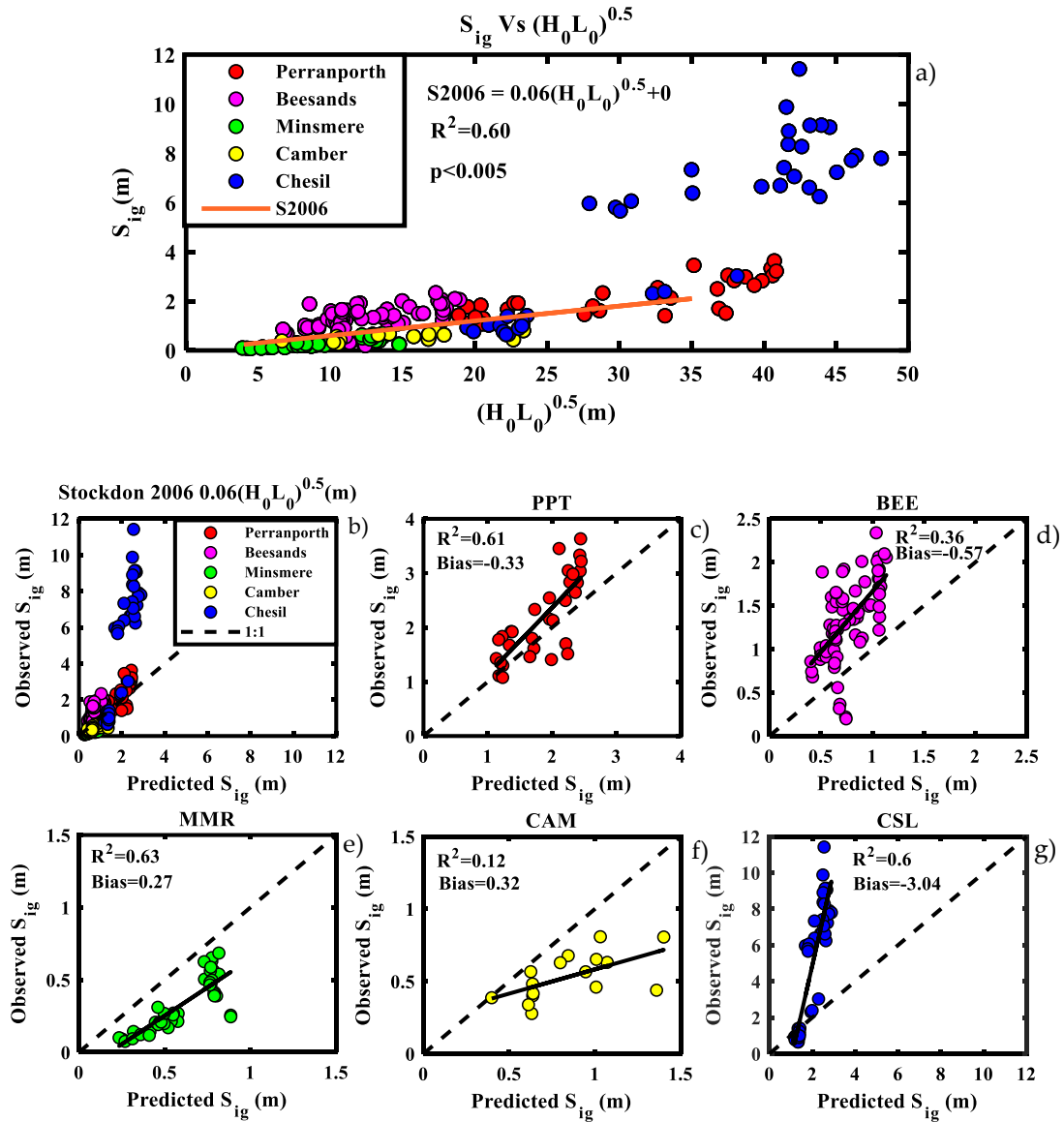
Figure 5-4 (a) Significant infragravity swash height S_{ig} against $(H_0L_0)^{0.5}$ after Stockdon et al. (2006). Linear best fit for Stockdon 2006 data (solid orange line), limited to the original range of $(H_0L_0)^{0.5}$. (b): Comparison of S_{ig} heights observed and those predicted by S2006 at all sites. (c–g): as above but for individual sites.

5.3.6 <u>Predicting significant infragravity swash height (S_{ig}) on gravel beaches</u>

While no gravel-specific predictors of S_{ig} exist, Poate et al. (2016) (P2016) developed a predictor of runup elevation using a range of data from four gravel beaches and synthetic data from the gravel-specific numerical model, X-beach-G, finding that inclusion of a beach slope term yielded the most accurate predictor: $R2\% = C \tan \beta^{0.5} H_0 T_p$ where C is a constant. Given that P2016 was designed to predict runup, as opposed to S_{ig}, the constant suggested by Poate et al. (2016) (C = 0.33) is not applicable to the prediction of S_{ig}. Instead, using the terms in P2016, a value of C was derived here by applying a linear best fit to the combined set of data from the gravel sites (Beesands and Chesil) (Figure 5-5a), yielding a gravel-specific predictor of S_{ig}, Eq. (5-3):

$$S_{ig} = 0.15 \tan \beta^{0.5} H_0 T_p + 0.43 \qquad \text{Eq. (5-3)}$$

Given that in S2006 wave height is square rooted, a greater emphasis is placed on H_0 in Eq. (5-3). This increased emphasis on H_0, combined with the introduction of a $\tan \beta$, implies that wave height and beach slope play a more critical role in the control of S_{ig} on gravel beaches than sandy ones.

On the compound/mixed sites, S_{ig} was reasonably well-predicted at Minsmere, although Figure 5-5e reveals a small but systematic over-prediction of S_{ig}, yielding a bias of 0.34 m while Camber showed no significant relationship between S_{ig} and Eq. (5-3). Of the significantly related sites (all except Camber) S_{ig} was least well-predicted by Eq. (5-3) at Perranporth (Figure 5-5 a–c), with a large negative bias (−0.73) representing an under-

prediction of S_{ig}. The enhanced infragravity levels at Perranporth may result from the efficient transfer of energy to lower frequencies across the wide, dissipative surf zone.
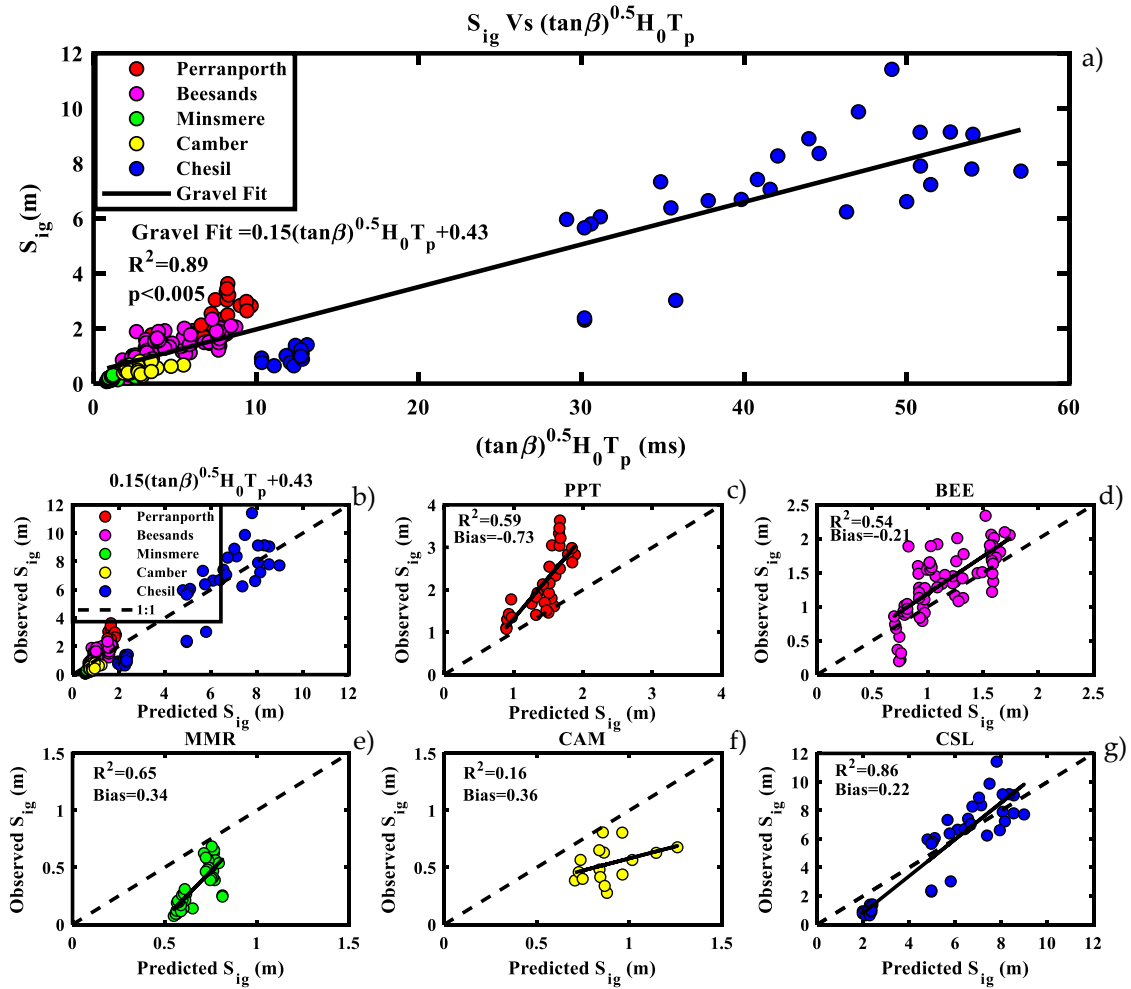
Figure 5-5 (a): Significant infragravity swash height Sig against tan $β_{0.5}H_0T_p$. Linear best fit for Beesands and Chesil (Eq. (5-3)), black line. (b): Comparison of Sig heights observed and those predicted by Eq. (5-3) at all sites. (c–g): As above but for individual sites. Eq. (5-3) has a y-axis intercept (c) of 0.43 resulting from the linear fit being extended beyond the lowest observed values of 0.15tan $β^{0.5}H0T_p$. Given the positive intercept, Eq. (5-3) should not be extended beyond the range of observed values of tan $β^{0.5}H_0T_p$ and is therefore only applicable for values above 0.8 ms.

5.3.7 Relationship between significant infragravity swash height (S_{ig}) and deep water wave power (H_0^2T)

S2006 and Eq. (5-3) have been shown to predict S_{ig} at a specific type of beach over a specific range of conditions. In order to examine whether S_{ig} could be predicted with any skill during the extreme waves at contrasting sites, the relationship with deep water wave power was tested. Wave power has frequently been used in the parameterisation of storm hydrodynamics (Scott et al., 2011; Burvingt et al., 2017; Wiggins et al., 2019). Removing the constants from the deep water waver power equation yields $P \alpha H_0^2T$, a useful parameterisation previously applied to infragravity waves on a dissipative sandy beach by Inch et al. (2017). S_{ig} was regressed against H_0^2T for the combined data set of all five sites (Figure 5-6a), deriving a linear equation for predicting S_{ig}:

$$S_{ig} = 0.02H_0^2T + 0.42 \hspace{4cm} \text{Eq. (5-4)}$$

Eq. (5-4) predicted S_{ig} at Beesands, Perranporth and Chesil with small biases of -0.23, 0.30 and 0.38 m respectively (Figure 5-6 d,c,g respectively), suggesting that infragravity swash height is proportional to deep water wave power in extreme wave conditions at these three contrasting sites, all of which are susceptible to infragravity dominance at the shoreline (Figure 5-3). Eq. 5-4 was a less suitable predictor of S_{ig} at the mixed sand and gravel sites, yielding larger biases at Minsmere (0.49 m) (Figure 5-6 e) and showing no significant relationship with S_{ig} at Camber ($p = 0.248$) (Figure 5-6 f).
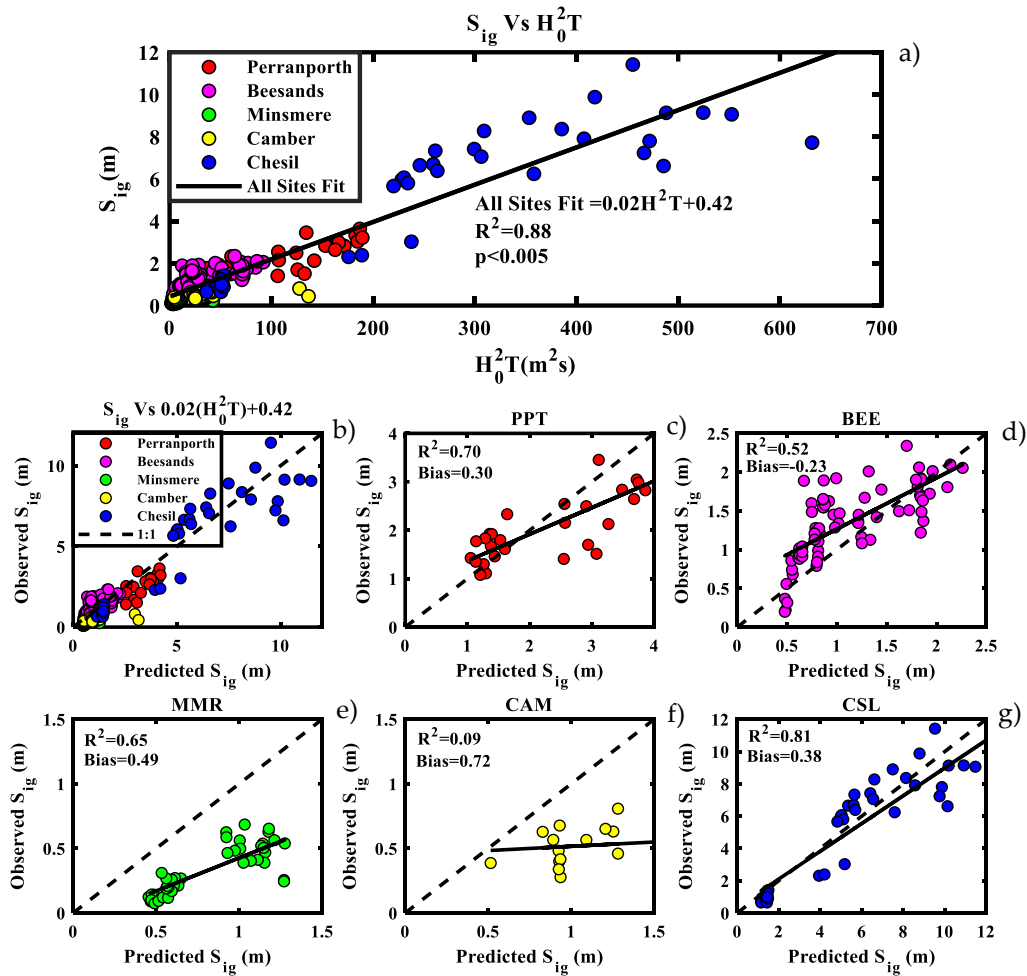
Figure 5-6 (a): Significant infragravity swash height S_{ig} against ($H_0{}^2T$). Linear best fit for all sites (Eq. 5-4), black line. (b): Comparison of S_{ig} heights observed and those predicted by Eq. (5-4) at all sites. (c–g): As above but for individual sites. Eq. (5-4) only valid for high energy conditions.

5.3.8 Comparison of parameterisations

Chapter 5.3 thus far has demonstrated that the relationship between wave and beach statistics and S_{ig} varies between sites. The predictive skill of S2006, Eq. (5-3) and (5-4) at the five contrasting sites is compared in Table 5-3.

S_{ig} at Perranporth was accurately predicted by both S2006 and Eq. (5-4), with marginally higher R^2 for the latter. At Beesands both Eq. (5-3) and (5-4) were strong predictors of S_{ig}. The low levels of S_{ig} observed at Minsmere were well predicted by all three equations, with S2006 yielding the lowest biases. S_{ig} at Camber was generally low and showed no relationship with any of the 3 equations. At Chesil, S_{ig} was well predicted by Eq. (5-3) and (5-4).

Given that Eq. (5-3) was derived from data collected at Beesands and Chesil, a more skilful predictor is Eq. (5-4). Of the sites susceptible to IG dominance (Perranporth, Beesands and Chesil), S_{ig} can be accurately predicted by Eq. (5-4), under high energy conditions, demonstrating that large offshore wave powers associated with big swell waves are the main driver of large infragravity energy in the swash across these widely varying beach types.

Table 5-3 Comparison of relationships between observed S_{ig} and S_{ig} predicted by S2006, Eq. (5-3) and (5-4).

Equation	Site	R^2	Bias	p-Value
S2006 $S_{ig} = 0.06 \, (H_0 L_0)^{0.5}$				
	Perranporth	0.61	−0.33	<0.005
	Beesands	0.36	−0.57	<0.005
	Minsmere	0.63	0.27	<0.005
	Camber	0.12	0.32	0.014
	Chesil	0.60	−3.0	<0.005
Equation (5-3) $S_{ig} = 0.15(\tan \beta)^{1/2} H_0 T_p + 0.43$				
	Perranporth	0.59	−0.73	<0.005
	Beesands	0.54	−0.21	<0.005
	Minsmere	0.65	0.34	<0.005
	Camber	0.16	0.36	0.123
	Chesil	0.86	0.22	<0.005
Equation (5-4) $S_{ig} = 0.02 \, H_0^2 T + 0.42$				
	Perranporth	0.70	0.3	<0.005
	Beesands	0.52	−0.23	<0.005
	Minsmere	0.65	0.49	<0.005
	Camber	0.09	0.72	0.248
	Chesil	0.81	0.38	<0.005

5.4   **Discussion**

5.4.1   **Parametrising infragravity swash across contrasting morphologies**

The importance of collecting data over the wide range of morpho- and hydrodynamic conditions presented here was demonstrated when comparing the performance of previously published empirical predictors of significant infragravity swash height (S_{ig}). A previously published empirical predictor of S_{ig} derived using data collected exclusively on sandy beaches (Stockdon et al., 2006) performed well on the sandy beach and the mixed sand and gravel beach, over a comparable range of conditions over which it was developed. The Stockdon equation was shown to under-predict S_{ig} for higher energy conditions and for data collected on gravel beaches. This reaffirms our previous suggestion that infragravity motions resulting from storm waves are enhanced on gravel beaches compared to sandy ones and should therefore be considered a key contributor to storm impacts at such sites.

A new predictor of S_{ig} specific to gravel beaches was proposed, adapting a gravel beach runup equation published by Poate et al. (2016). As was seen with the Stockdon equation, the new gravel equation performed well on the beaches for which it was designed but poorly on non-gravel beaches.

To the author's knowledge, prior to this research a universal predictor of S_{ig} applicable on both sand and gravel beaches did not exist. The accuracy of various combinations of beach

slope, sediment grain size, wave height and period as predictors of S_{ig} were evaluated using the new dataset.

Of the combinations tested, H_0^2T, proportional to offshore wave power predicted S_{ig} accurately on both the pure sand and gravel beaches, but poorly on the mixed sediment/ compound beaches. As demonstrated above, infragravity could become dominant over incident frequency motions at the shoreline on the pure sand and gravel but not the mixed/ compound beaches. This implied that under extreme wave conditions, wave height and period became more important than local morphology as a control on infragravity motions in the swash on pure morphology beaches. Conversely, at the mixed/ compound sites where IG rarely dominated, infragravity swash height remained small at the shoreline regardless of offshore conditions.

5.4.2 Conceptual diagram – When and where are infragravity waves important at the shoreline?

Table 5-4 and Figure 5-7 summarise the contrasting behaviour of wave energy from offshore to the shoreline, under extreme conditions, on three distinct morphologies: sand, gravel and compound/mixed. Taking the data runs presented in Figure 5-1 as examples of high energy/ extreme conditions, from right to left the diagram displays the following for each of the five study sites: incoming wave power (H_0^2T) and representative conditions; representative profile; significant infragravity swash height (S_{ig}); resultant infragravity to

gravity ratio at the shoreline (S_{ig}/S_g); and a relative size and dominance of IG response

attributed to each of the three distinct morphologies.

Table 5-4 Representative infragravity heights and dominance at the shoreline and coincident parameterized wave power (H_0^2T) during the times of high incident wave energy presented in Figure 5-1.

	Shoreline:		Offshore:	
Site	S_{ig} (m)	S_{ig}/S_g	H_0^2T (m^{2}s)	T_p
MMR	0.7	1.1	40	6.7
CAM	0.8	0.97	125	8.9
BEE	1.9	1.8	70	9.0
CSL	6.6	1.3	240	17.5
PPT	2.5	4.4	125	19.0

The five sites can be separated into being typically swell dominated (PPT) and wind-wave

dominated (MMR and CAM). The two gravel sites, CSL and BEE have the potential to be

impacted by both swell and wind-waves and can be thought of as 'bi-modal'. During

storms CSL is more prone to large swell waves while at BEE, storm waves are typically

shorter period wind waves. As such, the sites are ordered from top to bottom by increasing

period of incoming conditions in Figure 5-7.

Despite only experiencing the second largest incoming wave power ($H_0^2T = 125$ m^{2}s) in the

example presented in Figure 5-7, the sandy site (Perranporth) produced the second largest

S_{ig} (2.5 m) and the largest ratio of S_{ig}/S_g (4.4). Interestingly, even though the offshore

forcing observed at BEE ($H_0^2T = 70$ m^{2}s) was almost half that of PPT, responses at the

shoreline were more closely matched, with S_{ig} at BEE equal to 1.9 m, only 30% smaller

than PPT. The largest H_0^2T (240 m^{2}s) and S_{ig} (6.4 m) were observed at Chesil but only the

third highest S_{ig}/S_g (1.3). This demonstrated that a lack of short-wave dissipation on the

steep gravel morphology, compared to the sandy example, limited infragravity dominance

at the shoreline. Of the two gravel sites, the relatively steeper waves and lower beach slope

at Beesands compared to Chesil resulted in more efficient short-wave dissipation, and an

increased ratio of S_{ig}/S_g (1.8).

Despite being subjected to equal incoming H_0^2T (125 m^{2}s) to Perranporth, S_{ig} (0.8 m) and

S_{ig}/S_g (0.97) at Camber were far lower. Even though offshore forcing at Minsmere was less

than a third of that seen at CAM ($H_0^2T = 40$ m^{2}s) a comparable infragravity response was

observed at the shoreline ($S_{ig} = 0.7$ m and $S_{ig}/S_g = 1.1$).

Size of IG Response / IG Response · **S_{ig}/S_g** · **S_{ig} (m)** · **Beach Type** · **Site** · **Incoming conditions** · **H_0^2T (m²s)**

Size of IG Response / IG Response	S_{ig}/S_g	S_{ig} (m)	Beach Type	Site	Incoming conditions	H_0^2T (m²s)
Small	1.1	0.7	Mixed/Compound	Minsmere	Wind Sea Dominated	40
Rarely I.G. Dominated	0.97	0.8		Camber		125
Occasionally large	1.8	1.9	Gravel Reflective	Beesands	Bi-Modal	70
Occasionally I.G. Dominated	1.3	6.6		Chesil		240
Large / **Commonly I.G. Dominated**	4.4	2.5	Sandy Dissipative	Perranporth	Swell Dominated	125

Figure 5-7 Conceptual diagram summarizing the contrasting development of infragravity energy at the shoreline on 3 distinct morphologies: Sand, gravel and mixed/compound. The numerical values used in the diagram are taken from Figure 5-1 and are representative of high energy conditions at each site.

Differences in the amount of IG energy observed at the shoreline across the five sites may result either from contrasting amounts of energy being supplied to the IG band during generation or contrasting levels of dissipation en route to the shoreline. Once generated or released, IG waves on beaches can lose energy through breaking (e.g. van Dongeren et al., 2007; de Bakker et al., 2014, 2015) or the transferring of energy to higher and lower frequencies (e.g. Henderson et al., 2006; Inch et al., 2017). Bed friction had also been implicated in IG energy loss (e.g. Henderson and Bowen, 2002), but this has been shown to be negligible on sand and therefore of secondary importance on beaches (e.g. van Dongeren et al., 2007; de Bakker et al., 2014).

Such energy losses may explain the relatively low value of S_{ig} observed at CAM, compared to the relatively high H_0^2T. During storm '*Angus'*, waves at CAM were large and short period ($H_s > 3.7$ m and a $T_p < 8s$). Baldock (2012) suggested that during storms, when incident waves are particularly steep, like at CAM, short wave breaking can occur in intermediate water depths, before the shallow water dispersion relationship is satisfied, meaning that the long wave's energy begins to dissipate before it's released. It is therefore possible at CAM that bound long waves were not released at the short-wave break point, meaning IG energy decayed significantly before reaching the shoreline. In order to assess whether this was the case, measurements of free surface elevation through the surf zone and seaward of the short-wave break point would be required.

Another reason for the observed differences in IG energy at the shoreline of the five sites was that there was less energy supplied in total (e.g., low values of H_0^2T at MMR), or less transferred into the IG band during short wave dissipation. The importance of incoming wave period (and therefore length) has been reported in multiple field studies on sandy sites (e.g. Elgar et al., 1992; Ruessink, 1998; Stockdon et al., 2006; Senechal et al., 2011b; Contardo and Symonds, 2013; Inch et al., 2017), with longer period waves

typically eliciting a larger infragravity response. This may partially explain why such low levels of IG energy were detected at the shoreline of the fetch limited CAM and MMR, compared to the other sites. Despite the observed wave height being larger, peak wave period was roughly half the value observed at CAM (H_s = 3.7 m, $T_p \approx 9$ s) compared to PPT (H_s 3.1 m, $T_p \approx 18$ s) (Figure 5-1), suggesting the swell conditions observed at PPT contributed to the increased levels of IG at the shoreline of PPT (S_{ig} = 2.5 m) compared the wind-wave dominated CAM (S_{ig} = 0.97 m).

The observed smaller difference in S_{ig} (30%) compared to that in H_0^2T (56%) between BEE and PPT implies that energy was more efficiently transferred to the IG band on the gravel beach than the sandy one. This may result from the two sites having contrasting IG generating mechanisms. Several authors have shown that steeper bed slopes can lead to increased IG energy originating from break point forcing, while lower slopes are more conducive the bound long wave release generation mechanism (e.g. List, 1992; Battjes, 2004; de Bakker et al., 2015). Furthermore, Baldock and Huntley (2002) suggested that break point forcing becomes more relevant during storms when incident waves are steeper, like was the case at BEE but less likely under swell conditions, like at PPT. Using a physical and numerical model of a coral reef, Masselink et al. (2019) showed that steep slopes (>$\tan \beta$ = 0.1) were dominated by breakpoint-forced long waves, whereas bound long wave release became increasingly important for slopes <$\tan \beta$ = 0.05. They also concluded that the breakpoint-forced long wave mechanism was the more effective generator of IG energy. This would suggest that break point forcing may be the dominant IG generation mechanism on the steep gravel BEE ($\tan \beta \approx 0.1$), while bound long wave release is likely to be more important on the low sloping sandy PPT ($\tan \beta \approx 0.02$). This theory is investigated further in Chapter 6, using in-situ measurements from seaward of the break point, through the surf zone to the shore.

5.5   <u>Summary and conclusions</u>

Significant swash height in the gravity (S_g) and infragravity band (S_{ig}) was obtained from video runup data, under an unprecedented range of wave and beach conditions. Observations included extreme waves, in excess of the 95th percentile at five contrasting sites ranging from both wind-wave and swell-dominated gravel beaches, through fetch-limited mixed sand and gravel, to a swell-dominated, low-sloping sandy beach.

- Infragravity waves were observed in the swash at all sites, becoming important when H_0 exceeded approximately 1.3 m. For a given wave height, infragravity waves in the swash were enhanced on gravel and sandy beaches but suppressed on mixed/compound beaches.

- Infragravity waves were observed to become most dominant in the swash on the low sloping sandy beach, where S_{ig}/S_g exceeded 4. They occasionally dominated the gravel beaches but to a lesser extent (<1.8) and rarely or never dominated the mixed/compound sites (<1.1). This was attributed to differences in short wave dissipation patterns resulting from contrasting morphology and wave steepness.

- A previously published empirical relationship $S_{ig} = 0.06 \, (H_0L_0)^{0.5}$ (Stockdon et al., 2006), developed on sandy beaches, predicted S_{ig} well on the sandy beach and the mixed sand and gravel beach, over a comparable range of conditions over which it was developed. The Stockdon equation was shown to under-predict S_{ig} for higher energy conditions and for data collected on gravel beaches, suggesting S_{ig} was enhanced under these conditions.

- A new gravel-specific predictor of S_{ig} was proposed, by linearly fitting observations of S_{ig} from two separate field deployments to terms from Poate's

gravel runup equation, $(\tan \beta)^{1/2} H_0 T_p$. This was seen to underestimate values of S_{ig} on the sandy beach.

- $H_0^2 T$, proportional to offshore wave power, was a good predictor of S_{ig} at the sites where IG could become dominant, yielding the equation: $S_{ig} = 0.02(H_0^2 T) + 0.42$, valid for high energy conditions.

- The relationship between S_{ig} and $H_0^2 T$, across a diverse range of sites, implied that under extreme wave conditions, wave height and period became more important than local morphology as a control on infragravity in the swash. Conversely, at sites where IG rarely dominated, infragravity swash height remained small at the shoreline regardless of offshore conditions. This highlights the importance of collecting data over the unique range of heights and periods present here.

- A conceptual model was presented summarising the contrasting development of infragravity energy at the shoreline on three distinct morphologies: sand, gravel and compound/mixed. Variability in IG energy observed at the shoreline of the five sites were attributed to likely differences in the levels of incoming IG (controlled by wave height and period and bed slope) and dissipation en route to the shoreline. Infragravity energy became more dominant in the swash on sand rather than gravel sites. This resulted in the swash being commonly IG dominated on low sloping sandy beaches, occasionally IG dominated on gravel beaches and rarely IG dominated on compound/mixed beaches.

Of the morphologies which became IG dominated, sand and gravel, levels of IG energy growth from offshore to the shoreline varied, implying contrasting processes within the surf zone of the two beach types. This is investigated further using in-situ observation in Chapter 6 which follows.

6 In-situ observations of infragravity response during extreme storms on sand and gravel beaches

This Chapter contains work published in the following paper:

6.1 Introduction

It is well established that infragravity (herein IG) waves, typically of frequencies between 0.005 – 0.05 Hz, play a crucial role in nearshore hydro- and morphodynamics of sandy beaches (Bertin et al., 2018). In particular, their importance has been shown to increase during storms (Billson et al., 2019a) where they have been implicated in the inundation (e.g. Roelvink et al., 2009) and extreme erosion (e.g. Russell, 1993; de Bakker et al., 2016) of beaches and dunes. Despite this, current understanding of IG waves is based on observations collected almost exclusively on low sloping sandy beaches. Further, due to experimental limitations, the majority of field deployments to date were carried out during moderate or low energy wave conditions. Even over this limited parameter space, how IG wave development and transformation relate to variations in offshore significant wave height (H_0) (Guza and Thornton, 1982), peak period (T_p) (Contardo and Symonds, 2013; Inch et al., 2017), beach slope (Stockdon et

al., 2006) and morphodynamic beach state (Gomes da Silva et al., 2018) varies between sites.

One potential explanation for observed differences lies in how the IG waves were generated. Two mechanisms, bound long wave release (Longuet-Higgins and Stewart, 1962) and breakpoint forcing (Symonds et al., 1982) (introduced in Chapter 1.3.2.2) are known to be the main generators of IG waves, either acting alone or in combination. Modelling studies have shown that the relative contribution of each mechanism varies with bed slope (e.g. Battjes, 2004; Masselink et al., 2019) and short wave steepness (e.g. Baldock, 2012). The theory underpinning infragravity wave generation via bound long wave release (BLW) and breakpoint forcing (BPF) is explained in further detail in the following three paragraphs.

Bound long wave theory can be explained by considering an idealised bichromatic wave field, i.e. two waves trains of equal amplitude but differing wavelength travelling at differing speeds. As the two trains propagate they begin to interact constructively (when in phase) and destructively (when out of phase). As a result, the water surface elevation takes on the form of groups of larger amplitude waves separated by smaller ones (Figure 6-1a). The frequency of the wave group is typically one order of magnitude lower than that of the short waves of which it is comprised. The momentum of the short waves exert a force on the water column below which can be thought of as a momentum flux (termed radiation stress by Longuet-Higgins and Stewart (1962)). Larger waves result in a larger momentum flux than the smaller ones meaning that mean water level is supressed more under the wave groups than between them. This results in a second order wave, equal in length, bound to and 180º out of phase with the short wave group, known as a bound long wave or bound infragravity wave (Figure 6-1b).
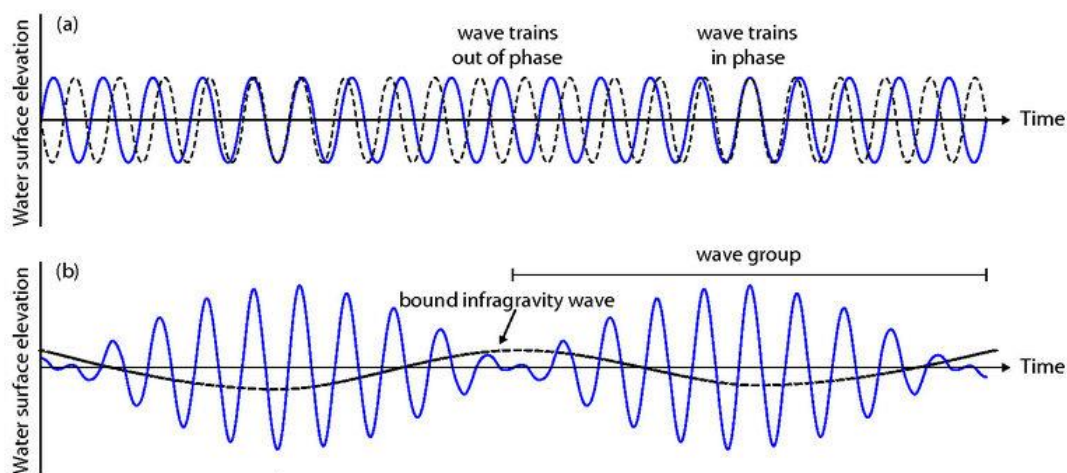
Figure 6-1a. The merging of waves of slightly different wavelengths, but the same amplitude. Figure 6-1b. The two wave trains form wave groups and induce a long bound wave. Modified from Open University – Waves, Tides and Shallow water processes, 1st edition, 1994.

As the bound wave approaches the coast, interaction with the bed causes the short waves to shoal, break and dissipate their energy leading to a progressive decay in the short wave grouped structure. The breakdown of the wave group motivates the progressive release of the bound long wave which, owing to its large wavelength, shoals on its approach to the shoreline but is less inclined to break than its short wave counter part and is typically fully or partially reflected at the shoreline. For a more detailed discussion around bound long wave release, infragravity shoaling, reflection and dissipation the reader is referred to Chapter 1.3.2.2.

As well as generating bound long waves, wave groups also drive break point forced infragravity wave generation. The larger waves, at the peak of the group break further offshore than the smaller waves between the groups. As a result, the break point oscillates landward and seaward with passing wave groups. This time varying break point leads to a time varying momentum flux gradient which is balanced by variation in the steady state wave set up (Figure 6-2). The balance produces two infragravity waves, one progressing shoreward and the other seaward from the breakpoint. The landward directed infragravity wave can be reflected at the shoreline and interact destructively or constructively with the next shoreward progressive wave potential leading to (quasi)

standing infragravity waves in the surf zone. Further, the reflected wave can interact

with seaward directed BPF wave, again either constructively or destructively.

Therefore, the relative contribution of, and interaction between, reflected and BPF

infragravity waves should be considered when examining infragravity wave dynamics

in the nearshore.
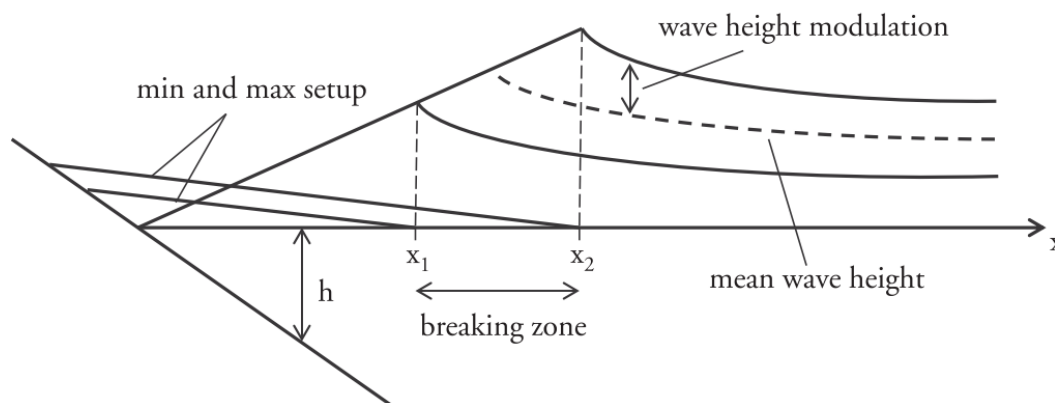
Figure 6-2 Schematic representation of the cross-shore variation of the minimum, mean and maximum short wave height, with the associated steady state set-up through the surf zone. x1 and x2 are the minimum and maximum positions of the breakpoint, and h is the water depth. Reproduced from Symonds et al. (1982) by Bertin et al. (2018).

Given the contrasting wave climates, beach slope and wave breaking processes

associated with gravel beaches compared to sand (Masselink et al., 2008), IG wave

dynamics also differ on gravel beaches. Therefore, merely applying existing empirical

understanding may not be accurate, as has been shown for extreme runup (Poate et al.,

2016), sediment transport rates (McCarroll et al., 2019) and most recently, infragravity

swash oscillations (Billson et al., 2019b), who collected video observations of swash

under high energy wave conditions on a single gravel beach. Comparing this data to that

previously published on sandy sites, they demonstrated that infragravity motions can

dominate the swash under high energy wave conditions, even on steep gravel beaches.

An early study of IG waves was carried out on gravel beaches by Huntley (1976). Since

then only a handful of studies have deployed *in-situ* arrays of sensors on gravel beaches

to investigate IG development, the majority of which were under low wave conditions ($H_s < 0.5$ m) (e.g. Austin, 2005). Under such low energy conditions, Austin (2005) found that cross-shore hydrodynamics were dominated by incident frequency oscillations, attributing a lack of infragravity energy to the narrow breaker region remaining unsaturated to incident energy. This was in contrast to the findings of Billson et al. (2019b) who observed dominance of IG energy over gravity energy in the swash zone of a gravel beach.

Here, a unique new dataset is presented comprising observations in energetic wave conditions (significant wave heights of 3.3 m and peak periods of 18 s) from two contrasting sites: a low-sloping sandy beach and a steep gravel beach. Wave measurements were collected seaward of the breakpoint by wave buoys, acoustic Doppler current profilers (ADCP) and pressure transducers (PT) and through the surf zone using arrays of PTs with the aim of investigating how infragravity wave response in the surf zone varies between sand and gravel beaches.

The research methods are outlined in Chapter 6.2, followed by a description of the study sites and the data collection and processing. In Chapter 6.3, the hydrodynamic conditions during the deployment are described first, followed by a comparison of the offshore wave spectra at the two sites. Next, the contrasting development of wave spectra through the surf zone is presented, and comparisons are drawn between the offshore and surf zone spectra at the respective sites. The reasons for the differences between the sites are discussed in Chapter 6.4, including consideration of the different IG wave generating mechanisms. The main conclusion are drawn in Chapter 6.5.

6.2 Method

6.2.1 Experimental set-up

The two study sites, located in the south west of the UK, were selected as typical examples of a sandy, dissipative beach (Perranporth) and gravelly, reflective beach (Beesands). Perranporth (PPT) is a high energy site with relatively low beach face slope ($\tan\beta \approx 0.02$), exposed to oceanic swell and locally generated wind waves (Figure 6-3a + b). Beesands (BEE) is typically a low energy site with a relatively high beach face slope ($\tan\beta \approx 0.1$), dominated by wind waves and occasional refracted oceanic swell (Figure 6-3c + d).
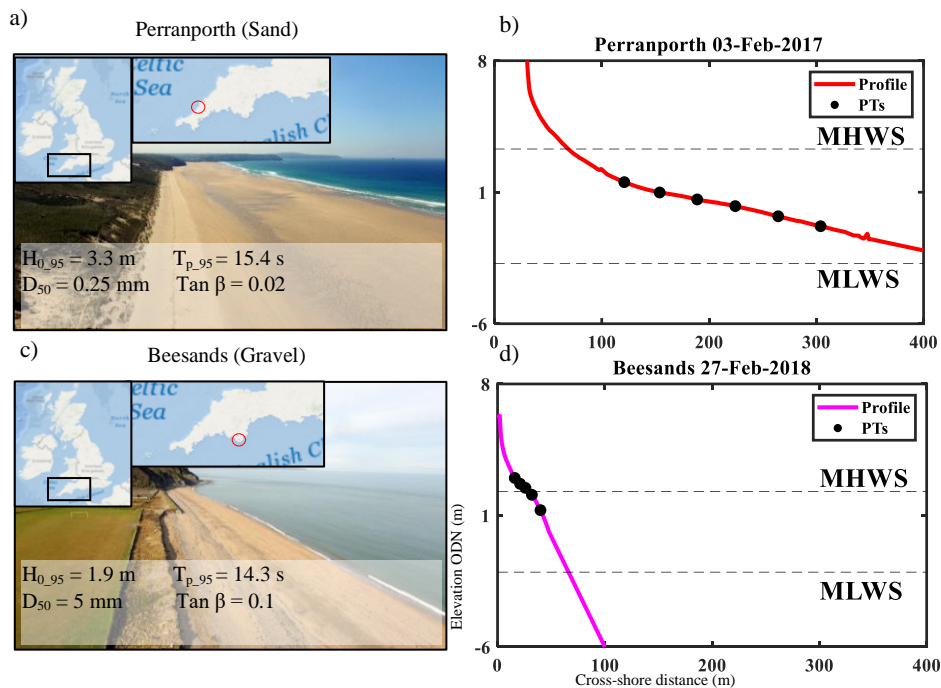
Figure 6-3 Comparison of two field sites (Perranporth a + b) (Beesands, c + d). a and c: photographs of respective sites (Peter Ganderton) with 95 % threshold deep water significant wave height (H_{0_95}) and period (T_{p_95}), sediment grain size (D_{50}) and mean beach slope (Tan β). b and d: Indicative beach profile and location of pressure transducers (black filled circles), measured during the deployments.

A statistic frequently used to define and quantify storm events (Harley, 2017), the 95% threshold values of offshore wave height (H_{0_95}) and period (T_{p_95}) were calculated using the full 12-year data record at each local wave buoy (Figure 6-3).

Field campaigns were targeted around storm events using Plymouth University's Rapid Coastal Response Unit (RCRU). The RCRU is a versatile unit facilitating the collection of hydrodynamic and topographic data during extreme storms. Housing an array of instrumentation, the RCRU is highly mobile and can be deployed with just hours' notice, to capture conditions preceding, during and following a storm (Billson et al., 2019a).

Estimates of offshore significant wave height (H_0) were obtained by linearly de-shoaling H_s, measured at local wave buoys, to a depth of 80 m. Approximate water depths of the PPT and BEE wave buoy are 15 and 10 m respectively, relative to the chart datum (CD). The range and mean of H_0 and T_p for the two deployments are presented in Table 6-1.

Table 6-1 Site and storm name, return period and range and mean of wave height and period sampled during the presented study. N = number of ~17-minute data runs. Maximum values in bold.

Site Storm Name Return Period	Date	H_0 (m)	T_p (s)	N
Perranporth (PPT) *Unnamed Storm* 1 in 1 year	31 Jan – 07 Feb 2017	1.6-**3.3** 2.4	11.1-**18.2** 15.7	50
Beesands (BEE) *Storm 'Emma'* 1 in 60 years	20 – 27 Feb 2018	0.4-**3.3** 2.0	5.1-**15.0** 7.4	19

In addition to the offshore wave statistics measured by wave buoys, presented in Figure 6-3 and Table 6-1, measurements of incoming energy in the infragravity band were required. The wave rider buoys used here were only able to detect wave motions at frequencies above 0.033 Hz, rendering them inadequate for accurate detection of IG waves.

To overcome this issue bed-mounted acoustic Doppler current profilers (ADCP) were deployed at each site. At PPT, a Nortek Signature 1000 AD2CP was deployed in an average water depth of 23 m and at BEE an RDI 600kHz ADCP in 15 m depth.

~17-minute time series of free surface track were obtained using the respective wave sampling modes of the ADCPs. Wave height spectra were then estimated from these data. To minimise the effect of tidal signal, data runs were collected as close to the high water (HW) standstill as possible.

6.2.2 <u>Deploying arrays of pressure sensors</u>

To examine how wave energy spectra developed through the surf zone, a cross-shore array of RBR Solo Pressure Transducers was deployed, spanning as much of the intertidal zone as was accessible. These were re-adjusted every second low tide to bed-level. At PPT seven PTs spanned ~250 m cross-shore distance, and at BEE, 6 PTs spanned 40 m (Figure 6-3 b and d respectively). Continuously logging at a rate of 8 Hz, coincident data runs with those isolated from the ADCP record were extracted, linearly de-trended and converted from pressure to depth using linear wave theory.

At PPT, the PTs were fixed in position using metal land anchors or sand screws. Given how rapidly the profile of gravel beaches is known to adjust during storm conditions, a sufficiently resilient technique for securing the PTs was required at BEE. An 'arrowhead' design was implemented with the thought that three points of contact with

the beach profile would brace the frame from movement. 2 m long vertical scaffold poles were driven into the gravel to try and overcome potential rapid and large adjustments to the profile. Figure 6-4 shows how the PT array was successfully deployed at BEE (upper) and the how the rigs failed when H_0 exceeded 3 m (lower). The success of the method used to deploy an intertidal array of PTs at BEE is discussed further in Chapter 7.2.1.

Figure 6-4 Deploying pressure sensor arrays on a gravel beach: Top left: Close up of pressure transducer, in housing, fixed to an arrow head scaffold frame; Top right: Pressure transducer array successfully collecting data through the swash to the inner surf zone during The Beast From The East storm, where offshore wave heights in exceeded of 4 m; Bottom: Damage to pressure transducer array caused by The Beast From the East storm during which offshore wave height exceed 5 m. All photographs taken by the author at Beesands during February/ March 2018.

Figure 6-5 is a schematic diagram showing how the PT array spanned the intertidal zone at BEE. The profile was chosen as it formed part of the national monitoring programme, meaning that it was surveyed at least twice a year prior to and following the storm deployment. The video tower was co-located at the top of the PT profile to enable comparison of the in-situ and remote sensed data.
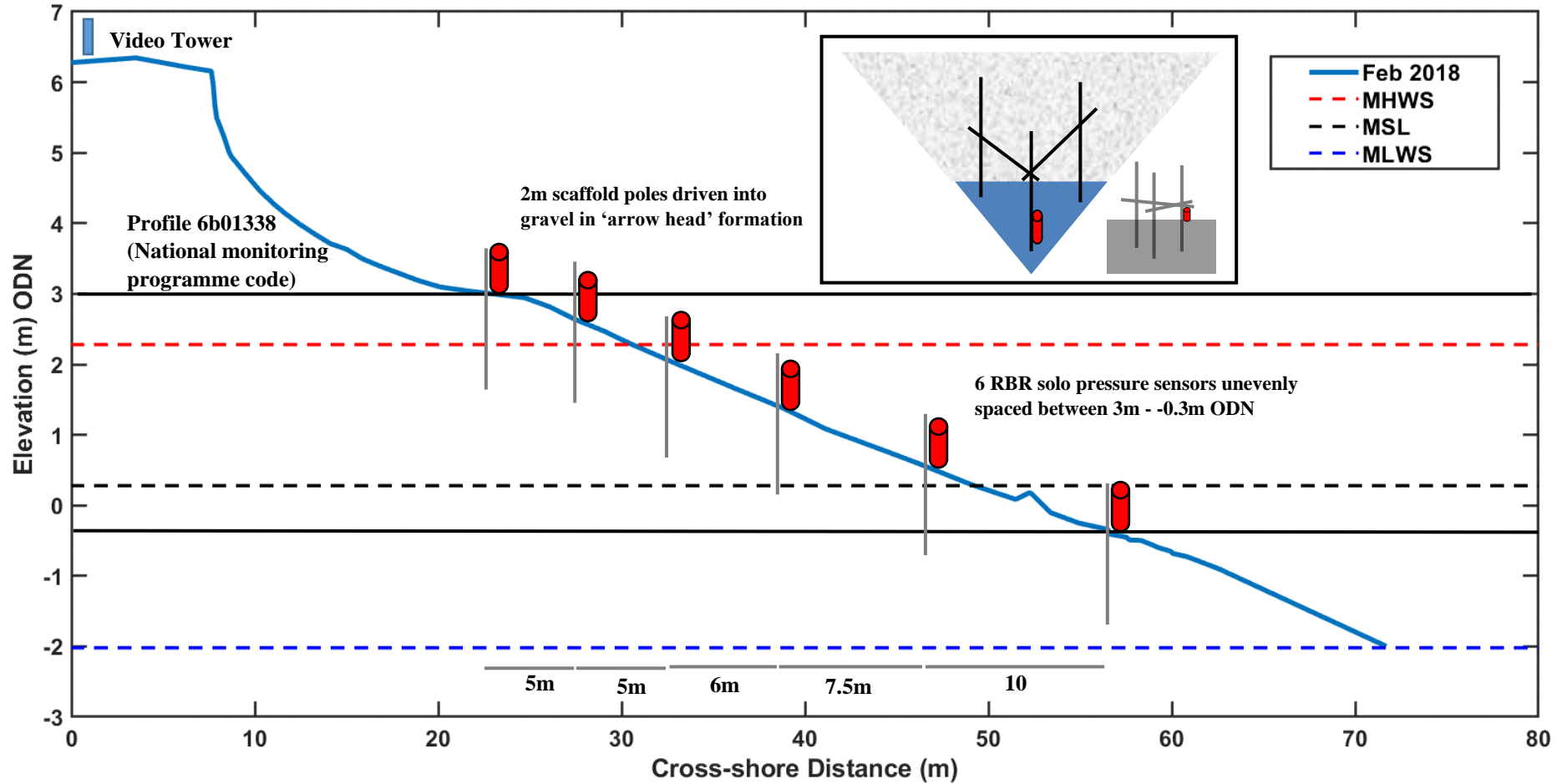
Figure 6-5 Schematic of pressure transducer deployment at Beesands detailing: The cross-shore profile measured on the day of deployment (19/02/2018), the relative cross-shore position and elevation of each of the six sensors, mean high water spring (MHWS) mean sea level (MSL) and mean low water spring (MLWS) elevations relative to ODN. The camera used for video analysis was positioned at the top of this profile.

PT data were given a normalised surf zone position by taking the ratio of local water depth (h) to the breaker depth (h_b), (h/h_b.) where $h_b = H_b/\gamma_b$, and H_b is the breaking wave height, approximated using linear wave theory. γ_b is the breaker coefficient defined after Komar (1997) as:

$$\gamma_b = 1.2\ \xi^{0.27} \qquad\qquad\text{(Eq. 6-1)}$$

where ξ, is the Iribarren number given by:

$$\xi = \tan\beta/(H_0/L_0)^{1/2} \qquad\qquad\text{(Eq. 6-2)}$$

where $\tan\beta$ is the beach gradient, and H_0 and L_0 are the deep water (offshore) significant wave height and wavelength respectively.

Frequency smoothed spectral estimates were computed for each data run at the ADCPs and each PT, each with a frequency bandwidth of 0.0078 Hz and 16 degrees of freedom. A frequency cut-off, separating the gravity from the infragravity band was defined at each site via examination of the ADCP spectra (Figure 6-6). For PPT this was 0.04 Hz and for BEE 0.05 Hz, reflecting the generally shorter period wave climate of BEE compared to PPT. These values also agreed well with previous research from swell (Inch et al., 2017) and wind-wave dominated beaches (de Bakker et al., 2016).

6.3   Results

Wave conditions offshore of the two sites are summarised by spectral estimates calculated at the ADCPs (Figure 6-6).
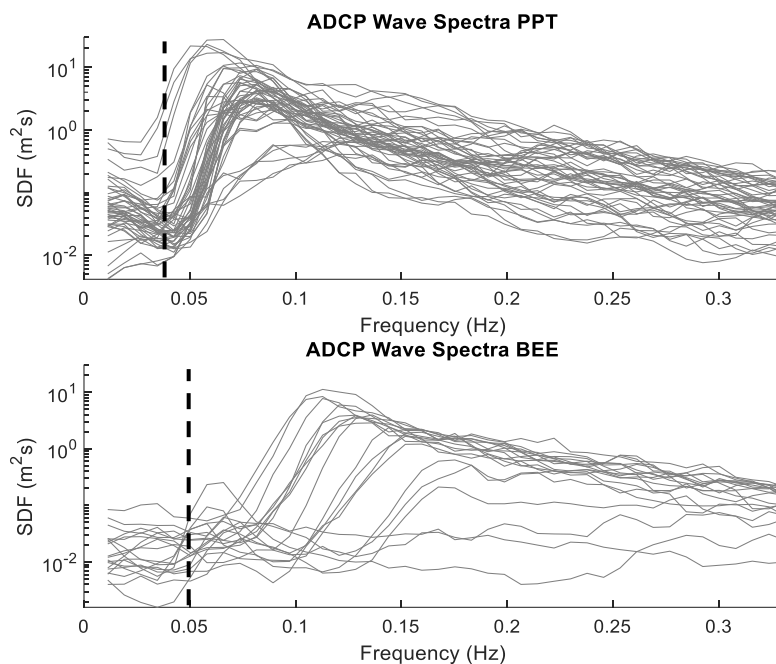
Figure 6-6 Comparison of wave spectra estimated at offshore ADCPs at Perranporth, a) and Beesands, b). Note Y-axis log scale. Vertical dashed lines indicate the IG cut-off, 0.04 Hz for PPT and 0.05 Hz for BEE, reflecting the contrasting short wave climate at the respective sites.

PPT spectra were dominated by energetic swell with occasional lower energy wind waves (Figure 6-6a). Mean primary peak frequency was 0.083 Hz (T_p = 12 s) ranging from 0.05 Hz (T_p = 20 s) to 0.14 Hz (T_p = 7.4 s). BEE spectra were dominated by lower energy wind waves. Mean primary peak frequency was 0.11 Hz (T_p = 9.1 s), ranging from 0.05 Hz (T_p = 20 s) to 0.1675 Hz (T_p = 6.0 s). Energetic conditions were observed at PPT with spectral density (SD) ranging from 0.6 to 27 m^2s, with a mean of 6 m^2s at the primary peak frequency. This compared to the less energetic conditions at BEE, where SD ranged from 0.05 to 11 m^2s

and had a mean of 3.2 m²s at primary peak frequency. Incoming energy in the infragravity

band was apparent at PPT, with secondary peaks ranging from 0.011 Hz ($T_{p\_IG} = 90$ s) to

0.027 Hz ($T_{p\_IG} = 37$ s) and SD on the order of $0.1 - 0.7$ m²s. In contrast, energy was rarely

apparent and in small amounts (<0.1 m²s) in the IG band of the Beesands spectra.

The average of spectra at all cross-shore positions, during all high tides (50 PPT, 19 BEE),

were interpolated to generate ensemble average energy density spectra through a normalized

surf zone at PPT (Figure 6-7a) and BEE (Figure 6-7b). Figure 6-7 shows how energy

transferred between frequencies as it approached the shore.
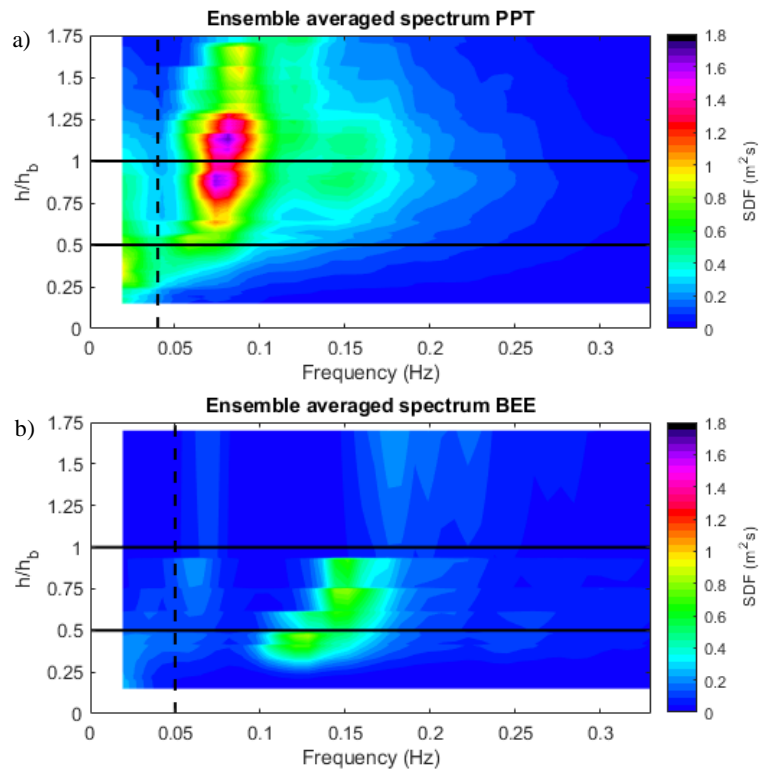
Figure 6-7 Ensemble average energy density spectra from PPT, a) and BEE, b) measured through the surf zone by the PT array. Averaged over 50 ~17-minute data runs at PPT and 19 at BEE. Vertical dashed line indicates threshold separating gravity and IG bands. Horizontal black lines indicate the edge $h/h_b = 1$ and mid surf zone $h/h_b = 0.5$

At PPT, a primary (most energetic) peak spectral density was observed at 0.075 – 0.08 Hz and $h/h_b = 1.25 – 0.8$ associated with short wave shoaling as waves approach the edge of the surf zone (Figure 6-7a).

Landward of this, spectral density decreased as waves broke and dissipated energy, steadily transferring to both higher and lower frequencies. In particular, transfers from short wave to IG frequencies were apparent between $h/h_b = 0.8 – 0.25$, where spectral density in the gravity band reduced from $1.6 – 0.2$ m^{2}s, and IG band spectral density increased from $0.6 – 0.9$ m^{2}s. Initially, secondary to the gravity band peak, the IG band peak became apparent approximately at the edge of the surf zone (SD = 0.5 m^{2}s, h/hb = 0.8), dominating over the gravity band peak around the mid surf zone (h/hb = 0.5) and reaching a maximum (SD = 0.9 m^{2}s) where $h/h_b = 0.3$ and frequency = 0.02 Hz.

In contrast, BEE generally had far lower SD with the most distinct feature an incoming wind-wave peak (SD = 0.6 – 0.9 m^{2}s, frequency = 0.175 – 0.1 Hz) apparent through the outer 75% of the surf zone ($h/h_b = 1 – 0.25$). Small transfers to IG frequencies were apparent through the inner 50% of the surf zone where SD in the IG band increased from 0.17 m^{2}s to 0.27 m^{2}s (frequency = 0.027 Hz).

IG development from offshore to the inner surf zone was examined by calculating variance gain spectra at each pressure transducer, during every high tide. These were calculated by dividing each pressure transducer spectrum by the coincident spectrum at the ADCP, to calculate 'gain'. When gain > 1 an increase in energy relative to the ADCP has been observed, while values < 1, represent a reduction in energy relative to the ADCP.

Figure 6-8 shows an ensemble average of gain spectra for all data runs, interpolated over a normalized surf zone. The log of the gain was used, with warm colours representing positive gain, cold negative and grey, minimal change.
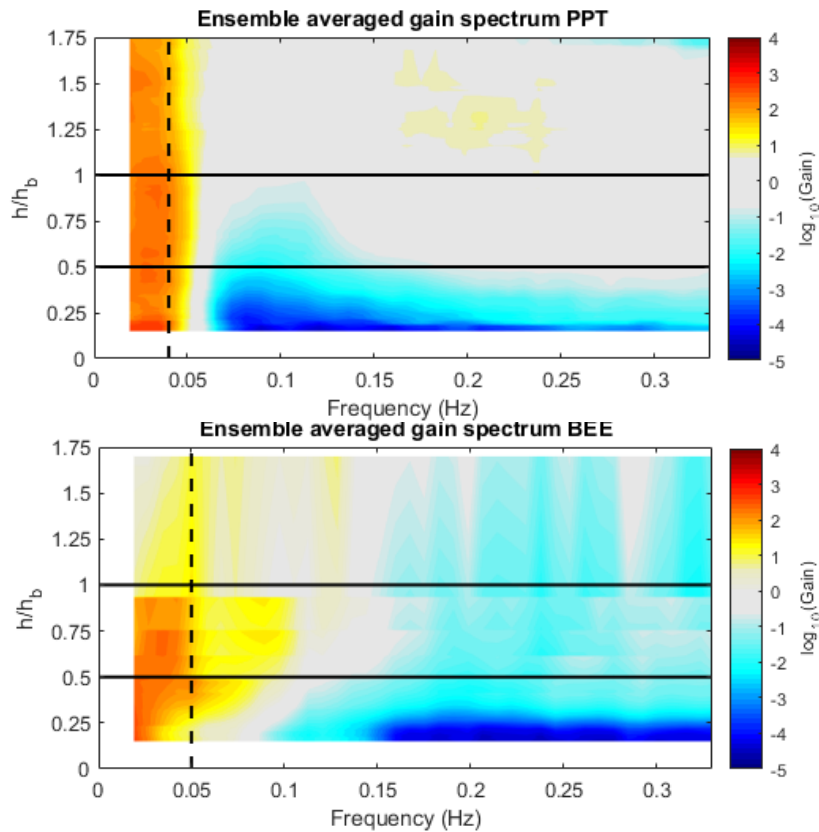
Figure 6-8 Ensemble average variance gain spectra from PPT, a) and BEE, b), measured through the surf zone by the PT array. Averaged over 50 ~17-minute data runs at PPT and 19 at BEE. Vertical dashed line indicates threshold separating gravity and IG bands. Horizontal black lines indicate the edge $h/h_b = 1$ and mid surf zone $h/h_b = 0.5$

At PPT, positive gains in the IG band extended from $h/h_b = 1.75$ to a maximum at $h/h_b = 0.25$ (Figure 6-8a). This implies that seaward of the short-wave breakpoint, predominantly bound IG waves were shoaling, and landward of the short-wave breakpoint energy was being transferred from the gravity band into the IG band.

At BEE, a rapid increase in positive gain occurred around the edge of the surf zone ($h/h_b = 1$), persisting to a maximum around $h/h_b = 0.25$. The majority of energy transferred to IG frequencies did so at, or landward of, the short-wave breakpoint ($h/h_b = 1$). Given that

negligible IG energy was observed seaward of the breakpoint, with rapid growth occurring inside the surf zone, the implication is that IG energy was being generated via breakpoint forcing, rather than bound long wave release at BEE.

6.4   <u>Discussion</u>

The contrasting patterns of energy transfer between the gravity and IG band observed between PPT and BEE (Figure 6-8) may depend on which IG generating mechanism is most prevalent at each site. Introduced in Chapter 1.3.2.2, Baldock (2012) proposed the surf beat similarity parameter to identify conditions favourable to either mechanism, :

$$\xi_{surfbeat} = \beta_{norm}\sqrt{\frac{H_0}{L_0}} \qquad \text{(Eq. 6-3)}$$

where L_0 is the short-wave deep water wavelength, H_0 is the wave height at the breakpoint, and β_{norm} is the normalized bed slope as proposed by Battjes (2004):

$$\beta_{norm} = \frac{h_x}{\omega_{low}}\sqrt{\frac{g}{h_b}} \qquad \text{(Eq. 6-4)}$$

where h_x is the beach slope, h_b the depth at breaking, ω_{low} the longwave frequency, and g acceleration due to gravity. Masselink et al. (2019) identified a range of $\xi_{surfbeat}$ $0.05 - 0.1$ separating the two IG wave regimes.

Calculating values of $\xi_{surfbeat}$ for PPT and BEE (Figure 6-9), alongside the threshold suggested by Masselink et al. (2019) (Figure 6-9, black box) supports the theory that the dominant generating mechanism at PPT is bound longwave release, while at BEE is breakpoint forcing.
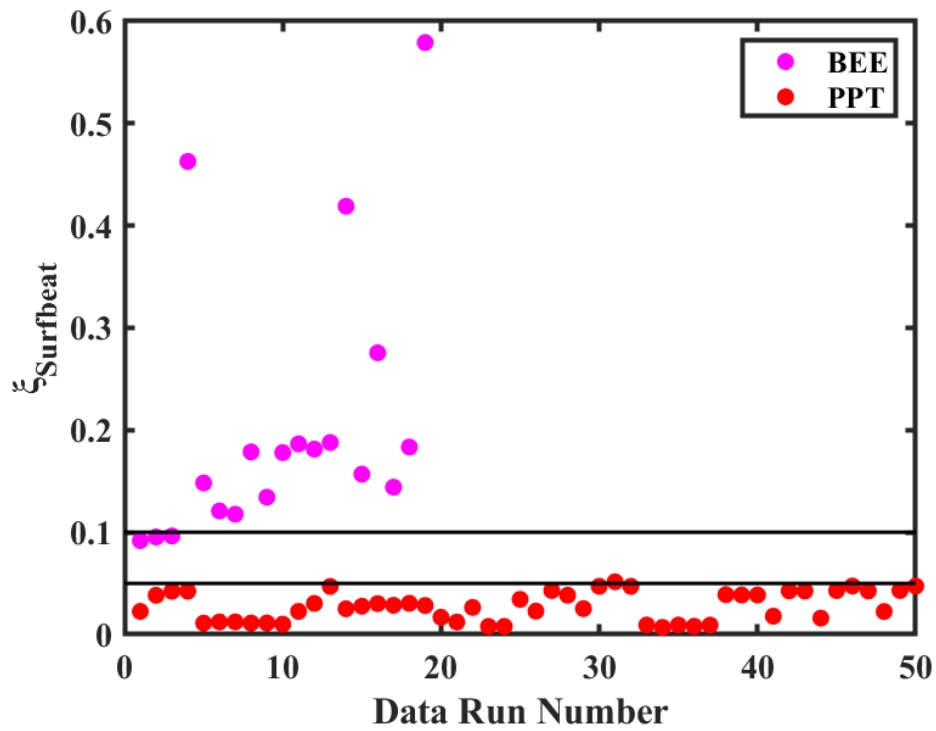
Figure 6-9 Surf beat similarity parameter ($\xi_{Surfbeat}$) per data run for PPT (diamonds) and BEE (squares). Blue lines mark the range over which the transition from bound longwave release (<0.05) to breakpoint forcing (>0.1) occurs.

A tendency toward breakpoint forcing on steeper sites as observed here agrees with observations across a range of environments; sandy beaches (Inch et al., 2017), fringing coral reefs (Pomeroy et al., 2012) and recently, shore platforms (Poate et al., 2020).

6.5 <u>Conclusions</u>

Data were collected during storm wave conditions, exceeding the 95th percentile wave height and period on a sand and gravel beach, facilitating a unique comparison of infragravity response in the surf zone of each site. Comparing wave energy levels and frequency distribution from spectral estimates through the surf zone, with those offshore revealed that energy transferred to the infragravity band seaward of the surf zone at the sandy beach site (PPT) but was limited to landward of the short-wave breakpoint at the gravel beach site (BEE). Values of the surf beat similarity parameter indicated that bound long wave release was the most dominant IG generating mechanism on the low sloping sandy beach (PPT), whilst breakpoint forcing dominated on the steep gravel beach, BEE).

7   <u>Synthesis</u>

The thesis synthesis begins by highlighting the key findings of the present research, relating back to the aims and objectives set in Chapter 1.2 and exploring how they contribute to the existing body of knowledge and address gaps in the understanding of infragravity waves during storms. This section is deliberately kept succinct to tie the findings together. Following this, each finding is revisited and discussed more thoroughly, offering possible explanations and limitations of the results before finally, suggestions for further research are made.

7.1   <u>Key findings</u>

In this thesis, a bespoke rapid response technique was deployed to collect in-situ and remote measurements of infragravity motions spanning from the shoreline to seaward of the surf zone during exceptional (both in terms of wave height and period) wave conditions on shallow sloping sand, steep gravel and mixed gradient and grain size beaches.

Motions in the shallowest region of the sandy beach were infragravity dominated, increasing in magnitude linearly with incoming wave height, as had previously been observed (e.g. Guza and Thornton, 1985). Infragravity motions were also observed in the shallowest reaches of both pure gravel and mixed grain/compound beaches under high energy wave conditions. Similarly to sandy beaches, infragravity motions were observed dominating over short-wave motions at the shoreline of the gravel beaches and shown to increase in magnitude with increasing incoming wave height. The linear relationships between shoreline infragravity magnitude and incoming wave height on the gravel beaches were found to have a larger constants of proportionality than those previously reported on sandy ones (Ruessink et al., 1998b; Ruggiero et al., 2004; Senechal et al., 2011b), meaning that, for a given increase in

wave height, a larger infragravity response resulted on the gravel beaches than sandy ones. While infragravity waves were shown to be present at the shoreline of the mixed sand-gravel sites, they never became dominant over incident waves.

The importance of collecting data over the wide range of morpho- and hydrodynamic conditions presented here was demonstrated when comparing the performance of previously published empirical predictors of significant infragravity swash height (S_{ig}). A previously published empirical predictor of S_{ig} derived using data collected exclusively on sandy beaches (Stockdon et al., 2006) performed well on the sandy beach and the mixed sand and gravel beach, over a comparable range of conditions over which it was developed. The Stockdon equation was shown to under-predict S_{ig} for higher energy conditions and for data collected on gravel beaches. This reaffirms our previous result that infragravity motions resulting from storm waves are enhanced on gravel beaches compared to sandy ones and should, therefore, be considered a key contributor to storm impacts at such sites by those making numerical forecasts of storm erosion and inundation.

A new predictor of S_{ig} specific to gravel beaches was proposed here, adapting a gravel beach runup equation published by Poate et al. (2016). The new gravel equation performed well on the beaches for which it was designed but poorly on non-gravel beaches, highlighting the contrasting characteristics of infragravity energy at the shoreline of sand and gravel beaches. To the author's knowledge, prior to this research a universal predictor of S_{ig} applicable on both sand and gravel beaches did not exist. The accuracy of various combinations of beach slope, sediment grain size, wave height and period as predictors of S_{ig} were evaluated using the new dataset. Of the combinations tested, H_0^2T, proportional to offshore wave power predicted S_{ig} accurately on both the pure sand and gravel beaches, but poorly on the mixed sand-gravel beaches. As demonstrated above, infragravity could become dominant over incident frequency motions at the shoreline on the pure sand and gravel but not the mixed/

compound beaches. This implied that under extreme wave conditions, wave height and period became more important than local morphology as a control on infragravity in the swash on pure sand and gravel beaches. Conversely, at the mixed/ compound sites where IG rarely dominated, infragravity swash height remained small at the shoreline regardless of offshore conditions.

Examination of infragravity waves as they travelled from outside the surf zone to the shoreline revealed contrasting energy dissipation on the low sloping sand and steep gravel beach. Results implied that bound long wave release was the dominant infragravity generating process on the lower sloping sandy beach while a tendency toward breakpoint forcing was apparent on the steeper gravel beach. The transition to breakpoint forcing with increasing shore face slope on gravel beaches agrees with observations from a range of environments; sandy beaches (Inch et al., 2017), fringing coral reefs (Pomeroy et al., 2012; Masselink et al., 2019) and recently, shore platforms (Poate et al., 2020). The efficiency of the respective infragravity-generating mechanisms may not be equal. Masselink et al. (2019) showed that the breakpoint-forced long wave mechanism was a more effective generator of IG energy than bound long wave release on fringing coral reefs. If the same were true on gravel beaches, this could lead to increased energy at infragravity frequencies propagating shoreward, explaining the enhanced run-up reported by Poate et al. (2016).

7.2   Discussion

7.2.1 Infragravity wave rapid coastal response unit

The data gathering phase of the presented research was remarkably successful, with a near 100 % success rate for data recovery. This was attributed to the rigorous planning that preceded each deployment, the availability of 'state-of-the-art' instrumentation and highly experienced technical support. Further, this kind of rapid response deployment is only possible with a willing and able team of experts, such as The Coastal Processes Research Group at The University of Plymouth. The success of the data collection effort reported here is clear evidence of the benefits of working within a collaborative research unit. While conducting the storm surveys, lessons were learned which should stand to benefit future research efforts, these are described as follows.

The survivability of the gravel beach pressure sensor rigs was tested to its limit during the Storm *'Emma'* deployment at Beesands. To the author's knowledge this was the only occasion to date that in-situ data were collected and used to analyse infragravity waves on a gravel beach, when significant wave heights exceeded 3 m. When waves exceeded 3.5 m, the beach profile changed substantially over a single high tide so that the rigs were either buried or undermined to the extent that they, and the sensors mounted on them, were permanently lost. This provides a guide for future research that data collection on gravel sites should consider a transition to exclusively remote techniques above this threshold. Further, at sites where rigs were fixed in sand, sand screws or land anchors were found to be sufficiently robust up to the largest wave height encountered ($H_0 = 3.8$ m at Camber Sands during storm *'Angus'*).

During the Storm *'Emma'* deployment at Beesands, insight was gained into the importance of cross-shore spacing of intertidal arrays of pressure transducers (PTs) on gravel beaches. The

relatively high slope (Tanβ > 0.1) of gravel beaches means that large changes in elevation occur over short cross-shore distances. In many parts of the UK, this is combined with a macro-tidal regime, making the design of an intertidal array with sufficient spatial extent and resolution difficult. An ideal array would sample from the shallowest region that remained consistently immersed to seaward of the break point.

At Beesands, 6 PTs were deployed for 19 tides, spanning between mean high and low water springs, increasing in cross-shore spacing in the seaward direction (Figure 7-1). The number of sensors in the array was limited by the availability of sensors and the short deployment window around spring low tide. Under high energy conditions, swash excursions spanned half the array, meaning that during these tides, three sensors recorded usable data. On gravel beaches, wave shoaling, breaking and swash are focused into a narrow cross-shore region, meaning that sensors must not be spaced too widely. In addition, the most seaward sensor was lost during the peak of the storm and never recovered. Fortunately, data loss was minimised by downloading of data mid-way through the experiment in anticipation of such losses. Figure 7-1 summarises the data availability for Beesands. Despite the potential difficulties highlighted with collecting in-situ data on gravel beaches, 95 half hour data runs of acceptable quality were collected by the intertidal array over 19 tides.
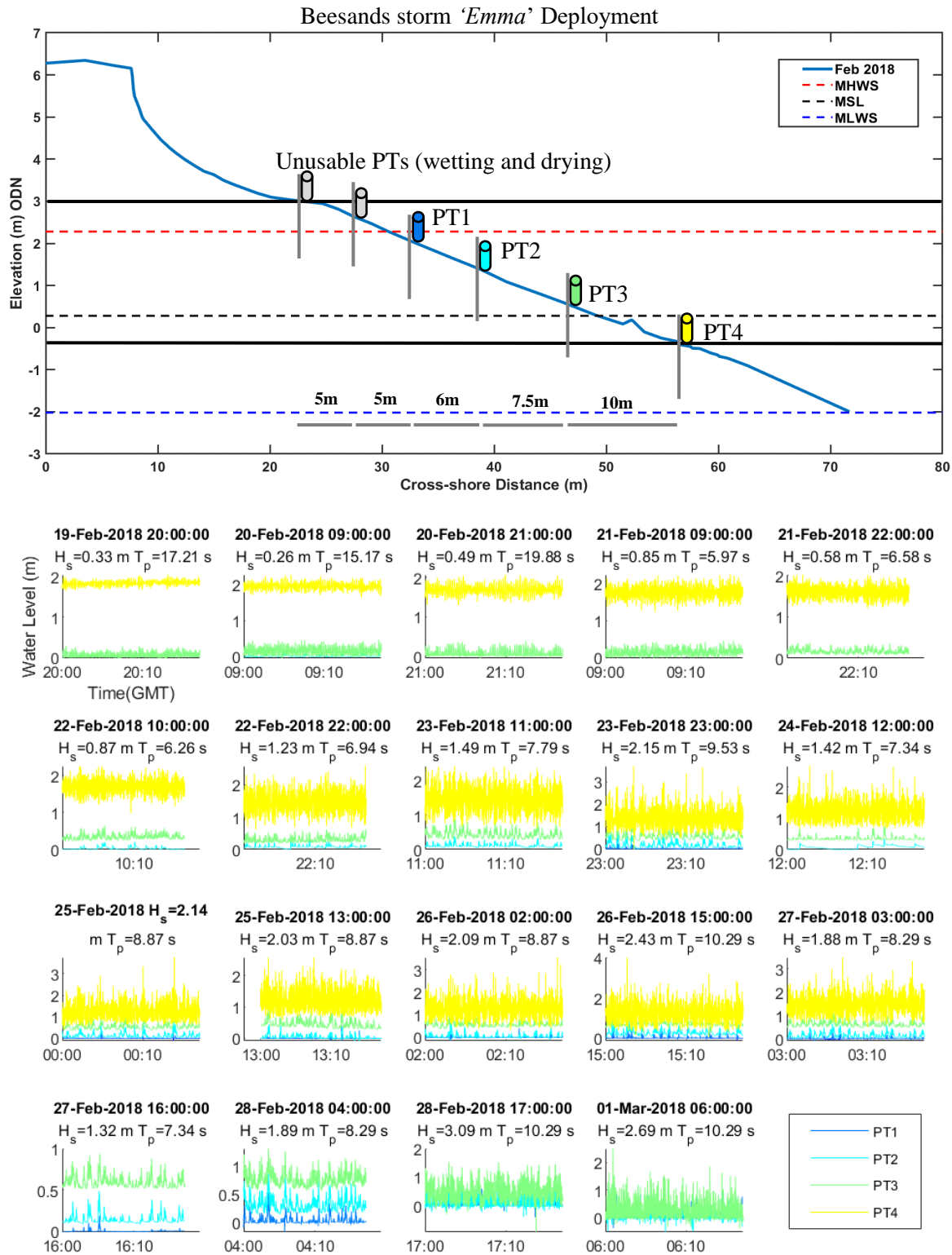
Figure 7-1: Beesands storm *'Emma'* intertidal array. Upper panel; as Figure 6-3 Schematic of pressure transducer deployment at Beesands detailing: The cross-shore profile measured on the day of deployment (19/02/2018), the relative cross-shore position and elevation of each of the six sensors, mean high water spring (MHWS) mean sea level (MSL) and mean low water spring (MLWS) elevations relative to ODN. Lower panel; time series of water level measured at each pressure transducer (PT). Colours of PTs in upper panel correspond to time series in lower panel.

In future, researchers deploying pressure transducer arrays on gravel beaches during storms should limit cross-shore spacing to less than 5 m, provided they have sufficient sensors to span the inter tidal zone. Given the risk of data loss, all opportunities to download data mid-way through the deployment should be taken with preference given to sensors capable of wirelessly transmitting data live.

In order to overcome the issues faced in collecting data in the shallowest regions of the surf zone described above and reported in the literature, this study combined in-situ (pressure transducer array) methods of data collection with remote (video analysis) techniques. This facilitated the investigation of infragravity waves from seaward of the break point, through the surf zone, to the landward extreme of the swash. In order to examine the levels of incoming infragravity energy from deep water, ADCPs were deployed at two of the five study sites. Having a clear understanding of the boundary conditions was important if accurate conclusions about the processes occurring inside the surf zone were to be drawn. The possibility of using wave buoys in the absence of ADCPs was explored given the excellent temporal and spatial coverage of the Channel Coastal Observatory (CCO) wave buoy network around the UK. However, it was found that the current network, which use accelerometers to track surface elevation are not capable of accurately measuring motion occurring at infragravity frequencies. However, it has been shown that wave buoys which rely on differential GPS (DGPS) data track surface elevation to a higher precision than those using accelerometers and are better suited to detecting motions at infragravity frequencies (Davies, 2000; de Vries et al., 2003). If the CCO were to adopt DPGS buoys, their network could become a hugely valuable method for monitoring incoming infragravity energy, perhaps improving forecasts of extreme erosion, overtopping and inundation.

In the future, improved weather forecasts will be able to predict where a storm will arrive, further in advance than at present. According to the UK Met Office, their four-day forecast

today is more accurate than a one-day forecast in 1980. This will provide greater opportunity to prepare for rapid response deployments and reduce the risk of missing an event due to lack of warning or targeting the incorrect location.

7.2.2 <u>Dataset</u>

The dataset analysed in Chapters 3-5 is unique for two reasons. Firstly, it includes the first example of in-situ and remote observation of infragravity waves on a steep gravel beach under high energy conditions ($H_s > 3m$). Secondly, by collecting comparable data at three additional beaches and re-analysis of high energy data from a fifth site, unique comparisons between IG dynamics on a wider range of beach types than ever before can be made. Accordingly, the presented dataset and analysis are a significant contribution to both the infragravity and coastal storm literature.

Each of the events measured during this research can be thought of as a representative storm for the stretch of coastline on which it was located. Dhoop and Mason (2018) suggested that the coastline of England can be partitioned into six discrete coastal regions, each of which is impacted by storms as a relatively coherent unit. Comparing the location of the sites studied here to the regions defined by Dhoop, it can be seen that storms were measured in five of the six regions (Figure 7-2). By measuring a storm in five of the six regions, the dataset characterises UK storms exceptionally well.
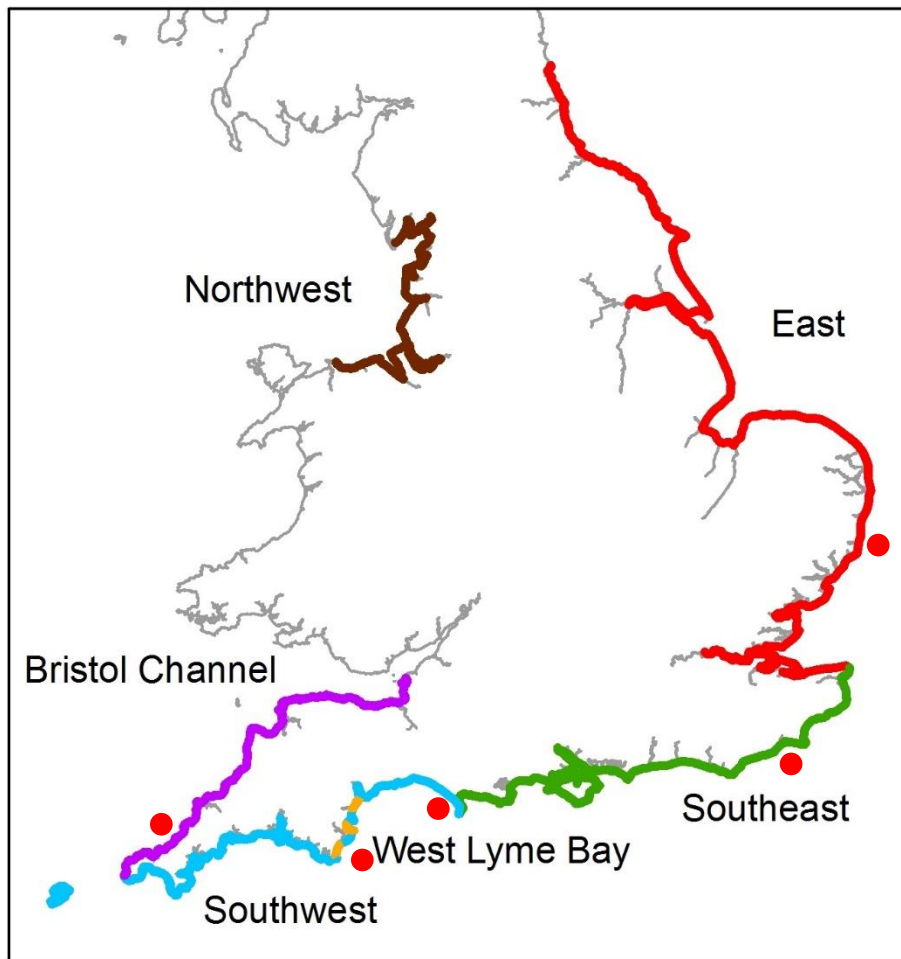
Figure 7-2 Coastal regions of coherent storm impact define by Dhoop and Mason (2018) with sites studied in this thesis shown by red circles

Given the differing exposure and wave climate of each of the beaches, how the waves observed during a storm compared to those in the long-term record is more informative than the magnitude of H_s and T_p. Figure 7-3 shows how the measured peak in H_s and T_p during each of the storms, compares to the long-term record at each of the local wave buoys. It can be seen that peak H_s observed during storm '*Angus*' at Camber and storm '*Emma*' at Beesands were the largest on record. In the Chesil dataset, waves were only larger than the observed storm '*Petra*' peak on two occasions. Further, the peak T_p at Camber and Chesil coincided with exceptionally large waves, with only a handful of examples on record of waves of equal T_p being larger H_s. Therefore, it can be stated with confidence that the presented dataset is truly ground breaking at 3 out of 5 of the study sites by taking

measurements under more energetic conditions than previous field campaigns. By collating a dataset collected during the most energetic and damaging conditions, understanding and predictive skill of such events can be enhanced through analysis and modelling, ultimately reducing the impact of storms.
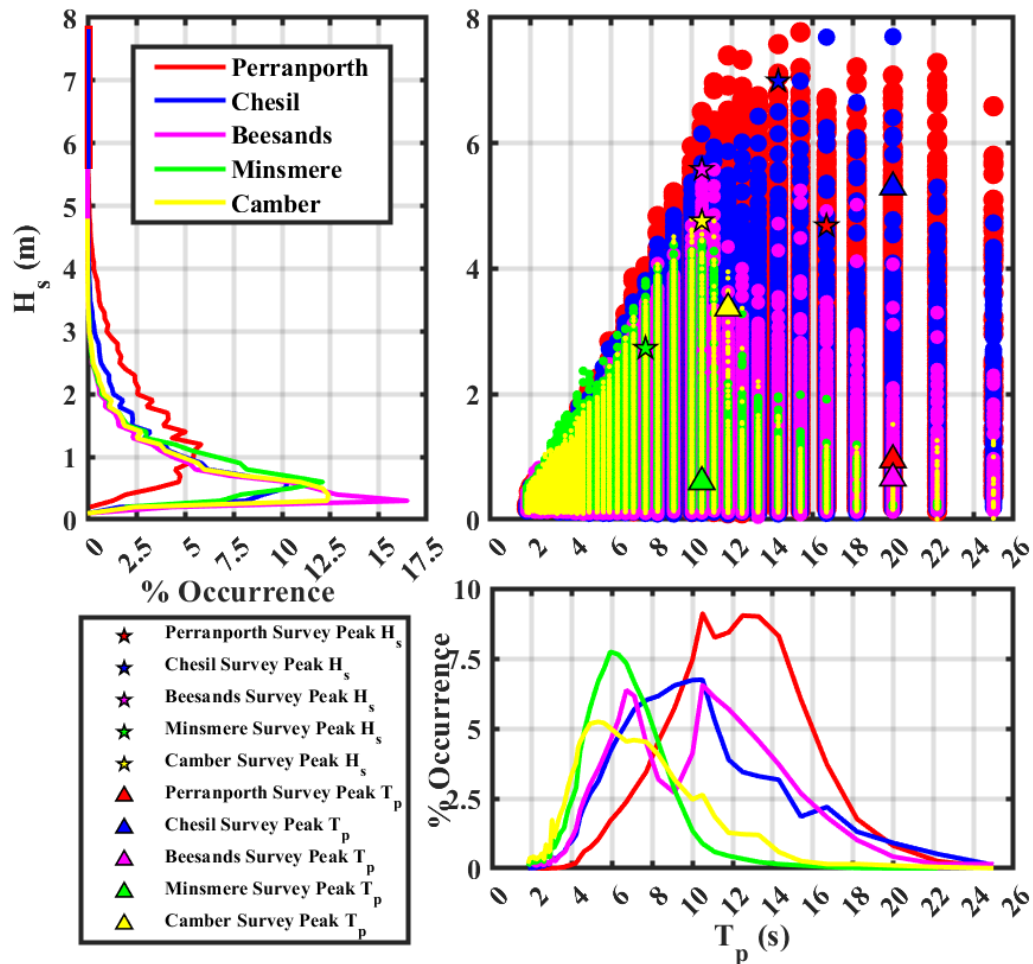
Figure 7-3 As Figure 1-4 with peak observed H_s (stars) and T_p (triangles) during each storm survey added for reference. Scatter plot of peak period (Tp) against significant wave height (H_s) measured at local wave buoys to each of the five study sites. Adjacent to the relevant axis is a plot of percentage occurrences of T_p and H_s respectively

As well as beaches, infragravity waves have been shown to play a key role in processes on rocky shore platforms (e.g., Poate et al., 2020) and coral reefs (e.g.) in studies conducted under moderate wave conditions. However, almost none have drawn comparisons between

observations on beaches and other morphologies (e.g., Inch, 2016). Further research should aim to compare the beach findings presented in this thesis against platform and reef observations under extreme storm conditions.

7.2.3 <u>Infragravity waves on gravel beaches</u>

The newfound importance of infragravity waves on gravel beaches has far reaching applications in the UK, Europe and beyond. Gravel beaches occur widely along the wave dominated coastlines of The USA, Canada, Latin America, Japan, New Zealand and Northern Europe (Buscombe and Masselink, 2006). In England and Wales, pure shingle occurs along almost 900 km of coastline and is particularly prevalent in North Norfolk, Suffolk, Kent, Sussex and Dorset along the Channel coast (Fuller and Randall, 1988).

While no estimate exists for the number of gravel beaches globally, it was recently demonstrated through analysis of satellite imagery that up to 31% of the planet's ice free coastline are beaches, encompassing all grain sizes (Luijendijk et al., 2018). At regional scale, empirical relationships with beach face slope have been used to infer sediment grain size (Vos et al., 2020). Using their newly derived satellite estimate of beach face slope and an empirically fitted equation linking beach face slope and median grain size (Bujan et al., 2019), Vos et al. were able to estimate the grain size across thousands of beaches in eastern Australia and California, USA with reasonable success.

This technique could be applied globally to approximate how many gravel beaches exist in the world. While gravel beaches can occur in a variety of geological settings, several authors have identified a prominent latitudinal control (>40° N and S) on the common occurrence of gravels in continental shelf and shore zone sediment budgets (e.g. Hayes, 1967; Ranwell and Davies, 1973; Orford et al., 2002). Assuming that beaches occurring above or below 40 ° N

and S longitude with a slope of over Tanβ = 0.125 are likely to be gravel, a conservative estimate can be made of how many gravel environments exist globally. This is important as, following this contribution, these sites should now be considered susceptible to dominance by motions of infragravity frequencies during storms which could in turn lead to increased runup, overtopping and erosion than currently accounted for.

XBeach-G is a version of the XBeach model, developed to simulate storm impacts on gravel beaches. Similar to the SWASH model of Zijlema et al. (2011), XBeach-G uses the one-layer, depth-averaged, non-hydrostatic version of XBeach model, to solve wave-by-wave flow and surface elevation variations due to short waves in intermediate and shallow water depths. When the model was designed, it was thought that '*for applications on gravel beaches, infragravity wave motion, which dominates the inner surf and swash zone on sandy beaches during storms, is of secondary importance.*' (XBeach, 2020). In fact, it was demonstrated in this thesis that infragravity wave motion dominates the inner surf and swash zone of gravel beaches, when H_0 exceeds 2 m. Failure to account for the possible dominance of infragravity frequency motion in the swash zone of gravel beaches during storms as demonstrated in this research may lead to the under prediction of the contribution of low frequency motions to nearshore processes resulting in turn in the underestimation of storm-driven overtopping and erosion. Presently, flood risk from overtopping on gravel coastlines may be seriously under-assessed with significant consequences in terms of achieving effective climate change adaptation.

7.2.4 Implications for sediment transport by infragravity waves

During storm *'Emma'*, significant levels of cross-shore driven shore face erosion were observed across Start Bay with up to $2.3 \pm 0.8 \times 10^5$ m^3 of gravel transported from the sub-

aerial to the sub-tidal (McCarroll et al., 2019). However, they did not examine the cross-shore hydrodynamic processes driving the observed erosion. The dominant mechanism inducing offshore-directed transport is undertow (e.g. Ruessink et al., 1998a), particularly on steep beaches where local intensification of wave breaking leads to stronger undertow (Aagaard et al., 2002). Prior to this research, infragravity (IG) waves have been shown to contribute to cross-shore driven erosion (e.g. Russell, 1993) but this was thought to be inherently limited to inner surf zone of gently sloping beaches during storms (de Bakker et al., 2016). The newfound potential for IG waves to dominate over short-wave frequency motions on gravel beaches reported here has implications for sediment transport during storms.

The conceptual model of De Bakker et al. (2016) presented in Chapter 1.3.2.3 constrained previously observed variability in IG sediment transport by considering the process on a 'gently' ($\text{Tan}\beta \approx 0.0125$) and a 'moderately' ($\text{Tan}\beta \approx 0.0285$) sloping sandy beach (right side of Figure 7-4). They suggested that the direction and magnitude of cross-shore sediment transport due to IG waves can be explained by the ratio of significant infragravity wave height to sea-swell wave height (H_{ig}/H_{g}) combined with the correlation between the short-wave envelope and IG velocity, the reasons for which were described in full in Chapter 1.3.2.3.

In the model, in the inner surf zone of gently sloping beaches where infragravity waves can be very energetic, sediment transport by infragravity waves is offshore directed if $H_{ig}/H_{g}>0.4$ regardless of the local sea-swell waves. Further seaward, where $0.3< H_{ig}/H_{g} <0.4$ and the largest sea-swell waves tend to coincide with an IG wave crests, IG sediment transport tends to be onshore directed.

On the moderately sloping beach, even close to shore and under high energy conditions, a lack of short-wave dissipation limits values of H_{ig}/H_g (<0.4). As a result, sediment suspension by the IG waves is reduced meaning the direction of sediment transport at IG frequencies depends entirely on the correlation between the short-wave envelope and infragravity velocity. This becomes negative, onshore transport in the inner surf zone and positive, offshore transport in the outer surf zone.

De Bakker et al. (2016) hypothesised that for significant IG driven transport to occur, both H_{ig} and H_{ig}/H_g must be large. Figure 7-4 compares data collected during storm '*Emma*' at Beesands and an un-named storm at Perranporth analysed in Chapter 6 with the data used by de Bakker et al. (2016) to formulate their conceptual model. It should be noted that Beesands is significantly steeper (Tan$\beta \approx 0.1$) than the 'moderately' sloping Sand Motor (Tan$\beta \approx 0.0285$) and Perranporth (Tan$\beta \approx 0.02$) sits between Sand Motor and the 'gently' sloping Ameland (Tan$\beta \approx 0.0125$). The addition of Perranporth and Beesands data tests the model beyond the parameter space over which it was conceived.

Figure 7-4 (a – d) plots significant infragravity wave height (H_{ig}) against offshore significant wave height (H_0) at the four sites. H_0 in the Beesands (BEE) data was typically larger than the Sand Motor (SM) data, with the majority of points from BEE being $H_0 > 2$ m, while at SM H_0 was mainly less than 1.5 m. H_{ig} was typically larger at BEE exceeding 0.3 m the majority of the time. Conversely, H_{ig} at SM was almost always below 0.3m. Despite the largest H_0 observed at SM (4.3 m) exceeding that of BEE (3.3 m) by 1 m the associated H_{ig} was comparable at both sites (≈ 0.5 m). Interestingly, despite the markedly different beach slopes, the scatter of data at Beesands was more closely comparable to that of Ameland than SM, with evidence of H_{ig} saturation above H_0 2.5 m. The tendency of H_{ig} to be larger at BEE than SM for comparable H_0 suggests that something other than wave height was impacting H_{ig}. Offshore wave period at SM ranged from 3.1 – 7 s, compared to 6 – 16 s at BEE, meaning

that $H_0^2 T_P$ was approximately < 25 m^{2}s (not shown in figure) the majority of the time at SM compared to 30 m^{2}s or higher at BEE.

Figure 7-4 (e – h) shows the dominance of infragravity wave height, relative to short wave height (H_{ig}/H_g) at the four sites. In the conceptual model of de Bakker et al. (2016), $H_{ig}/H_g <$ 0.3 indicates offshore transport outside of the surf zone, 0.3-0.4, onshore transport in the inner surf zone and > 0.4, offshore transport in the inner surf zone (confined to the gently sloping beach).

A marked difference can be seen between H_{ig}/H_g at BEE and SM. At SM, values were typically low, rarely exceeding 1 with the majority of points below 0.3. In contrast, only 26 % of the Beesands data fell below 0.3, with 16 % between 0.3 and 0.4 and 58 % above 0.4. This places the majority of the data in the inner surf zone offshore directed transport regime ($H_{ig}/H_g > 0.4$). Taking into account depth, it can be seen values of $H_{ig}/H_g < 0.3$ were typically associated with the deepest measurement depths (h > 2 m) while $H_{ig}/H_g > 0.4$ with the shallowest (h < 1 m), providing further evidence that the highest ratios of H_{ig}/H_g were observed in the inner surf zone and therefore most conducive to offshore directed transport.

The moderate values of H_{ig}/H_g (≈ 0.5) associated with shallowest measurement depths provide further evidence of saturation of the IG band, close to shore at Beesands.

The criteria set by de Bakker et al. (2016) for significant IG driven transport to occur ('*both H_{ig} and H_{ig}/H_g must be large*') were met convincingly at Beesands, Further, larger values of H_{ig}/H_g were associated with shallower water depths. This leads to a suggested modification to the conceptual model, (marked in red on Figure 7-4 (i)), whereby under high energy conditions, infragravity driven sediment transport can be offshore directed in the inner surf zone of steep gravel beaches as well as gently sloping sandy ones. In order for this to occur, certain conditions must be met; In Chapter 4, we demonstrated that for infragravity

dominance to occur at the shoreline of Beesands, a surf zone must be present with the beach in a morphodynamically intermediate state, subjected to plunging breakers ($\xi_0 < 1$). Comparing Figure 7-4 (a + e) to (b + f), divergence in H_{ig} and H_{ig}/H_g at the two sites when $H_0 > 2$ m suggests that this may be a reasonable threshold to bound the newly proposed offshore transport regime. Finally, only data collected in less than 1 m of water met the $H_{ig}/H_g > 0.4$ requirement set out by de Bakker et al. (2016).

Comparing data from Perranporth (PPT) and Ameland (AM), it can be seen that despite having similar ranges of H_0 (~0.7 - 4.4 m), H_{ig} was significantly larger at PPT than AM when H_0 exceeded ~2 m (Figure 7-4c +d). As was the case with BEE and SM, the disparity of wave period between PPT and AM (7 – 22 s and 3 – 7 s respectively) is likely responsible for the larger values of H_{ig} observed at PPT, given the importance of wave period to infragravity waves (Inch et al., 2017). Unsurprisingly, when examining values of H_{ig}/H_g this placed 52% of the PPT data in the inner surf zone offshore directed transport regime ($H_{ig}/H_g > 0.4$) in contrast to AM where the majority of H_{ig}/H_g values were less than 0.4. This suggests that gently sloping sandy beaches, exposed to long period swell, such as Perranporth, are more prone to offshore directed infragravity driven sediment transport and therefore shore face erosion than fetch limited sites.

Direct measurement of sediment transport over the range of conditions sample in this study are required to test de Bakker's model exhaustively. On sandy sites this could be achieved by combining measurements of sediment concentration in the water column with current velocities, taking care to collect observations at the correct height above the bed to capture transport occurring at IG and incident frequencies. On gravel beaches, direct measurement of sediment transport is not feasible owing to the destructive forces exerted on sensors by suspended gravel particles. Instead, using the topographic and hydrodynamic data collected in this study, X-Beach G could be modified to include IG driven cross-shore gravel transport.
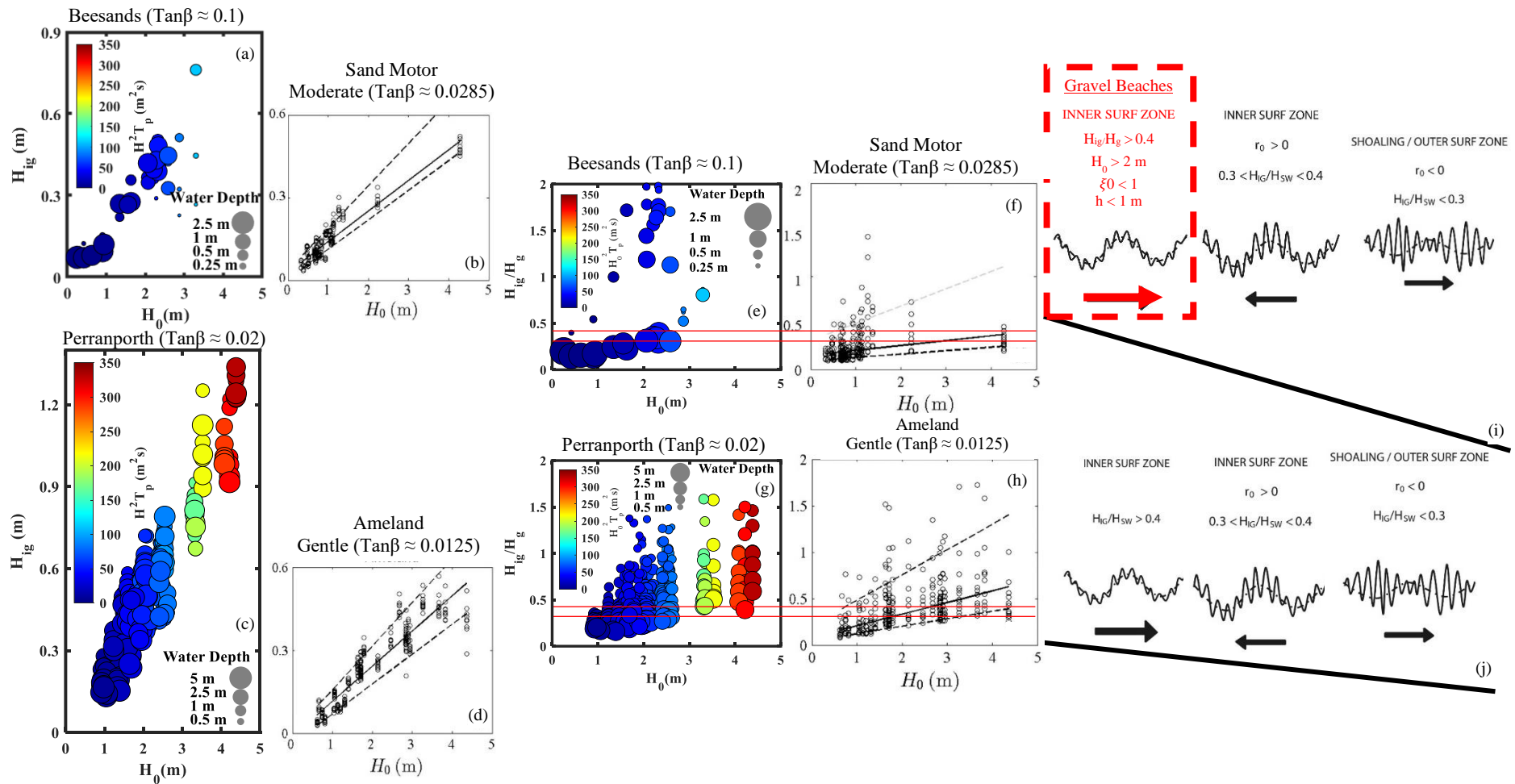
Figure 7-4 Comparing results from Beesands and Perranporth to the results and conceptual model of de Bakker et al. (2016). Left: Significant infragravity wave height H_{ig} versus offshore significant wave height H_0, at Beesands (a), Sand Motor (b) Perranporth (c) and Ameland (d). Centre: H_{ig}/H_g versus H_0 at Beesands (e), Sand Motor (f) Perranporth (g) and Ameland (h). Colour of points in (a,c,e + g) represents $H_0^2 T_p$ and size, water depth (m). Red lines on (e,f,g,h) mark the transition between the transport regimes in de Bakker et al.'s model ($H_{ig}/H_g < 0.3$ and < 0.4.) Beesands (a + e) and Perranporth data (c + g) are plotted on axes matching the de Bakker et al., sites (b + d) and (f + h) respectively, facilitating direct comparison between their study and the presented work. Right: Conceptual model for sand suspension mechanism and transport direction on moderately (i) and gently sloping (j) beaches with new gravel beach regime added in red. For a full description of (b, d, f + h) the reader is referred to de Bakker et al. (2016) their Figure 3 and for (i + j), their Figure 10.

7.2.5 <u>**Applications of this research**</u>

At present, the variability in the role of infragravity waves across differing types of beach is not accurately accounted for in operational forecasts of inundation and erosion, potentially leading to the under prediction of storm driven flooding and damage to coastal infrastructure particularly on gravel flanked coasts.

One of the best examples of storm research dissemination to coastal practitioners is 'The South West Partnership for Environment & Economic Prosperity – Operational Wave and Water Level' model (SWEEP-OWWL), developed at the University of Plymouth. At present, the parametrisation of wave runup on gravel beaches published in Poate et al. (2016) and discussed in Chapter 5.3.6 is combined with existing empirical equations, to provide accurate 3-day forecasts of overtopping risk at 183 sites in south west England. Given the newfound importance of infragravity band motions leading to the enhancement of wave runup on gravel beaches, this forecast could be made more accurate by accounting for the variability of low frequency contributions constrained in the gravel specific infragravity swash equation proposed in Chapter 5.3.6. Shoreline management decisions, for example whether or not an area of coastline requires strategic intervention can be better informed by accounting for the increase potential for flooding and erosion identified in this study.

A less well developed but promising example is the early warning system for erosion risk along the coast of New South Wales, under development by researchers at the Water Research Laboratory – University of New South Wales (WRL – UNSW). Whilst not yet operational, the project represents the most advanced tool of its kind. Again, the system was designed through extensive data collection.

It is hoped that the findings presented here will assist coastal managers and communities in mitigating against coastal storm impacts. By demonstrating that infragravity waves play a key role in storm processes across a wider range of beach types than previously thought and identifying

hydrodynamic conditions conducive with their presence, forecasting of coastal inundation and erosion can be improved. This will assist in both reduction of risk to existing infrastructure and planning for future coastal development.

8 Thesis conclusions

The overarching aim of this thesis is to understand how the prevalence and significance of infragravity waves varies across an extensive range of natural hydro- and morphodynamic conditions.

Objective 1 was achieved via rapid deployment of instruments, targeting four storms, between November 2016 and March 2018. Measurements were successfully collected on sand, gravel and mixed sediment beaches, each with techniques sympathetic to the nuances of the specific environment (Chapter 2.2.2).

This data collection approach was used to address objective 2, compiling a new observational dataset, collected over an unprecedented environmental parameter space. The dataset combined observations collected during significant wave heights (H_s) of up to 7 m, peak periods (T_p) in excess of 20s, on beach slopes of up to $Tan\beta < 0.3$ and median sediment grain size (D_{50}) of up to 60 mm (Chapter 3).

Objective 3 was explored by analysing video observations of the swash at Beesands, a steep (mean $Tan\beta = 0.1$) gravel (median sediment grain size, $D_{50} = 5mm$) beach, (Chapter 4), concluding the following:

- As observed on some sandy beaches, swash motions on the gravel beach became dominated by the infragravity band, with gravity swash motions appearing to be saturated, when offshore wave heights exceeded approximately 1.5 m.

- A linear relationship between significant infragravity swash height (S_{ig}) and H_0 was observed with larger constants of proportionality than previously observed on lower sloping sandy beaches. This highlighted the contribution of and IG component to the enhanced runup on gravel compared to sandy beaches previously reported in the literature.

- S_{ig} scaled inversely with ξ_0, becoming infragravity dominated for values less than one, when conditions transitioned from morphodynamically reflective to intermediate, implying that short wave breaking is needed for there to be infragravity dominance in the swash.

In answer to objective 4, the conclusions drawn from the gravel beach data were put into wider context with other beach types comparing video observations of the swash at a further four contrasting sites (Chapter 5). These ranged from both wind-wave and swell-dominated gravel beaches, through fetch-limited mixed sand and gravel, to a swell-dominated, low-sloping sandy beach. Waves in excess of the 95th percentile were observed at all sites. The following conclusions were drawn:

- Infragravity waves were observed in the swash at all five contrasting sites. When grouped together, data from the five sites showed a strong and significant linear correlation between S_{ig} and H_0. The line of best fit intercepted the x-axis, facilitating the tentative definition of a threshold of H_0 of around 1.3 m, above which infragravity energy becomes apparent and therefore important in the swash.

- For a given wave height, infragravity motions in the swash were enhanced on exposed gravel and sandy beaches but suppressed on more sheltered mixed/compound beaches.

- Infragravity waves were observed to become most dominant in the swash on the low sloping sandy beach, where S_{ig}/S_g exceeded 4. They occasionally dominated the gravel beaches but to a lesser extent (<1.8) and rarely or never dominated the mixed/compound sites (<1.1). This was attributed to differences in short wave dissipation patterns resulting from contrasting morphology and wave steepness.

- $H_0^2 T$, proportional to offshore wave power, was a good predictor of S_{ig} at the sites where IG could become dominant, yielding the equation: $S_{ig} = 0.02(H_0^2 T) + 0.42$, valid for high energy conditions (when $H_0 > 1.3$ m).

- The relationship between S_{ig} and H_0^2T, across a diverse range of sites, implied that under extreme wave conditions, wave height and period became more important than local morphology as a control on infragravity in the swash. Conversely, at sites where IG rarely dominated, infragravity swash height remained small at the shoreline regardless of offshore conditions. This highlights the importance of collecting data over the unique range of heights and periods present here.

Objective 5 examined why the observed differences in infragravity importance and dominance occurred at the contrasting sites by comparing infragravity development through the surf zone of a sand and a gravel beach (Chapter 6).

- Comparing wave energy levels and frequency distribution from spectral estimates through the surf zone with those offshore revealed that energy transferred to the infragravity band seaward of the surf zone at the sandy beach site (PPT) but was limited to landward of the short-wave breakpoint at the gravel beach site (BEE).

- Values of the surf beat similarity parameter indicated that bound long wave release was the most dominant IG generating mechanism on the low sloping sandy beach (PPT), whilst breakpoint forcing dominated on the steep gravel beach, BEE).

9 <u>References</u>

Aagaard, T., Black, K.P., Greenwood, B., 2002. Cross-shore suspended sediment transport in the surf zone: A field-based parameterization. Mar. Geol. 185, 283–302. https://doi.org/10.1016/S0025-3227(02)00193-7

Aagaard, T., Greenwood, B., 2008. Infragravity wave contribution to surf zone sediment transport - The role of advection. Mar. Geol. 251, 1–14. https://doi.org/10.1016/j.margeo.2008.01.017

Aagaard, T., Greenwood, B., 1994. Suspended sediment transport and the role of infragravity waves in a barred surf zone. Mar. Geol. 118, 23–48. https://doi.org/10.1016/0025-3227(94)90111-2

Almeida, L.P., Masselink, G., McCall, R.T., Russell, P.E., 2017. Storm overwash of a gravel barrier: Field measurements and XBeach-G modelling. Coast. Eng. 120, 22–35. https://doi.org/10.1016/j.coastaleng.2016.11.009

Almeida, L.P., Masselink, G., Russell, P.E., Davidson, M.A., 2015. Observations of gravel beach dynamics during high energy wave conditions using a laser scanner. Geomorphology 228, 15–27. https://doi.org/10.1016/j.geomorph.2014.08.019

Almeida, L.P., Masselink, G., Russell, P.E., Davidson, M.A., Poate, T.G., McCall, R.T., Blenkinsopp, C.E., Turner, I.L., 2013. Observations of the swash zone on a gravel beach during a storm using a laser-scanner (Lidar). J. Coast. Res. 65, 636–641. https://doi.org/10.2112/si65-108.1

Alsina, J.M., Caceres, I., 2011. Sediment suspension events in the inner surf and swash zone. Measurements in large-scale and high-energy wave conditions. Coast. Eng. 58, 657–670. https://doi.org/10.1016/j.coastaleng.2011.03.002

Austin, M.J., 2005. Swash, groundwater and sediment transport processes on a gravel beach. Ph.D.

Thesis. Loughborough University.

Austin, M.J., Masselink, G., 2006. Observations of morphological change and sediment transport on a steep gravel beach. Mar. Geol. 229, 59–77. https://doi.org/10.1016/j.margeo.2006.02.003

Baldock, T.E., 2012. Dissipation of incident forced long waves in the surf zone-Implications for the concept of "bound" wave release at short wave breaking. Coast. Eng. 60, 276–285. https://doi.org/10.1016/j.coastaleng.2011.11.002

Baldock, T.E., Huntley, D.A., 2002. Long-wave forcing by the breaking of random gravity waves on a beach. Proc. R. Soc. A Math. Phys. Eng. Sci. 458, 2177–2201. https://doi.org/10.1098/rspa.2002.0962

Baldock, T.E., Manoonvoravong, P., Pham, K.S., 2010. Sediment transport and beach morphodynamics induced by free long waves, bound long waves and wave groups. Coast. Eng. 57, 898–916. https://doi.org/10.1016/j.coastaleng.2010.05.006

Battjes, J., 2004. Shoaling of subharmonic gravity waves. J. Geophys. Res. 109, 1–15. https://doi.org/10.1029/2003JC001863

Battjes, J.A., 1974. Surf Similarity. Coast. Eng. Proc. 14, 466–480. https://doi.org/10.1061/9780872621138.029

BAVEN, A.J., INMAN, D.L., 1971. EDGE WAVES AND CRESCENTIC BARS. J. Geophys. RES. 76, 8662–8671. https://doi.org/10.1029/jc076i036p08662

Beach, R.A., Sternberg, R.W., 1988. SUSPENDED SEDIMENT TRANSPORT IN THE SURF ZONE: RESPONSE TO CROSS-SHORE INFRAGRAVITY MOTION. Mar. Geol. 108, 275–294. https://doi.org/10.1016/0025-3227(92)90201-r

Bertin, X., de Bakker, A.T.M., van Dongeren, A., Coco, G., André, G., Ardhuin, F., Bonneton, P., Bouchette, F., Castelle, B., Crawford, W.C., Davidson, M., Deen, M., Dodet, G., Guérin, T., Inch, K., Leckler, F., McCall, R., Muller, H., Olabarrieta, M., Roelvink, D., Ruessink, B.G.,

Sous, D., Stutzmann, É., Tissier, M., 2018. Infragravity waves: From driving mechanisms to impacts. Earth-Science Rev. 177, 774–799. https://doi.org/10.1016/j.earscirev.2018.01.002

Bertin, X., Martins, K., de Bakker, A.T.M., Chataigner, T., Guérin, T., Coulombier, T., de Viron, O., 2020. Energy Transfers and Reflection of Infragravity Waves at a Dissipative Beach Under Storm Waves. J. Geophys. Res. Ocean. 125. https://doi.org/10.1029/2019JC015714

Bertin, X., Prouteau, E., Letetrel, C., 2013. A significant increase in wave height in the North Atlantic Ocean over the 20th century. Glob. Planet. Change 106, 77–83. https://doi.org/10.1016/j.gloplacha.2013.03.009

Biésel, F., 1952. Equations générales au second ordre de la houle irrégulière. Houille Blanche 3, 372–376. https://doi.org/10.1051/lhb/1952033

Billson, O., Russell, P.E., Davidson, M.A., 2019. Storm waves at the shoreline: When and where are infragravity waves important? J. Mar. Sci. Eng. 7, 139. https://doi.org/10.3390/jmse7050139

Billson, Oliver., Russell, P.E., Davidson, M.A., Wiggins, M., McCarroll, R.J., Poate, T.G., Nicoletta, L., 2019. OBSERVATIONS OF INFRAGRAVITY DOMINANCE IN THE SWASH ZONE OF A STEEP GRAVEL BEACH, in: Coastal Sediments 2019. WORLD SCIENTIFIC, pp. 1866–1878. https://doi.org/10.1142/9789811204487_0161

Bowen, A.J., 1980. Simple Models of Nearshore Sedimentation, Beach Profiles and Longshore Bars, in: The Coastline of Canada, Littoral Processes and Shore Morphology -. p. Paper 80-10, 1-11. https://doi.org/10.4095/102213

Brodie, K.L., McNinch, J.E., 2009. Measuring Bathymetry, Runup, and Beach Volume Change during Storms: New Methodology Quantifies Substantial Changes in Cross-Shore Sediment Flux. AGU Fall Meet.

Bujan, N., Cox, R., Masselink, G., 2019. From fine sand to boulders: Examining the relationship

between beach-face slope and sediment size. Mar. Geol. 417, 106012. https://doi.org/10.1016/j.margeo.2019.106012

Burvingt, O., Masselink, G., Russell, P., Scott, T., 2017. Classification of beach response to extreme storms. Geomorphology 295, 722–737. https://doi.org/10.1016/j.geomorph.2017.07.022

Burvingt, O., Masselink, G., Scott, T., Davidson, M., Russell, P., 2018. Climate forcing of regionally-coherent extreme storm impact and recovery on embayed beaches. Mar. Geol. 401, 112–128. https://doi.org/10.1016/j.margeo.2018.04.004

Buscombe, D., Masselink, G., 2006. Concepts in gravel beach dynamics. Earth-Science Rev. 79, 33–52. https://doi.org/10.1016/j.earscirev.2006.06.003

Butt, T., Russell, P., 2000. Hydrodynamics and cross-shore sediment transport in the swash-zone of natural beaches: A review. J. Coast. Res. 16, 255–268. https://doi.org/10.2307/4300034

Caballeria, M., Coco, G., Falqués, A., Huntley, D.A., 2002. Self-organization mechanisms for the formation of nearshore crescentic and transverse sand bars. J. Fluid Mech. 465, 379–410. https://doi.org/10.1017/S002211200200112X

Castelle, B., Marieu, V., Bujan, S., Splinter, K.D., Robinet, A., Sénéchal, N., Ferreira, S., 2015. Impact of the winter 2013-2014 series of severe Western Europe storms on a double-barred sandy coast: Beach and dune erosion and megacusp embayments. Geomorphology 238, 135–148. https://doi.org/10.1016/j.geomorph.2015.03.006

Coco, G., Murray, A.B., 2007. Patterns in the sand: From forcing templates to self-organization. Geomorphology 91, 271–290. https://doi.org/10.1016/j.geomorph.2007.04.023

Coco, G., Senechal, N., Rejas, A., Bryan, K.R., Capo, S., Parisot, J.P., Brown, J.A., MacMahan, J.H.M., 2014. Beach response to a sequence of extreme storms. Geomorphology 204, 493–501. https://doi.org/10.1016/j.geomorph.2013.08.028

Conley, D.C., Beach, R.A., 2003. Cross-shore sediment transport partitioning in the nearshore during a storm event. J. Geophys. Res. 108, 3065. https://doi.org/10.1029/2001JC001230

Contardo, S., Symonds, G., 2013. Infragravity response to variable wave forcing in the nearshore. J. Geophys. Res. Ocean. 118, 7095–7106. https://doi.org/10.1002/2013JC009430

Davidson, M.A., Splinter, K.D., Turner, I.L., 2013. A simple equilibrium model for predicting shoreline change. Coast. Eng. 73, 191–202. https://doi.org/10.1016/j.coastaleng.2012.11.002

Davies, J., 2000. Long period wave effects as measured by a dual frequency DGPS buoy. Coast. Eng. 2000 - Proc. 27th Int. Conf. Coast. Eng. ICCE 2000 276, 953–964. https://doi.org/10.1061/40549(276)74

de Bakker, A.T.M., 2016. Infragravity-wave dynamics in shallow water. Ph.D. Thesis.

de Bakker, A.T.M., Brinkkemper, J.A., van der Steen, F., Tissier, M.F.S., Ruessink, B.G., 2016. Cross-shore sand transport by infragravity waves as a function of beach steepness. J. Geophys. Res. Earth Surf. 121, 1786–1799. https://doi.org/10.1002/2016JF003878

de Bakker, A.T.M., Herbers, T.H.C., Smit, P.B., Tissier, M.F.S., Ruessink, B.G., 2015. Nonlinear infragravity-wave interactions on a gently sloping laboratory beach. J. Phys. Oceanogr. 45, 589–605. https://doi.org/10.1175/JPO-D-14-0186.1

de Bakker, A.T.M., Tissier, M., Marieu, V., Sénéchal, N., Ruju, A., Lara, J., Ruessink, B.G., 2013. Infragravity Wave Propagation and Dissipation on a Low-Sloping Laboratory Beach, in: Coastal Dynamics 2013. pp. 443–452.

de Bakker, A.T.M., Tissier, M.F.S., Ruessink, B.G., 2014. Shoreline dissipation of infragravity waves. Cont. Shelf Res. 72, 73–82. https://doi.org/10.1016/j.csr.2013.11.013

de Vries, J.J., Waldron, J., Cunningham, V., 2003. Field tests of the new datawell DWR-G GPS wave buoy. Sea Technol. 44, 50–55.

Denbigh, A., 2017. THE SLAPTON LINE-LIVING WITH COASTAL CHANGE. https://fsj.field-studies-council.org/media/3261364/fs2017_denbigh.pdf.

Dhoop, T., Mason, T., 2018. Spatial characteristics and duration of extreme wave events around the English coastline. J. Mar. Sci. Eng. 6. https://doi.org/10.3390/jmse6010014

Dodet, G., Bertin, X., Taborda, R., 2010. Wave climate variability in the North-East Atlantic Ocean over the last six decades. Ocean Model. 31, 120–131. https://doi.org/10.1016/j.ocemod.2009.10.010

Donat, M.G., Renggli, D., Wild, S., Alexander, L. V., Leckebusch, G.C., Ulbrich, U., 2011. Reanalysis suggests long-term upward trends in European storminess since 1871. Geophys. Res. Lett. 38, 1–6. https://doi.org/10.1029/2011GL047995

Earlie, C.S., Young, A.P., Masselink, G., Russell, P.E., 2015. Coastal cliff ground motions and response to extreme storm waves. Geophys. Res. Lett. 42, 847–854. https://doi.org/10.1002/2014GL062534

Elgar, S., Herbers, T.H.C., Okihiro, M., Oltman-Shay, J., Guza, R.T., 1992. Observations of infragravity waves. J. Geophys. Res. 97, 15573. https://doi.org/10.1029/92JC01316

Falqués, A., Coco, G., Huntley, D.A., 2000. A mechanism for the generation of wave-driven rhythmic patterns in the surf zone. J. Geophys. Res. Ocean. 105, 24071–24087. https://doi.org/10.1029/2000jc900100

Fiedler, J.W., Brodie, K.L., McNinch, J.E., Guza, R.T., 2015. Observations of runup and energy flux on a low-slope beach with high-energy, long-period ocean swell. Geophys. Res. Lett. 42, 9933–9941. https://doi.org/10.1002/2015GL066124

Fuller, R.M., Randall, R.E., 1988. The Orford Shingles, Suffolk, UK-Classic conflicts in coastline management. Biol. Conserv. 46, 95–114. https://doi.org/10.1016/0006-3207(88)90094-8

Gallagher, B., 1971. Generation of surf beat by non-linear wave interactions. J. Fluid Mech. 49, 1–

20. https://doi.org/10.1017/S0022112071001897

Garrote, J., Díaz-Álvarez, A., Nganhane, H., Garzón Heydt, G., 2018. The Severe 2013–14 Winter Storms in the Historical Evolution of Cantabrian (Northern Spain) Beach-Dune Systems. Geosciences 8, 459. https://doi.org/10.3390/geosciences8120459

Gomes da Silva, P., Medina, R., González, M., Garnier, R., 2018. Infragravity swash parameterization on beaches: The role of the profile shape and the morphodynamic beach state. Coast. Eng. 136, 41–55. https://doi.org/10.1016/j.coastaleng.2018.02.002

Guedes, R.M.C., Bryan, K.R., Coco, G., 2013. Observations of wave energy fluxes and swash motions on a low-sloping, dissipative beach. J. Geophys. Res. Ocean. 118, 3651–3669. https://doi.org/10.1002/jgrc.20267

Guedes, R.M.C., Bryan, K.R., Coco, G., Holman, R.A., 2011. The effects of tides on swash statistics on an intermediate beach. J. Geophys. Res. Ocean. 116, 1–13. https://doi.org/10.1029/2010JC006660

Guérin, T., de Bakker, A.T.M., Bertin, X., 2019. On the Bound Wave Phase Lag. Fluids 4, 152. https://doi.org/10.3390/fluids4030152

Guza, R.T., Thornton, E.B., 1985. Observations of surf beat. J. Geophys. Res. 90, 3161. https://doi.org/10.1029/JC090iC02p03161

Guza, R.T., Thornton, E.B., 1982. Swash oscillations on a natural beach. J. Geophys. Res. 87, 483–491. https://doi.org/10.1029/JC087iC01p00483

Haigh, I.D., Nicholls, R.J., Penning-Rowsell, E.C., Sayers, P., 2020. Impacts of climate change on coastal flooding, relevant to the coastal and marine environment around the UK. MCCIP Sci. Rev. 2020 546–565. https://doi.org/10.14465/2020.arc23.cfl

Harley, M.D., 2017. Coastal Storm Definition, in: Coastal Storms. pp. 1–21. https://doi.org/10.1002/9781118937099.ch1

Hayes, M.O., 1967. Relationship between coastal climate and bottom sediment type on the inner continental shelf. Mar. Geol. 5, 111–132. https://doi.org/10.1016/0025-3227(67)90074-6

Henderson, S.M., Bowen, A.J., 2002. Observations of surf beat forcing and dissipation. J. Geophys. Res. Ocean. 107, 3193. https://doi.org/10.1029/2000jc000498

Henderson, S.M., Guza, R.T., Elgar, S., Herbers, T.H.C., Bowen, A.J., 2006. Nonlinear generation and loss of infragravity wave energy. J. Geophys. Res. Ocean. 111. https://doi.org/10.1029/2006JC003539

Holland, K.T., Holman, R. a, Lippmann, T.C., Stanley, J., Plant, N., 1997. Practical Use of Video Imagery in Nearshore Oceanographic Field Studies - Oceanic Engineering, IEEE Journal of. IEEE J. Ocean. Eng. 22, 81–92.

Holland, K.T., Raubenheimer, B., Guza, R.T., Holman, R.A., 1995. Runup kinematics on a natural beach. J. Geophys. Res. 100, 4985–4993. https://doi.org/10.1029/94JC02664

Holman, R.A., Bowen, A.J., 1982. Bars, bumps, and holes: Models for the generation of complex beach topography. J. Geophys. Res. 87, 457. https://doi.org/10.1029/JC087iC01p00457

Hunt, I.A., 1959. Design of seawalls and breakwaters. J. Waterw. Harbours Div. ASCE 85, 123–152.

Huntley, D.A., 1976. LONG-PERIOD WAVES ON A NATURAL BEACH. J Geophys Res 81, 6441–6449. https://doi.org/10.1029/JC081i036p06441

Huntley, D.A., Bowen, A.J., 1975. Field observations of edge waves and their effect on beach material. J. Geol. Soc. London. 131, 69–81. https://doi.org/10.1144/gsjgs.131.1.0069

Inch, K., Davidson, M., Masselink, G., Russell, P., 2017. Observations of nearshore infragravity wave dynamics under high energy swell and wind-wave conditions. Cont. Shelf Res. 138, 19–31. https://doi.org/10.1016/j.csr.2017.02.010

IPCC, 2019. Summary for Policymakers. In: IPCC Special Report on the Ocean and Cryosphere in a Changing Climate.

Iribarren, C.R., Nogales, C., 1949. C.R. Iribarren, C. Nogales Protection Des Ports, XVIIth International Naval Congress, Lisbon (1949), 31–80.

Jennings, R., Shulmeister, J., 2002. A field based classification scheme for gravel beaches. Mar. Geol. 186, 211–228. https://doi.org/10.1016/S0025-3227(02)00314-6

Jouffray, J., Blasiak, R., Norström, A. V., Österblom, H., Nyström, M., 2020. The Blue Acceleration: The Trajectory of Human Expansion into the Ocean. One Earth 2, 43–54. https://doi.org/10.1016/j.oneear.2019.12.016

Komar, P.D., 1997. Beach processes and sedimentation, by Paul D. Komar. Pearson Education (US), United States.

Kularatne, S., Pattiaratchi, C., 2014. The Role of Infragravity Waves in Near-Bed Cross-Shore Sediment Flux in the Breaker Zone. J. Mar. Sci. Eng. 2, 568–592. https://doi.org/10.3390/jmse2030568

List, J.H., 1992. A model for the generation of two-dimensional surf beat 97, 5623–5635.

Longuet-Higgins, M.S., Stewart, R.W., 1962. Radiation stress and mass transport in gravity waves, with application to 'surf beats.' J. Fluid Mech. 13, 481. https://doi.org/10.1017/S0022112062000877

Luijendijk, A., Hagenaars, G., Ranasinghe, R., Baart, F., Donchyts, G., Aarninkhof, S., 2018. The State of the World's Beaches. Sci. Rep. 8, 1–11. https://doi.org/10.1038/s41598-018-24630-6

Lyddon, C.E., Brown, J.M., Leonardi, N., Saulter, A., Plater, A.J., 2019. Quantification of the Uncertainty in Coastal Storm Hazard Predictions Due to Wave-Current Interaction and Wind Forcing. Geophys. Res. Lett. 46, 14576–14585. https://doi.org/10.1029/2019GL086123

Macclenahan, P., Mckenna, J., 2001. IDENTIFICATION OF HIGHEST MAGNITUDE

    COASTAL STORM EVENTS OVER WESTERN IRELAND ON THE BASIS OF WIND

    SPEED 842, 829–842.

Martinez-Alvarado, O., Gray, S.L., Hart, N.C.G., Clark, P.A., Hodges, K., Roberts, M.J., 2018.

    Increased wind risk from sting-jet windstorms with climate change. Environ. Res. Lett. 13.

    https://doi.org/10.1088/1748-9326/aaae3a

Mason, T., Bradbury, A., Poate, T., Newman, R., 2009. NEARSHORE WAVE CLIMATE OF

    THE ENGLISH CHANNEL – EVIDENCE FOR BI-MODAL SEAS, in: Coastal Engineering

    2008. World Scientific Publishing Company, pp. 605–616.

    https://doi.org/10.1142/9789814277426_0051

Masselink, G., 1995. Group bound long waves as a source of infragravity energy in the surf zone.

    Cont. Shelf Res. 15, 1525–1547. https://doi.org/10.1016/0278-4343(95)00037-2

Masselink, G., Austin, M., Scott, T., Poate, T., Russell, P., 2014. Role of wave forcing, storms and

    NAO in outer bar dynamics on a high-energy, macro-tidal beach. Geomorphology 226, 76–93.

    https://doi.org/10.1016/j.geomorph.2014.07.025

Masselink, G., Austin, M., Tinker, J., O'Hare, T., Russell, P., 2008. Cross-shore sediment transport

    and morphological response on a macrotidal beach with intertidal bar morphology, Truc Vert,

    France. Mar. Geol. 251, 141–155. https://doi.org/10.1016/j.margeo.2008.01.010

Masselink, G., Castelle, B., Scott, T., Dodet, G., Suanez, S., Jackson, D., Floc, F., 2016. Extreme

    wave activity during 2013/2014 winter and morphological impacts along the Atlantic coast of

    Europe 2135–2143. https://doi.org/10.1002/2015GL067492.Received

Masselink, G., Puleo, J.A., 2006. Swash-zone morphodynamics. Cont. Shelf Res.

    https://doi.org/10.1016/j.csr.2006.01.015

Masselink, G., Russell, P., Blenkinsopp, C., Turner, I., 2010. Swash zone sediment transport, step

dynamics and morphological response on a gravel beach. Mar. Geol. 274, 50–68. https://doi.org/10.1016/j.margeo.2010.03.005

Masselink, G., Tuck, M., McCall, R., van Dongeren, A., Ford, M., Kench, P., 2019. Physical and Numerical Modeling of Infragravity Wave Generation and Transformation on Coral Reef Platforms. J. Geophys. Res. Ocean. 124, 1410–1433. https://doi.org/10.1029/2018JC014411

McCall, R.T., Masselink, G., Poate, T.G., Roelvink, J.A., Almeida, L.P., 2015. Modelling the morphodynamics of gravel beaches during storms with XBeach-G. Coast. Eng. 103, 52–66. https://doi.org/10.1016/j.coastaleng.2015.06.002

McCarroll, R.J., Masselink, G., Wiggins, M., Scott, T., Billson, O., Conley, D.C., Valiente, N.G., 2019. High-efficiency gravel longshore sediment transport and headland bypassing over an extreme wave event. Earth Surf. Process. Landforms esp.4692. https://doi.org/10.1002/esp.4692

Meucci, A., Young, I.R., Hemer, M., Kirezci, E., Ranasinghe, R., 2020. Projected 21st century changes in extreme wind-wave events. Sci. Adv. 6, eaaz7295. https://doi.org/10.1126/sciadv.aaz7295

Mölter, T., Schindler, D., Albrecht, A.T., Kohnle, U., 2016. Review on the projections of future storminess over the North Atlantic European region. Atmosphere (Basel). 7, 1–40. https://doi.org/10.3390/atmos7040060

Munk, W.H., 1949. Surf Beats. Eos Trans. AGU 30, 849–854.

Nicolae Lerma, A., Bulteau, T., Lecacheux, S., Idier, D., 2015. Spatial variability of extreme wave height along the Atlantic and channel French coast. Ocean Eng. 97, 175–185. https://doi.org/10.1016/j.oceaneng.2015.01.015

Orford, J.D., Forbes, D.L., Jennings, S.C., 2002. Organisational controls, typologies and time scales of paraglacial gravel-dominated coastal systems. Geomorphology 48, 51–85.

https://doi.org/10.1016/S0169-555X(02)00175-7

Osborne, P.D., Greenwood, B., 1992. Frequency dependent cross-shore suspended sediment
transport. 2. A barred shoreface. Mar. Geol. 106, 25–51. https://doi.org/10.1016/0025-
3227(92)90053-K

Passarella, M., Goldstein, E.B., De Muro, S., Coco, G., 2018. The use of genetic programming to
develop a predictor of swash excursion on sandy beaches. Nat. Hazards Earth Syst. Sci. 18,
599–611. https://doi.org/10.5194/nhess-18-599-2018

Péquignet, A.C.N., Becker, J.M., Merrifield, M.A., Aucan, J., 2009. Forcing of resonant modes on
a fringing reef during tropical storm Man-Yi. Geophys. Res. Lett. 36, 20–23.
https://doi.org/10.1029/2008GL036259

Pinto, J.G., Gómara, I., Masato, G., Dacre, H.F., Woollings, T., Caballero, R., 2014. Large-scale
dynamics associated with clustering of extratropical cyclones affecting Western Europe. J.
Geophys. Res. Atmos. 119, 704–719. https://doi.org/10.1002/2014JD022305.Received

Poate, T., Masselink, G., Austin, M.J., Inch, K., Dickson, M., Mccall, R., 2020. Geomorphology
Infragravity wave generation on shore platforms : Bound long wave versus breakpoint forcing.
Geomorphology 350, 106880. https://doi.org/10.1016/j.geomorph.2019.106880

Poate, T.G., McCall, R.T., Masselink, G., 2016. A new parameterisation for runup on gravel
beaches. Coast. Eng. 117, 176–190. https://doi.org/10.1016/j.coastaleng.2016.08.003

Pomeroy, A., Lowe, R., Symonds, G., Van Dongeren, A., Moore, C., 2012. The dynamics of
infragravity wave transformation over a fringing reef. J. Geophys. Res. Ocean. 117, 1–17.
https://doi.org/10.1029/2012JC008310

Puleo, J. a., Blenkinsopp, C., Conley, D.C., Masselink, G., Turner, I.L., Russell, P., Buscombe, D.,
Howe, D., Lanckriet, T., McCall, R., Poate, T., 2014. Comprehensive Field Study of Swash-
Zone Processes. I: Experimental Design with Examples of Hydrodynamic and Sediment

Transport Measurements. J. Waterw. Port, Coastal, Ocean Eng. 140, 14–28. https://doi.org/10.1061/(ASCE)WW.1943-5460.0000210.

Ranwell, D.S., Davies, J.L., 1973. Geographical Variation in Coastal Development (Geomorphological Texts Series). J. Ecol. 61, 928. https://doi.org/10.2307/2258660

Reguero, B.G., Losada, I.J., Méndez, F.J., 2019. A recent increase in global wave power as a consequence of oceanic warming. Nat. Commun. 10. https://doi.org/10.1038/s41467-018-08066-0

Reniers, A.J.H.M., van Dongeren, A.R., Battjes, J.A., Thornton, E.B., 2002. Linear modeling of infragravity waves during Delilah. J. Geophys. Res. C Ocean. 107, 1–1. https://doi.org/10.1029/2001jc001083

Roelvink, D., Reniers, A., van Dongeren, A., van Thiel de Vries, J., McCall, R., Lescinski, J., 2009. Modelling storm impacts on beaches, dunes and barrier islands. Coast. Eng. 56, 1133–1152. https://doi.org/10.1016/j.coastaleng.2009.08.006

Roelvink, J.A., Stive, M.J.F., 1989. Bar-generating cross-shore flow mechanisms on a beach. J. Geophys. Res. 94, 4785. https://doi.org/10.1029/JC094iC04p04785

Ruessink, B.G., 1998. Bound and free infragravity waves in the nearshore zone under breaking and nonbreaking conditions. J. Geophys. Res. Ocean. 103, 12795–12805. https://doi.org/10.1029/98jc00893

Ruessink, B.G., Houwman, K.., Hoekstra, P., 1998a. The systematic contribution of transporting mechanisms to the cross-shore sediment transport in water depths of 3 to 9 m. Mar. Geol. 152, 295–324. https://doi.org/10.1016/S0025-3227(98)00133-9

Ruessink, B.G., Kleinhans, M.G., van den Beukel, P.G.L., 1998b. Observations of swash under highly dissipative conditions. J. Geophys. Res. 103, 3111. https://doi.org/10.1029/97JC02791

Ruggiero, P., Holman, R.A., Beach, R.A., 2004. Wave run-up on a high-energy dissipative beach.

J. Geophys. Res. C Ocean. 109. https://doi.org/10.1029/2003JC002160

Ruiz De Alegria-Arzaburu, A., Masselink, G., 2010. Storm response and beach rotation on a gravel beach, Slapton Sands, U.K. https://doi.org/10.1016/j.margeo.2010.09.004

Ruosteenoja, K., Vihma, T., Venäläinen, A., 2019. Projected changes in european and north atlantic seasonal wind climate derived from CMIP5 simulations. J. Clim. 32, 6467–6490. https://doi.org/10.1175/JCLI-D-19-0023.1

Russell, P.E., 1993. Mechanisms for beach erosion during storms. Cont. Shelf Res. 13, 1243–1265. https://doi.org/10.1016/0278-4343(93)90051-X

Scott, T., Masselink, G., Russell, P., 2011. Morphodynamic characteristics and classification of beaches in England and Wales. Mar. Geol. 286, 1–20. https://doi.org/10.1016/j.margeo.2011.04.004

Senechal, N., Abadie, S., Gallagher, E., MacMahan, J., Masselink, G., Michallet, H., Reniers, A., Ruessink, G., Russell, P., Sous, D., Turner, I., Ardhuin, F., Bonneton, P., Bujan, S., Capo, S., Certain, R., Pedreros, R., Garlan, T., 2011a. The ECORS-Truc Vert'08 nearshore field experiment: presentation of a three-dimensional morphologic system in a macro-tidal environment during consecutive extreme storm conditions. Ocean Dyn. 61, 2073–2098. https://doi.org/10.1007/s10236-011-0472-x

Senechal, N., Castelle, B., R. Bryan, K., 2017. Storm Clustering and Beach Response, in: Coastal Storms. John Wiley & Sons, Ltd, pp. 151–174. https://doi.org/10.1002/9781118937099.ch8

Senechal, N., Coco, G., Bryan, K.R., Holman, R.A., 2011b. Wave runup during extreme storm conditions. J. Geophys. Res. Ocean. 116, 1–13. https://doi.org/10.1029/2010JC006819

Shibayama, T., Okayasu, A., Kashiwagi, M., 1993. Long period wave and suspended sand transport in the surf zone, in: Proceedings of the Coastal Engineering Conference. pp. 2438–2449. https://doi.org/10.1061/9780872629332.186

Splinter, K.D., Turner, I.L., Davidson, M.A., Barnard, P., Castelle, B., Oltman-shay, J., 2014. A generalized equilibrium model for predicting daily to interannual shoreline response. J. Geophys. Res. Earth Surf. 1–23. https://doi.org/10.1002/2014JF003106.Received

Stive, M.J.F., Aarninkhof, S.G.J., Hamm, L., Hanson, H., Larson, M., Wijnberg, K.M., Nicholls, R.J., Capobianco, M., 2002. Variability of shore and shoreline evolution. Coast. Eng. 47, 211–235. https://doi.org/10.1016/S0378-3839(02)00126-6

Stockdon, H.F., Holman, R.A., Howd, P.A., Sallenger, A.H., 2006. Empirical parameterization of setup, swash, and runup. Coast. Eng. 53, 573–588. https://doi.org/10.1016/j.coastaleng.2005.12.005

Stokes, C., Davidson, M., Russell, P., 2015. Observation and prediction of three-dimensional morphology at a high-energy macrotidal beach. Geomorphology 243, 1–13. https://doi.org/10.1016/j.geomorph.2015.04.024

Symonds, G., Huntley, D.A., Bowen, A.J., 1982. Two-dimensional surf beat: Long wave generation by a time-varying breakpoint. J. Geophys. Res. 87, 492. https://doi.org/10.1029/JC087iC01p00492

Tucker, M.J., 1950. Surf beats: sea waves of 1 to 5 min. period. Proc. R. Soc. London. Ser. A. Math. Phys. Sci. 202, 565 LP – 573.

U.K. Met Office, 2018. Snow and low temperatures February to March 2018 - Met Office https://ww, 2019-01–20.

Valiente, N.G., McCarroll, R.J., Masselink, G., Scott, T., Wiggins, M., 2019. Multi-annual embayment sediment dynamics involving headland bypassing and sediment exchange across the depth of closure. Geomorphology 343, 48–64. https://doi.org/10.1016/j.geomorph.2019.06.020

van Dongeren, A., Battjes, J., Janssen, T., van Noorloos, J., Steenhauer, K., Steenbergen, G.,

Reniers, A., 2007. Shoaling and shoreline dissipation of low-frequency waves. J. Geophys. Res. Ocean. 112, 1–15. https://doi.org/10.1029/2006JC003701

Vos, K., Harley, M.D., Splinter, K.D., Simmons, J.A., Turner, I.L., 2019. Sub-annual to multi-decadal shoreline variability from publicly available satellite imagery. Coast. Eng. 150, 160–174. https://doi.org/10.1016/j.coastaleng.2019.04.004

Vos, K., Harley, M.D., Splinter, K.D., Walker, A., Turner, I.L., 2020. Beach Slopes From Satellite-Derived Shorelines. Geophys. Res. Lett. 47, e2020GL088365. https://doi.org/10.1029/2020GL088365

Vousdoukas, M.I., Mentaschi, L., Voukouvalas, E., Verlaan, M., Jevrejeva, S., Jackson, L.P., Feyen, L., 2018. Global probabilistic projections of extreme sea levels show intensification of coastal flood hazard. Nat. Commun. 9, 1–12. https://doi.org/10.1038/s41467-018-04692-w

Wang, X.L., Feng, Y., Swail, V.R., 2012. North atlantic wave height trends as reconstructed from the 20th century reanalysis. Geophys. Res. Lett. 39, 1–6. https://doi.org/10.1029/2012GL053381

Werner, B.T., Fink, T.M., 1993. Beach cusps as self-organized patterns. Science (80-.). 260, 968–971. https://doi.org/10.1126/science.260.5110.968

Wiggins, M., Scott, T., Masselink, G., Russell, P., McCarroll, R.J., 2019. Coastal embayment rotation: Response to extreme events and climate control, using full embayment surveys. Geomorphology 327, 385–403. https://doi.org/10.1016/J.GEOMORPH.2018.11.014

Wolf, J., Woolf, D., Bricheno, L., 2020. Impacts of climate change on storms and waves relevant to the coastal and marine environment around the UK. Mar. Clim. Chang. Impacts Partnersh. Sci. Rev. 2020, 456–481. https://doi.org/10.14465/2020.arc07.saw

XBeach, 2020. User manual — XBeach Revision 51bb68d9 https://xb, 2021-01–23.

Young, I.R., Ribal, A., 2019. Multiplatform evaluation of global trends in wind speed and wave

height. Science (80-.). 364, 548–552. https://doi.org/10.1126/science.aav9527

Young, I.R., Zieger, S., Babanin, A. V., 2011. Global Trends in Wind Speed and Wave Height.
Science (80-.). 332, 451–455. https://doi.org/10.1126/science.1197219

Zijlema, M., Stelling, G., Smit, P., 2011. SWASH: An operational public domain code for
simulating wave fields and rapidly varied flows in coastal waters. Coast. Eng. 58, 992–1012.
https://doi.org/10.1016/j.coastaleng.2011.05.015

Appendix A – Field work log

	Date	Site	Type	Days	Comment
Field work log					
	18/08/2016	Perran	Topo	1	First experience, saw Bathy set up (cancelled due to fog). Walked topo lines in front of Perran sands BLU with NG
	10/10/2016	Perran	GCP Deplyment Quadcopter	1	First experience of Quad copter survey, deployed GCPs for 3 flights from Perranporth Dunes to Penhale corner, top line of the dunes
	03/11/2016	Perran	GCP Deplyment Quadcopter	1	First experience of UAV fixed wing. GCP deployed over bottom line of dunes from Perran sands BLU to Penhale corner. Rain curtailed flights after 1 test flight
	10/11/2016	Start Bay	Bathy	1	First experience of Start Bay and CODY launch and recovery. Helped to set up base at Blackpool Sands and then moved around with repeater to assist in Bathy Survey of South Start Bay
	18 - 23/11/2016	Camber	Storm Survey	5	See main thesis
	28-30/11	Ventnor	Drifter deployment	2	Assisted CMAR (KS and TP) in a drifter experiment at Ventnor harbour IoW, examining potential mechanisms for seaweed becoming trapped in the harbour. Met Dave Brew from Royal Haskoning and discussed environmental consultancy
	15/12/2016	Penhale	Set up new base	1	Set up new base at Northern end of Perranporth. Went with NG and OPB. Surveyed sediment traps lines and checked weather station for GM.
	16/12/2016	Penhale	Collected Key	1	Met Andy Hewitt (Land Mark) to gain access via MOD entrance to Penhale dunes. Also accessed beach at high tide to assess how high close to the dunes the shoreline would be on such a large swell. Observed waves at lower tide at Perran and Cribbar
	23/01 - 08/02/2017	Penhale	Storm Survey	14	See main thesis
	15/03/2017	Slapton	Bathy	1	Bathy Survey of Start Bay
	28/03/2017	Downderry	Demonstrating	1	Student field trip
	15/05/2017	Perran	Topo and weather station	1	Monthly survey
	01/12/2017	STB Winter Deployment Prep	Scoping	1	Find suitable locations for long term PT deployment
	10/12/2017	STB Winter Deployment Prep	Deploying PTs	1	Fixing PTs for long term deployment (contributing to McCarrol et al. (2019))
	02 - 10/01/2018	Minesmere	Storm Survey	7	See main thesis
	18/01/2018	STB Winter Deployment Prep		1	Maintaining PTs for long term deployment (contributing to McCarrol et al. (2019))

31/01/2018	STB Winter Deployment Prep		1	Maintaining PTs for long term deployment (contributing to McCarrol et al. (2019))
15/02 - 05/03/2018	STB Storm deployment	Storm Survey	21	See main thesis
28/03/2017	Downderry	Demonstrating	1	Student field trip
01/04/2018	Sediment analysis	Analysis and demonstrating	2	Took over the monthly sediment sample analysis from Sam Prodger. This involves settling samples from low, mid and high tide to obtain sediment statistics. This was passed onto an Msci student during 04/18 under mine and Paul's supervision
03/04/2018	STB	Topo	1	Standard monthly topo at Slapton
09/05/2018	STB	SBE	1	Standard SBE at STB and priority lines
15/05/2018	STB	Topo	1	Standard monthly topo at Slapton
18/05/2018	STB	UAV	1	Standard UAV at Slapton
13/06/2018	PPT	Topo	1	Standard monthly topo at PPT
14/06/2018	STB	Topo	1	Standard monthly topo at Slapton PCO were at Blackpool that day
13/08/2018	PPT	Topo	1	Standard monthly topo at PPT
14/08/2018	STB	Topo	1	Standard monthly topo at Slapton Will Russell joined
12/09/2018	STB	Topo	1	Standard monthly topo at Slapton
25/09/2018	PPT	SBE	1	Standard SBE at PPT
03/10/2018	STB	SBE	1	Standard SBE at STB
11/10/2018	PPT	Topo	1	Standard monthly topo at PPT
04 - 05/12/2018	North Devon Biosphere	PT Deployment	2	Deploying PTs in Tor/Torridge estuaries for SWEEP 'North Devon Biosphere' project.
22/04/2019	PPT	Topo	1	Standard monthly topo at PPT
23/04/2019	STB	Topo	1	Standard monthly topo at Slapton
17/05/2019	PPT	Topo	1	UAV and Monthly Topo
16 - 17 /06/2019	Chapel Porth/ Porth Towan/Holywell	Depth to bed rock (Trimino)	1	Depth to bedrock experiment for North Cornish Coast
18/06/2019	STB	Topo	1	Standard monthly topo at Slapton
21/06/2019	St Agnes	Depth to bed rock (Trimino)	1	Depth to bedrock
19/07/2019	PPT	Topo	1	Standard monthly topo at PPT
02/09/2019	PPT	Topo	1	Standard monthly topo at PPT
03 - 05/10/2019	Crantock	Lorenzo Storm Survey	3	Storm Survey attempting to capture dune erosion
		Days in field	90	

Appendix B – Survey Kit List

Video Logging				
Equipment	**Quantity**	**Location**	**Status**	**Last check or comment**
Computer with StreamPix	1	Ali Box1 (Brunel WR1)		
Desktop power supply cable	1	Brunel WR1		
Desktop Monitor (Philips)	1			
Desktop keyboard	1			
Desktop mouse	1			
USB GPS receiver	2			
Video camera lens*	1			
Point Grey Video camera	2			
Video camera housing + bolts	2			
Cleaning cloth and brush	1			
Gopro + USB power supply + MicroSD	1			
Camera POE GigE cable 100m	2	Brunel WR1		
UPS	1	Ali Box 2 (Brunel WR1)		
Extension cable	2			
Power bars	2			
* Set of lens available: 12mm L1; 12 mm L2; 8 mm L3; 8 mm L4; 25 mm L1.				

Video Tower				
Equipment	**Quantity**	**Location**	**Status**	**Last check or comment**
Aluminium tower sections	5	Trailer		
Scaffold: 8ft Pointed	9			
Aluminium plate (tower base)	2			
Scaffold H frame	2			
Scaffold Claps	20+			
Tower bolts		Brunel W15 (small Green Box)		
U bolts for the tower base				
U bolts nuts for the tower base				
U bolts washers for the tower base				
Guys ropes				
Tonker	1	Brunel W15		
Spirit level	1	Brunel W15		

Solo Pressure Transducers				
Equipment	**Quantity**	**Location**	**Status**	**Last check or comment**
RBR Solo- Dwave	15	Dedicated Box		
RBR Solo- Dwave Mount	15	Black Peli W15		
RBR Solo- Dwave Mount bolt	15	Black Peli W15		
RBR Solo Batteries	~	W1		
Jubilee clamps (70-90 mm)				
Long Sand screws	6	Trailer		Order 6 more

Short Sand screws	6			<mark>There are >15 in total</mark>
Pellet Buoys for sand screws	18			

Vectors				
Equipment	**Quantity**	**Location**	**Status**	**Last check or comment**
Vector Logger + Battery	3	W1R		
Communication cable + USB RS232 converter + vector power supply unit (PSU)	1	W1R		Preferable to have 2
Alan keys (7/32 and 3/16)	1	W1R		
Vector Analog cable + PT + OBS	2	W1R		
Vector Battery cable	2	W1R		
Silicon spray (for the connectors)	1	W1R		
Silicon tube (for the o-rings)	1	W1R		
<mark>Jubilee clamps (110-140 mm)</mark>	<mark>12</mark>	<mark>W1R</mark>		?
Rubber roll	12	Plastic box (Brunel WR1)		
Notepad Laptop	1	W1		Preferable to have 2

GPS Survey kit				
Equipment	Quantity (min)	Location	Status	Last check or comment
Trimble GPS Base	1	Brunel WR1		
Trimble GPS Rover	2			
Receiver battery	4			
Receiver battery charger	1			
Base battery charger	1			
Tripod	1			
GPS staff	2			
GPS staff plastic base	1			
Walkie talkies + chargers	2			

ATV Survey kit				
Equipment	Quantity	Location	Status	Last check or comment
ATV	1	Brunel W8		
Gloves + Helmet	2	(black box) Brunel w8		
Jerrycan (with unleaded petrol)	1	trailer		
ATV oil	1	Brunel		
Funnel	2	Brunel		
Black box	1	Brunel W8		

Scaffold and frames

Equipment	Quantity	Location	Status	Last check or comment
Scaffold for Video tower	4 Verticals			12 8ft for rigs 4 8ft for tower 6 6ft for horizontals on rig + 3 6ft guys for the tower
Video tower guy Lines	3 <3ft			
Scaffold for Pressure transducers	5 verticals			Not for Perran
Scaffold for H frame – Verticals	12 Spiked 8ft verticals	Trailer		8ft
Scaffold for H frame – Cross bar	6 x 5-6ft, non spiked			Aluminium or scaffold
Stainless down bar including white plastic skirt	2			Taken from stainless triangle frame box
Scaffold Clamps (fixed and rotational)	1 box of each			All lubricated, preferably cast clamps

Toolbox

Equipment	Quantity	Location	Status	Last check or comment
Spanners (number: 13, 15, 19, 21 and adjustable)	1	Toolbox		
Screw drivers (flat head and philips)	1	Toolbox		
Allen keys set	1	Toolbox		
Cordless drill	1			

Safety Equipment

Equipment	Quantity	Location	Status	Last check or comment
Working suites				
Waterproof suites				
Neoprene Wellies				
First aid bag	1			
Working gloves				
Protective headphones				

Met Station

~~Equipment~~	~~Quantity~~	~~Location~~	~~Status~~	~~Last check or comment~~
~~Met Station Sensor~~	~~1~~	~~Black Peli Case (W1)~~		
~~Sensor mounting pole~~	~~1~~	~~Black Peli Case (W1)~~		
~~Batteries (Same as TWR 2050)~~	~~1~~	~~Black Peli Case (W1)~~		

Trailer + Other

Equipment	Quantity	Location	Status	Last check or comment
Door Locks and keys	1	Peter		
Portable table	1	Trailer		
Generator	1	W15		
Generator Box	1	W15		

Utilities				
Equipment	**Quantity**	**Location**	**Status**	**Last check or comment**
Trailer Light				
Head torch				
Cable ties				
Black tape				
WD40 spray				
Silicon lube				
Silicon Oil	1			Required for vector
AAA battery (duracell)				
AA battery (duracell)				
Permanent pens				
Sediment Sample bags				
Backup Hardrives	2	Tims Office		

Appendix C – Preparing an RBR Solo DWave pressure transducer for deployment

RBR Solo DWave – Pressure transducer (PT).

Storage

- 20 x PTs stored in Peli case. Each PT numbered and stored in corresponding numbered hole.
- All servicing kit and other equipment required to deploy/download and maintain PTs can be found in zip pockets in the lid of the Peli case.

Servicing

- Before deployment the PTs should be removed from their yellow housing by unscrewing the yellow case from the blue top. Inside should be inspected to check:
  - o Battery (only replace shortly before deployment to avoid power down while not in use.)
  - o Desiccant (if not bright blue, replace.)
  - o D – ring (If **ANY** grit/hair/dirt is on the ring, the casing will not seal, and the sensor will be water damaged! Gently wipe away any dirt and apply a very small amount of silicone compound using the brush provided.)

Programming

- Open Ruskin software.

- Once software has loaded and yellow casing is removed, connect the PT to a laptop via mini usb lead. The following screen should appear. Note that the sensor serial number, battery and firm ware can been seen under 'logger details'. The warning triangle next to calibration can be ignored, PTs were calibrated in October 2017 by Oli Billson and Peter Ganderton.
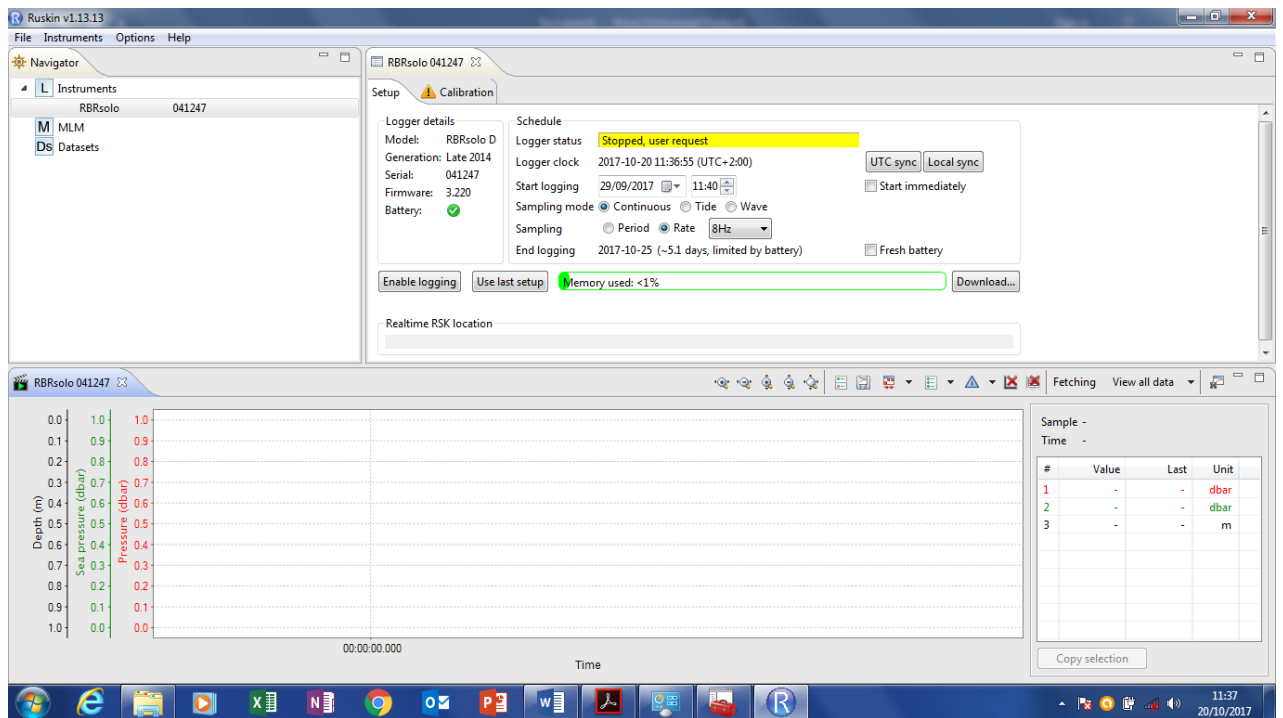
- Before the PTs can be programmed, the PC time must be set to GPS time as the PC clock will not be correct! Set the clock and then click 'local sync' to match the PT's clock to the PC's. GPS time can be checked using a mobile phone. Also note, PTs should only be programmed from 1 PC to ensure the time is uniform across the sensors.
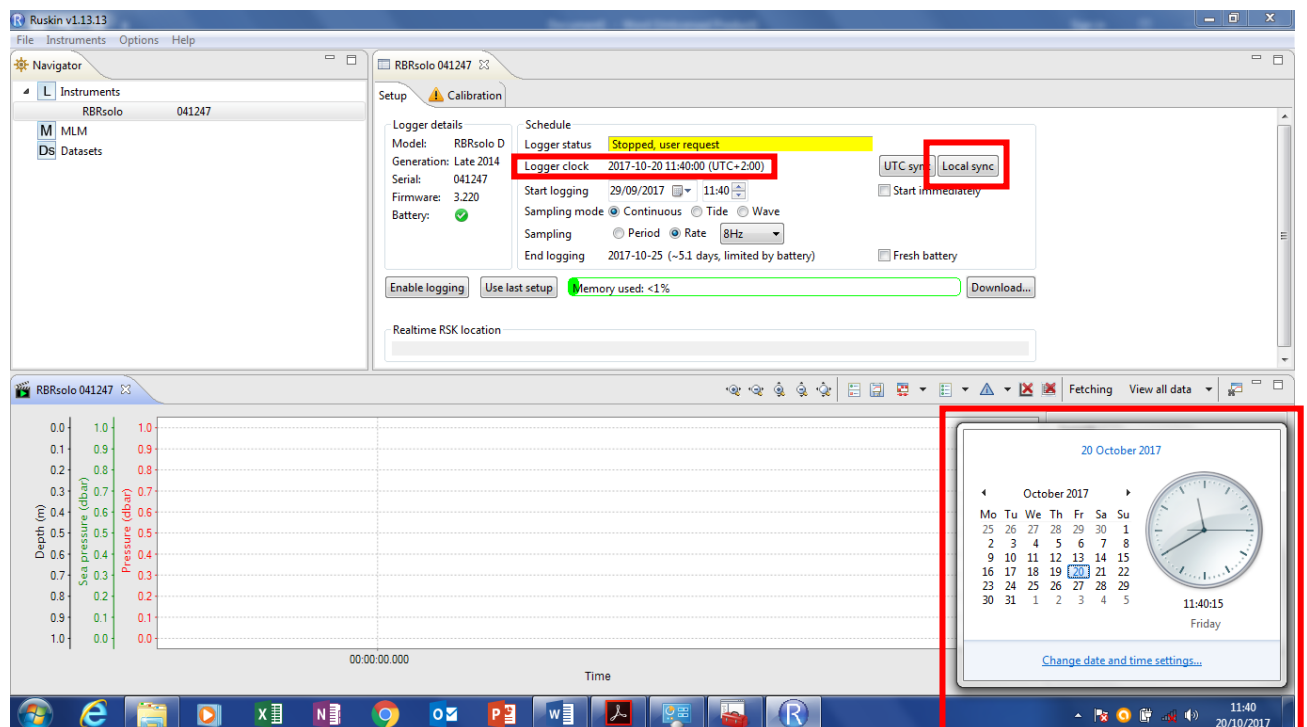
- Ensure the 'start immediately' radio button is unchecked, and us the dropdown calendar to set the desired start date and time for the deployment.
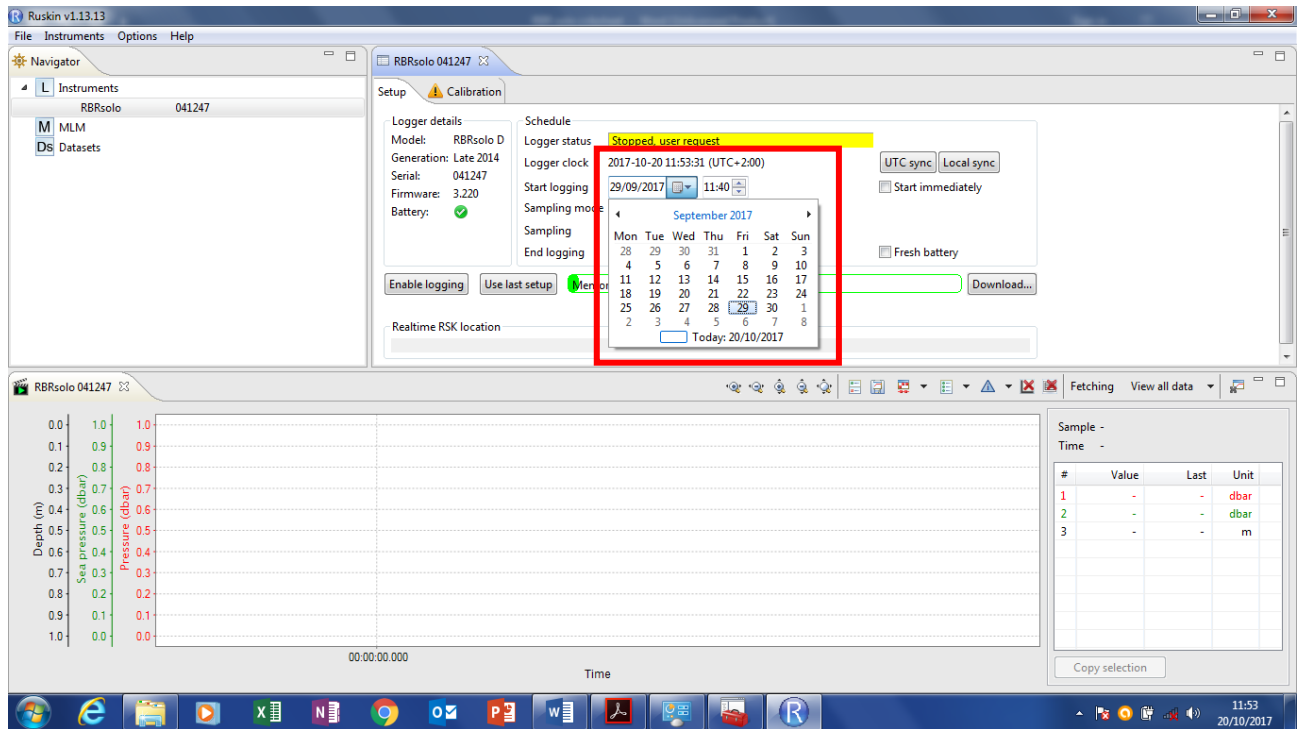
- Set the sampling mode to 'continuous' and select a 'rate' from the drop down (usually 8Hz).
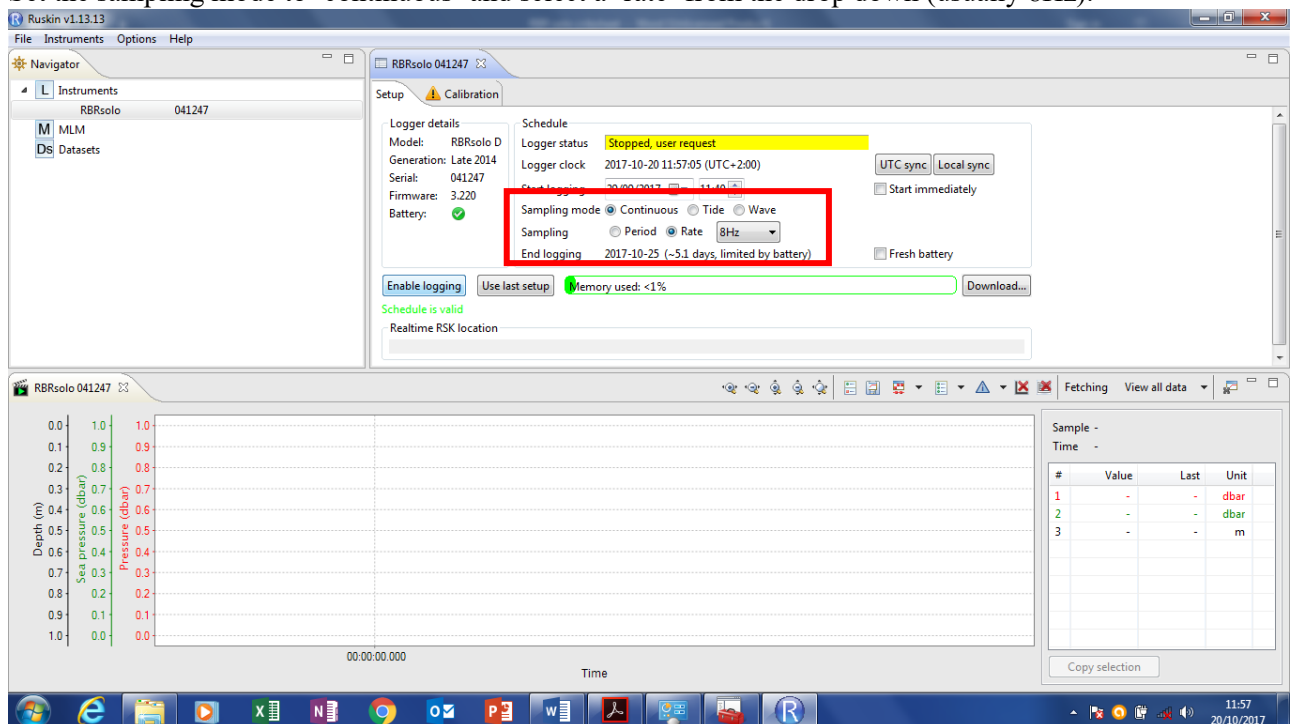
- Click 'enable logging', a warning window may pop up, click 'erase and enable logging.' The sensor is now programmed, and the logger status should read 'Schedule enabled' in light blue. The sensor can be disconnected and prepared for deployment.
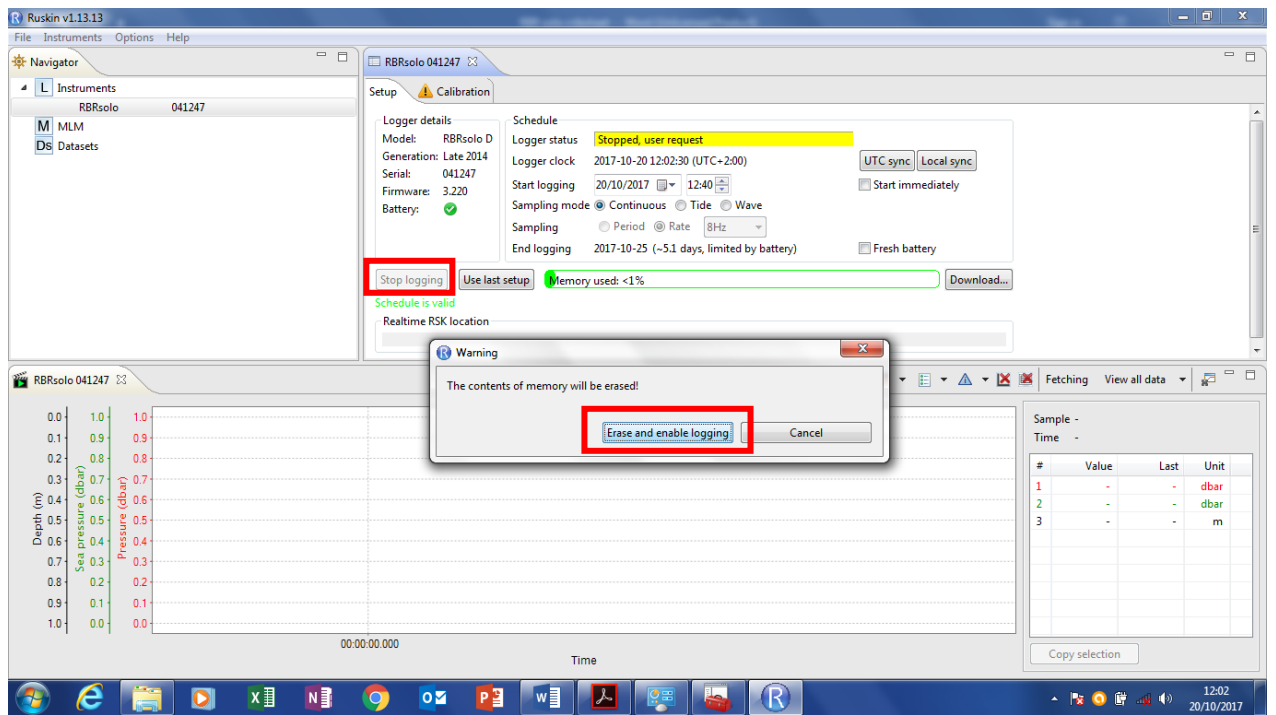
Downloading

-   Open RSK, remove yellow casing and connect the sensor to the PC via mini usb. The logger status will likely be 'logging in progress' in green. Click 'Stop logging'. The logger status will change to 'stopped, user request' in yellow. Click 'Download'.
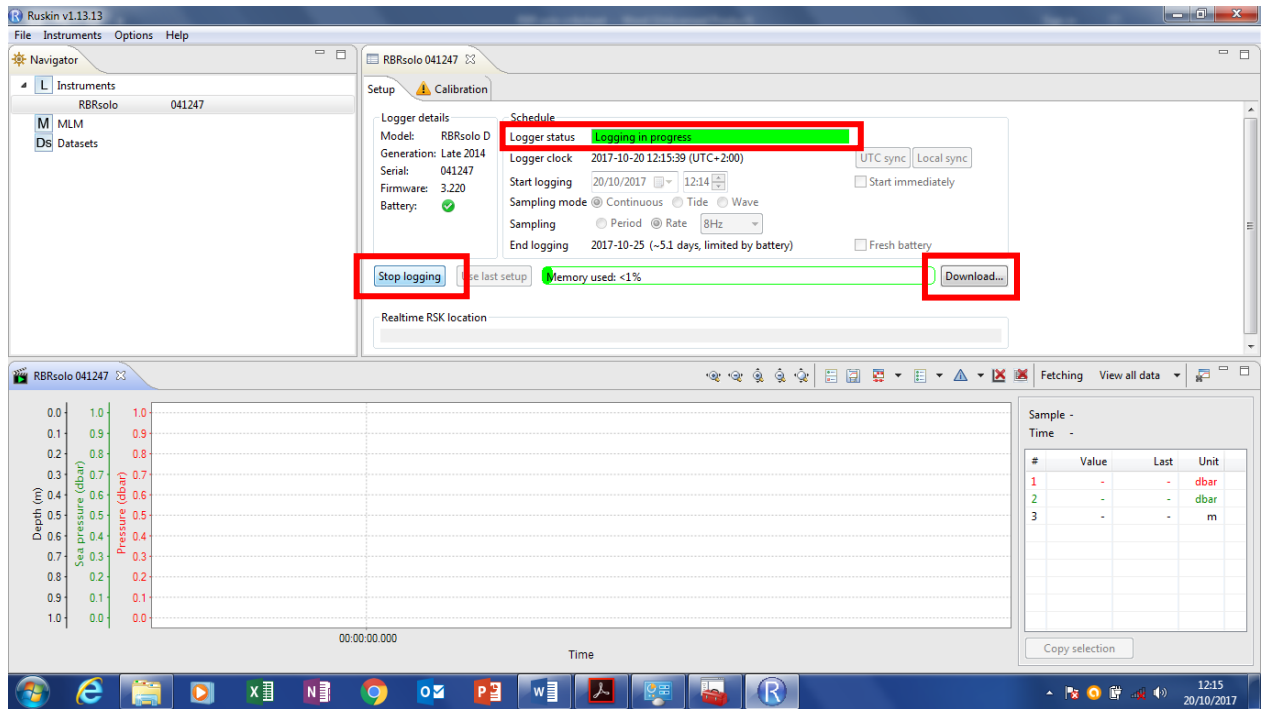
- A 'Save as RSK' window will pop up. Set the folder you wish to save the file to. The file name will default to 'Serialnumber_YYYMMDD' i.e., '041247_20171020_1219'. It is a good idea to add the sensor number onto the end of the filename, i.e, '041247_20171020_1219_PT11.' Click Save.
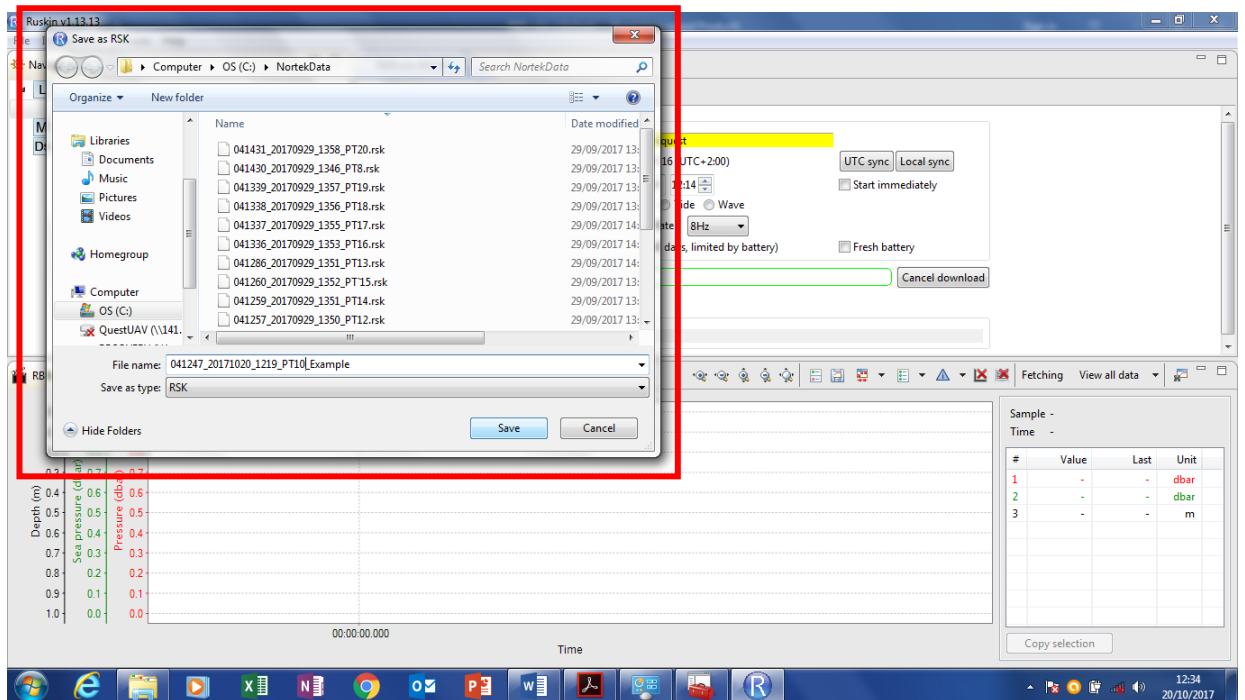
- The data will be displayed as preview.

Appendix D - Storm survey plan (Camber)

About

This document is a short overview of the three sites targeted for storm surveys this winter as part of BLUE coast. To help inform our site visits on the 26th and 27th of September it would be good to get some feedback on possible scenarios with regard to instrument locations/data collection etc.

Post visits we shall put together a detailed plan for each site to ensure the storm events are captured as required.

Instrumentation

- **14 self-logging RBR Solo pressure sensors**; Can log at 8Hz for duration of storm. Housed in a scaffold tube they can be fixed to a structure or embeddedinto sand/gravel using scaffold/sand screws.
- **Video cameras**; two cameras logging at 4Hz during daylight. Require powerand dry space for computers (usually our trailer) within 100m of cameras. Mounted on 5 m tower looking alongshore.
- **ADV**; three available to measure the nearshore current direction and strength. **Usually mounted on a triangular rig than can be carried into place or a scaffold "H" frame if required**
- **Scanning LiDAR**; single beam LiDAR proving profile measurements of morphological response on a wave by wave basis. Mounted on a 5 m tower.
- **RTK GPS**; On foot or via ATV for profile/baseline work where permissible.

Survey Logistics

The table below gives a rough idea of the timeline for these surveys with 5-6 days on site expected- storm depending.

Days to storm peak	Activity
-7	Storm tracking
-4	Go/no go decision
-3	Drive to site
-2	Instruments deployed and surveys
-1	Low tide surveys
0	**Storm Peak**
+1	Low tide surveys
+2	Low tide surveys
+3	Leave Site

Site: Dungeness

Tide conversion: -4.1 CD-ODN

MHWS	3.7
MHWN	1.8
MSL	0
MLWN	-1.6
MLWS	-3.2

Site Overview;

Figure 1, GE aerial overview of Dungeness. Numbered boxes refer to possible survey site/instrument deployment locations

The four areas in Figure 1 reflect possible access points/areas of interest (Powerstation). West of the power station no regional monitoring takes place and access is likely to be difficult (important for camera positions).
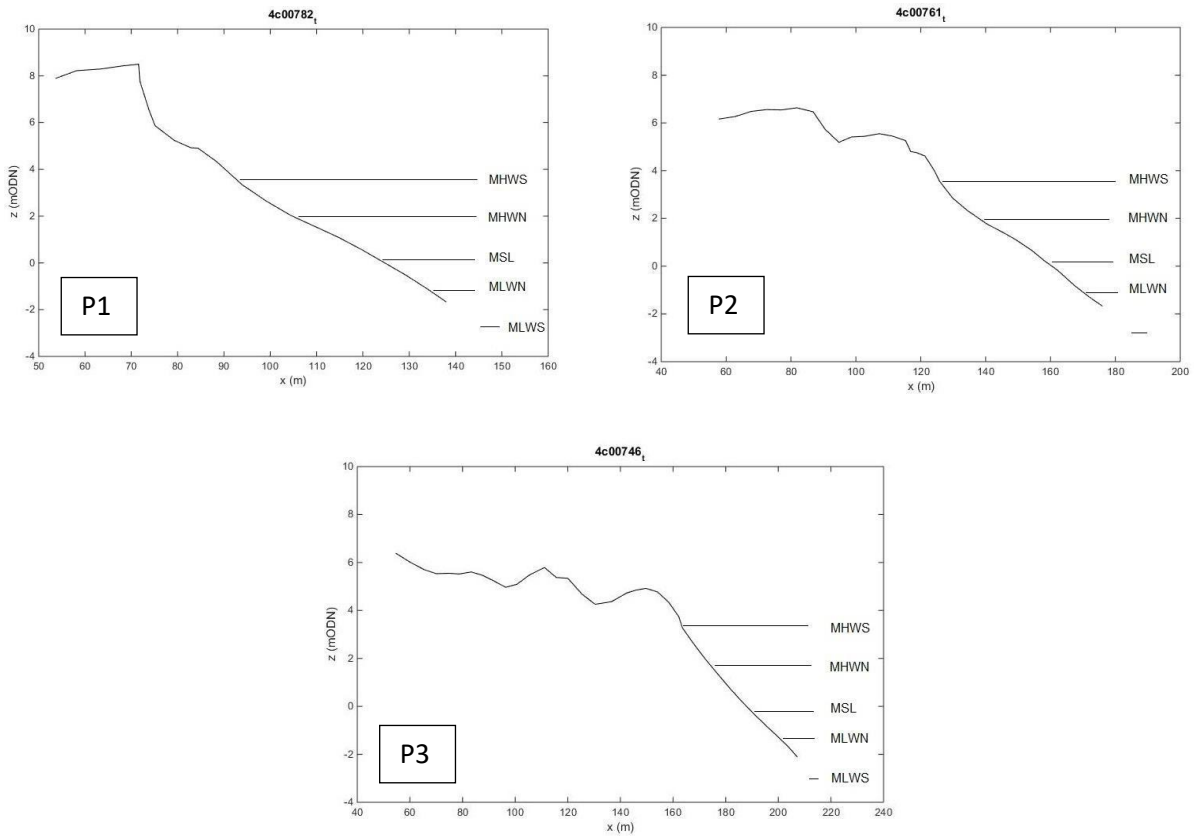
Figure 2, Aerial Image of Sites B, C and D with representative profiles at each location. Profiles via CCO, none extend to MLWS. There are no measured profiles at Site A.

The profiles steepen to the East. Beyond P3 a very wide low tide sand flat is evident in the aerial imagery and Figure 2. Therefore the suggested location for the storm surveys would be between Sites A-D which is a 4km section of coast.

<u>Survey Plan</u>

Option A: Full area between Site A-D

- Topo- Intertidal profiles ~ every 100m (or ATV if possible)
- Alongshore array of PTs at MLWS ~every 300m
- Alongshore spaced ADV deployed at MLWS
- Video cameras located at Site C, one east and one west looking alongshore.
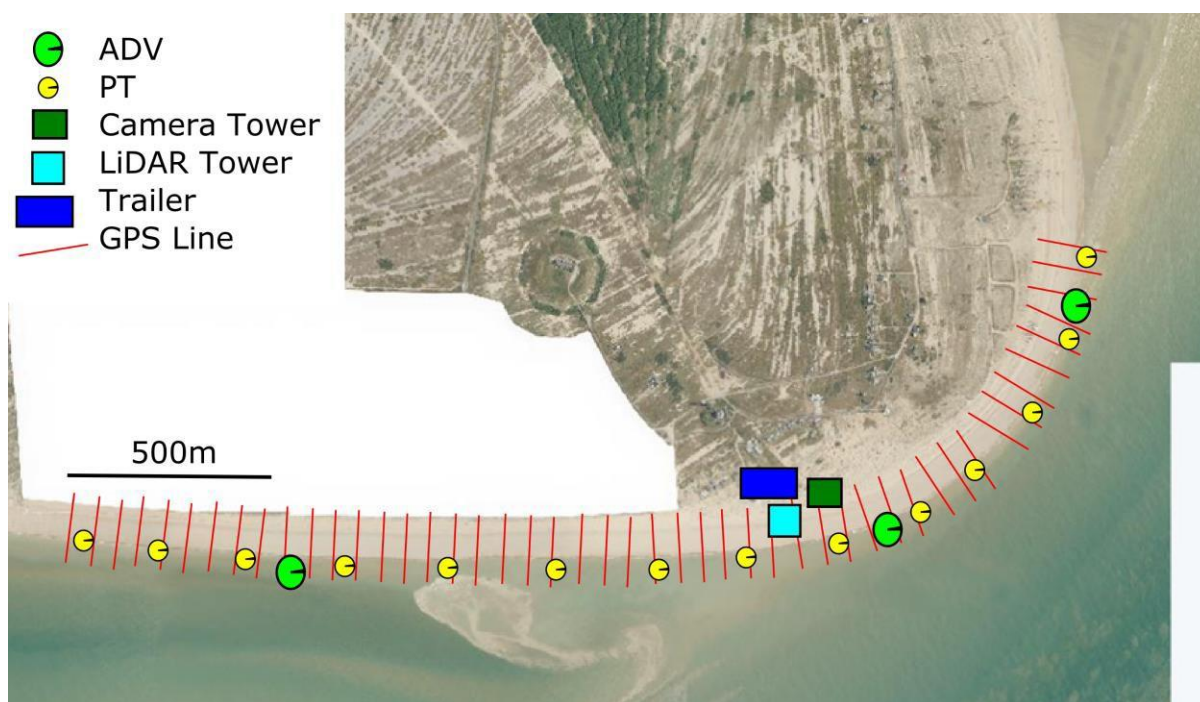
Figure 3, Option A, Full extent storm survey

Option B: Two sites e.g Site B and Site D, contrasting response depending on storm track

At each site;

- Topo- Intertidal profiles ~ every 50m for 1 km section
- Alongshore array of 7 PTs at MLWS ~every 150m
- Single ADV deployed at MLWS
- Video cameras located at one site or Site C, one east and one west looking alongshore.
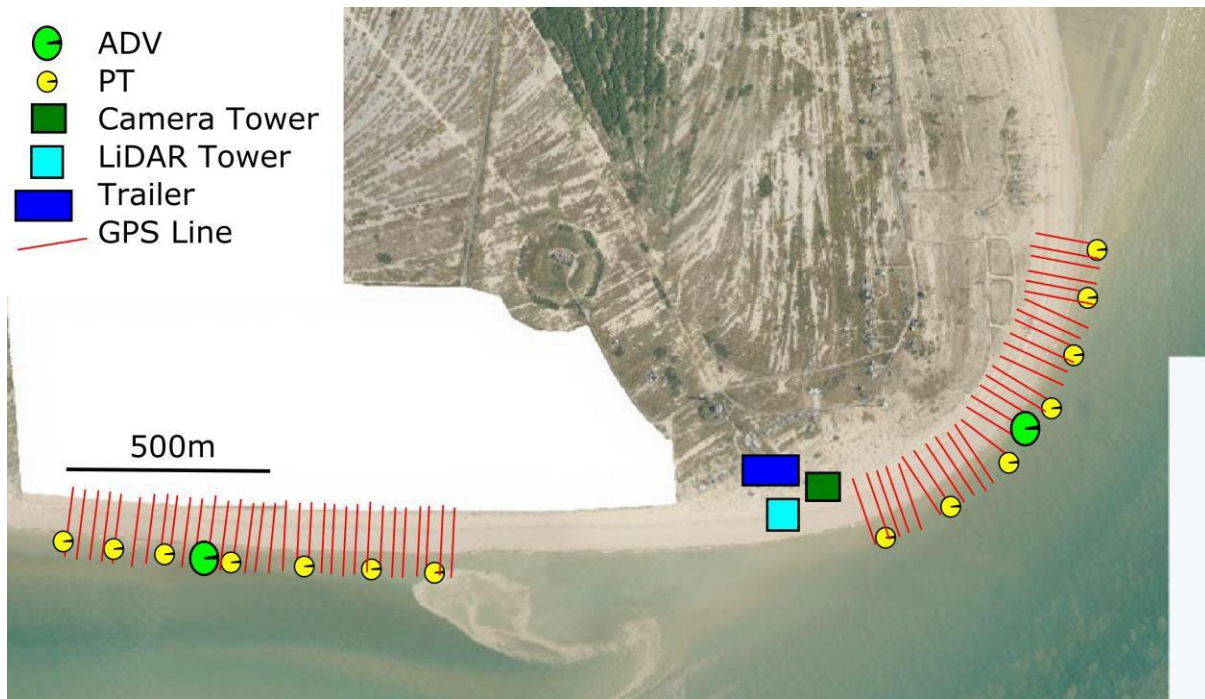
Figure 4, Option B, Two site storm survey

Naturally there are other combinations that can be considered. The site visits will tellus much about the possibly instrument locations, the bed material, access and otherlogistics.

Appendix E - Storm survey plan (Perranporth)

Storm Survey Planning Document: Perranporth

About
This is a planning document to be used during storm surveys undertaken at Perranporth (Perran Sands) as part of BLUE-coast.

Contacts for Permissions/Access;

Jon Cripps

Penhale Dunes Ranger
Cornwall Wildlife Trust
Tel: (01872) 273939 or 07500080385
Email: jon.cripps@cornwallwildlifetrust.org.uk

Lt Col (Ret'd) Andy Westcott

Commandant Cornwall
DIO SD Training, RAF St Mawgan, Newquay,
Cornwall, TR8 4HP
Civ: 01637 857157
Mil: 95423 7157
Mob: 07770 855048
Andrew Hewitt *will be the Key holder*

Survey Logistics

- Perranporth is 1.5hr drive (car/van) from Plymouth.
- Accommodation- preferably at Cubert as this is nearest to MOD access. More options in Perranporth town and Perran Sands holiday park.

Potential Plan – Post Call

Storm -3 days - Decide on team (minimum 5 persons required until all kit is deployed and surveyed in, options in table 1) preferably programme kit.
Storm -2 days - Pack and go to PPT, set up trailer and video. Programme and set up 2 x ADV, 2 x OBS and 14 PTs, if this has not already been completed prior to travelling. Construct 2 x scaffold frames and fix instruments to sand screws and frames.
Storm -1 day - Deploy and survey kit (total station of PTs), low tide surveys (unless very soon after monthly RTK). 1 frame will be fixed around neap low tide and 1 will be mobile. Both recovered at each low tide, batteries changed, data downloaded and redeployed. 1 to same neap low location, the other aiming for the inner surf zone during mid/high tide. 2 staff could leave at this point.
Storm - Check kit, deploy frame at low tide prior to peak, low tide surveys, turn cameras on at mid to high, recover frame on next low tide as detailed above.
Storm + 1 - Check kit, frame deployment and recovery and surveys, cameras on at mid to high. Review whether conditions warrant staying
Storm + 2/3/4/5 - Over these days following the storm, if conditions are worth sampling, low tide deployment and recovery of mobile frame as above, option to reduce survey effort. Pull out kit (takes 3 hours either side of low), take down camera, pack up and leave site.

Table 1: *Working windows and staff availability, see also table 2*

		HW				LW						Activity	Personnel				
		AM		PM		AM		PM									
		Time (GMT)	Height (m)	Time (GMT)	Height (m)	Time (GMT)	Height (m)	Time (GMT)	Height (m)	First light (GMT)	Last Light (GMT)		Oli Billson	Tim Poate	Kit Stokes	Aaron B	Jak McCaroll
M	9	01:49	6	14:23	6.3	08:22	1.7	20:54	1.5	07:40	17:17	Planning					
T	10	02:53	6.4	15:23	6.6	09:26	1.4	21:52	1.2	07:39	17:18						
W	11	03:50	6.8	16:17	6.9	10:22	1	21:44	0.9	07:38	17:20	Deployment					
T	12	04:41	7.1	17:07	7.1	11:13	0.7	23:32	0.7	07:37	17:21	Logging					
F	13	05:29	7.3	17:54	7.2					07:36	17:22						
S	**14**	06:14	7.3	18:38	7.1	00:18	0.7	12:46	0.6	07:35	17:24						
S	**15**	06:58	7.2	19:21	6.9	01:01	0.7	13:28	0.7	07:34	17:25						
M	16	07:39	7	20:01	6.6	01:41	0.9	14:08	1	07:33	17:27	Recovery					
T	31	07:13	7.1	19:32	6.8	01:14	1	13:37	0.9	07:18	17:49						

On site	O
Available	A
Not Available	X

Instrumentation:

- **3 self-logging RBR Solo pressure sensors alongshore (1 of which is both along and cross-shore)**;
    - Located above MLWN depending on tides. Move west ~50m for each PT at same elevation.
    - **Fixed in place with Sand screws, sensors inside scaffold housings**
    - **One cross-shore array of 13 sensors (including one of the alongshore ones)**
- **Video cameras**; two cameras logging at 4Hz during daylight. Require power and dry space for computers (usually our trailer) within 100m of cameras. Mounted on 5 m tower looking South alongshore and West, offshore.
- **ADV**; two mounted on scaffold H-frames carried into place, 1 fixed for entirety of the experiment, the other deployed and recovered on consecutive low tides, aiming to maximise time in the inner surf zone.
- **OBS**; two mounted alongside ADV on scaffold frames
    - Batteries changed and data downloaded on both frames whenever dry or every other low tide
- **RTK GPS**; Profile measured via ATV or on foot. Upper beach may need to be done on foot.
- **Total Station;** Used to survey in PTs

Set up shown in figure 1.

Site Overview:

Fig. 1a

Legend:
- ADV/OBS (green triangle)
- Weather Station (red circle)
- PT (black dot)

226
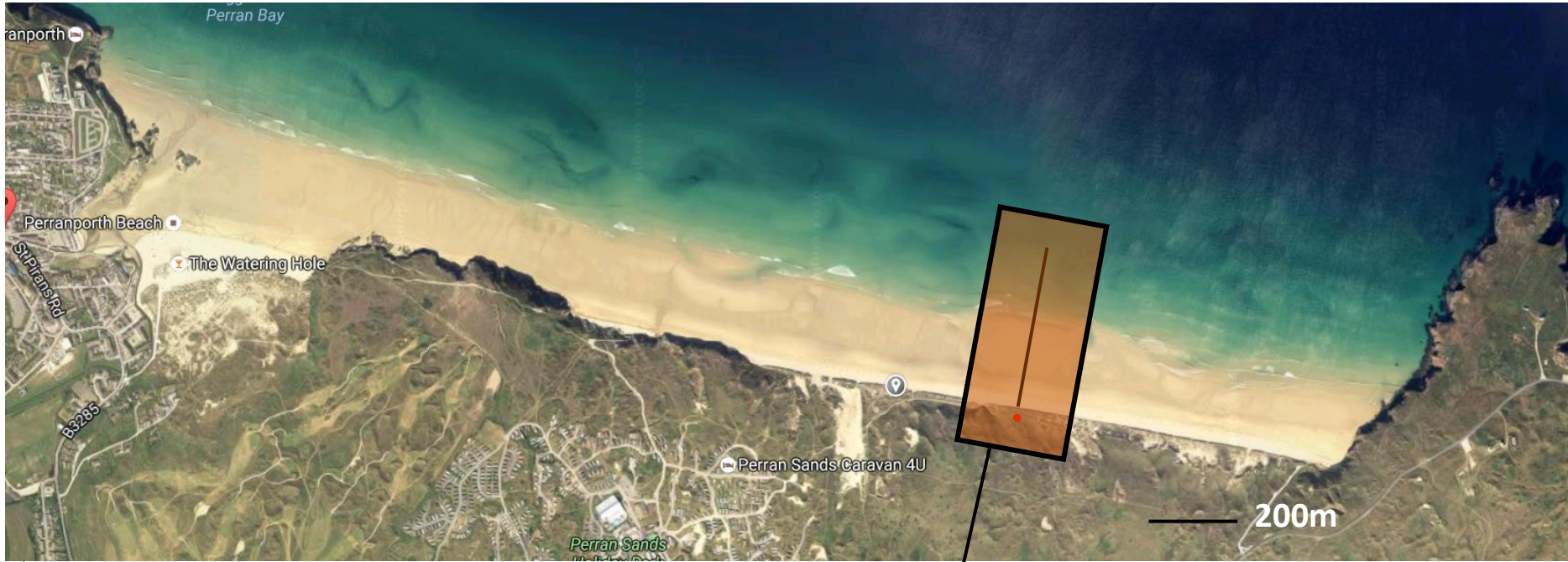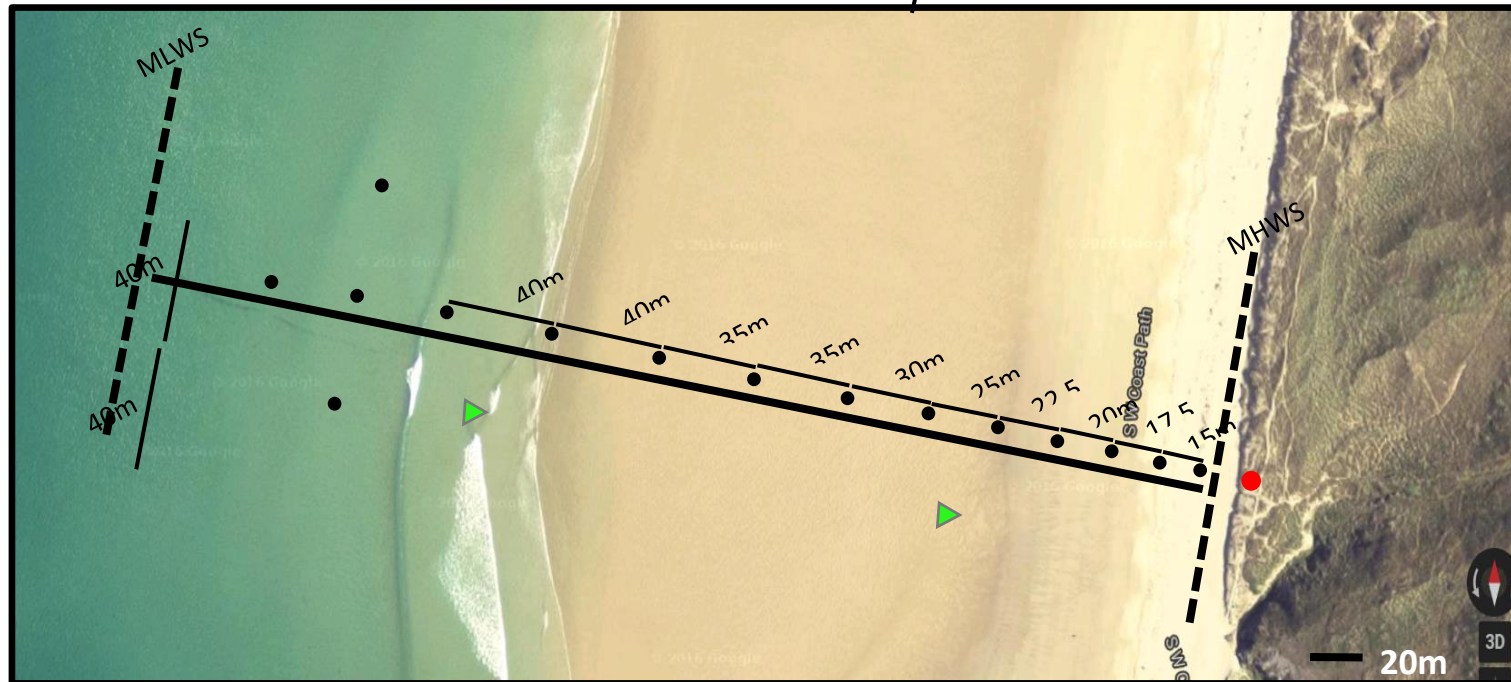
Table 2: Tidal information for January, colours vary dependant on range, from green (Springs) to

| | | | HW | | | | LW | | | | | |
| | | | AM | | PM | | AM | | PM | | | |
			Time (GMT)	Height (m)	Time (GMT)	Height (m)	Time (GMT)	Height (m)	Time (GMT)	Height (m)	First light (GMT)	Last Light (GMT)
January	S	1	06:50	6.9	19:07	6.6	00:50	1.3	13:13	1.3		
	M	2	07:28	6.8	19:46	6.5	01:27	1.4	13:51	1.4		
	T	3	08:08	6.6	20:28	6.3	02:05	1.5	14:31	1.5		
	W	4	08:52	6.4	21:15	6	02:47	1.7	15:17	1.7		
	T	5	09:43	6.2	22:11	5.8	03:35	1.9	16:10	1.9		
	F	6	10:44	6	23:18	5.7	04:34	2.1	17:16	2	07:33	17:12
	S	7	11:56	5.9			05:47	2.2	18:31	2	07:42	17:14
	S	8	00:35	5.7	13:13	6	07:08	2	19:47	1.8	07:41	17:16
	M	9	01:49	6	14:23	6.3	08:22	1.7	20:54	1.5	07:40	17:17
	T	10	02:53	6.4	15:23	6.6	09:26	1.4	21:52	1.2	07:39	17:18
	W	11	03:50	6.8	16:17	6.9	10:22	1	21:44	0.9	07:38	17:20
	T	12	04:41	7.1	17:07	7.1	11:13	0.7	23:32	0.7	07:37	17:21
	F	13	05:29	7.3	17:54	7.2					07:36	17:22
	S	14	06:14	7.3	18:38	7.1	00:18	0.7	12:46	0.6	07:35	17:24
	S	15	06:58	7.2	19:21	6.9	01:01	0.7	13:28	0.7	07:34	17:25
	M	16	07:39	7	20:01	6.6	01:41	0.9	14:08	1	07:33	17:27
	T	17	08:19	6.7	20:42	6.3	02:20	1.2	14:47	1.3	07:32	17:28
	W	18	08:59	6.3	21:23	5.9	02:58	1.5	15:26	1.7	07:31	17:29
	T	19	09:41	5.9	22:09	5.5	03:37	1.9	16:08	2.1	07:30	17:31
	F	20	10:31	5.5	23:07	5.3	04:23	2.3	17:01	2.4	07:29	17:33
	S	21	11:35	5.3			05:24	2.5	18:10	2.6	07:28	17:34
	S	22	00:21	5.1	12:55	5.2	06:41	2.6	19:28	2.6	07:27	17:35
	M	23	01:37	5.3	14:06	5.4	07:58	2.5	20:34	2.3	07:26	17:36
	T	24	02:38	5.6	15:01	5.7	08:58	2.2	21:25	2.1	07:25	17:37
	W	25	03:27	5.9	15:46	6	09:47	1.9	22:08	1.8	07:24	17:39
	T	26	04:07	6.3	16:25	6.3	10:28	1.6	22:46	1.5	07:23	17:42
	F	27	04:45	6.6	17:02	6.6	11:06	1.3	23:23	1.3	07:22	17:43
	S	28	05:21	6.9	17:38	6.8	11:43	1.1			07:21	17:45
	S	29	05:57	7	18:15	6.9	00:00	1.1	12:21	0.9	07:20	17:46
	M	30	06:35	7.1	18:53	6.9	00:37	1	12:59	0.9	07:19	17:48
	T	31	07:13	7.1	19:32	6.8	01:14	1	13:37	0.9	07:18	17:49

Appendix F - Storm survey plan (Minsmere)

About

This is a planning document to be used during storm surveys undertaken at Minsmere and Sizewell as part of BLUE-coast.

Contacts for Permissions/Access;

Minsmere

NT Dunwich Richard Gilbert dunwichheath@nationaltrust.org.uk 01728648501

Natural England; Emma Hay Emma.hay@naturalengland.org.uk 01379788814

Sizewell

All these people will need to be notified when we are going out for the survey – pass on mobile number in case they need to contact you (Mark S and Dave S are key).

- Mark Scrancher (Safety Head) and Angus Bloomfield (Sizewell B) (angus.bloomfield@edf- energy.com and mark.scrancher@edf-energy.com)
- Dave Sayer (security; Sizewell B and C) (david.sayer@edf-energy.com; 01728 653005)
- Pat Kearney and Paul Stanton (Sizewell A) (patrick.k.kearney@magnoxsites.com and paul.j.stanton@magnoxsites.com)
- Alastair Bissett (Waveney & Suffolk Coastal DCs) (Alistair.Bissett@eastsuffolk.gov.uk)
- Tony Dolphin and Dean Foden (CEFAS) (tony.dolphin@cefas.co.uk and dean.foden@cefas.co.uk)
- Noel Cattermole (local fisherman) (pathogan2011@hotmail.co.uk; 01728 830282; Gap House)
- Colin Taylor (environmental manager who leads on new build) (colin.taylor@edf- energy.com; 01452 652383)

Survey Logistics

- Minsmere is 6/7hr drive (car/van) from Plymouth.
- Accommodation locally lots available, with luck NT coastguard houses. Decision to Go

Day 0 – Kit check and packed. PTs Programed (fixed to sand screws if necessary e.g. tide limited)

Day 1 – Drive. Arrival = Low tide, get PTs in and start survey. High tide, get Video tower in place. Day 2 - Full Survey of beach and Instruments

Day 3 – Ideally storm peak. Surveys.

Day 4 – Surveys and recover instruments

Day 5 – Drive

Tide Times and Personnel Availability

Tide Times and Personnel Availability

Date	HW	Elev	LW	Ele	LW	Activity	Tim Poate	Kit Stokes	Peter Ganderton	Aaron Barrett	Kris Inch	Oli Billson	?
01/10/2016						Deployment							
02/10/2016													
03/10/2016													
04/10/2016						Logging							
05/10/2016													
06/10/2016													
07/10/2016						Recovery							
08/10/2016													

On site = O
Available = A
Not Available = X

Tides

Tide conversion: -1.6 CD-ODN

MHWS	0.8
MHWN	0.4
MSL	-0.19
MLWN	-0.8
MLWS	-1.3

Site Overview;

These two sites cover a 4km stretch on the east coast. Sizewell is a site we are familiar with having previously explore the site for another project.

The focus will be Minsmere, but we will also do topo surveys and deploy PTs at Sizewell.

They are both exposed to the same storm weather systems and therefore the principal interest would be the alongshore variability in the morphological response and hydrodynamics.

Access is good at Sizewell with parking close to the beach.

At Minsmere just north of the reserve is a national Trust car park that offers parking very close to the beach and importantly at an elevated position which will be of great benefit for the video cameras.

Figure 1, Site overview for Minsmere andSizewell

Figure 2, PT locations and Survey lines for Minsmere. 100m profile lines.

Figure 3, View south from cliff top (similar to video camera view)
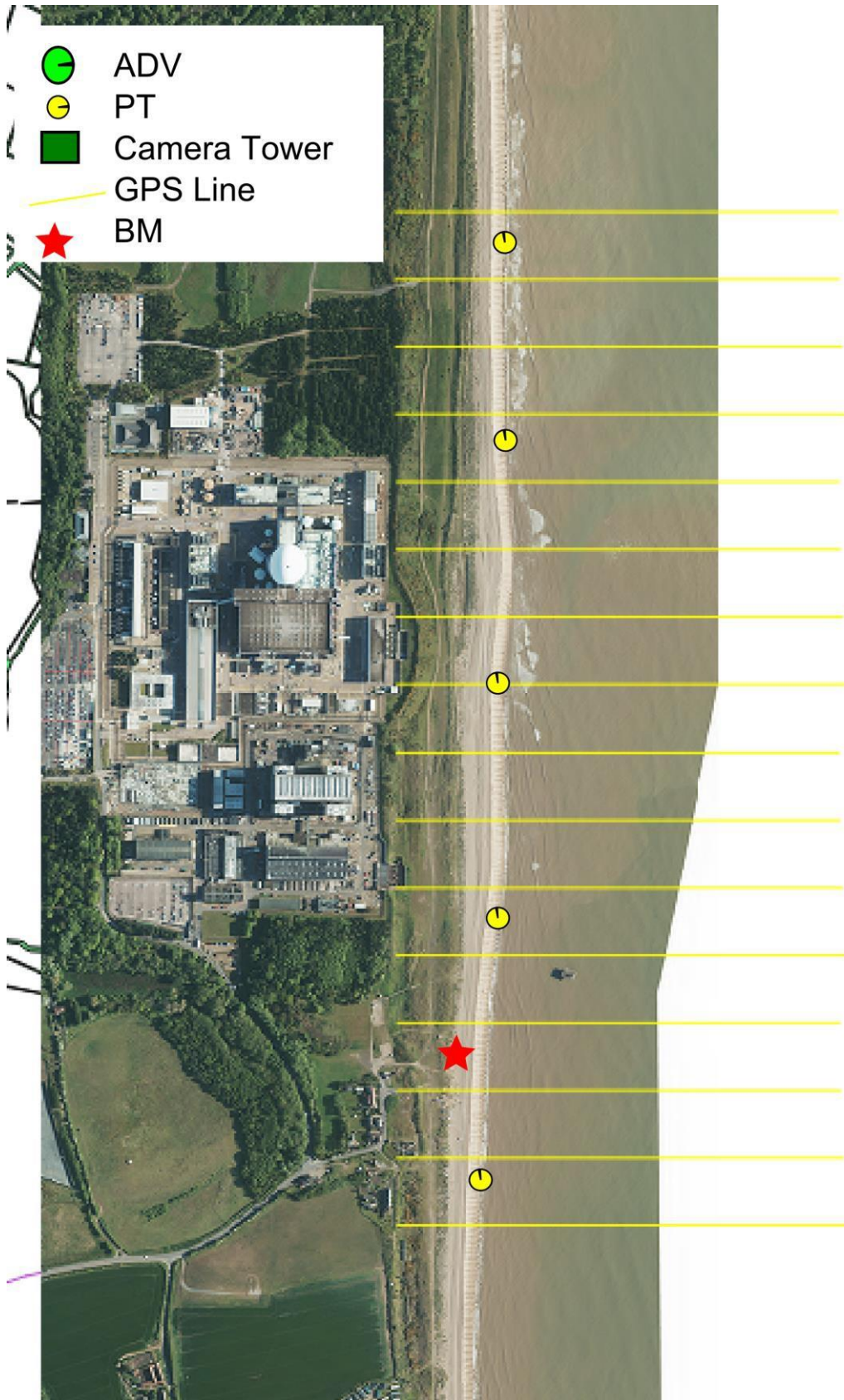
Figure 4, Survey lines and PT locations for Sizewell

Instrumentation

Minsmere

5 self-logging RBR Solo pressure sensors alongshore;

Located MLWN depending on tides.

Fixed in place with Sandscrews, sensors inside scaffold housings

One cross-shore array of 3/4 sensors

Video cameras; two cameras logging at 4Hz during daylight from Dunwich NT parking. Mounted on 5 m tower looking South alongshore.

ADV; One mounted on triangular frames carried into place, spread alongshore. Likely single scaffold pole to provide support.

RTK GPS; Profile measured on foot. ATV for carrying kit.

Dunwich

5 self-logging RBR Solo pressure sensors alongshore;

Located MLWN depending on tides.

RTK GPS; Profile measured on foot. ATV for carrying kit.

GPS Base

Coordinates base station: X = 647613.026 m; Y= 263013.851 m; Z = 3.879 m

Red paint mark on seaward-most of several concrete slabs, but buried by gravel and vegetation

Currently requesting further benchmarks closer to Dunwich

WPS Insurance Brokers

& **Risk Services**

Spargo House

10 Budshead WayPlymouth

Devon PL6
5FE

Email: mail@wpsinsurance.co.uk

www.wpsInsurance.co.uk

Tel: 01752 670440

Fax: 01752 229125

TO WHOM IT MAY CONCERN

Re: **UNIVERSITY OF PLYMOUTH & SUBSIDIARY COMPANIES**

We act as insurance brokers to the above company and at their request confirm they hold the following liability insurances for their business operations of Educational establishment & property owners

Insurer Policy	**Zurich Municipal**
No Renewal	**NHE-05CA02-0013**
Date	**01/08/2017**
Employers' Liability	**£50 million**
Public Liability	
	£50 Million
Products Liability	
	£50 Million
Professional Negligence -	
	£10 Million
Governors Liability	
	£ **5 Million**
Third Party Property Damage Excess	
	£100

Please note this summary of cover has been prepared purely as confirmation of the insurance available and is subject to the terms and conditions of the policy detailed.

We accept no responsibility for any inadvertent or negligent act, error or omission on our part in preparing the statement or for any loss, damage or expense incurred by the recipient arising fromreliance on the information given.

We owe no legal duty or otherwise to any third party.

Kind regards.

Yours sincerely

ARiddell.

Anita Riddell Cert CII MlnstLM Assoc CIPDBroker

Direct Line: 01752 675496

E Mail: anita.r@wpsinsurance.co.uk

Appendix G - Storm survey plan (Beesands)

Storm Survey Planning Document: Start Bay: Jan-Mar 2018

1. About

This planning document is to be used during the storm survey to be undertaken at Start Bay as part of BLUE-coast WP1. The deployment can be separated into a longer (STBW18) and shorter (STB_Storm18) deployment.

STBW18 –Jak McCarroll

The longer deployment comprises pressure transducers in 5 locations around Start Bay (Fig 1), 4 subtidal ADCPs and an offshore directional wave buoy as well as single beam bathymetry and walked topographic profiles at ~30 locations around the embayment. These data will be used to calibrate a Delft3D model, which will be used to examine longshore sediment transport within the embayment, focusing on headland bypassing, and the role of the Skerries Bank in modifying hydro-morphodynamics.

STB_Storm18 – Oliver Billson (PhD Student)

The short term deployment, located at North Beesands, comprises of a cross-shore array of 5 PTs and a video tower located on the village green. An ADV on triangular frame will also be deployed on the rock platform at the northern end of Beesands/southern end of Slapton (Torcross). Data collected by the ADV also plays a key role in the STBW18 research. Of the 31 profiles mentioned above, 11 located in the vicinity of Beesands will be surveyed at least once daily. This deployment aims to collect wave, current and topographic data in order to examine how the role of infragravity waves in sediment transport varies under a range of offshore wave conditions and beach states.

2. Contacts for Permissions/Access;

Name	Organisation	Email	Mobile	Phone	Comment
Gill Claydon	Stokenham Council	clerk@stokenham-pc.gov.uk			Given access to Beesands
Winky					
Alan	(Winky's son)		07968 483 588		
Charles Dixon	Toll Estates	CDixon@savills.com	44 (0) 7798 627 664	+44 (0) 1392 294 892	Has given quad access to Strete
Andy Pratt	Slapton Field Centre	andy.sl@field-studies-council.org	07791 498274	01548 581514	Has given quad access to Torcross
Sarah Clark	IFCA - Devon and Severn Inshore Fisheries and Conservation Authority	s.clark@devonandsevernifca.gov.uk		01803 854648	
Beshlie Pool	South Devon and Channel Shellfishermen	sdandcshellfishermen@gmail.com	07480 858 260		
Ruth Crundwell	Natural England	rcrundwell@naturalengland.org.uk			Approved intertidal work.
Jon Grimes	Natural England	Jon.Grimes@naturalengland.org.uk	07789 278621	0208 026 7464	Has given quad access to Strete
	MMO - Marine Management Org.	Exemptions obtained through online applications			
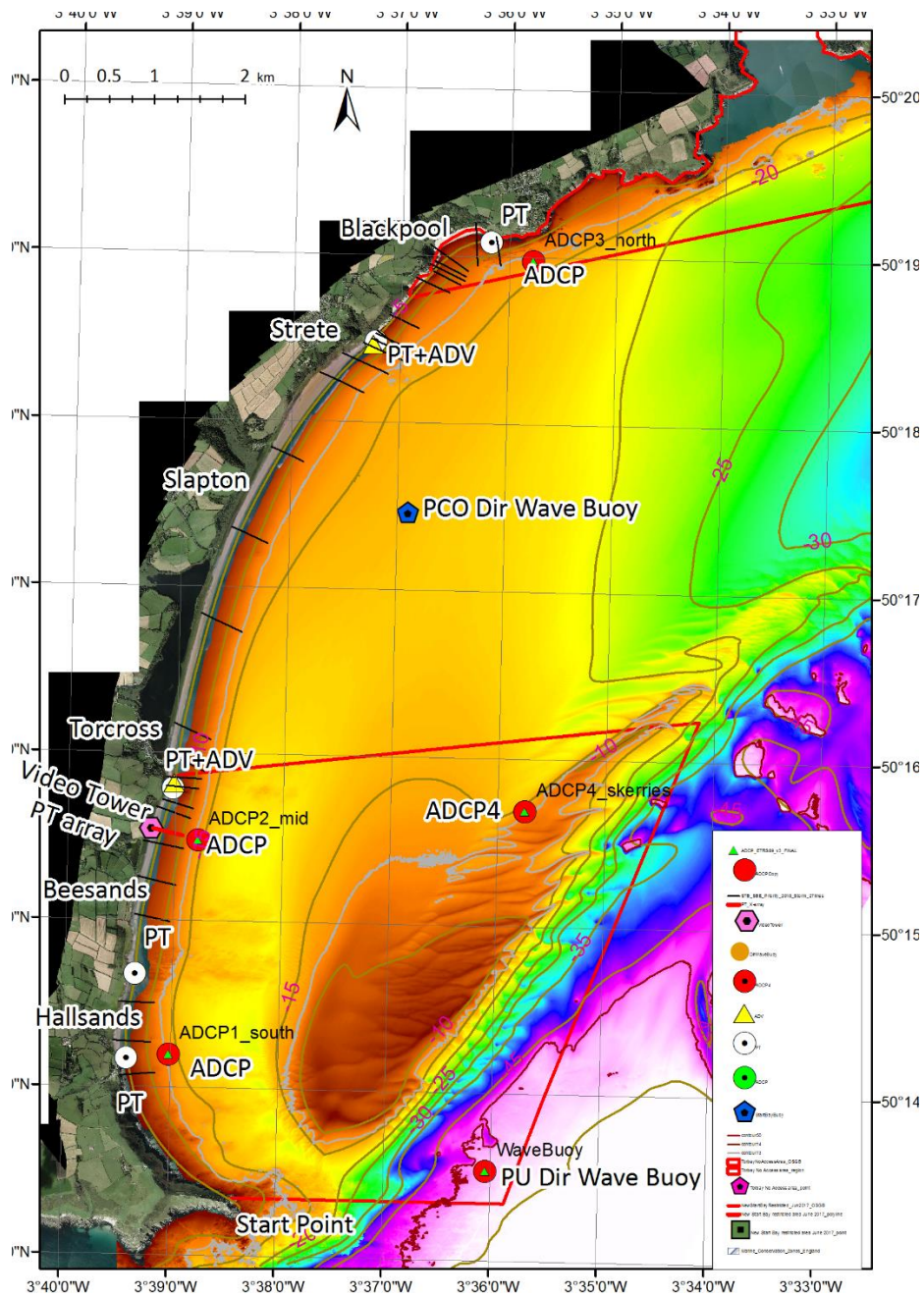
Fig 1. Map of Start Bay with instrument positions. Priority lines in black. Red polygons are no trawling areas.

3. Survey Logistics

- Beesands is a 75 minute drive (car/van) from Plymouth.
- Accommodation for 6 people- Cob Cottage, Beeson
    - Initially booked 18/02-25/02
    - Keys in safe in porch, code: 0515A

3.1 Potential Plan – Post Call

Storm -3 days - Decide on team (minimum 5 persons required until all kit is deployed and surveyed in, options in table 1) preferably programme kit before packing but not essential.

Storm -2 days - Pack and travel to Beesands, ≥2 people set up trailer and video. ≥2 people programme and set up 1 x ADV, 5 PTs, if this has not already been completed prior to travelling. ≥2 people Tonk in 8 x long vertical scaffold poles and fix PTs. Deploy ADV frame. Ideally 3 people will then do GCPs for the camera tower.

Storm -1 day – Survey kit, low tide topo surveys. Check ADV is logging and download every 3 days (conditions permitting). Do camera GCPs if not already done. Team could drop to 2 people staying on site with a further 2/3 people travelling down daily for low tide.

Storm - Check kit, low tide surveys, turn cameras on during day light hours.

Storm + 1/2/3/4/5 – Remain on site until conditions subside. Plan for post storm single beam. *SURVEY PRIORITY TOPO LINES DAILY (see Section 3.3)*.

Storm pull out - Requires ≥4 people (takes 3 hours either side of low), clear accommodation, pull out scaffold, remove ADV, take down camera, pack up and leave site.

Table 1: *Worked example of working windows and staff availability, tidal heights in ODN, see also table 2*

On site	O
Available	A
Not Available	X

		HW				LW						Activity	Personnel									
		AM		PM		AM		PM					Oli Billson	Jak	Aaron B	Jet	Ben Hall	Tim P	Tim S	Gerd	Paul	Peter G
		Time (GMT)	Height (m)	Time (GMT)	Height (m)	Time (GMT)	Height (m)	Time (GMT)	Height (m)	First light (GMT)	Last Light (GMT)											
M	12	03:18:00	1.5	15:44	1.5	09:52	-0.7	21:17	-0.6				O	O		O	O					X
T	13	04:08:00	1.8	16:30	1.7	10:41	-1	22:14	-0.8			ADV dep.	O	O	O	O	O					X
W	14	04:50:00	2	17:11	1.9	11:22	-1.2	22:58	-1.1				O	O		O	O					X
T	15	05:29:00	2.2	17:50	2	11:59	-1.4	23:36	-1.3			Topo	O			O	O					X
F	16	06:06:00	2.3	18:27	2.1	00:12	-1.5	12:34	-1.6			Topo/ADV	O	O	O	O	O					X
S	17	06:43:00	2.4	19:04	2.2	00:47	-1.6	13:09	-1.7			Prep	O									
S	18	07:20:00	2.4	19:40	2.2	01:21	-1.7	13:42	-1.8			Prep	O									
M	19	07:55:00	2.3	20:14	2.1	01:55	-1.7	14:16	-1.7	06:40	18:05	Deploy/Bathy	O	O	O		O	O	O	O	O	A
T	20	08:27:00	2.2	20:44	2	02:28	-1.6	14:49	-1.6	06:38	18:07	Topo/ADV	O	O		O	O					
W	21	08:55:00	2	21:12	1.8	03:02	-1.4	15:23	-1.4	06:36	18:09		A									
T	22	09:25:00	1.8	21:47	1.6	03:39	-1.2	16:03	-1.2	06:34	18:11		A									
F	23	10:10:00	1.6	22:44	1.5	04:23	-1	16:52	-0.9	06:32	18:13		A				X					
S	24	11:21:00	1.4			05:23	-0.7	18:01	-0.7	06:30	18:15		A				X					
S	25	00:10:00	1.4	13:02	1.3	06:45	-0.6	19:31	-0.6	06:28	18:17		A				X					

3.2 Tides

Tide conversion: from CD to ODN -3m
Max Tide range: 5.3m
MHWS: 2.2m ODN
MHWN:
MSL: 0.2m ODN
MLWN:
MLWS: -2m ODN
See table 2

3.3 Instrumentation:

- **5 self-logging RBR Solo pressure sensors cross-shore**
    - Located above MLWN depending on tides. Move west ~50m for each PT at same elevation.
    - **Fixed to long scaffold pole with jubilee clips, sensors inside scaffold housings.**
- **Video cameras**; two cameras logging at 4Hz during daylight. Require power and dry space for computers (usually our trailer) within 100m of cameras. Mounted on 5 m tower looking north alongshore and east, offshore.
- **ADV**; One mounted on triangle frame carried into place, fixed in predefined position at North Beesands.
- **RTK GPS**; Profiles measured via ATV or on foot. Lower beach may need to be done on foot.

Set up shown in Figure 2.

3.4 Daily PRIORITY line surveys during storm deployment

The ~30 PRIORITY topo lines will be surveyed ~daily during the storm period. It is likely the Beesands lines will be able to be surveyed every day, but the other lines (HS, SS, Forest Cove, BK) may be surveyed every second day.
- 2 teams of 2-3 people.
- 2 bases, extra teaching kit for rovers.
- Team 1 surveys Beesands (and Hallsands).
- Team 2 surveys Torcross to Blackpool sands.

Oli's proposed deployment for STB storm survey, aiming to record the presence (or otherwise) and response to (or otherwise) infragravity waves under a range of wave and tidal heights:

- Revised design to improve reliance to berm migration. 18 x 2m vertical and 12 x 2m horizontals.
- 6 PTs, spaced between 3m and -0.3m ODN, fixed to vertical scaffold arrow head, comprising of 3, 2m verticals driven into gravel, join by 2 horizontals.
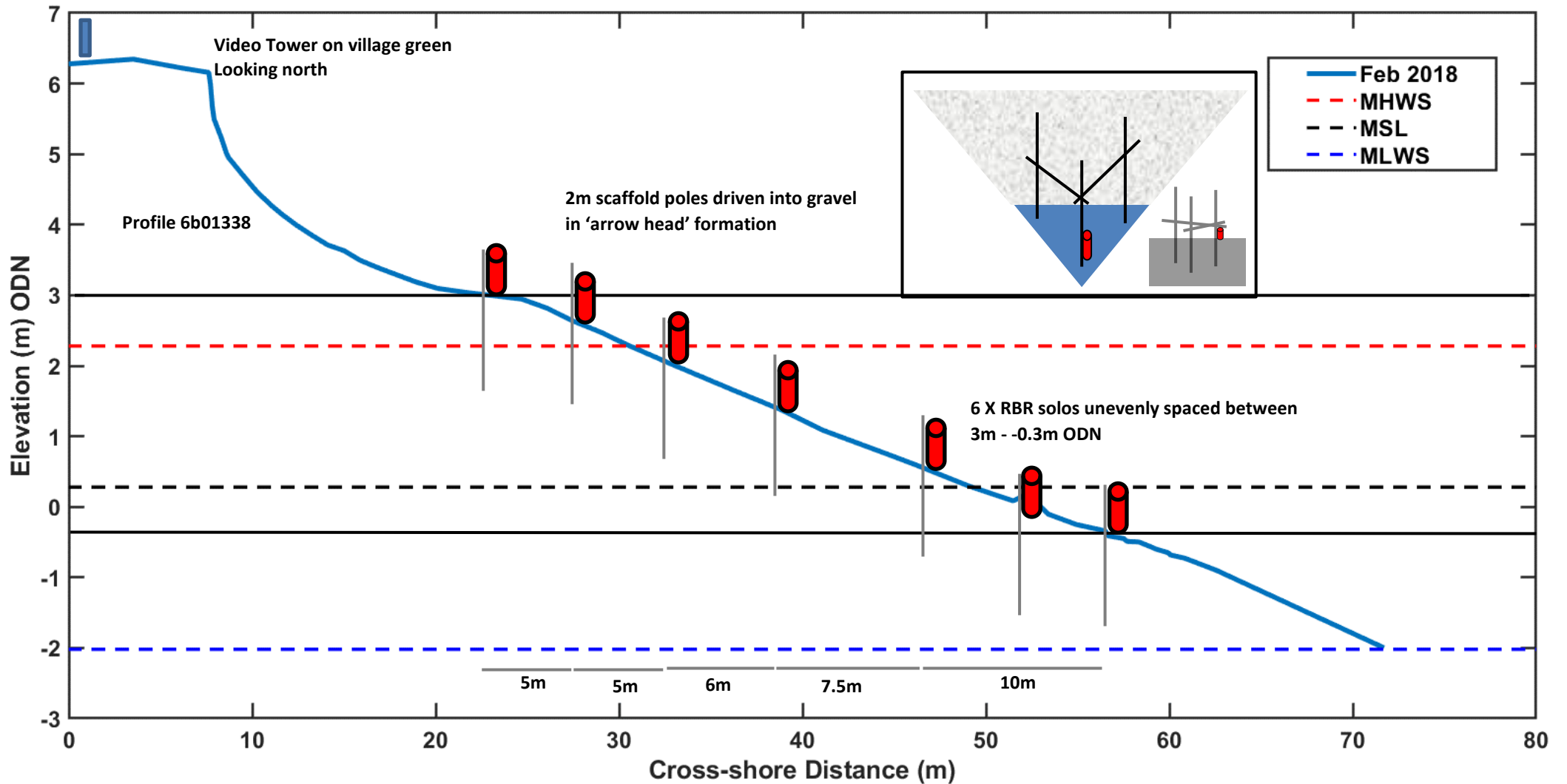- Video tower data useful for record of infragravity swashes.
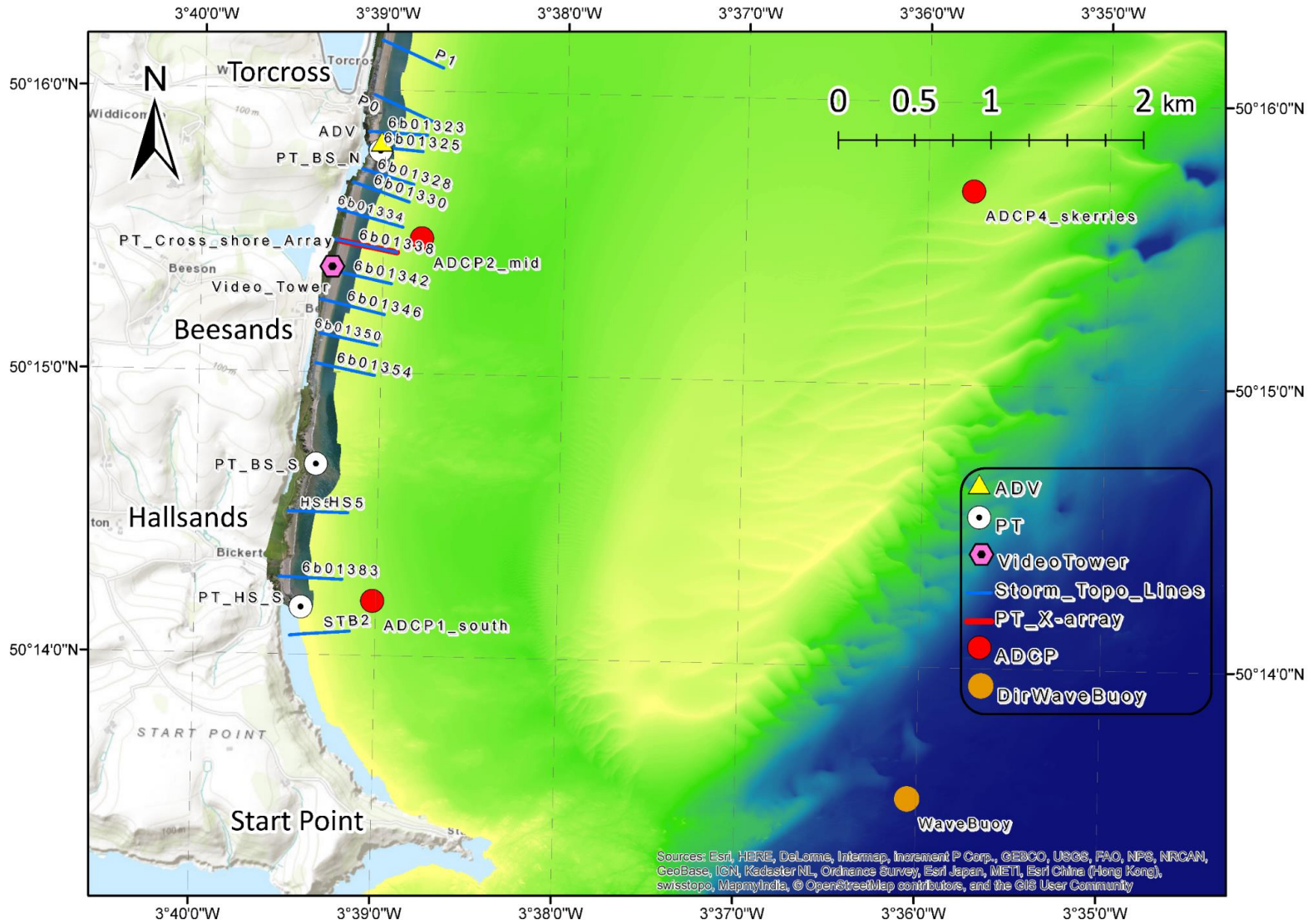
Fig 2. Cross-shore PT array.

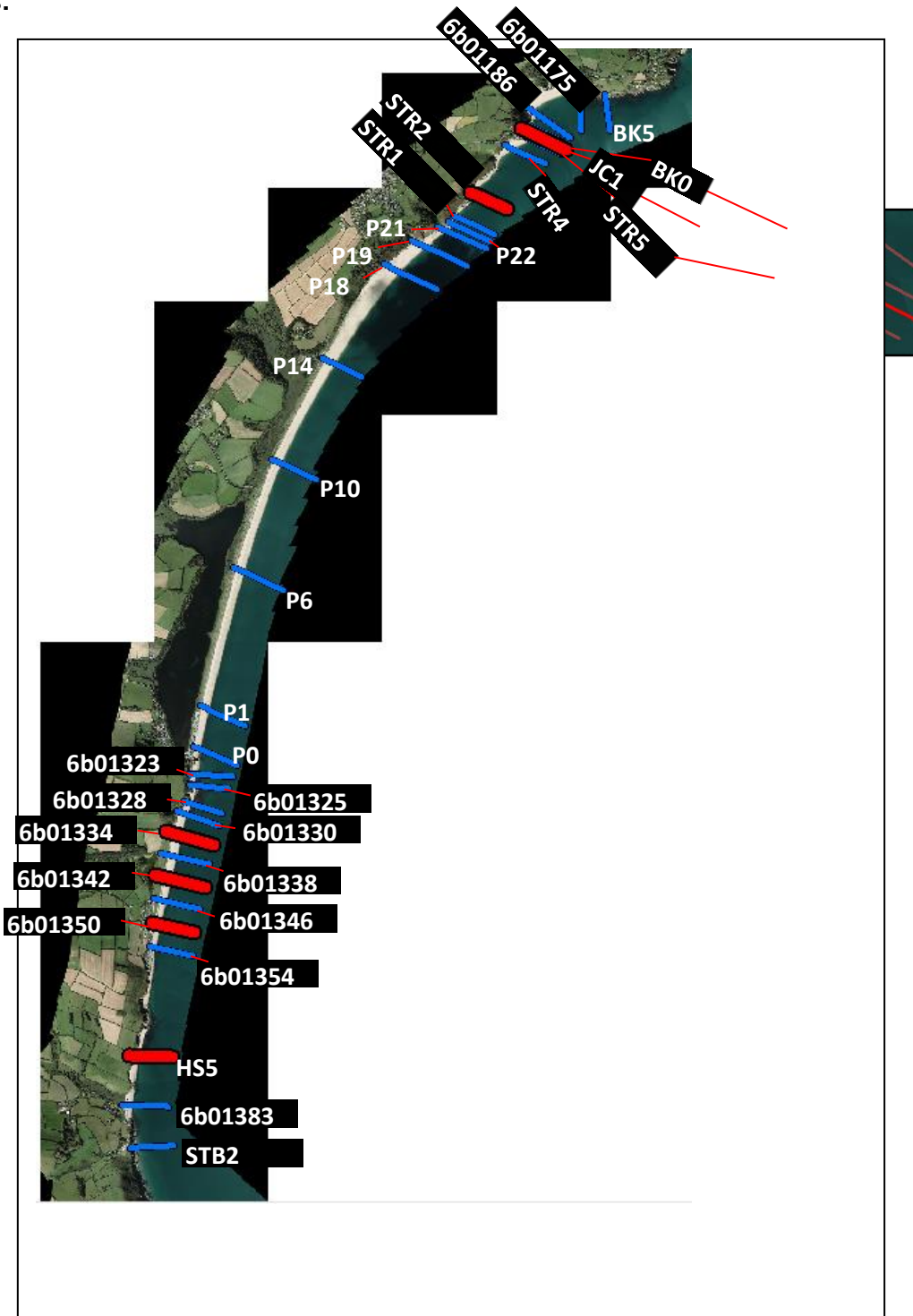Fig 3. Beesands lines and instruments.

STB Tidal Height predictions (Tides for Fishing)

Table 2

			HW						LW					
			AM			PM			AM			PM		
			Time (GMT)	CD (m)	ODN (-3m)	Time (GMT)	CD (m)	ODN (-3m)	Time (GMT)	CD (m)	ODN (-3m)	Time (GMT)	CD (m)	ODN (-3m)
T	1		06:14	5.6	2.6	18:42	5.5	2.5	00:17	1	-2	12:44	0.8	-2.2
F	2		07:02	5.7	2.7	19:28	5.5	2.5	01:04	0.8	-2.2	13:30	0.7	-2.3
S	3		07:45	5.7	2.7	20:09	5.4	2.4	01:49	0.8	-2.2	14:14	0.7	-2.3
S	4		08:24	5.5	2.5	20:45	5.2	2.2	02:31	0.9	-2.1	14:55	1	-2
M	5		08:58	5.3	2.3	21:18	4.9	1.9	03:10	1.2	-1.8	15:33	1.3	-1.7
T	6		09:31:00	5	2	21:50	4.7	1.7	03:47	1.6	-1.4	16:09	1.7	-1.3
W	7		10:05:00	4.7	1.7	22:28	4.4	1.4	04:23	1.9	-1.1	16:47	2	-1
T	8		10:48:00	4.4	1.4	23:20	4.2	1.2	05:04	2.3	-0.7	17:31	2.4	-0.6
F	9		11:52:00	4.2	1.2				05:57	2.6	-0.4	18:33	2.6	-0.4
S	10		00:44:00	4.1	1.1	13:27	4.1	1.1	07:13	2.7	-0.3			
S	11		02:14:00	4.2	1.2	14:46	4.3	1.3	08:45	2.6	-0.4	19:56	2.6	-0.4
M	12		03:18:00	4.5	1.5	15:44	4.5	1.5	09:52	2.3	-0.7	21:17	2.4	-0.6
T	13		04:08:00	4.8	1.8	16:30	4.7	1.7	10:41	2	-1	22:14	2.2	-0.8
W	14		04:50:00	5	2	17:11	4.9	1.9	11:22	1.8	-1.2	22:58	1.9	-1.1
T	15		05:29:00	5.2	2.2	17:50	5	2	11:59	1.6	-1.4	23:36	1.7	-1.3
F	16		06:06:00	5.3	2.3	18:27	5.1	2.1	00:12	1.5	-1.5	12:34	1.4	-1.6
S	17		06:43:00	5.4	2.4	19:04	5.2	2.2	00:47	1.4	-1.6	13:09	1.3	-1.7
S	18		07:20:00	5.4	2.4	19:40	5.2	2.2	01:21	1.3	-1.7	13:42	1.2	-1.8
M	19		07:55:00	5.3	2.3	20:14	5.1	2.1	01:55	1.3	-1.7	14:16	1.3	-1.7
T	20		08:27:00	5.2	2.2	20:44	5	2	02:28	1.4	-1.6	14:49	1.4	-1.6
W	21		08:55:00	5	2	21:12	4.8	1.8	03:02	1.6	-1.4	15:23	1.6	-1.4
T	22		09:25:00	4.8	1.8	21:47	4.6	1.6	03:39	1.8	-1.2	16:03	1.8	-1.2
F	23		10:10:00	4.6	1.6	22:44	4.5	1.5	04:23	2	-1	16:52	2.1	-0.9
S	24		11:21:00	4.4	1.4				05:23	2.3	-0.7	18:01	2.3	-0.7
S	25		00:10:00	4.4	1.4	13:02	4.3	1.3	06:45	2.4	-0.6	19:31	2.4	-0.6
M	26		01:50:00	4.5	1.5	14:33	4.5	1.5	08:24	2.2	-0.8	21:05	2.1	-0.9
T	27		03:08:00	4.8	1.8	15:44	4.8	1.8	09:47	1.8	-1.2	22:15	1.7	-1.3
W	28		04:12:00	5.1	2.1	16:44	5.1	2.1	10:47	1.3	-1.7	23:11	1.2	-1.8

February

STB Control points (OSTN15)

6bMU26-1_E2_01	282823.6	44086.88	6.202	E2
6bMU26-1_E2_02_Slapton	282824.1	44083.2	6.269	E2
E21130120_2015	282357.4	42190.4	5.317	E2
6bMU25-2_E2_01_check	285500	47875.29	6.433	E2
6bMU25-2_E2_02_base	285454.9	47861	6.455	E2
6bMU26-3_E2_01_check	281746.1	38816.64	5.917	E2
BEE2	281976	40475.26	6.288	RTK
BEECHECK	281971.8	40475.06	6.305	E2
E21130103	281987.4	40526.36	6.079	E2
6bSU26-3_E3_01	281775.1	38770.11	16.086	E3

Profile Names:

South Hams
District Council

Licensor	South Hams District Council, Follaton House, Plymouth Road, Totnes, Devon, TQ9 5NE.
Licensee	Plymouth University Coastal Research Group, Third Floor, Marine Building, Artillery Place, Plymouth, PL4 0LU.
The Permission	The licensee will be permitted to site a small trailer and erect a 5m high camera tower on "The Village Green" Beesands, adjacent to the public car parking area.
Duration of the Licence	The Licence to commence on the 1st February & expire on the 30th March 2018. Permitted hours of access 24 hours 7 days per week.
Use	To provide access and a site for Plymouth University Research Equipment, for research purposes.
Indemnity	The Licensee shall indemnify South Hams District Council against any loss or damage, or liability suffered, by the District Council or any third party, howsoever arising from the grant of this licence, and the Licensee's activities.
Public Liability	The Licensee shall hold public liability insurance of at least £5,000,000 for any single incident and shall indemnify the Licensor against all third party losses, injuries or claims. It will be the responsibility of the licensee to determine the appropriate level of cover reflecting the nature of the Licensee's activities and the perceived level of risk.
Forfeiture	In the event of the Licensee being in breach of any of the terms and conditions of this agreement or for any other Health & Safety reason, the Licensor will be permitted to terminate the agreement forthwith.
Nuisance	The Licensee shall not permit anything to be done in or upon the land or any part thereof which in the opinion of the Licensor may cause a nuisance or unreasonable annoyance or inconvenience to the Licensor or the owners or occupiers of nearby properties, or visitors, or infringe in any way the enjoyment and use of "The Village Green".
Maintenance	The Licensee shall keep the land in a clean and tidy condition.
Works	On termination of the Licence, the Licensee shall vacate the land and leave it in a good repair and in a clean and tidy condition. Any damage shall be reinstated to the Licensors reasonable satisfaction.
Security	The Licensee shall be responsible for any security arrangements that may be required in respect of their equipment.

ZURICH
MUNICIPAL

To Whom It May Concern

Our ref: PG\IND   4 July, 2017

Zurich Municipal Customer: **University of Plymouth and Subsidiary Companies**

This is to confirm that University of Plymouth and Subsidiary Companies has in force with this Company until the policy expiry on 31 July 2018 Insurance incorporating the following essential features:

Policy Number:	NHE-05CA02-0013	
Limit of Indemnity:		
Public Liability:	£ 50,000,000	any one event
Products Liability:	£ 50,000,000	for all claims in the
Pollution:		aggregate during period of insurance
Employers' Liability:	£ 50,000,000	any one event inclusive of costs

Excess:
Public Liability/Products Liability/Pollution: Nil any one event
Employers' Liability: Nil any one claim

Indemnity to Principals:
Covers include a standard Indemnity to Principals Clause in respect of contractual obligations.

Full Policy:
The policy documents should be referred to for details of full cover.

Yours faithfully

Underwriting Services
Zurich Municipal
Farnborough